CRANFIELD UNIVERSITY

Eduardo Sepulveda Palacios

Conceptual Design Synthesis and Multidisciplinary Optimisation of Unmanned Combat Aerial Vehicles

School of Aerospace, Transport, and Manufacturing
PhD in Aerospace

PhD
Academic Year: 2015 - 2019

Supervisors: Professor Howard Smith
and Professor John Fielding
December 2019

CRANFIELD UNIVERSITY

School of Aerospace, Transport, and Manufacturing
PhD in Aerospace

PhD

Academic Year 2015 - 2019

Eduardo Sepulveda Palacios

Conceptual Design Synthesis and Multidisciplinary Optimisation of
Unmanned Combat Aerial Vehicles

Supervisors: Professor Howard Smith
and Professor John Fielding

December 2019

ABSTRACT

The purpose of this research is to investigate and develop conceptual design methodologies and computational tools appropriate to the design and analysis of low-observable Unmanned Combat Aerial Vehicles (UCAVs), performing a wide variety of missions, with various payload and performance requirements, as well as a wide range of operational constraints, from subsonic to high supersonic flight regimes.

Undoubtedly, unmanned aircraft have transformed many aspects of aeronautics and aviation, with military applications often leading these transformational efforts. UCAVs have emerged as a potential strategy to counter technological, operational, and economical challenges to the future of aerial warfare. These challenges include an aging fleet of 4th generation fighters, the deployment of new, advanced 4^{+} and 5th generation platforms, the reported high vulnerability of current unmanned aerial vehicles, as well as the future development of hypersonic vehicles and weapons.

In order to investigate future aircraft configurations, the GENUS aircraft design environment was envisioned by Prof. Howard Smith at Cranfield University's Aircraft Design Group in 2012. This framework relies on a central architecture with high degrees of modularity and flexibility capable of designing, analysing, and optimising several *species* of aircraft with similar analysis tools, revealing the real differences and potential advantages of new designs.

Mass estimation, propulsion, aerodynamics, performance, radar cross section estimation, and aero-thermal analysis tools have been integrated into the GENUS framework in order to investigate the design space of UCAVs. Validation of these methods has been hampered due to the often restricted access to quality data of UCAVs and similar configurations against which to compare and from which to generate higher fidelity models. Specific steps for improving the accuracy of the methods in the future have been identified and proposed in §9.2.

Design space explorations performed in this research include a mission parameter trade study for subsonic UCAVs in Hi-Lo-Hi missions, the conceptual and preliminary design of a UCAV platform with performance matching that of current 5th generation fighters, a fully supersonic deep-interdiction mission trade study, and a high-supersonic (M ≥ 3.0) carrier-based UCAV for time-critical strike missions.

Keywords: Multidisciplinary design optimisation; unmanned combat aerial vehicles; drone; stealth; aircraft conceptual design; design space exploration.

ACKNOWLEDGEMENTS

TABLE OF CONTENTS

LIST OF FIGURES

LIST OF TABLES

LIST OF ABBREVIATIONS

AOA	Angle of Attack
AVT	Advanced Vehicle Technology
BMI	Bismaleimide composites
BPR	Bypass Ratio
Cdr	Commander
CFRP	Carbon Fibre Reinforced Plastics
DARPA	Defense Advanced Research Projects Agency
DEAD	Destruction of Enemy Air Defences
DEW	Directed Energy Weapons
DLR	German Aerospace Center
DOD	Department of Defence (US)
DSI	Divertless Supersonic Inlet
FAC	Forward Air Control
FTMS	Fuel Thermal Management System
HAL	Hindustan Aeronautics Limited
HALE	High Altitude Long Endurance
HSUAV	High Speed Unmanned Aerial Vehicle
HVT	High Value Target
IR	Infrared
ISR	Intelligence, Surveillance and Reconnaissance
JNI	Java Native Interface
LANCA	Lightweight Affordable Novel Combat Aircraft
LCAAT	Low Cost Attritable Aircraft Technology
LO	Low-observability
LSP	Lightning Strike Protection
Lt	Lieutenant
MALE	Medium Altitude Long Endurance
MDAO	Multidisciplinary Design Analysis and Optimisation
MDO	Multidisciplinary Design Optimisation

MoD	Ministry of Defence
NATO	North Atlantic Treaty Organisation
OPR	Operating Pressure Ratio
PCA	Penetrating Counter Air
RCS	Radar Cross Section
RDT&E	Research, Development, Testing and Evaluation
SACCON	Stability and Control Configuration
SEAD	Suppression of Enemy Air Defences
SEP	Specific Excess Power
S&C	Stability and Control
TBCCE	Turbine-Based Combined Cycle Engine Propulsion
TMS	Thermal Management System
TRL	Technology Readiness Level
TSFC	Thrust Specific Fuel Consumption
UAS	Unmanned Aerial System
UAV	Unmanned Aerial Vehicle
UCAS	Unmanned Combat Aerial System
UCAV	Unmanned Combat Aerial Vehicle
UK	The United Kingdom
US	The United States
USAF	United States Air Force
WWI	World War I
WWII	World War II

1 INTRODUCTION

1.1 Research Background

There can be no doubt that Unmanned Aerial Vehicles (UAVs) have proven their worth and prominence in military conflicts all over the world. Some of the lessons learned on the use of unmanned vehicles during *Operation Allied Forces* in the late 1990s over Kosovo are summarised as *"[real time surveillance] may significantly help the operational commander"* and to *"Aggressively continue UAV research and development"* [1, p.12,14].

Partially based on this success, in the year 2000 the US Office of Naval Research Strike Technology Division conceived an ambitious and futuristic vision for fully autonomous aerial vehicles in the battlespace, from low-speed high-altitude surveillance platforms to high-performance strike and air combat aircraft; these requirements were considered unrealistic but *"[...] a worthwhile challenge and a useful direction in which to point R&D efforts"* [2, p.8]. Today, transformational efforts aiming towards fifth generation configurations and operations demand a more widespread use of high-performance configurations, with increased levels of stealth and autonomy [3].

Furthermore, it is estimated that by 2030, 4th generation fighters will be retired creating a need to *"[…] develop a combat air system based on a mix of fifth generation manned, and sixth generation manned, remotely piloted or unmanned […]"* [4].

This need has been confirmed by the recent international efforts to develop advanced fighter configurations. Several countries within the European Union are currently engaged in the design and development of the Future Combat Air System (FCAS) intended to complement and, eventually, replace 4th generation fighters such as *Eurofighter Typhoon* and *Rafale* by the year 2035 or 2040 [5]. On the other hand, the UK-based defence authorities and their industrial partners are currently developing the next generation combat air system, referred to as *Tempest* which emphasizes flexibility, connectivity, upgradeability, and affordability, having as a main design driver:

To deliver significant information advantage and mission effectiveness, the future combat air system will act as a 'force multiplier', interoperating with a wide range of other civil and military platforms and services across air, land, sea, space and cyber domains – as well as unmanned systems[6].

Having identified these needs, and recognising that while several UAV platforms have been armed and used in combat since the early 2000s, the term UCAV will be used in the context of this research as an aircraft capable of operating in contested or denied airspace through a combination of low-observability (stealth), high-speed, high-performance and advanced sensors, performing pre-emptive and reactive missions such as Suppression and Destruction of Enemy Air Defences (S/DEAD), penetrating and sustained surveillance, and strike of high-value targets (HVT).

1.2 Aim and Objectives

To address the need of novel unmanned configurations, this research project was launched as part of the GENUS project, which aims to develop a multidisciplinary aircraft conceptual design environment capable of designing and analysing different classes of aircraft under a common architecture. Specifically, the aim of this research project is to develop the capabilities of GENUS for the analysis of low-observable unmanned combat aerial vehicles, establishing a flexible and robust design environment under which to investigate a variety of mission profiles, operational capabilities, and design constraints including low-observability and packaging in the design loop.

In order to achieve this, the main research objectives have been identified as:

First: to identify appropriate design methodologies for conceptual design level of UCAVs and related platforms. These methodologies should provide a sufficient level of accuracy while allowing a broad design space exploration under time and computational cost constraints. Verification and validation of said methodologies should be carried out where possible.

Second: to integrate the selected methodologies into the GENUS aircraft design environment, maintaining flexibility, modularity, and robustness in mind, and increasing the capabilities of the framework as a whole.

And last: to explore the design space of UCAVs through the GENUS design environment, for a wide variety of mission requirements, from subsonic to high supersonic speeds, addressing the current and future operational envelopes.

1.3 Thesis Structure

This thesis is organised as follows:

Chapter 2 provides a brief historical perspective on the development of unmanned aerial vehicles emphasizing their military applications from the earliest stages of *aerial torpedoes* through modern conflicts. Subsequently, UCAVs are defined in the context of this research and a brief outlook on the future of joint operations is introduced. The main technology demonstrator programmes and current UCAV designs are introduced. This section finishes with a review of the technological challenges behind the design and development of UCAVs.

Chapter 3 introduces the GENUS aircraft design environment, its core philosophy, an overview of its general architecture, data hierarchies and data sharing between modules, and finally the set-up of optimisation problems within the framework; a brief example of *quasi* multi objective optimisation is provided.

Chapter 4 provides the technical details on the UCAV design methodologies integrated into each of the GENUS framework's analysis modules; the verification and validation of mass estimation, aerodynamics, propulsion modelling, and radar cross section are provided. These methodologies were developed with flexibility and expandability in mind due to the broad design space available for UCAV configurations, from subsonic to high supersonic. Besides the typical aircraft design analysis modules a set of special modules have been created to analyse non-typical disciplines: radar cross section estimation has been added through a physical optics approximation method; a vehicle thermal load analysis and fuel thermal management system has been included as a key aspect of high supersonic operations.

Chapter 5 presents a study on the mission and performance trade-offs for low-observable subsonic UCAV configurations operating in typical ground strike missions (Hi-Lo-Hi). The effects of leading edge sweep angle, cruise Mach number, combat radius, and specific excess power are quantified for lambda-wing UCAV configurations under constant wing area.

Chapter 6 establishes the conceptual and preliminary design efforts towards establishing a 5th generation UCAV design intended to operate in highly integrated and coordinated combat operations alongside current 5th generation fighters and future 6th generation fighters. The mission design for this UCAV includes a subsonic ground strike profile combined with limited supersonic combat capabilities. Preliminary design studies have been carried out for the overall structural concept, engine sizing and integration, fuel, power, and actuation systems, as well as landing gear sizing, and avionics systems design.

Chapter 7 deals with the studies regarding supersonic design concepts under various combat missions, payloads, and operational requirements. A study on a Mach 2.0 deep interdiction mission (Hi-Hi-Hi) is shown, along with operational trade studies for the cruise and dash Mach numbers. Subsequently, operational trade studies are presented for a carrier-based high-supersonic strike UCAV. The effects of cruise Mach number, cruise altitude, and combat radius are evaluated against important performance parameters such as time-to-target, and thermal management constraints.

Chapter 8 presents the main discussion which summarises the principal results and findings for the various classes of UCAVs under various mission and operational constraints.

Finally, achievements, conclusions, and the identified further work are summarised in Chapter 9.

2 LITERATURE REVIEW

This section will introduce a brief historical account of unmanned aircraft and their role in military conflicts around the world. Subsequently, the most important UCAV demonstrator programs will be introduced, followed by a discussion on the main technological challenges behind the design and development of UCAVs, from subsonic to high supersonic missions.

2.1 Unmanned Aerial Vehicles: A brief history

Contrary to common belief, unmanned aircraft are not a recent engineering feat. Some of the earliest unmanned aircraft date back to the 1910s, when both the US Army and Navy started experimenting with what were known at the time as *aerial torpedoes* to counter U-boat threats. The first of these aircraft was designed by Elmer Sperry and Peter Hewitt, and it was a radio controlled, gyro-stabilized wood and fabric aircraft designed to carry 300 lbs of explosives over a distance of 50 miles. However, this design was not very successful with its longest flight being only a thousand feet long.

By 1917, Charles Kettering was tasked by the US Army to design and build another *flying bomb* that could travel a distance of 40 miles at speeds up to 55 mph. The *Kettering Bug*, as it was later known, used a system of vacuum-pneumatic and electric controls and pre-programmed engine revolutions as its automatic guidance. When the vehicle was near its destination it would shut off the engine, jettison its wings, and fall towards the target. Despite the advances achieved, the *Kettering Bug* was never used in combat[7].

During the First World War it became clear to British Navy officials that naval gunners were not adequately prepared to counter aerial targets. By 1933 the Royal Navy was using radio controlled De Havilland Tiger Moth trainers, known as *DH-82B Queen Bee*, as unmanned target practice. At the 1935 Disarmament Conference in London, US Admiral William H. Standley had the opportunity to see a live demonstration of these unmanned aircraft, and he immediately recommended the US Navy to adopt the practice, and by 1938 the use of unmanned *N2C-2 Fledgling* as target drones was standard practice in the US

Navy. In fact, the term drone was first used in a 1936 report by Lt. Cdr. Delmer Farhney to pay respect to the original *DH-82B Queen Bee* target aircraft[8].
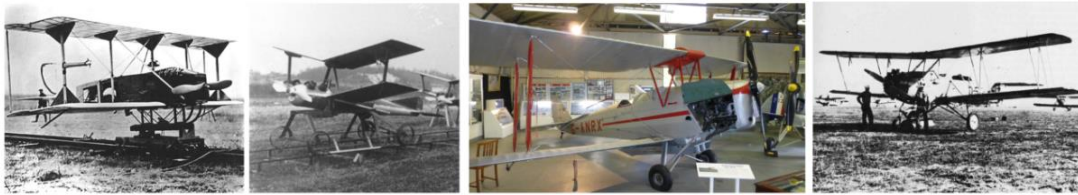
Figure 2-1 - Sperry's aerial torpedo, Kettering Bug, DH-82 Queen Bee[1], and N2C-2 drone

By September 1939 the Second World War had officially begun, and German forces quickly turned to the idea of an unmanned flying bomb. Initially, the *Ferfeuer* project intended to create a radio-controlled drone capable of delivering one ton of explosives, and then return to base. The German forces did not show interest in this project however, but it opened the path for the *V-1* cruise missile. This new threat was countered by the American *Radioplnae-4*, designed and built by Reginal Denny, later known as *OQ-2* drone. These drones were used for artillery practice by flying in the same paths as *V-1* missiles from 1944 to 1945.

Simultaneously, advances in television and the radar altimeter proved effective for remote piloting of aircraft. By 1942, a pilotless aircraft was developed by Interstate Aircraft to carry a 1000 lb bomb and to be used in naval roles. The *TDR-1* drone, as it was known, was deployed in 1944 in attack roles against strategic Japanese locations, with mixed success[9]. Similar projects consisted of modifying *B-17 'Flying Fortresses'* and *B-24 'Liberators'*. A pilot and a flight engineer would take off loaded with 25 thousand lbs of explosives, and would abandon the plane close to their target after switching control to a 'mothership' aircraft, see Figure 2-2. These efforts were not successful mainly due to flight control issues[10, chap.3].

---

[1] Source: de Havilland Aircraft Museum
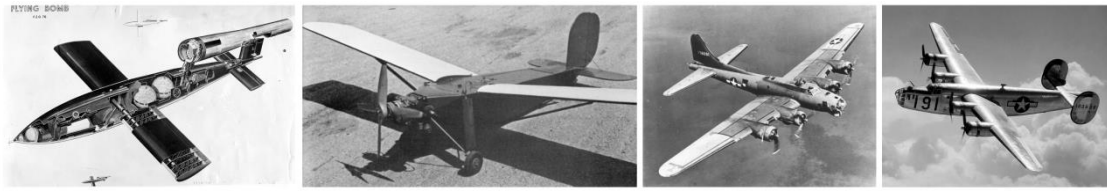
Figure 2-2 - V-1 cruise missile, OQ-2 drone, B-17 'Flying Fortress', and B-24 'Liberator'

The Second World War revealed the importance of aerial reconnaissance and intelligence. During the Cold War, the newly created US Air Force (USAF) developed a number of unmanned platforms, initially to act as decoys for the Soviet radars, and then as reconnaissance and surveillance aircraft. In 1961 McDonnel Douglas designed the *GAM-72 Quail* as a decoy drone launched from *B-52* bombers; it became steadily obsolete as Soviet radar technology improved. Similarly, in 1958 Ryan Aeronautical Company started operating the turbojet powered *Q-2C Firebee* target drone, which was able to fly at 60 thousand ft with a range of 800 miles. However, during this period of time, the development of unmanned aircraft slowed down due to political differences and prioritisation of projects like the *U-2* high-altitude reconnaissance aircraft, and the supersonic *SR-71 Blackbird*.

The *Firebee* drone was later modified to serve as an aerial reconnaissance platform, while also being enhanced for stealth; it was renamed as *Fire Fly*, and subsequently changed to *Lightning Bug*. These vehicles were first used in 1964 over Chinese territory and later over Vietnam in the same year. More than 160 *Lightning Bug* sorties were registered during 1965-1966. These aircraft had proven vulnerable to surface-to-air missiles, so the *Compass Arrow* high performance drone was designed by Ryan Aeronautical in order to counter this vulnerability[11]. Another impressive project developed around this time, was the supersonic decoy drone *Firebee II*, which could reach speeds of Mach 1.7 at altitudes up to 50 thousand feet; these vehicles are shown in Figure 2-3.

In more recent conflicts, such as the Afghanistan and Iraq wars, the use of low speed, long-endurance UAS such as Northrop Grumman's *Global Hawk* proliferated, initially serving in intelligence and reconnaissance roles; however, in 2001, *MQ-1 Predator* UAVs were armed with laser-guided missiles and fired

against active targets, marking a new stage of UAV employment in combat[12]. Predator's larger variant, the *MQ-9 Reaper* can be further equipped with up to 3750 lbs of laser-guided missiles and Joint Direct Attack Munitions (JDAM), while also being able to achieve a range of 1000 nautical miles at altitudes up to 50 thousand feet[13]. A further evolution of persistent surveillance UAS that incorporates combat related performance, such as being jet-powered, with maximum speeds of 400 KTAS, and low observability design choices is the *Predator C Avenger*[14]. This vehicle can carry up to 3000 lbs in its internal weapon bays as well as providing up to 20 hours of endurance at altitudes up to 50 thousand feet. This class of UAS is shown in Figure 2-4. The Bureau of Investigative Journalism reports that, from January 2004 up to the last trimester of 2019, a total of 6786 confirmed drone strikes have been carried out by the US[15].

Figure 2-3 - GAM-72 Quail, Q-2C Firebee, Firebee II, and Compass Arrow

Today unmanned aerial vehicles have diversified to cover all sorts of public and private needs; from recreational drone racing, to urban package delivery, and agricultural remote sensing. It is clear that UAVs are and will continue to be an important aspect of aeronautical engineering and technology, both in the operational sense and in the R&D sphere. Indeed, currently more than 70 countries are making use of unmanned platforms, while approximately 50 countries are engaged in research and development programmes. It is expected that by 2022, the UAV market will grow to a gross value of $11.4 Bn[16].
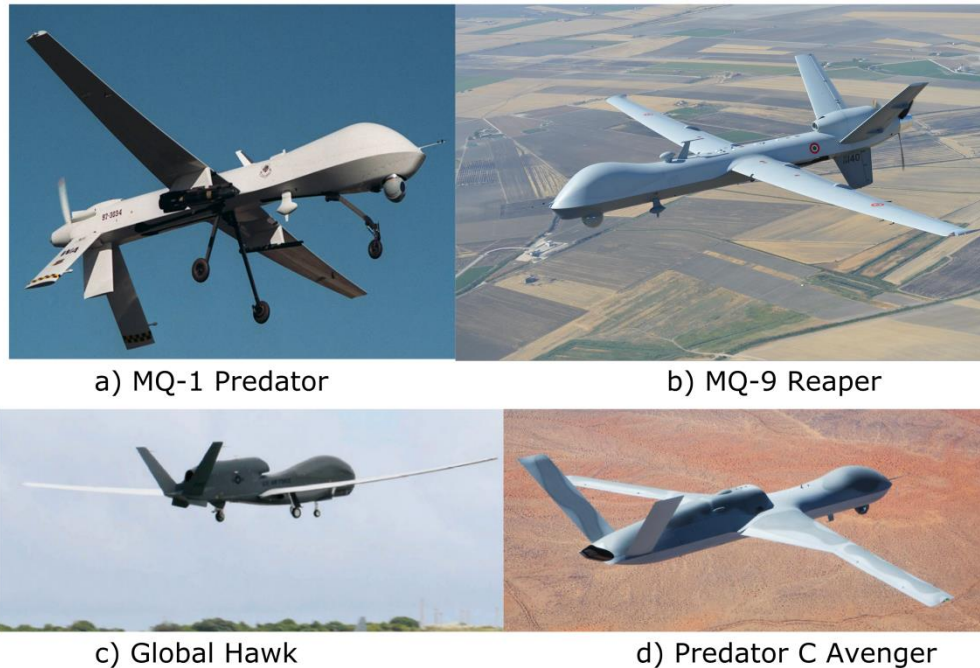
a) MQ-1 Predator   b) MQ-9 Reaper

c) Global Hawk   d) Predator C Avenger

Figure 2-4 - Persistent surveillance UAS and combat UAS

2.2 Unmanned Combat Aerial Vehicles

As seen from the previous section, UAVs have a long history of military applications. The logical progression is for UAVs to take on a more predominant role in aerial warfare through an increasing combination of operational capabilities, high performance, and higher levels of autonomy.

UAVs are currently defined by the US Department of Defence (DOD) as:

> *"[…]a powered, aerial vehicle that does not carry a human operator, uses aerodynamic forces to provide vehicle lift, can fly autonomously or be piloted remotely, can be expendable or recoverable, and can carry a lethal or nonlethal payload. Ballistic or semiballistic vehicles, cruise missiles, and artillery projectiles are not considered unmanned aerial vehicles."* [17]

For the purposes of this research, the term UCAV will be applied to unmanned aerial vehicles able to operate in highly contested air spaces through a combination of high speed, high performance, manoeuvrability, low-observable technologies (LO), and advanced sensor packages and data fusion algorithms that allow their integration to future air forces.

9

This definition aligns well with the transformational efforts towards the future *fifth generation air forces*, where not only the aircraft are considered as fifth generation designs, but the interactions between air force, army, and naval forces are complemented by advanced sensors and data fusion across manned and unmanned aircraft, ground personnel, and maritime vehicles[3], as exemplified in the envisioned joint operations shown in Figure 2-5.

Figure 2-5 – Lead F-35 with UCAV swarm in future joint operations (Source: US Air Force[2])

2.3 UCAV Advanced Technology Demonstrators

The need for the future generation of unmanned combat aircraft has been recognised by countries like the US, UK, France, India, and China. Demonstrator projects have emerged since the late 1990s and continuing to this day. Most designs take the shape of flying wings which have inherent LO, but the challenges are many. Future supersonic and hypersonic concepts have also started to appear on the map. The main projects worldwide will be presented below.

2.3.1 X-47B and X-45C

During the late 1990s Boeing/USAF/DARPA initiated a program focused on maturing technologies, processes, and system attributes required for UCAVs capable of supporting pre-emptive and reactive suppression of enemy air defences (SEAD), electronic attack, and strike missions. As a result the X-45A

---

[2] Still from US Air Force Research Lab promotional video "Air Force 2030 – Call to Action"

was designed, with flight testing taking place as early as 2002. This design included LO characteristics such as a blended body, a buried engine and internal weapon storage; it would serve as a proof of concept for the larger and more capable X-45C, Figure 2-6 (b)[18].

Simultaneously, the US Navy initiated studies for an unmanned vehicle to perform the roles of reconnaissance and target identification in protected airspace. Northrop Grumman built the X-47A which took flight in 2003. At the end of 2002, the Navy and Air Force programmes were joined into the Joint Unmanned Combat Air Systems (J-UCAS) programme intended to perform SEAD, EW, precision strike, penetrating surveillance, and persistent global attack. This programme was later terminated in 2006 due to managerial divergence and budgetary issues[19], and efforts were redirected towards a long range carrier-based aircraft with aerial refuelling capabilities for increased naval reach and persistence; this project became known as Navy-UCAS or N-UCAS, which resulted in the X-47B aircraft, Figure 2-6 (a), often called UCAS-D for Demonstrator. In 2013, the US Navy and Northrop Grumman successfully demonstrated take-off and landing from an aircraft carrier[20], with autonomous aerial refuelling happening in 2015[21].

From the lessons learned from these demonstrators, a completely new set of requirements has emerged which replaces the combat capabilities with an unmanned tanker capable of transferring 14,000 lbs of fuel at a range of 500 nautical miles from the carrier, this unmanned tanker will be known as MQ-25. Bids were put forward by Boeing's Phantom Works[22], and Lockheed Martin's Skunk Works[23], with the winner being Boeing.

a) X-47B   b) X-45C

Figure 2-6 - X47-B and X45-C UCAV demonstrators

2.3.2 Taranis

Officially unveiled in 2010, Taranis, shown in Figure 2-7 (a), is a BAE-led project in conjunction with the UK Ministry of Defense (MOD) and UK industry. Its purpose is to demonstrate design and manufacturing capabilities of a highly manoeuvrable unmanned combat aerial vehicle capable of sustained surveillance, intelligence acquisition, enemy deterrence and strike in hostile territories through a combination of advanced aerodynamics, propulsion systems, high levels of autonomy, and LO[24]. Flight tests took place in late 2013 and early 2014.

2.3.3 Neuron

Neuron, Figure 2-7 (b), is a French-International demonstrator programme initiated in 2003; it is led by Dassault Aviation. Its aim is to demonstrate maturity of technical solutions for military unmanned aircraft. Neuron completed its first flight test in 2012, and has currently carried out a number of simulated missions including air-to-ground subsonic strike, automatic detection and localisation of ground targets, and air-to-surface weapon release from an internal weapon bay. Since 2016 Neuron has served as the basis for a carrier-based unmanned combat aircraft study, as well as a test bed for electromagnetic signature measurements[25].

a) Taranis   b) Neuron

Figure 2-7 - Taranis and Neuron UCAV demonstrators

2.3.4 Sharp Sword and Rainbow 7

The Chinese *Lijian* (Sharp Sword) UCAV, Figure 2-8, is the first non-NATO stealth unmanned aircraft to be produced. Design and development is led by the Aviation Industry Corporation of China and the Hongdu Aviation Industry Group.

Lijian is believed to carry up to 2,000 kg of payload, and it underwent taxi and flight testing as early as 2013. It is expected to enter service around 2019-2020[26].

Figure 2-8 - China's Lijian UCAV

More recently, China's Aerospace Science and Technology Corporation (CASC) has unveiled a turbofan, high-altitude UCAV called *Cai Hong* (Rainbow) 7. This design resembles the X-47B with its truncated diamond and kite design, as shown in Figure 2-9. Low-observability features have been included through the buried engine, low-observable intake, and saw-toothed edges for landing gear doors and all internal weapon bays. This UCAV is intended to perform in heavily contested environments in deep strike roles, as well as serving as an efficient ISR platform[27].

Figure 2-9 - Chinese *Cai Hong 7 (Rainbow 7)* UCAV

2.3.5 Su-70 Okhotnik

In January 2019, pictures of a Russian UCAV prototype appeared on social media. This stealthy design is named *Okhotnik* or *Hunter*, and it is shown in Figure 2-10. From promotional videos, it can be see that the *Okhotnik* is a lambda-wing design, with a buried engine with a low-observable engine intake, and possibly a thrust vectoring nozzle for improved manoeuvrability and take-off performance.

The estimated design characteristics are a span of approximately 19 meters, a possible gross mass of 20 tonnes, and a top speed of 1000 km/h. It is believed

that it can carry the latest generation of missiles and munitions developed for the Su-57 programme, as well as having radar absorbent coatings for additional stealth measures[28].

Figure 2-10 - Russian Okhotnik UCAV prototype

2.3.6 GHATAK

Indian authorities have authorised funds for the design and development of critical technologies related to the GHATAK UCAV prototype shown in in Figure 2-11, and a potential 5th generation stealth fighter. GHATAK aims to develop and advance model based engineering, autonomous flight control, advanced aerodynamics and propulsion, stealth computations, measurements, structures and materials. Flight control laws, thrust vectoring, and stealth will be tested through a $1/6^{th}$ scale model[29].
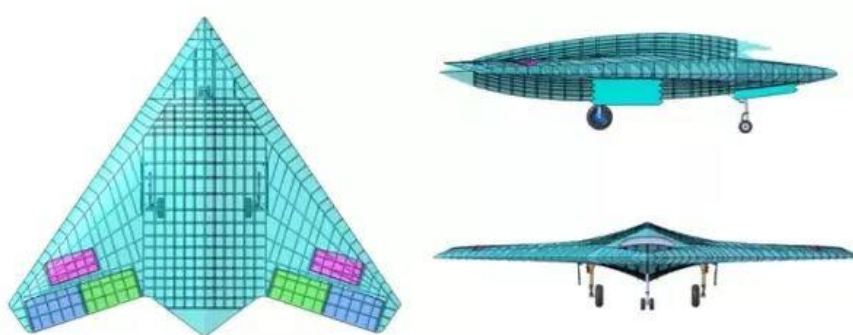
Figure 2-11 - GHATAK UCAV design (as of 2016)

2.3.7 Loyal Wingmen

A recent development in the field of unmanned combat aircraft includes what are now commonly referred to as the *loyal wingmen* configurations. These vehicles

deviate somewhat from the stealth dominated designs with large payload requirements; *loyal wingmen* performance is focused on strength by numbers, with reduced costs and production time. These projects have recently emerged in countries like the USA, UK, India, and Australia.

In the USA, the USAF has recently began testing the XQ-58 *Valkyrie*, which is a long range, high subsonic vehicle with a reported payload capability starting at 250 kg. This programme falls under the Low Cost Attritable Aircraft Technology (LCAAT) portfolio, which aims to reduce costs and mature the commercial manufacturing processes for combat UAVs[30].

The UK MoD has recently unveiled their plans and a bid to design and develop the next generation of Lightweight Affordable Novel Combat Aircraft (LANCA), also known as *Project Mosquito*, which aims to develop a combat platform for 10% the cost of new generation fighters and 20% the development time[31,32]. The reported performance falls within the transonic flight regime, with capability to operate with manned and unmanned systems, as well as being able to carry sensors and payload for electronic warfare.

India's Hindustan Aeronautics Limited (HAL) recently unveiled its loyal wingman concept at the Aero India 2019 exhibition. The reported range is 800 km at a cruise Mach number of 0.7, with a take-off mass of 1300 kg, and a ventral payload bay capable of carrying 250 kg of stores, including air-to-surface weapons, surveillance sensors, and electronic warfare payloads[33].

Boeing is currently developing the *Airpower Teaming System*, consisting of a smart UCAV intended to provide *fighter-like* performance in tactical early warning missions, relying heavily on artificial intelligence and integrated sensor packages for a "truly transformational capability". It is expected to take flight in 2020[34,35].

The various *loyal wingmen* platforms mentioned above are shown in Figure 2-12.

a) XQ-58 Valkyrie

b) HAL Unmanned Wingman

c) Boeing Loyal Wingman

d) UK LANCA prototype
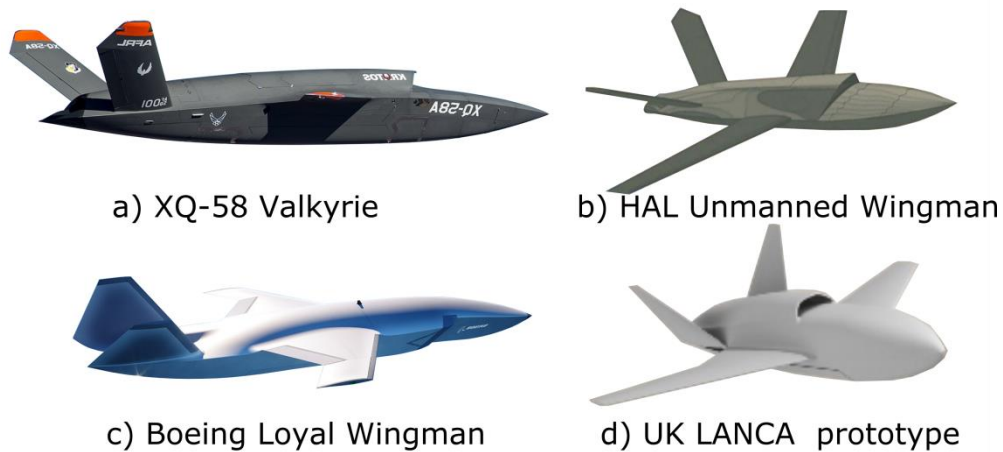
Figure 2-12 - Loyal wingmen configurations

2.3.8 Future Supersonic and Hypersonic UCAV Concepts

Several projects have emerged around the world consisting of supersonic and hypersonic UCAV designs, intended mainly for surveillance and strike roles. Examples of this are Lockheed Martin's SR-72 hypersonic unmanned aircraft, Figure 2-13 (a) intended to perform at Mach 6. Similarly, Boeing has unveiled a Mach 5 demonstrator design, Figure 2-13 (b). Both of these designs would employ Turbine-Based Combined Cycle Engine Propulsion (TBCCE), which employs a turbine engine to take the vehicles from static up to Mach ≤ 3, and a ramjet/scramjet to accelerate the vehicles to their top speeds[36].

China has recently unveiled a supersonic stealth drone known as *Anjian* (Dark Sword), Figure 2-13 (c). Estimates of its characteristics are a maximum weight of 15 tonnes, highly manoeuvrable up to 9g with a combat radius of 1000 km and payload of 1 tonne[37].

a)   b)   c)
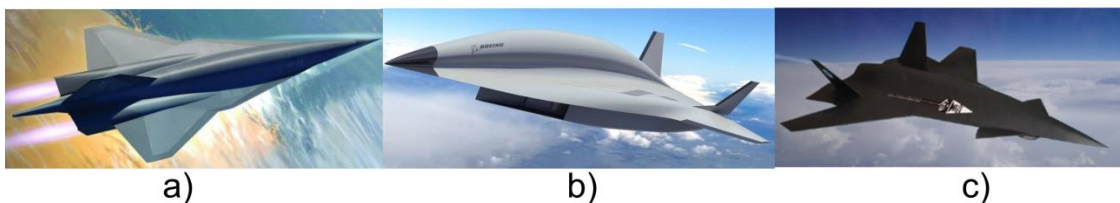
Figure 2-13 - a) Lockheed Martin's SR-72; b) Boeing Mach 5 UCAV; c) China's Anjian or Dark Sword

2.4 Technological Challenges

It can be seen from the different technology demonstrator programmes, the recent loyal wingmen developments, and the supersonic and hypersonic future concepts, that UCAV designs face many technological challenges that severely constrain different design aspects. The inclusion and prioritisation of low-observable characteristics often result in tailless configurations or highly blended geometries. The different challenges and design interactions and compromises will be reviewed in the following sections.

2.4.1 Impacts of Stealth

The inclusion of stealth has the primary purpose of increasing the aircraft's survivability. There are many ways to consider survivability including mission planning, i.e. time of day and conditions, mission profile, use of electronic countermeasures, missile detectors, and the use of stealth design features.

The complete vehicle signature can be divided into active and passive signatures, with the subdivision given in Figure 2-14. Reducing or eliminating the vehicle's signature falls under the susceptibility aspect of survivability[38], and it is most commonly included during the early design stages through vehicle shaping, structural and system architecture choices, material selection, and mission planning.

The radar signature is commonly measured by the radar cross section (RCS), which is the area of an imaginary reflector that would reflect the same amount of energy back to the receiving radar antenna, as reflected by the actual target. Most aircraft's RCS lies in the optical region, where the incoming radar wavelength is many times smaller than the characteristic target dimension ($\lambda << a$), and the signature is highly sensitive on the target's shape, size and material characteristics. The radar range equation, Eq. (2-1), shows that to decrease the detection range (R) of a vehicle by a certain factor, its RCS (σ) must be decreased by the same factor to the fourth power, which translates to severe engineering challenges when it comes to the design of low-observable configurations.

$$R^4 = \frac{P_t G^2 \lambda^2 \sigma}{(4\pi)^3} \qquad \text{(2-1)}$$
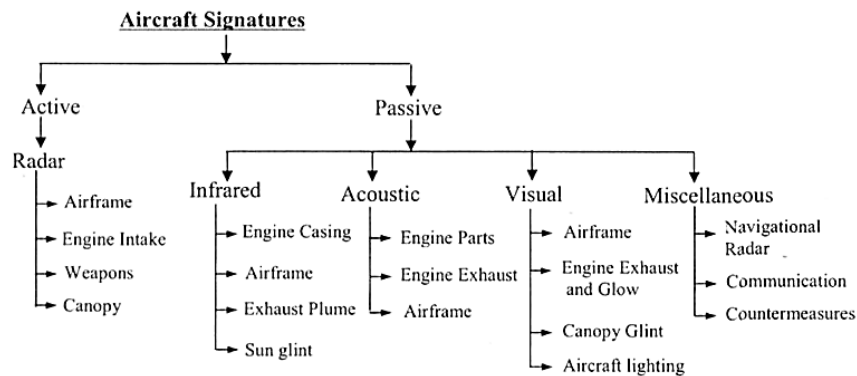
Figure 2-14 - Aircraft Signatures[39]

RCS can be reduced through the following strategies:

Shaping: The main objective is to reduce the scattered waves in the direction of the receiver(s); this can be achieved via the following strategies:

o Compact and smooth blended geometries, clean external geometries without discontinuities and protuberances.
o Highly swept leading edges with rounded wing tips.
o Planform alignment, parallel edges and surfaces.
o Avoid external surfaces with reflection angles normal to the incident waves.
o Buried engines with curved intakes and exhausts to avoid direct wave reflection.
o All internal fuel and payload.

These strategies often result in highly swept, tailless aircraft as can be seen from the advanced technology demonstrator programmes and the B-2 stealth bomber. Eliminating the horizontal and vertical tails has the consequence of losing very efficient control devices for pitch and yaw that must be compensated by the use of additional spoilers, split flaps and other control surfaces without disrupting the low-observability characteristics of the design. Furthermore, the all internal payload requirement imposes severe volumetric constraints on the configurations, often translating into very limited payload capacities when compared to conventional fighters with external weapons.

Low-observable intakes and exhausts not only result in packaging and structural trade-offs, but they can also affect the engine performance and thus the fuel consumption. The detailed S-shaped geometry of the intake must balance pressure recovery (good internal aerodynamic characteristics) with low visibility at various flight conditions. Figure 2-15 shows the trade-offs between visibility, fuel consumption and pressure recovery (or pressure loss) for a serpentine inlet in a low-observable tailless UCAV. It can be seen that reducing the visibility results in higher pressure losses due to the more pronounced curvatures along the intake[40]. High-fidelity CFD tools and experimental data are often required for the detailed design of such complex geometries.
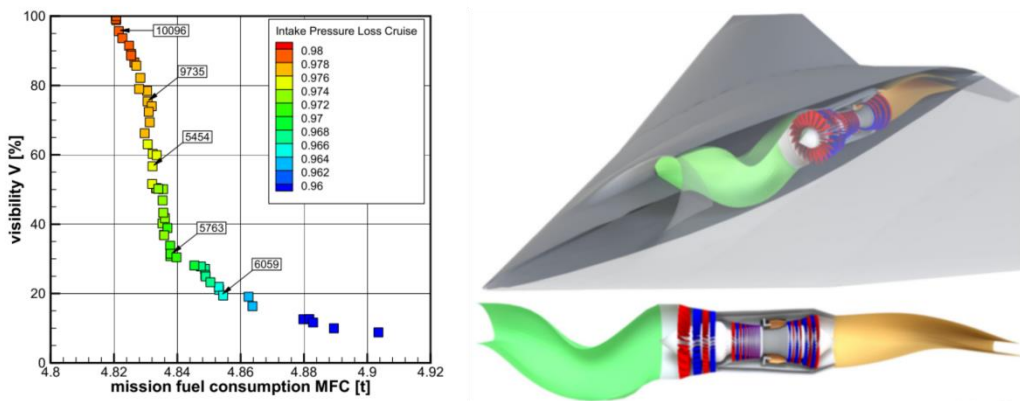
Figure 2-15 - Low-observable intake multi-objective optimisation

The vehicle's after-body design must also balance the aerodynamic performance of the exhaust, the low-observability requirements, and the effects of potential thrust vectoring on the aircraft's stability and control[41,42]. Similarly to the intake design, a careful after-body design requires high-fidelity tools and experimental data.

Radar absorbent materials: This strategy consists on covering the aircraft with a material that can dissipate a substantial part of the incident energy and thus reduce the amount of energy reflected. The basic principle of a radar absorbent material consists on matching the impedance of the incident medium, normally air, with an impedance value of 377 Ohms. Equation (2-2) establishes the reflection coefficient as the ratio between the material's impedance (Z) and the impedance of the incident medium, with a value of zero when $Z_M = Z_0$.

$$r = \frac{Z_M - Z_O}{Z_M + Z_O} \qquad \text{(2-2)}$$

The absorption of incident electromagnetic energy can be achieved through two strategies:

○ Admitting the incident wave and then dissipating its energy. This approach can be used for multiple frequencies. Broadband RAMs use this strategy.

○ Producing internal reflections of the incident wave that obstruct or destroy the reflected signals. This strategy is frequency-specific. Resonant RAMs use this strategy.

Composite materials have been used extensively to reduce the radar signature since the days of the SR-71 *Blackbird*, with large sections of the leading and trailing edges, vertical stabilizers, chines, and inlet spikes made of plastic laminates of phenyl silane, silicone-asbestos, and fiberglass, geometrically tailored to further reduce the reflection[43], as shown in Figure 2-16.
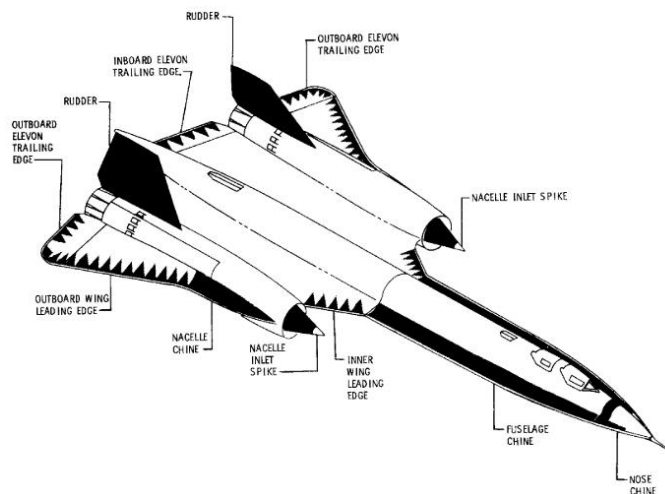
Figure 2-16 - Composite plastic laminates for reducer RCS in the SR-71

Furthermore, the vehicle's structure can incorporate radar absorbent materials in order to create a radar absorbent structure (RAS). A wide variety of magnetic particles such as ferrite can be added to various layers within the composite matrix to attenuate the radar reflection at specific frequencies and incidence angles. Carbon-based composite RAMs are an alternative to metallic particles;

carbon black particles can be added in single or multi-layer configurations to absorb up to 90% of the electromagnetic energy on load-bearing components[44]. Care must be taken when using carbon reinforced plastic, since they have been proven to become semi-reflectors at high carbon concentrations (60-70%). Other carbon-based options include carbon nanotubes (CNT) and graphene. CNT outperform carbon black due to their superior mechanical properties and equivalent electromagnetic absorption with only a fraction of the concentration on the matrix (0.35% CNT compared to 20% carbon black)[45].

Electronic countermeasures: This strategy refers to the intentional emission of electromagnetic signals in order to interfere with enemy radars, sonars, lasers, and other electronic detection systems by saturating the receivers or creating false information and noise. The mass and system penalty of carrying such countermeasures can be distributed in the case of cooperative UCAVs which can combine their jamming signals in order to reduce enemy detection and create a reduced risk path not only for other UCAVs but for other manned fighters as well at a fraction of the system cost[46].

Another major aspect of the overall vehicle detectability is its infrared (IR) signature, which makes the aircraft susceptible to detection and tracking by heat seeking missiles such as those used by man-portable air defence systems, and air-to-air missiles. The basic principle of IR detection relies in differentiating the IR emissions from the target against the background IR heat flux. For IR radiation, only two wavelengths are used for detection and tracking, the first atmospheric window (3-5 *µm*) being the most important due to its use in missile tracking of higher peak temperatures[47].

The main contributors to an aircraft's IR signature are the exhaust plume, the aerodynamically heated skin, hot engine parts and the surrounding hot structure. External heating sources include sky and earth reflection. Active IR countermeasures such as IR jammers, flares, and towed decoys are only effective if the passive signature from the aircraft is significantly lower than the active emission from the countermeasures. The addition of such active countermeasures obviously results in mass and performance penalties.

Passive IR signature reduction can be achieved by careful shaping and masking of the hot structure surrounding the engine, cooling mechanisms for the nozzle, high aspect ratio nozzles, and the use of heat absorbent materials, as seen in the nozzle area of the YF-23 and the B-2. These strategies often introduce mass, system complexity, and performance penalties. For a circular convergent nozzle, changes in exit area at a fixed thrust result in higher combustion temperature and thus higher IR; similarly, changes in exit area at a fixed turbine entry temperature reduce the thrust and increase the specific fuel consumption[48]. Studies on a serpentine, high aspect ratio nozzle integrated into a UCAV design show that high aspect ratio nozzles can reduce the plume length and maximum temperatures significantly, but result in a thrust reduction of more than 10% compared to a circular nozzle[49].

The acoustic signature can be reduced by minimising the discontinuities and gaps in the vehicle, as well as by shrouding and shielding the engine with the control surfaces. The engine noise can also be mitigated by increasing the engine's bypass ratio, which leads to slower exhaust jet velocities. Finally, subsonic flight eliminates the sonic boom associated with supersonic speeds.

The visual signature can be reduced by the use of tailored colour schemes for various terrains, as shown in Figure 2-17, and by reducing or eliminating the engine contrails. Several technologies have been proposed for eliminating the engine contrails such as the addition of chemicals to reduce the size of ice crystals rendering them sub-visible, or destroying the crystals via electromagnetic radiation or ultrasound waves[50–52]. This technology is reportedly used in the B-2 bomber to reduce its visual signature.

Figure 2-17 - Visual signature reduction through camouflage paint

2.4.2 Aerodynamics, stability and control

2.4.2.1 Vortex Flow

The extended operational envelope for combat aircraft includes high angle of attack manoeuvres and with it the presence of unsteady, separated flows. For highly swept wings, the flow is dominated by vortices that separate from the leading edge due to shear layer instabilities. These vortices induce axial and tangential velocities greater than the freestream velocity, producing a low pressure zone at the core of the vortex. This low pressure can result in considerable additional lift, and results in non-linear lift curve slopes that depend highly on sweep angle, as shown in Figure 2-18[53].
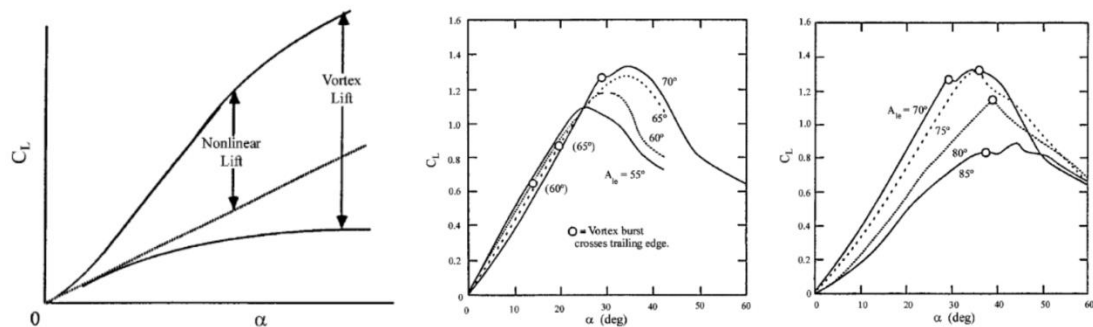
Figure 2-18 - Vortex lift and effect of sweep on lift coefficient

However, at high angles of attack, a sudden change in the flow topology characterised by the rapid deceleration of the vortex core, a rapid increase in vortex diameter, recirculation zones, and the degradation of the overall vortex structure can occur with detrimental effects to the lift leading to sudden changes to the pitching moment of the vehicle. This phenomenon is known as vortex breakdown[54], as illustrated in Figure 2-19.
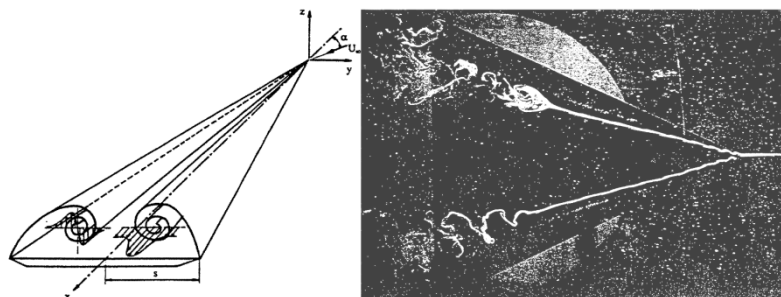
Figure 2-19 - Leading edge vortices (left) and vortex breakdown (right)

The literature on vortex flows and vortex breakdown over sharp, slender wings ($\Lambda_{LE} > 55°$) is extensive[55–59], and these phenomena are generally well understood; however, for configurations of moderate sweep angles, or non-slender configurations ($\Lambda_{LE} < 55°$) with blunt leading edges, understanding the vortex flow topologies and vortex breakdown, and their effects on aerodynamics, stability and control remain a pressing issue for the development of military aircraft, including UCAVs[60]. Furthermore, the interaction of the vortices with the structure and the propulsion system (vectored thrust jets) presents additional challenges[61].

2.4.2.2 NATO Vortex Flow and UCAV Design Studies

To this day, the most comprehensive work on understanding and validating methods for the prediction of vortex flow topologies and vortex breakdown behaviour over potential future combat aircraft configurations, including UCAVs, has been carried out by the Advanced Vehicle Technology (AVT) division of NATO, with several universities, research institutes and private enterprises contributing to several projects over the last two decades.

Established in the year 2000, AVT-080 project had the purpose to collect reliable experimental data in order to generate consistent test cases for the validation of numerical methods applied to vortex flows and vortex breakdown models over delta wings[62]. The selected test geometries include a 65° and a 70° sweep delta wing. Eight experimental cases, ten state-of-the-art CFD solutions, and three analytical solutions were selected and investigated in further studies as a result of this project.

Subsequently, the AVT-113 project was established to improve the technology readiness level of CFD methods applied to highly manoeuvrable military aircraft through a better understanding of the vortex flows over delta wings, wing leading edge extensions and strakes through the compilation and creation of high-fidelity experimental data[63]. The test case geometries consisted of F-16XL and a 65° delta wing. The effects of leading edge radius and a wide range of angles of attack were investigated in order to obtain a comprehensive database on the vortex shedding and breakdown behaviours over delta wings.

Following the vortex flow studies performed by the previous projects, AVT-161 project was created with the purpose of determining the validity of computational methods applied to the static and dynamic stability of highly manoeuvrable military aircraft. For this purpose, two configurations were selected; one was the X-31 aircraft, and the second was a generic UCAV with a 53° wing sweep called SACCON (Stability And Control CONfiguration), Figure 2-20[64].
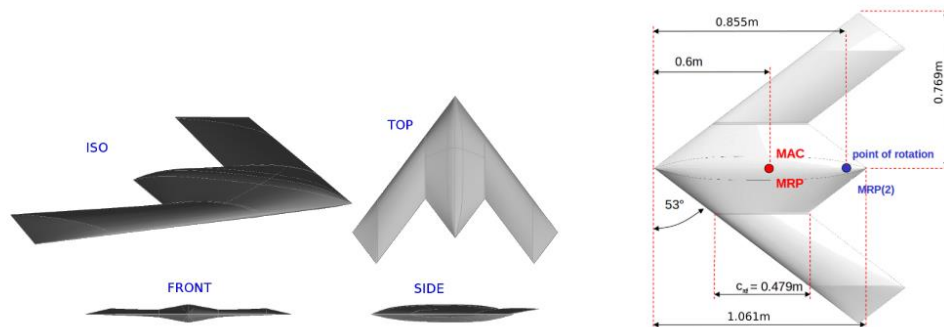
Figure 2-20 - SACCON planform and reference data

The main philosophy behind the AVT-161 project was a close integration between experimental and numerical studies. This required detailed wind tunnel set-ups that could capture not only the gross aerodynamics of the vehicles, but also the flow structures around leading and trailing edges and wing tips while having an accurate characterisation of the freestream conditions including the wind tunnel wall effects and the model deformation. Furthermore, quantifying the uncertainty of the measurements was a key request by researchers, so that important results could be replicated. The experimental model was prepared with more than 200 pressure taps, a special surface finish for improved PIV measurements, and a special leading edge roughness to simulate fully turbulent flow[65]. A variety of static and dynamic experimental and numerical tests were performed including the effects of control surface deflections[66].

By combining high-fidelity numerical data and experimental results, a thorough understanding of the flow physics of SACCON was obtained[67]; the flow topology evolution chart in the form of the pitching moment coefficient is shown in Figure 2-21. This interaction between the flow separation, vortex breakdown and the generated lift, and thus pitching moment, makes the stability and control of agile configurations extremely complicated, especially at high angles of attack. Indeed,

this 'maximum usable incidence' angle has been found to be one of the main sizing factors during the conceptual design of a lambda wing UCAV platform, UCAV 1303, specifically during low speed segments such as take-off and approach, as well as during high angle of attack manoeuvres[68]. This incidence limits the speeds at which the UCAV is able to take-off and land, which sizes the engine, which in turn has a large impact on the vehicle's central length, packaging, and the vehicle's response to changes in mission radius and performance requirements[69].
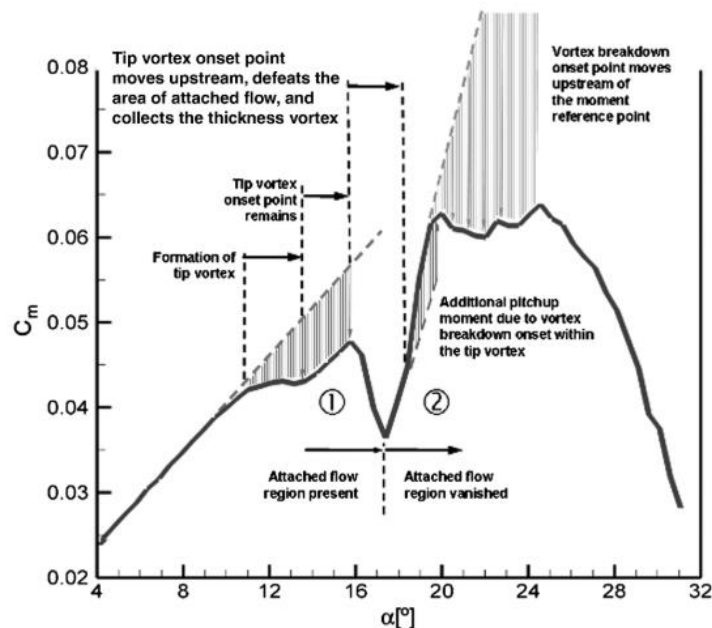
Figure 2-21 - Pitching moment coefficient vs angle of attack for SACCON

Several studies have been carried out in order to 'smooth out' this pitch up behaviour in order to extend the manoeuvrability envelope of future UCAV configurations. Tomac *et al.*[70] investigated the use of low-fidelity aerodynamic analysis tools including a panel method and a vortex lattice method added with vortex flow corrections to improve the static stability of SACCON for a limited range of angles of attack (*0°≤α≤10°*). Even at such moderate angles, these engineering methods were unable to accurately predict the pitching moment curve. However, changing the twist distribution, without any consideration of radar signature, seemed to alleviate these difficulties in pitching moment prediction, proving that, with a good understanding of the limitations of such

methods, simple tools can be of significant aide to the designers during the early stages.

Similarly, Coppin[71] used a three-dimensional geometry definition through Class Shape Transform (CST) coupled to a high-fidelity numerical solver to optimise the aerodynamic shape of UCAV 1303 for various cruise lift-coefficient designs. This method has shown that through a distribution of incidence angle, wing washout, and thickness distribution the pitch-up behaviour can be delayed by several degrees.

Further vortex flow separation studies for a generic configuration relevant to UCAV designs were carried out through the AVT-183 project which lasted six years[72]. This project investigated the effect of blunt leading edges on a 53° sweep diamond wing partially based on SACCON. High-fidelity CFD tools as well as wind tunnel models were used to determine the effects of leading edge radius and aerofoil thickness on the unsteadiness of the vortex flow topology. Results show that the leading edge vortices are highly dependent on leading edge radius and roughness, and not greatly dependent on aerofoil thickness[73]. CFD predictions had mixed success when predicting the shedding and overall strength of the leading edge vortices, as well as the pitching moment at high angles of attack; however, the data generated during these studies has served as an extensive data base for CFD validation and surrogate models for subsequent studies[74].

Subsequently, with the data obtained from AVT-161 and AVT-183 projects, the AVT-201 project was established to investigate the effects of control surface deflections on the S&C of the SACCON configuration through wind tunnel testing, and CFD numerical methods in order to develop flight simulation control algorithms and test them against flight test data[75]. The collection of experimental and numerical results show the importance of using computational tools during the early design stages, especially in the presence of non-linear aerodynamic effects and the effects of control surfaces for non-slender configurations relevant to present and future UCAV designs[76].

An initial conceptual design study of a feasible UCAV configuration based on the SACCON geometry was carried out by the AVT-201 group. The task was to resize the 1.54 m span wind tunnel model into a functional UCAV design. For this, the German Aerospace Centre's (DLR) aircraft design code was employed, coupled with linear potential flow aerodynamic solvers superimposed with experimental data of control surface deflection, an engine design tool, a mass and CG control spreadsheet, a structural sizing tool based on aerodynamic and inertial loads, and a six-degree of freedom flight simulator[77]. The low-fidelity aerodynamic tools have acceptable results for lift and drag prediction, but not for the pitching moment at moderate angles of attack, and cannot accurately predict the effects of side slip or rolling moments. The mission is shown in Figure 2-22 and it has not been changed during subsequent studies. Initially, a gross mass of 10000 kg was estimated with a wing span of 12.3 m and a thrust loading of 0.35. However, fuel and payload packaging requirements demanded an up-scaling of the vehicle's characteristics, resulting in a gross mass of 15000 kg, a wing span of 15.4 m and a thrust loading of 0.4.

Finally, a large high-fidelity integratory project that makes use of the aerodynamic, stability, and control information generated by all previous projects was established under the AVT-251 project. A multidisciplinary design analysis and optimisation of a UCAV platform, referred to as MULDICON (MULti-DIsciplinary CONfiguration), performing a subsonic ground strike mission, Figure 2-22, was carried out over a period of three years[78].

The MULDICON design was divided into several subgroups which include the Design specification and Assessment Group (DSAG), Aerodynamic Shaping Group (ASG), Engine Integration Group (EIG), Control Concept Group (CCG), and Structural Concept Group (SCG). These groups worked separately but cooperatively in order to arrive at a feasible configuration, including preliminary design aspects such as detailed control surface design, engine selection and intake design and integration, a thrust vectoring nozzle, and packaging and structural analysis of the major systems and avionic components.
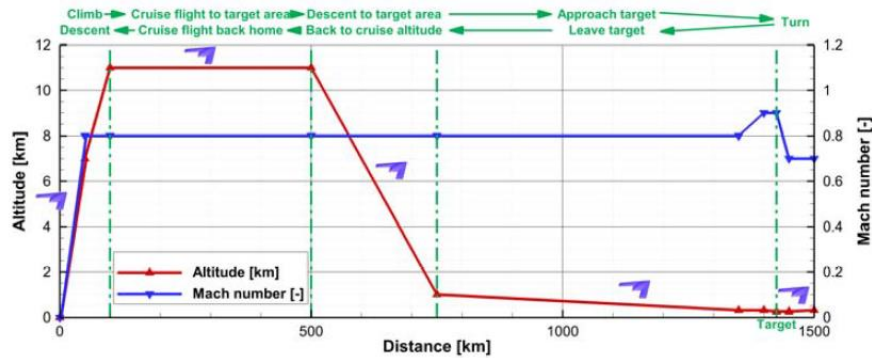
Figure 2-22 - MULDICON subsonic ground strike mission

The main changes from the SACCON conceptual design to MULDICON include a geometric change on the trailing edge sweep to improve internal volume and control surface effectiveness, which had been determined as poor at high trailing edge sweep angles; a parametric analysis of aerofoils and leading edge geometries for a smoother pitching moment coefficient profile and improved lift characteristics while also maintaining low-observability[79,80], numerical studies into several yaw control methods including wing tip split spoilers and split flaps[81], as well as various thrust vectoring nozzle configurations[82]. An engine sizing was also carried out, as well as an aerodynamic optimisation of a low-observable intake design[83].

No additional experimental data was used for the aerodynamic design of MULDICON thanks to the high levels of confidence generated by the extensive validation studies of SACCON. A multi-fidelity aerodynamic design approach was used for MULDICON, where low-fidelity analytical methods were complemented by high-fidelity data sets[84]. Figure 2-23 shows the planform changes between SACCON and MULDICON, as well as the optimum aerofoil distribution for the aerodynamics and control groups.

Furthermore, to increase manoeuvrability while avoiding the drastic pitching moment coefficient changes experienced at high angles of attack, as determined by the SACCON experimental and numerical data (Figure 2-21), the permitted CG range movement was reduced from 2-8% to 0-3% MAC on the stable side of the neutral point. This translates to a total CG movement of only 18 cm for MULDICON, which imposes severe constraints on the structural design, payload

29

integration, and fuel systems. A preliminary CAD three-view of MULDICON is shown in Figure 2-24 without the detailed intake, exhaust or structural concepts, since they were performed separately.
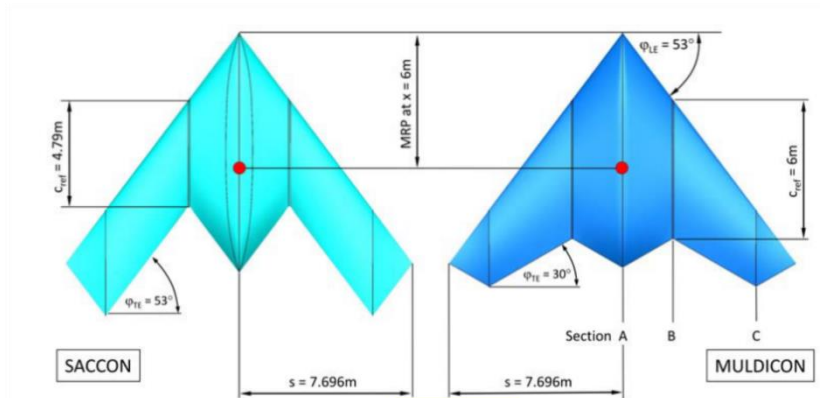
a) Planform changes between SACCON and MULDICON
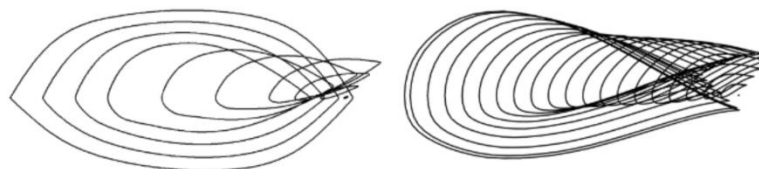
b) Aerofoil distribution for the ASG and the CCG

Figure 2-23 - Planform and aerofoil distribution for MULDICON

The structural concept sizing efforts were performed somewhat separately from the large multidisciplinary design and optimisation of MULDICON. The main sizing factors are the 'fuselage' section structure with its large cut-outs for the engine, payload, and landing gears integration, as well as the low-observability criteria which prohibits any external support structures[85].

For the central wing section, the presence of cut-outs leaves little depth for the reaction of loads through a central spar (bulkhead) which connects to the outer wing's aerodynamic centre, as shown in Figure 2-25. For the outer wing, the main problem relates to the limited height available for the integration of leading and trailing edge control actuators while maintaining the low-observability characteristics. This problem has not been fully resolved for the wing tip yaw control effectors through split flaps.
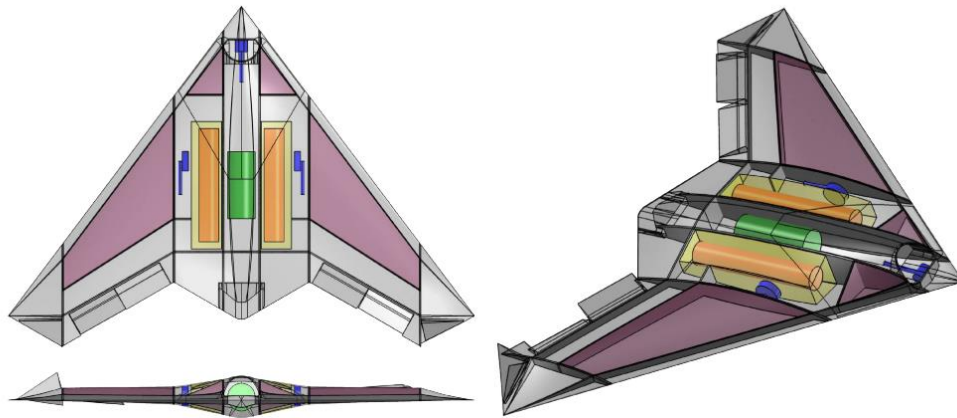
Figure 2-24 - Three-view of MULDICON CAD

Central frame

Remaining torque box cross section inside
the center section

Outer wing
aero centre
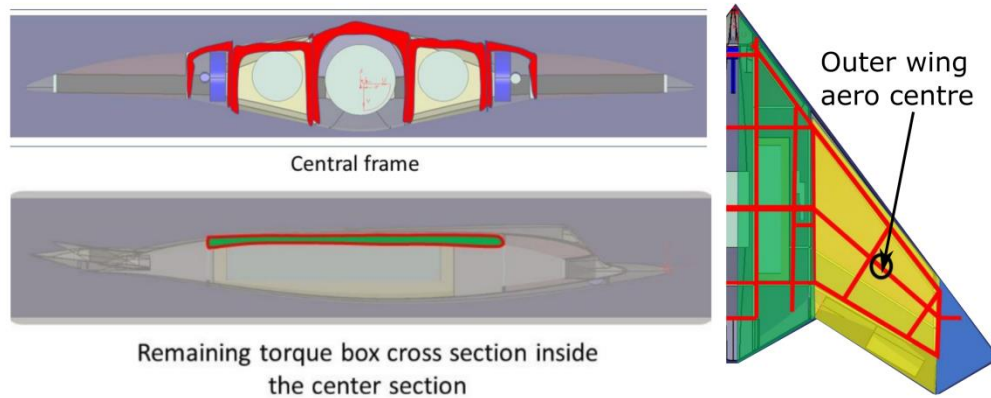
Figure 2-25 - Central wing section limited structural depth

A structural optimisation through FEM reports a structural mass reduction of 37%, from 2457 kg to 1550 kg. This result seems highly optimistic, representing a total structural mass of only 11% of the gross vehicle mass; however, since there is no real database for the structural properties of flying wings, it is hard to evaluate the validity of this result.

An initial aero-structural study for MULDICON has been carried through coupled structural Finite Element Methods (FEM) with vortex lattice (static) and double lattice (dynamic) aerodynamic methods for the evaluation of 654 load cases, including manoeuvres, gust loads, and landing loads. Composite layups and control system stiffness were varied in order to determine their effects on control surface effectiveness. Results show that the most important parameter is the torsional stiffness of the control system, and that the control effectiveness decreases drastically with flight speed, both for inner and outer control surfaces,

with a value of 45% at speeds as low as Mach 0.5, as shown in Figure 2-26. This means that aileron reversal is present at low speeds, and this result is aggravated by the fact that low-observability constraints demand the fully internal integration of the actuation system, resulting in small moment arms[86].
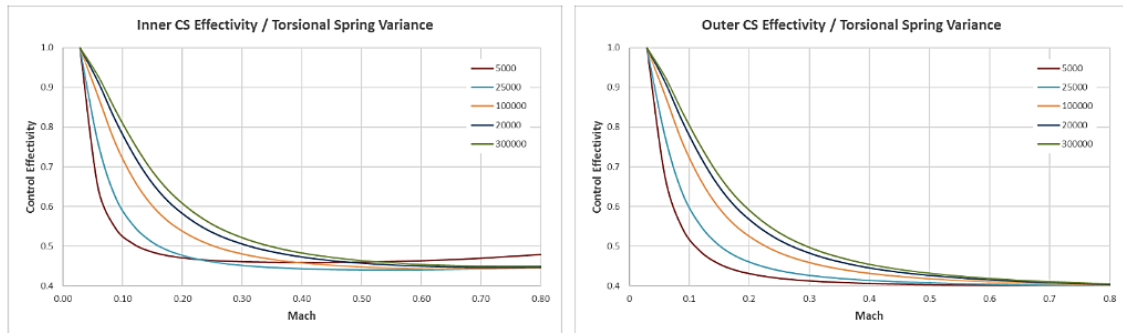
Figure 2-26 - Torsional stiffness and control effectiveness

Furthermore, a considerable amount of bending in the flight direction was found at the central wing section, reducing the effectiveness of the inner trailing edge controls, complicating even more the longitudinal control means.

2.4.2.3 Summary on NATO Research Projects

The large scale, international design effort towards establishing a feasible agile UCAV configuration, MULDICON, was achieved by the two decades of research, modelling, and validation of vortex flow topologies over non-slender wings. As shown by the numerical and experimental data, vortex breakdown results in dramatic pitching moment changes which are difficult to control without a horizontal tail and long moment arms. Low-observability constraints often result in the exclusion of the horizontal and vertical tails, which are very efficient means for longitudinal and lateral control; however, these difficulties can be overcome by innovative thrust vectoring nozzles, wing tip split flaps, as well as by novel concepts such as fluidic control.

Other major challenges include the integration of low-observable intakes and exhausts without a big impact on the engine and overall performance of the configuration, especially for high angle of attack manoeuvres. Structurally, the limited volume available requires complex actuation system designs that can comply with the control and aero-elastic demands without compromising the

stealth characteristics. One possible solution is to use of an 'Active Aero-elastic Wing', as demonstrated by Lockheed Martin's X-56 UAV[87].

A schematic of the different NATO projects leading to the multidisciplinary conceptual design studies on the MULDICON UCAV and their individual milestones is schematically shown in Figure 2-27.
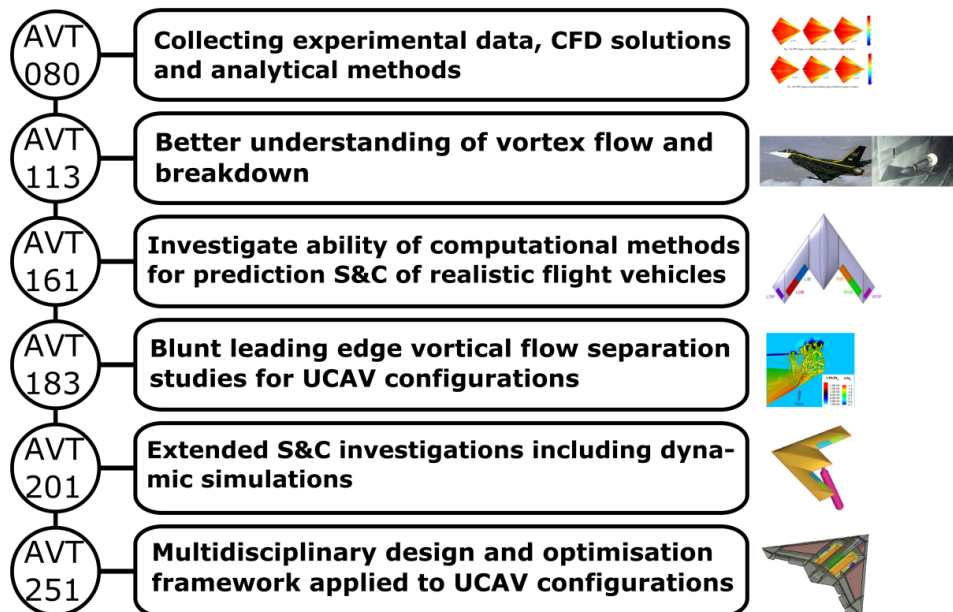
Figure 2-27 - NATO AVT projects timeline and milestones

2.4.3 Packaging and Structural Challenges

The basic principle of packaging refers to the allocation of the internal components within the aerodynamic shape of the vehicle, properly balancing the performance, aerodynamic, stability, structural, and systems requirements.

Due to the low-observability constraints prevalent in UCAV designs, packaging becomes a significant design issue. A low-observable UCAV designed at Cranfield University during the late 1990s demonstrated that stealth requirements had a major impact on the structural design due to the need to align internal structural components with leading and trailing edges, as well as having inefficient solutions to lateral controls due to the thin wings and trailing edges, little space for systems, and the need for a solution that would not compromise the stealth of the vehicle[88,89]

Compact geometries also have a major impact on the system distribution. A clear example is the fuel tanks and fuel system. A complex fuel tank distribution is required not only because of the low volume availability in the outer wings, but also for improved static stability and centre of gravity control, with trim tanks commonly required, as exemplified by the various UCAV concepts in Figure 2-28.

a) Storm Shadow   b) MULDICON   c) CU U-99
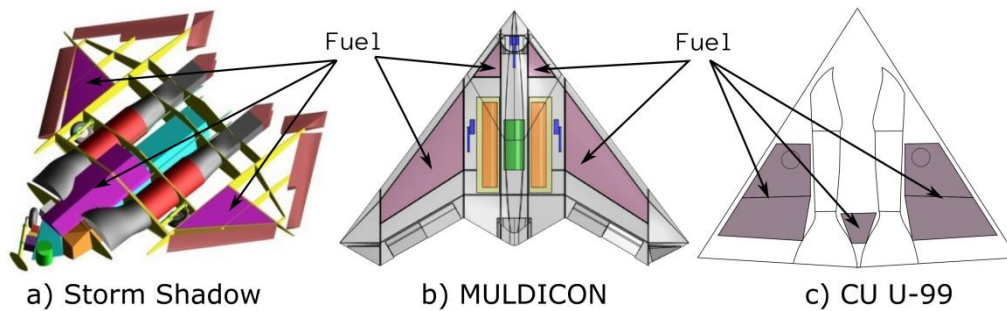
Figure 2-28 - Distributed fuel tanks in UCAV concepts

One of the main consequences of low-observability requirements is the inclusion of internal weapon bays. High speed air flow over open cavities generates intense aero-acoustic tones and pressure zones, which can cause damage to the systems inside the cavity, and compromise the integrity of the surrounding structure. Experimental results for an open cavity at a Mach number of 0.89 show sound pressure level peaks close to 150 dB[90], which can increase to 170 dB at Mach 1.19[91]. These aero-acoustic and aero-structural interactions are also influenced by the attitude of the vehicle, with pressure levels increasing with increases in angle of attack[92], while also being affected by the sequence and speed of the opening and closing of the cavity doors[93].

Furthermore, the highly unsteady flow in the vicinity of an open cavity has a significant influence on the separation trajectory of the weapons[94], which can be propelled towards the vehicle itself, as shown by the experimental weapon separation results for a fighter aircraft[95] in Figure 2-29.
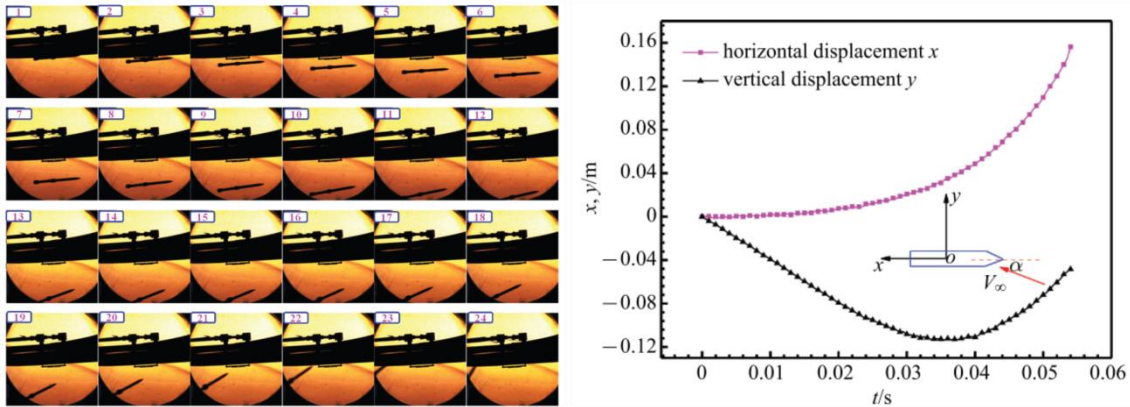
Figure 2-29 - Weapon separation trajectory issues

Other operational constraints like carrier-based operations and transportation requirements (to active operational zones) impact the packaging, structure, and systems of the vehicle by mandating wing folds, or large removable structural components. The wing-fold mechanism, and the effect on the wing geometry, is shown in Figure 2-30 for Boeing's *MQ-25 Stingray* and the X-47B. This structural requirement has a severe impact on the systems architectures and an obvious structural mass penalty.

The integration of specialised components and systems for intelligence and surveillance roles often results in geometrical discontinuities that could affect the vehicle's signature and performance, as can be seen from the *RQ-170 Sentinel* and Lockheed Martin's UCAV concept shown in Figure 2-31. These trade-offs are very difficult to evaluate during conceptual design studies, since they require an explicit system definition, and a high-fidelity approach to the aerodynamic, stability, performance, and stealth penalties.
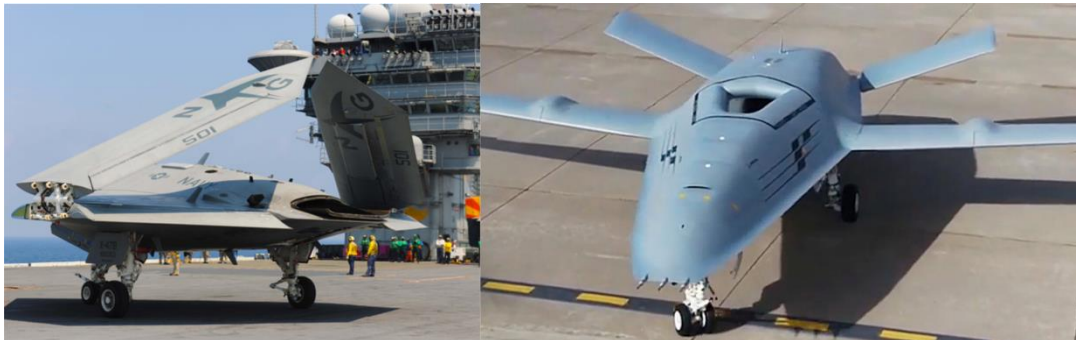
Figure 2-30 - Wing-fold on X-47B and MQ-25

Figure 2-31 - Observable but blended protuberances on flying wing UAVs

2.4.4 Material Choices

Due to the high load demands from typical combat missions, UCAVs are ideal candidates for the extensive use of composite materials for structural weight reductions with equivalent or superior strength and stiffness when compared to typical aerospace metallic alloys. The use of advanced manufacturing techniques such as automated fibre placement (AFP) and automated tape laying (ATL) can significantly reduce the production time and the number of components. As a result of cleaner aerodynamic surfaces and fewer discontinuities the low-observability characteristics of the vehicle can also be improved[96]. In the case of the X-47B, 90% of its outer surface structure and significant portions of the outer wing structure were constructed using carbon-based composite materials[97]. The Neuron UCAV demonstrator has also been designed with a large use of composite materials.

Composite materials also offer the possibility of directly integrating a wide variety of sensors into the structural components themselves for real-time *in situ* health monitoring[98]. Fibre optic sensors have been shown to accurately detect and monitor fatigue cracks in embedded composite structures, while also having small dimensions and weight, high durability and bandwidth capabilities, and being insensitive to electromagnetic interference.

One of the main challenges regarding the use of composite materials refers to lightning strike damage, which can cause embrittlement, delamination, resin evaporation, and structural failure. Lightning strike protection (LSP) in composites is provided through a metallic mesh, commonly aluminium or copper bonded directly into the composite laminates. Potential metal-free solutions such as carbon nanotubes, graphene, and graphite could provide sufficient electrical

36

conductivity while also improving the structural characteristics. Finally, LSP poses some maintenance and reparability issues[99].

Composite-based structural components can also suffer from delamination due to low velocity impacts such as tool drops during production and foreign object damage. Delamination specially affects structural components under compression loads where buckling can propagate through the delamination cracks, severely compromising the structural integrity of the vehicle[100,101]. Furthermore, combat aircraft can suffer in-field damage due to ballistic impacts or shrapnel damage on the aircraft's skin. In-field reparability is therefore a major concern for combat aircraft with extensive use of composite materials. Recently it has been shown that vacuum infusion is well suited for battle damage repair of composite structures through the use of portable composite curing units and low viscosity resins, providing a low cost solution[102].

The difficulty of selecting suitable materials increases as the design speed of the vehicle increases. At supersonic speeds, aerodynamic heating takes place due to friction, introducing mechanical and structural challenges due to thermal effects. Table 2-1 shows typical skin temperatures as a function of cruise Mach number.

The mechanical properties of composite materials and some aluminium alloys degrade with increases in temperature, with the upper operational limit being approximately 120 °C. However, state of the art carbon-reinforced composites such graphite fibre/PMR-15 and graphite fibre/PMR-11-55 have been proven to withstand thousands of hours of use at temperatures ranging from 290 °C to 345 °C, making them good candidates for their use in speeds up to Mach 4.0.

Table 2-1 - Skin temperature as a function of Mach number

	Mach Number				
	2.0	**2.5**	**3.0**	**3.5**	**4.0**
Temperature [°C]	100	150	200	300	370

A selection guideline[103] for appropriate materials for current supersonic and future high-supersonic and hypersonic concepts is summarised in Table 2-2.

Table 2-2 - Material selection guide for current and future supersonic aircraft

Aircraft Part	$M_{Cruise} \leq 2.0$	$2.0 \leq M_{Cruise} \leq 4.0$	$M_{Cruise} \leq 4.0$
Structure	*Fuselage*: Al 2090-T651, 7075-T6, 8090-T651 (nose) *Skeleton*: Ti-6Al-4V or other Ti alloys *Wing*: commercial grade CFRP	*Fuselage*: CFRP PMR-15, PMR 11-55, high modulus composites *Skeleton*: Ti alloys *Wing*: same as fuselage	*Fuselage*: polymides, MBIs, graphite fibre-phthalonitrile matrix or ceramic-metal composite Skeleton: Ti alloys Wing: same as fuselage, or stainless steel
Engine	*Compressor*: Ti alloy *Combustor and Turbine*: ceramic coated superalloys	*Compressor*: Ti-6Al-2Sn-4Zr-6Mo or similar Ti alloys *Combustor and Turbine*: ceramic coated superalloys or Nickel-based superalloys	*Compressor*: advanced Ti alloy *Combustor and Turbine*: ceramic coated superalloys or Nickel-based superalloys

2.4.5 Propulsion System

As mentioned previously, the low-observability requirements that often dominate UCAV designs have undesirable propulsion integration characteristics, mainly due to the buried engines, serpentine inlets and complex exhaust geometries, all having an impact on the vehicle's performance.

Serpentine inlets can suffer from extreme flow separation resulting in pressure losses and thrust penalties, as well as increased fuel consumption. One way to improve the flow uniformity through the inlet is through the addition of vortex generating rings. Furthermore, inlet structures can have aero-elastic responses that are hard to predict due to the unsteady flow, especially when considering the use of composite radar absorbent materials[104].

Another aspect of stealth integration is the compact geometries and low volume availability, which limits the diameter and bypass ratios of potential engines, resulting in poor propulsive efficiency. In addition, as aircraft architectures move towards a *more electric* philosophy, the power requirement of the vehicle

increases due to the numerous sensors and systems. Similarly, the thermal loads will increase due to the waste heat of such high-power systems. This trend poses a significant challenge for the integration of the propulsion system, as summarised in Figure 2-32 for current and future UCAVs[105].
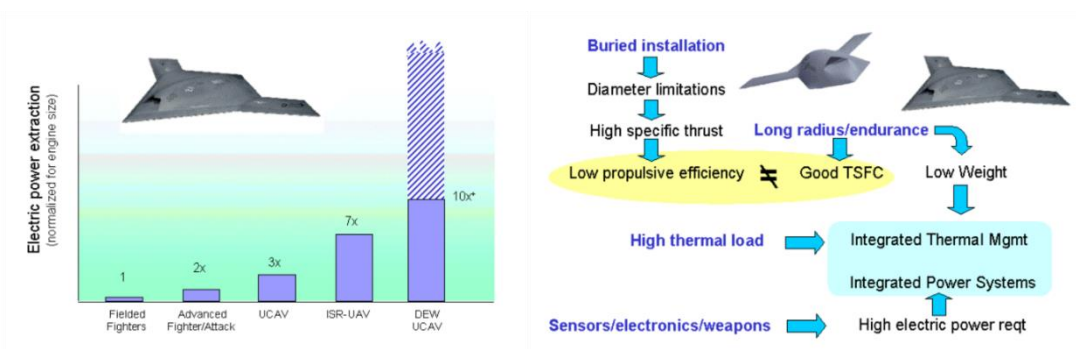
Figure 2-32 - Power and thermal issues on the propulsion integration of UCAVs (DEW: Directed Energy Weapons)

Propulsion integration issues increase as the speed of the vehicle increases, with the main complications resulting from the shock waves present at the inlet face. Variable geometry inlets result in complex mechanical and structural arrangements, with an obvious mass penalty. A fixed geometry solution to this problem exists for speeds up to Mach 2.0; these intakes are known as divertless supersonic inlets (DSI). Examples of current advanced fighters which employ DSI are the F-35 and the Chinese J-20. These inlets make use of a three dimensional compression surface geometry, or 'bump' in front of the inlet face in order to divert the turbulent boundary layer, as shown in Figure 2-33. Even though this type of inlet has been studied since the 1950's[106], the recent advances in numerical modelling has allowed improvements in the design and optimisation of the compression surfaces for various flight conditions and performance goals[107].

At higher speeds (Mach > 2.0), variable geometry mixed compression inlets are required to slow down the freestream through a series of oblique shockwaves. Mixed compression inlets can be two-dimensional or axisymmetric. Two-dimensional inlets can control the position and intensity of the shockwaves through variable angle ramps, while the axisymmetric inlets usually operate through the retraction or contraction of the spike, as seen in Figure 2-34 for the mixed compression inlet of the SR-71 at various Mach numbers. A series of

bypass doors can be added for improving the amount and quality of airflow at various speeds.
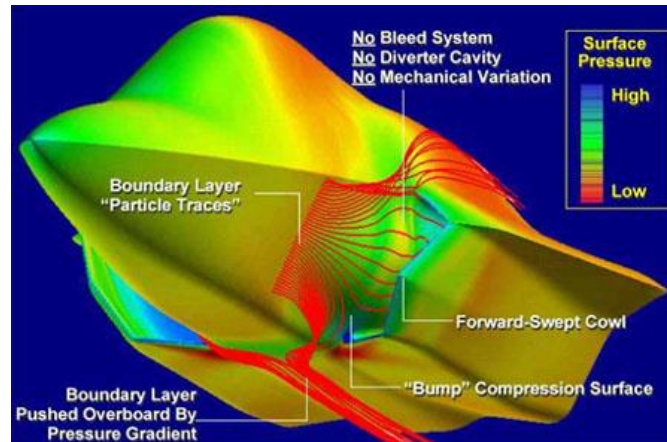
Figure 2-33 - DSI boundary layer streamlines
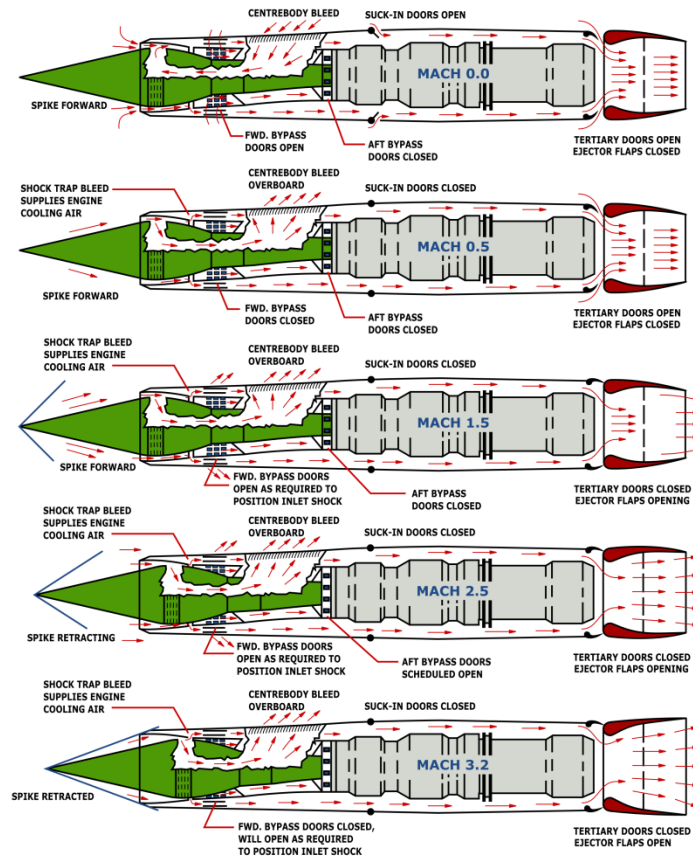
Figure 2-34 - SR-71 axisymmetric inlet operation at various Mach numbers

At high-supersonic and hypersonic speeds, various turbine-based combined engine architectures that combine a turbojet or turbofan component with typically supersonic engines such as ramjets and rockets can be employed. These

40

combined propulsion systems present unique design challenges due to the complicated mechanical system of the inlet, the high temperatures achieved (> 2800K) at high speeds, which impact the structural and material selection often requiring actively cooled structures. The design of such systems involves a much more coupled approach, considering many more design constraints such as secondary systems and cost constraints from the early design stages[108], as summarised in Figure 2-35.
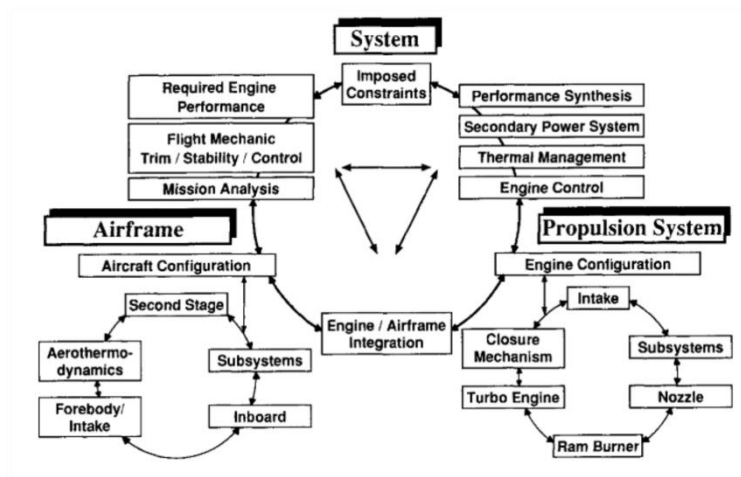
Figure 2-35 - Integrated high-supersonic propulsion system design

2.4.6 UCAV Conceptual Design Studies

Various UCAV conceptual design studies have been reported in the literature, most of which assume tailless geometries for improved low-observability. A summary of each study will be presented below. The MULDICON project[78], and Woolvin's performance trade studies[68] have already been mentioned in §2.4.2.2 and will not be repeated in this section.

Niyomthai has developed a custom aircraft design framework which emphasizes the packaging challenges for tailless low-observable subsonic UCAV configurations[109]. Aerodynamic estimates have been included through empirical lift and drag estimates including the effects of control surfaces during take-off and landing segments, statistical mass estimations have been used for fighter configurations modified for unmanned aircraft, the engine performance has been modelled through empirical regression methods, and stability characteristics have been obtained through DATCOM methods. Furthermore, Niyomthai makes

use of the robust LSGRG2 gradient-based optimiser and shows that the methods presented can converge for tailless UCAVs. Niyomthai has also defined explicit packaging configurations depending on the type of mission (avionics suite), number of engines, and number of internal weapon bays. Because this framework is specifically tailored for packaging studies, the mission definition has been limited to a single instance of a subsonic low level strike (Hi-Lo-Hi). Through the proposed framework, Niyomthai was able to quantify the effects of varying different aircraft parameters such as number of wing kinks, the number and dimension of weapon bays, number of engines, type of control surfaces, changes in desired CG location, and a comparison between a UCAV design and an equivalent manned version, with a mass increase of nearly 200% for the manned version.

Nguyen *et al.*[110] make use of an in-house Aircraft Design Synthesis Program (ADSP) for multi-fidelity modelling and optimisation of UCAVs. At the low-fidelity end, empirical aerodynamics, statistical mass predictions from Raymer, and empirical stability relations are used for during an initial sizing loop. At the second sizing loop, design of experiments is used in combination with CFD to create surrogate models for aerodynamics responses. They present validation data against a generic non-stealth UCAV designed by Jeon *et al.*[111]; however, this design has been achieved through low fidelity aerodynamics, mass estimation, propulsion, and stability methods. Nguyen *et al.* then apply Sequential Quadratic Programming (SQP) in a multi-objective scenario of a typical subsonic ground strike mission; no indication of payload mass or configuration has been specified. The objectives are: maximise range and minimise take-off weight. The results summarised in Figure 2-36 show similar trends but significant errors for the low fidelity methods.

$$f(x) = \omega(W_{TO}/W_{Base})+(1-\omega)(R/R_{Base})$$
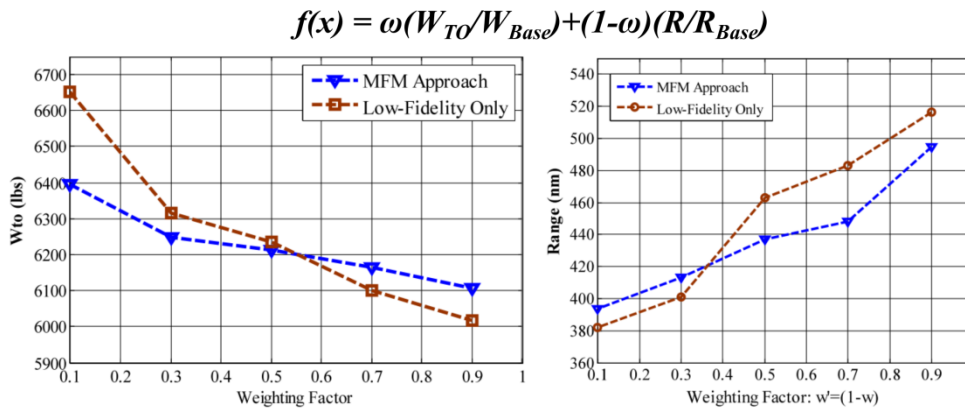
Figure 2-36 - Multi-fidelity UCAV design space exploration

The aircraft conceptual design environment presented by Amadori *et al.*[112] shows an integrated approach towards high-fidelity CAD and structural optimisation via finite element methods. Furthermore, it can account for the design and implementation of a control system and control surface design. However, it relies on low-fidelity, empirical aerodynamic estimations that cannot account for the unsteady flow topologies present in UCAV configurations and their interactions with the control system.

In the study presented by Lee *et al.*[113], a VLM supplemented with empirical friction drag estimations has been coupled to a physical optics approximation for RCS calculation, and a multi-objective optimisation of tailless UCAV planforms and aerofoils has been conducted through an evolutionary algorithm. Results show a drastic improvement in lift-over-drag of approximately 50% with a reduction in monostatic RCS of 25% for the non-dominated solutions. This study has been carried out for clean geometries using perfect electric conductor materials (no intake, exhaust, control surfaces) without any packaging considerations, as seen by the geometries in Figure 2-37.

Çavus[114] has applied a simulated annealing algorithm for the multi-objective optimisation of supersonic UCAVs. This work is based on very low fidelity aerodynamics and propulsion methodologies for configurations that do not consider low-observability characteristics. Engine and payload integration have not been considered, neither has the aerothermal effects been used in the vehicle

sizing. It is unlikely that this study reflects any real results or trends, but is only a demonstration of the optimiser in an aircraft design environment.
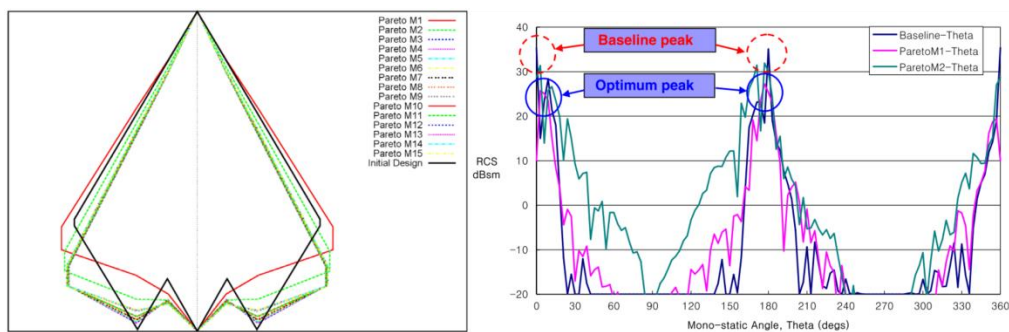
Figure 2-37 - Couple Aerodynamics-RCS optimisation

In the short study published by Sathe *et al.*[115] the effects of tailless UCAV planforms on field performance have been investigated through a VLM, empirical friction drag corrections, and a genetic algorithm. Results show that take-off distance is inversely proportional to the vehicle's span. Information on the mission, mass estimate methods, payload integration, or propulsion modelling are not discussed.

A large multidisciplinary design optimization framework for the design of the future generation of Efficient Supersonic Air Vehicles (ESAV) has been developed by Morris *et al.* at Virginia Tech[116,117]; these designs are intended to perform long-range bomber missions, but an option for unmanned configurations has been implemented, specifically in terms of the mass estimation. This framework consists of a fully parametric geometry definition using Kulfan's Class Shape Transform (CST)[118], which enables efficient aerodynamic optimisation of arbitrary configurations. A medium-fidelity commercial aerodynamic package called ZONAIR has been integrated into the framework, as well as a physical optics approximation for RCS calculations. Mass estimation methods consist of empirical regression methods for similar classes of aircraft. Medium-fidelity engine analysis tools have been integrated, including mass estimation for low-observable intake and exhaust support structures. Handling qualities have been added into the conceptual design stage through stability derivatives available from the aerodynamic analysis and the use of Digital DATCOM[119].

44

A performance study on UCAVs has been carried out by Ahn *et al.*[120] where, based on surface-to-air missile performance data, a volume of various degrees of probability of kill (P_K) has been defined, and UCAV speed and instantaneous manoeuvrability have been matched against values of P_K. This study shows that in order to reduce P_K to 0%, UCAVs should be able to safely operate at manoeuvrability loading factors as high as 14g. Subsonic vehicles, even at high loading factors of 9g, have approximately a 30% P_K. This study does not establish the potential advantages of low-observability, which would decrease the probability of detection.

2.5 Summary

Unmanned aircraft have existed and been employed in military roles since the early days of aviation, starting with the Aerial torpedo and the Kettering Bug before and during the First World War. Subsequent armed conflicts saw a more widespread use of unmanned aircraft in different roles such as target practice decoys, surveillance and reconnaissance, and even early versions of weapons delivery systems. Recent uses of UAVs and UAS in combat scenarios include low-speed, long-endurance configurations such as the MQ-1 Predator and the MQ-9 Reaper armed with laser-guided missiles and smart munitions. These configurations cannot operate in contested or denied environments due to their poor stealth, limited manoeuvrability and low speed.

Unmanned Combat Aerial Vehicles, or UCAVs, have emerged as the next generation of unmanned aerial vehicles intended to operate remotely alongside manned fighters and even autonomously in the near future. UCAVs include high degrees of stealth, while also partially matching speeds, performance, and payload requirements of modern manned combat systems, as is observed by the advanced technology demonstrator programmes, and the recent *loyal wingmen* developments in many countries around the world.

There is a wide range of capabilities currently being envisioned as forming part of the UCAV operational envelopes, from fully subsonic, low-payload configurations, to high-supersonic or even hypersonic global strike missions.

Through the literature review, it has been established that low-observability design requirements impact almost every aspect of UCAV design, from the choice of overall configuration, to the detailed design of systems and subsystems such as the intake and exhaust, as well as the material selection and structural arrangement, which includes tight packaging constraints for all internal fuel and payload configurations. The aspects of stealth that can be more comprehensibly addressed during the early design stages are the radar and infrared signatures; visual and acoustic signatures can be analysed further down the design process. In addition, the performance and mission planning can have a large impact on the susceptibility and survivability of the configuration.

The moderate to high sweep angles resulting from aerodynamic, performance, and stealth requirements result in unsteady, vortex dominated flow topologies which present special challenges for the stability and control of UCAV designs, as demonstrated by the extensive NATO research projects. This affects the design efforts from the early design stages, often requiring high-fidelity data from specialised numerical and experimental tests, especially for the analysis of manoeuvres and detailed analyses of certain performance criteria like high angle-of-attack manoeuvres.

From the conceptual design studies and aircraft design frameworks reported in §2.4.6, it can be seen that low fidelity models for the areas of propulsion, mass estimation, performance, and stability are commonly used. Furthermore, most studies focus on the aerodynamic configuration with little consideration to the low observability, packaging, and payload integration, except for Niyomthai, whose work is restricted to subsonic configurations. Large performance and mission trade studies have not been reported for subsonic or supersonic configurations. Additionally, these studies have a large disparity between the high-fidelity aerodynamic analysis tools and other design disciplines such as propulsion modelling; the real value of high-fidelity aerodynamics coupled to low fidelity methods is not clearly explained and no real comparisons are available to demonstrate the validity of this approach.

Moreover, none of the conceptual design studies shown above have the robustness and flexibility to investigate every aspect of the conceptual design in a consistent and highly-coupled way. Therefore, there is a need for developing conceptual design models that are flexible and robust enough to quickly evaluate large areas of the design space under a consistent set of analysis tools and fidelity levels. These methodologies should allow the designer to explore subsonic, transonic, and supersonic configurations under a variety of combat missions and performance requirements while maintaining low-observability design choices in mind, while also considering payload integration, cost, and supersonic effects such as aerodynamic heating in the design loop.

To address this need, aircraft conceptual design methodologies appropriate to low-observable UCAVs have been developed and integrated into the GENUS framework. Chapter 3 will introduce the basic philosophy and structure of the GENUS framework, while Chapter 4 will detail the methodologies developed throughout this research. The technological challenges of UCAV design and development have been published under the title *Technology challenges of stealth unmanned combat aerial vehicles* by the Aeronautical Journal (2017)[121].

3 THE GENUS AIRCRAFT CONCEPTUAL DESIGN ENVIRONMENT

3.1 Introduction

The GENUS aircraft conceptual design environment has been under development at Cranfield University's Aircraft Design Group since 2012[122]. Its name derives from the taxonomical classification of organisms representing its capability to design, analyse, and optimise a wide range of aircraft *species* under a common architecture, as is schematically shown in Figure 3-1.
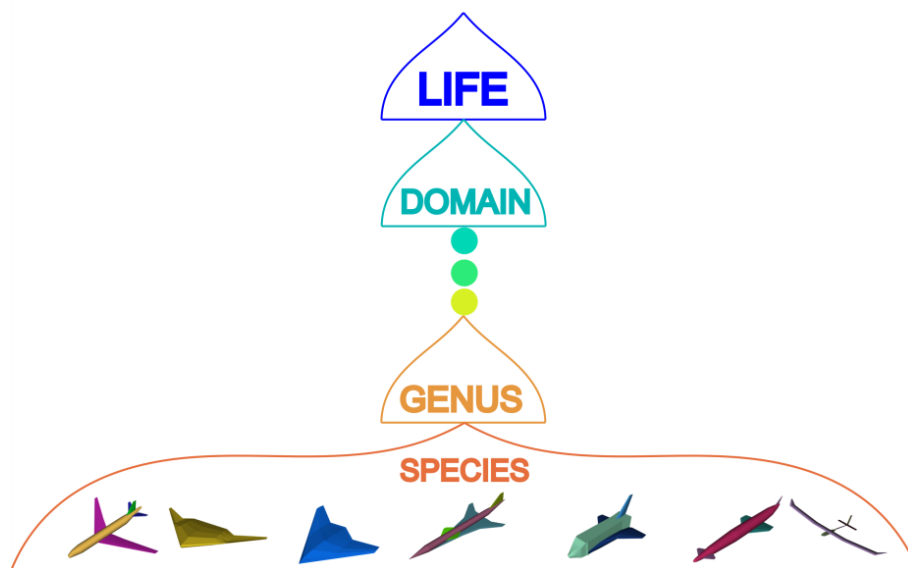
Figure 3-1 - Taxonomical classification of organisms, applied to aircraft

3.2 The GENUS Methodology

GENUS is a Java-based code, which makes it able to perform in any operating system without the need for a client license. Java's online support and development is extensive, with several numerical, mathematical, graphic, and post-processing libraries available for free, greatly increasing the potential capabilities of the framework at a reduced development cost[123, sect.3.4.2].

Another important feature is Java's capability to communicate with other programming languages such as FORTRAN and C/C++ through its Java Native Interface (JNI) implementation. Figure 3-2 shows the integration and communication process between Java and legacy aircraft design codes, often

written in C, C++, and FORTRAN. This functionality is used extensively across the analysis disciplines of the GENUS framework to add fidelity without requiring lengthy re-writing or independent development of complex code.
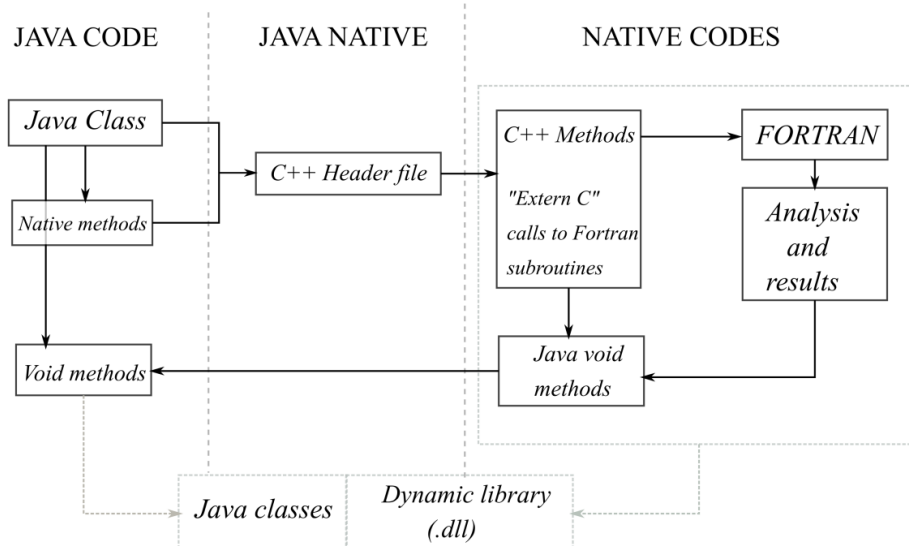
Figure 3-2 - General procedure for interaction between Java and legacy codes

The core philosophy behind the GENUS architecture can be summarised by the following key aspects:

o Modularity: Clear separation of distinct analysis disciplines organized in hierarchical programming levels. Abstract classes lie at the root of this functionality, also supported by Java's polymorphism.

o Flexibility: The analysis techniques can be applied, through high degrees of abstraction, to numerous species of aircraft without the need to modify the core framework.

o Expandability: The capacity to include various fidelity levels in the analysis modules, ranging from empirical methods up to numerical high-fidelity tools. Java's native interface and its polymorphism support this aspect. Special modules (explained below) can be used to add specialist analysis tools.

o Robustness: A cohesive framework that relies on well tested methods and appropriate error and exception handling practices.

o Independence: Avoid licensing and platform dependant software when appropriate.

The GENUS framework is not to be considered as a *black box* system that requires minimal input from and by the user; on the contrary, GENUS relies on a knowledgeable user/designer that interacts in a cyclic and constructive manner with the front and back ends of the framework. This interaction makes use of the designer's expertise, intuition, and assumptions in order to generate new knowledge. A top level schematic of the interaction of the user and the framework is shown in Figure 3-3.
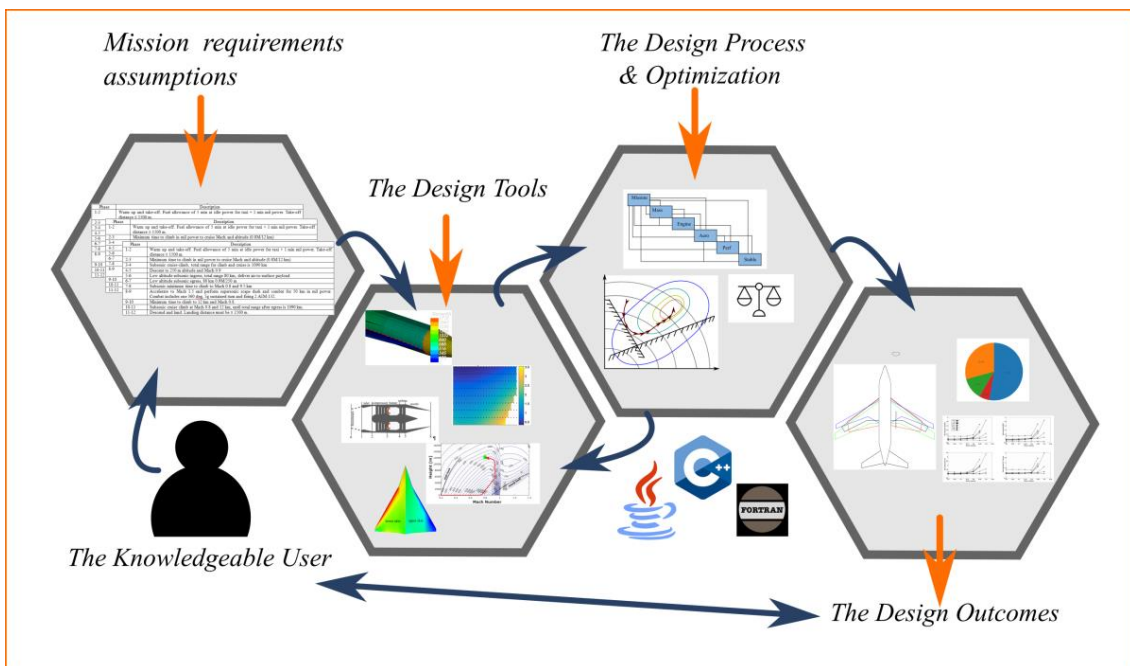
Figure 3-3 - The components and inter-relationships of the GENUS framework

The GENUS core framework consists of nine essential modules which include:

1. Geometry
2. Mission
3. Propulsion Specification
4. Mass Breakdown
5. Aerodynamics
6. Propulsion Analysis
7. Packaging
8. Performance
9. Stability

All modules implement the structure of an abstract 'Genus Module', shown schematically in Figure 3-4. Subsequently, an 'abstract' module exists for every one of the 9 essential modules. All particular modules are extensions and implementations of these abstract modules, as shown in Figure 3-5.
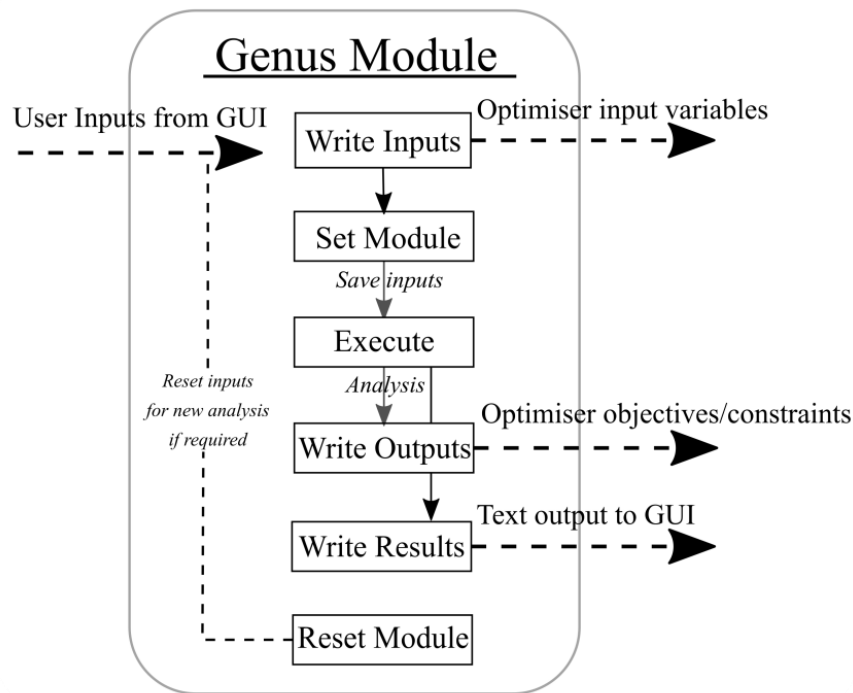
Figure 3-4 - General structure of the abstract 'Genus Module'
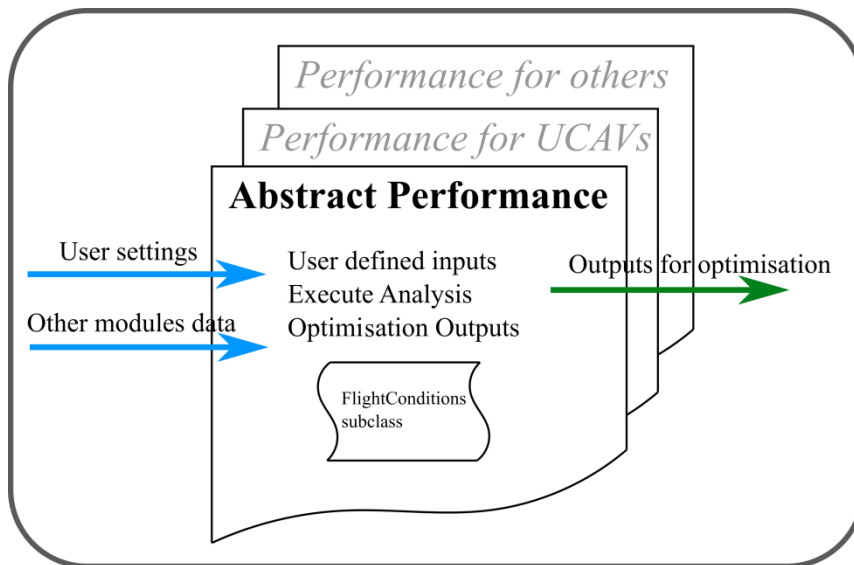
Figure 3-5 - Hierarchy and data flow of performance modules

A set of special modules can be implemented as extensions to the original Genus module in order to analyse non-conventional aspects of aircraft design. Examples of special modules include Radar Cross Section analysis, Sonic Boom intensity, Cost estimation, and Aero-thermodynamic analysis.

A framework schematic showing the initiation of a single design instance is shown in Figure 3-6. Each module can have as many inputs as needed by the user, which will then pass to the subsequent modules as shown by the information flow depicted by the connecting arrows and variables.
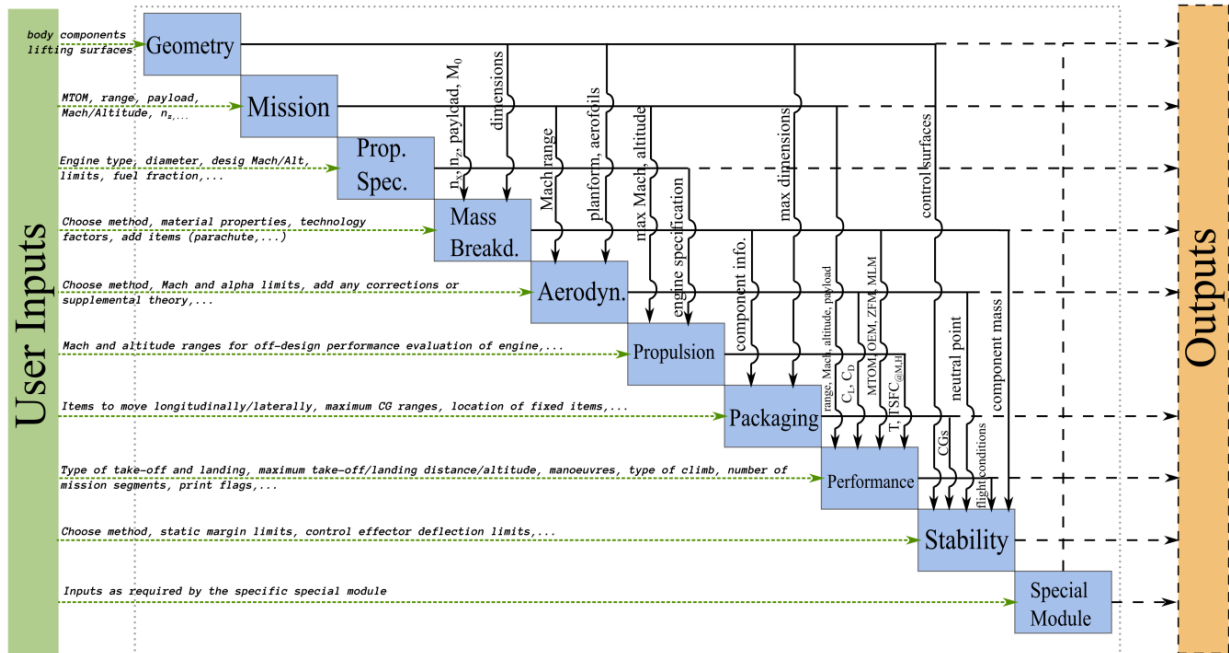
Figure 3-6 - N^2 diagram example for design instance initiation in GENUS

Figure 3-7 shows the N^2 diagram for an optimisation loop of with geometric and volumetric constraints, mass and fuel convergence errors, as well as thrust and stability constraints. The input variables correspond only to the geometry, mission (estimated take-off mass), and propulsion specification modules. This diagram represents a typical convergence optimisation loop for a fixed mission (range, speed, payload ...). The *Objective function* arrow is shown coming out of the framework domain in general representing the various objectives that can be selected; examples of typical objective functions are maximum take-off mass (MTOM), operating empty mass (OEM), total fuel consumption, RCS (at a certain viewing angle or average), amongst others.
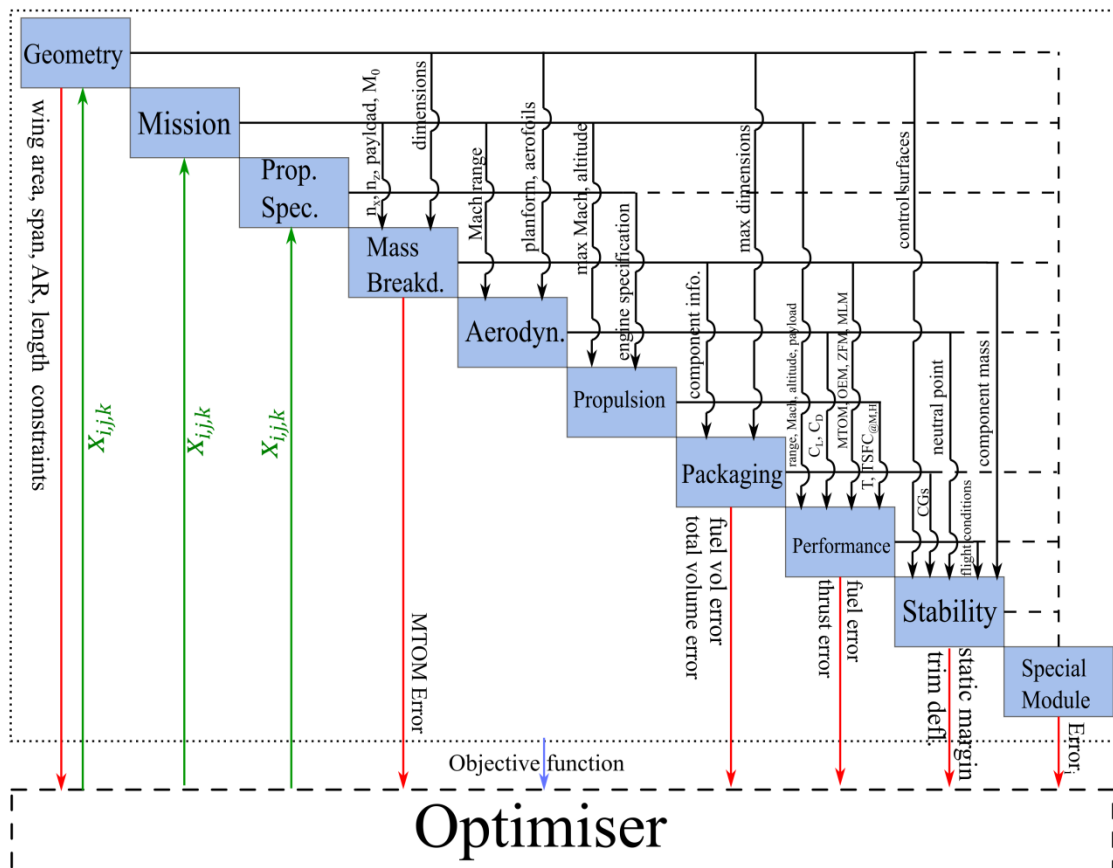
Figure 3-7 - N² diagram example for design optimisation in GENUS

3.3 Multivariate Optimisation in GENUS

GENUS offers an intuitive and simple to navigate user interface, with clear divisions between the analysis modules available, the user inputs, the analysis outputs, which are also the objectives and constraints for the optimisation problem, additional user-defined text outputs (which can include numerical results), and the optimisation tab. Figure 3-8 shows the *Inputs* tab with a single optimisation input, along with the lower and upper bounds, as set by the user. The inputs can be of three different types, namely *List* inputs for selecting pre-defined options that encompass a set of characteristics; *Value* inputs are used for real quantities and design characteristics; and finally *Integer* inputs for selecting number of wing kinks, fuselage stations, and number of engines, amongst others.

54
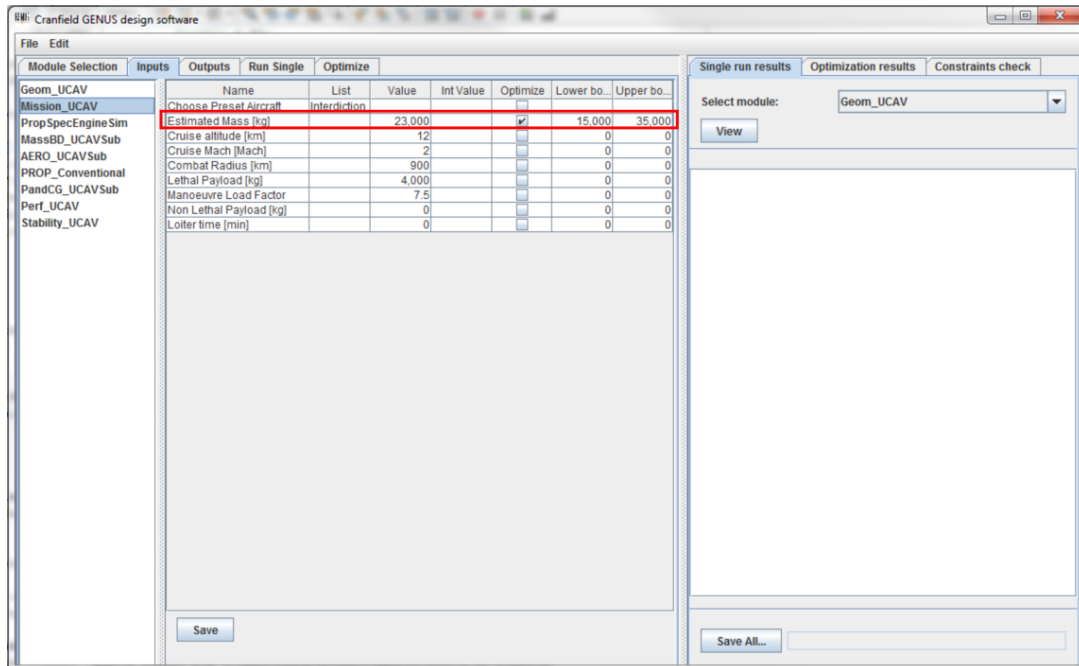
Figure 3-8 - GENUS GUI user inputs tab

In order to generate the numerical outputs from each analysis module, the user must perform a *Single Run*, which produces a single instance of the aircraft based on the current inputs. The objective function and the appropriate constraints are then selected in the *Outputs* tab, as shown in Figure 3-9. In this case, the objective function is the calculated take-off mass, and the constraint is the mass error between the estimated and the calculated value.

Finally, the *Optimize* tab is used to select whether the objective function is to be minimised or maximised, the types of constraints, and the optimisation algorithm to be used. A graphical output of the objective function's history is shown on the right hand side, as shown in Figure 3-10. Additionally, a *Constraints Check* table is available in order to verify if the constraints have been met or violated.

GENUS includes a custom made genetic algorithm[123, sect.3.3.2], and a commercial, well proven, and robust gradient-based optimiser LSGRG2[124], which together offer an efficient hybrid approach for large design space exploration and good convergence upon the global minima.
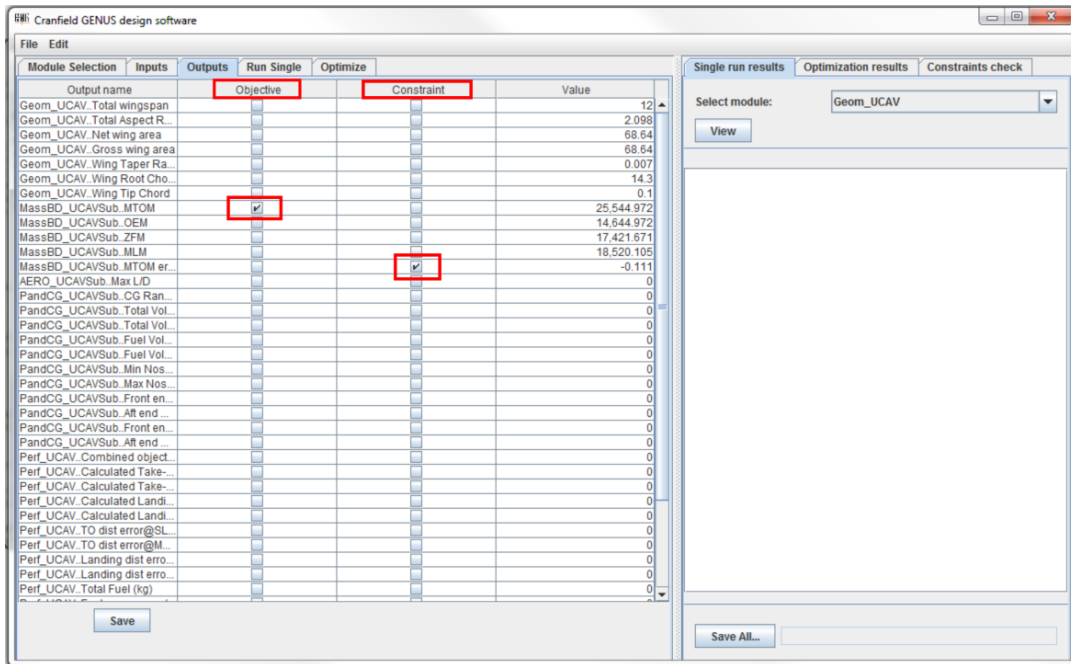
Figure 3-9 - GENUS GUI outputs tab, with objective function and constraint selected
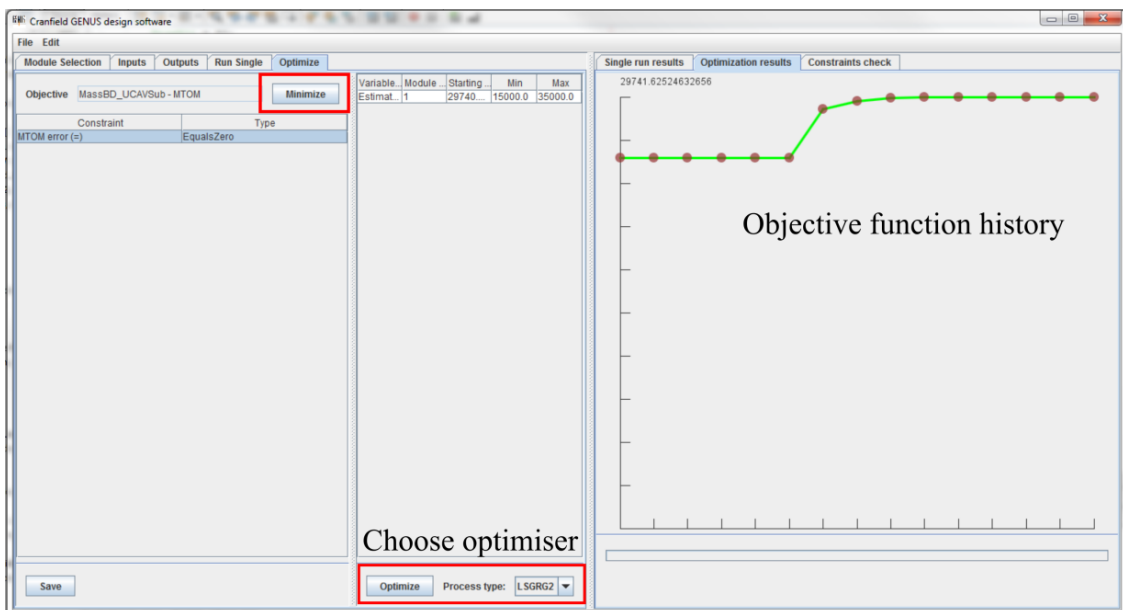
Figure 3-10 - GENUS GUI optimisation output

Formally defined, a single objective optimisation problem is defined by the objective function as:

$$\min f(\bar{x}) \tag{3-1}$$

Subject to:

$$g_j(\bar{x}) \leq 0 \; for \; j = 1,2,\dots,J \qquad \text{(3-2)}$$

$$h_k(\bar{x}) = 0 \; for \; k = 1,2,\dots,K \qquad \text{(3-3)}$$

$$x_i^L \leq x_i \leq x_i^U \; for \; i = 1,2,\dots,N \qquad \text{(3-4)}$$

Where:

$\bar{x}$ is an array of input variables, of dimension N;

$f(\bar{x})$ is the objective function, a scalar;

$g_j(\bar{x})$ are the inequality constraints, of dimension J;

$h_k(\bar{x})$ are the equality constraints, of dimension K; and

x_i^L and x_i^U are the lower and upper boundaries of the input variables.

The basic formula for a constraint error in GENUS is given by Eq. (3-5).

$$e_i = \frac{V_{calc_i} - V_{ref_i}}{V_{ref_i}} \qquad \text{(3-5)}$$

To evaluate the error of a variable which limits lie within a specified range of positive and negative values, $\left[V_{-Limit_i}, V_{+Limit_i}\right]$, the error in Eq. (3-6) can be defined as a *Less than Zero* inequality constraint:

$$e_i = \frac{\left|V_{calc_i} - V_{centrepoint_i}\right| - V_{average_i}}{V_{average_i}} \leq 0 \qquad \text{(3-6)}$$

Where:

$$V_{centrepoint_i} = \frac{V_{+Limit_i} + V_{-Limit_i}}{2} \qquad \text{(3-7)}$$

$$V_{average_i} = \frac{V_{+Limit_i} - V_{-Limit_i}}{2} \qquad \text{(3-8)}$$

Furthermore, several outputs can be combined into a single objective through weighting factors, increasing the capability of GENUS into *quasi* multi-objective optimisation, as shown by Eq. (3-9).

$$f_{comb} = \beta obj_1 + (1 - \beta)obj_2 \qquad \textbf{(3-9)}$$

Where $\beta = [0, 1]$.

For example, Figure 3-11 shows the behaviour of the nose-on RCS and the aspect ratio as a function of weighting factor β, with the combined objective function given by:

$$minimise\ f(x) = \ \beta \cdot RCS_{Nose} + \frac{(1 - \beta)}{AR} \qquad \textbf{(3-10)}$$

This objective function maximises aspect ratio for low values of β, and minimises RCS as β increases.

The changes in the geometries shown in Figure 3-11 are subject to a constant wing area constraint, as well as a maximum nose-on RCS value of -15 dBsm. Little to no change can be seen for values of $\beta \geq 0.6$ due to the lower and upper bounds of the selected geometry inputs.
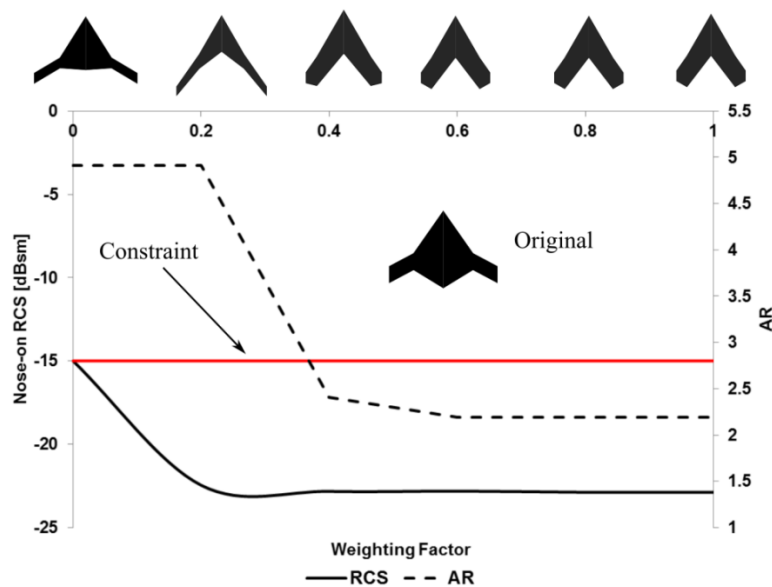
Figure 3-11 - Multi-objective optimisation within GENUS through combined objective functions and weighting factors

3.4 Summary

This chapter has introduced the general architecture of the GENUS aircraft design environment, which is the main design tool used and developed throughout this research. The GENUS framework has been under development since 2012 and it has been successfully applied in the conceptual design and analysis of re-usable hypersonic vehicles, blended wing body airliners, solar powered ultra-high aspect ratio UAVs, supersonic business jets, and –under this research– subsonic and supersonic UCAVs.

The principal philosophies behind the programming strategies and implementation of the GENUS framework have resulted in a highly flexible, modular, expandable, and robust framework capable of handling several *species* of aircraft under a common architecture (for a detailed description of the overall GENUS architecture and coding practices see[123,125,126]).

The next section will introduce the detailed methodologies selected, developed, and integrated for the design, analysis, and optimisation of low-observable unmanned combat aerial vehicles.

4 UCAV DESIGN METHODOLOGIES

4.1 Introduction

This section presents the various methodologies that were selected, developed, and integrated into the design and analysis modules of the GENUS framework.

4.2 Geometry

Aircraft geometries in the GENUS framework are specified through discrete elements which are divided into body components and lifting surfaces. Each class can be further divided into sub-classes which use a library of cross section shapes, planform dimensions, rotations, translations, and aerofoils for a full geometry definition, as shown in Figure 4-1.

Furthermore, a variety of geometry formats required for different analysis tools can be used and transformed from these discrete components. Examples of such formats are the XYZ point-cloud, the LAWGS (wireframe) format[127], DATCOM geometry, AVL panels, and PANAIR structured grids.
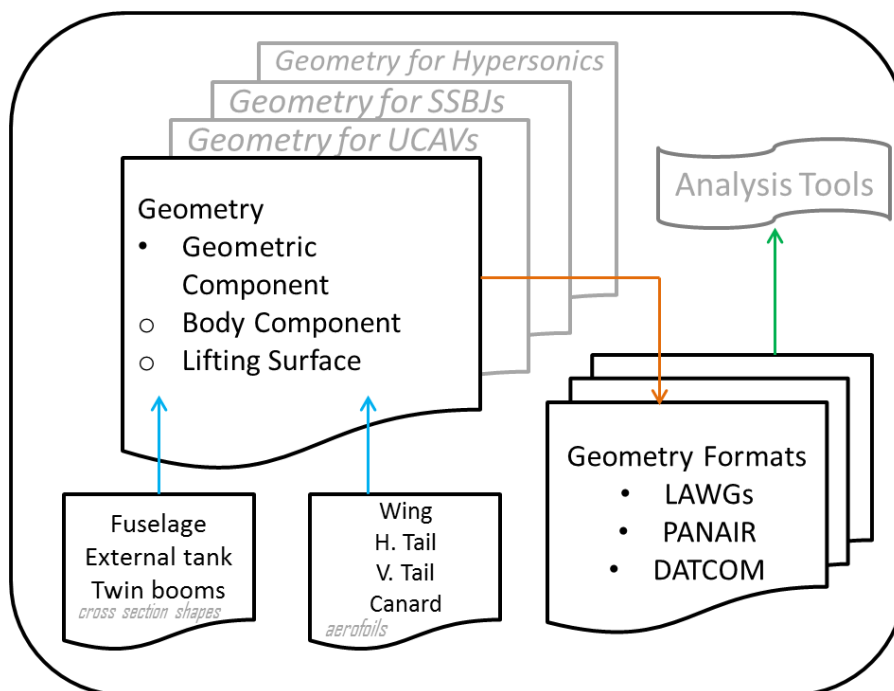
Figure 4-1 - Geometry package components in GENUS

Despite its simplicity, this geometrical definition offers great flexibility and allows the application of geometrical rules such as continuity between leading and trailing edges, parallel edges for reduced RCS, or subsonic leading edges, to mention a few. Figure 4-2 shows two solutions of equal wing reference area while enforcing parallel leading and trailing edges obtained though the GENUS optimisers; the figure on the left is the solution for minimum aspect ratio, while the figure on the right is the solution for maximum aspect ratio.
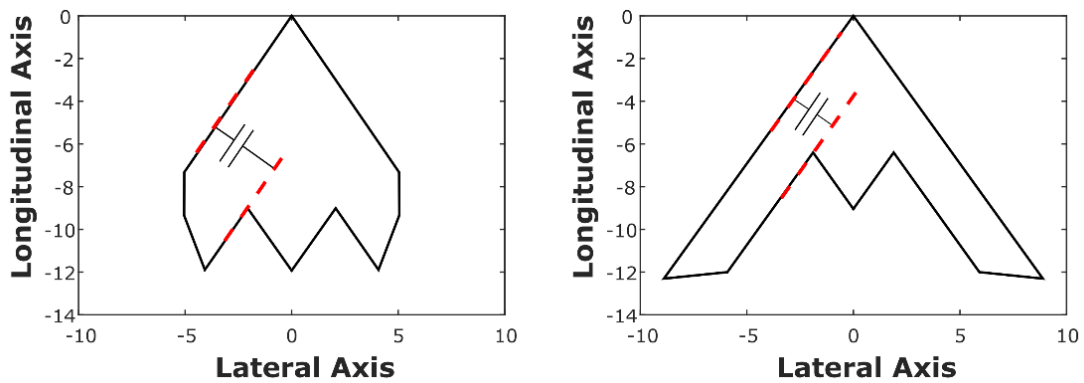
Figure 4-2 - Aligned leading and trailing edges for two configurations of equal area (left: min AR, right: max AR)

4.3 Mission Module

The mission module acts primarily as a user input module where some of the basic parameters required for the analysis of the design mission are specified. Table 4-1 shows the abstract-level inputs and their data type. Not all parameters are appropriate to unmanned vehicles, but the entirety of the inputs need not be specified for each class of aircraft. Additional performance requirements can be added directly in subsequent modules.

Table 4-1 - Mission module inputs

Input	Units	Type
Cruise Altitude	Meters	Real
Cruise Speed (TAS)	m/s	Real
Cruise Mach	-	Real
Target Range	Meters	Real

Target Endurance	Seconds	Real
Number of passengers	-	Integer
Number of crew	-	Integer
Payload	Kg	Real
Payload to drop	Kg	Real
Payload to pick up	Kg	Real
Estimated Take-Off Mass	Kg	Real
Maximum normal acceleration	-	Real
Maximum axial acceleration	-	Real
Take-Off Type (Vert., Hor.)	-	List

4.4 Mass Estimation

Class II, or statistical mass estimation methods have been developed through a combination of manned and unmanned equations, following well established sources such as Gundlach[128, chap.6], Raymer[129, chap.15], Howe[130, sect.AD4], and Roskam[131], as well as Cranfield University mass estimation methods[132].

The validation of the mass estimation for several UCAV demonstrators and conceptual designs is shown in Figure 4-3, achieving good agreement. The gross mass of Taranis has been taken from unofficial data due to the lack of official information[133].

A technology factor corresponding to a reduction in structural mass of 10% has been applied to compensate for the widespread use of composite materials for these novel configurations[134,135].

The mass estimation equations for systems, structural components, and miscellaneous items are given in Appendix B.
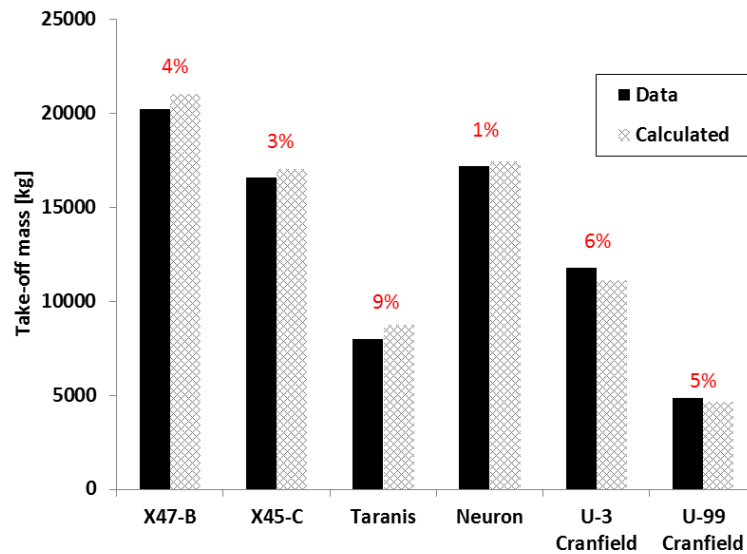
Figure 4-3 - Mass breakdown validation for subsonic UCAV designs

4.5 Propulsion

4.5.1 Propulsion Specification

The propulsion specification module offers the flexibility required to represent complex propulsion systems needed for complex vehicles such as hypersonic transports, or high-supersonic UCAVs, where combined propulsion systems are employed. Figure 4-4 shows the structure of the propulsion specification modules within GENUS, and the types of inputs that can be specified, with the main subclass being the *Powerplant* objects. Each powerplant subclass can be modelled independently under different assumptions and analysis tools, from low-fidelity regression models to medium fidelity thermodynamic analysis.

4.5.2 Propulsion Modelling

4.5.2.1 Empirical Methods

A low-fidelity propulsion model had already been included in the GENUS framework through the regression method given by Howe[130, sect.3.6.2], where thrust and fuel consumption are a function of a few engine characteristics such as static sea-level thrust T_0, bypass ratio R, and flight conditions (Mach number M_N, pressure ratio σ), as shown in Eqns. (4-1) to (4-3).

64
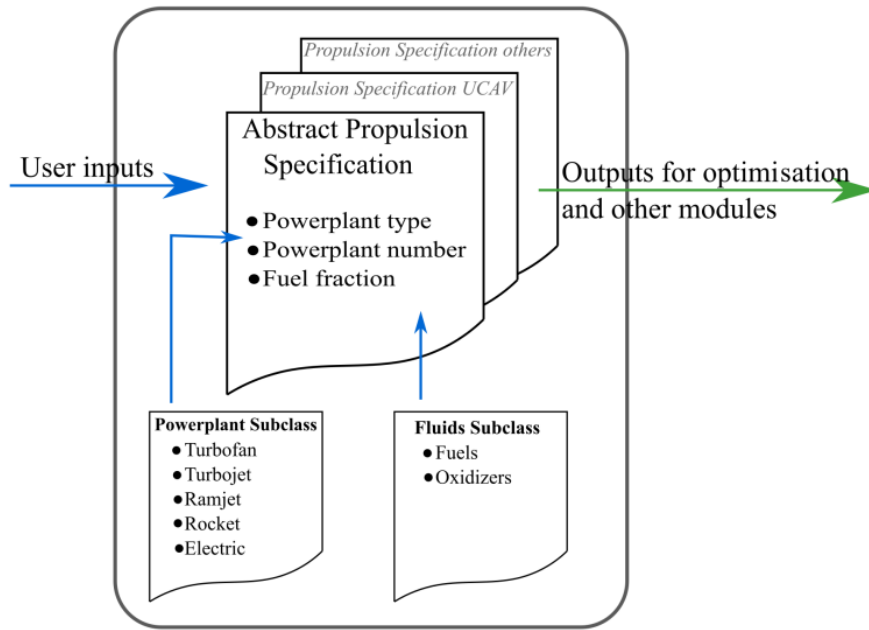
Figure 4-4 - Propulsion specification within GENUS

$$T = \tau T_0 \tag{4-1}$$

$$\tau = \begin{cases} F_\tau[k_1 + k_2 R + (k_3 + k_4 R)M_N]\sigma^s, & M < 0.9 \\ F_\tau[k_1 + k_2 R + (k_3 + k_4 R)(M_N - 0.9)]\sigma^s, & M \geq 0.9 \end{cases} \tag{4-2}$$

The value of F_τ allows for the use of afterburning engines, and is given by:

$$F_\tau = \begin{cases} 1, & \dfrac{T_{Wet}}{T_{Dry}} = 1 \\ \dfrac{\left(\dfrac{T_{Wet}}{T_{Dry}}\right)}{(1.32 + 0.062R)}, & \dfrac{T_{Wet}}{T_{Dry}} > 1 \end{cases} \tag{4-3}$$

The values for all other constants are shown in Figure 4-5.

Specific fuel consumption is given by Howe for non-afterburning engines through Eq. (4-4) and for afterburning engines through Eq. (4-5). The specific fuel consumption factor, c', is estimated as 27 mg/N/s for supersonic engines, 24 mg/N/s for low bypass ratio subsonic engines, and 20 mg/N/s for large subsonic turbofans; however, these values can be corrected by compiling data on newer engines and their performance, when available.

Bypass ratio R	Mach number range	Operating condition	$K_{1\tau}$	$K_{2\tau}$	$K_{3\tau}$	$K_{4\tau}$	$s*$
1 or lower	0-0.4	Dry	1.0	0	-0.2	0.07	0.8
		Wet	1.32	0.062	-0.13	-0.27	0.8
	0.4-0.9	Dry	0.856	0.062	0.16	-0.23	0.8
		Wet	1.17	-0.12	0.25	-0.17	0.8
	0.9-2.2	Dry	1.0	-0.145	0.5	-0.05	0.8
		Wet	1.4	0.03	0.8	0.4	0.8
3 to 6	0-0.4	Dry	1.0	0	-0.6	-0.04	0.7
	0.4-09	Dry	0.88	-0.016	-0.3	0	0.7
8	0-0.4	Dry	1	0	-0.595	-0.03	0.7
	0.4-0.9	Dry	0.89	-0.014	-0.3	+0.005	0.7

Figure 4-5 - Howe's propulsion modelling constants

$$c = c'(1 - 0.15R^{0.65})[1 + 0.28(1 + 0.063R^2)M_N]\sigma^{0.08} \qquad \textbf{(4-4)}$$

$$c = 1.05\left(\frac{T_{Wet}}{T_{Dry}}\right)(1 + 0.17M_N)\sigma^{0.08} \qquad \textbf{(4-5)}$$

4.5.2.2 EngineSim – Air Breathing Engine Analysis

A more flexible engine model has been adapted to improve on the simple empirical methods available in GENUS and to standardise the engine analysis tool. After reviewing several engine analysis tools shown in Table 4-2, it was concluded that EngineSim, while being the simplest of the tools mentioned below, has sufficient capability while also maintaining the open source, license free philosophy of GENUS.

EngineSim includes several analysis limitations, such as no analysis of emissions, no effect of air bleeding from the compressor, no account of heat leakage or rotor inertia, and no strength check for the components[136].

Table 4-2 - Engine Modelling Tools

Tool	Open Source	Purpose
EngineSim	✓	Educational/Gas turbine analysis
TurboMatch	✗	Gas turbine analysis
GasTurb	✗	Gas turbine analysis
GSP	✗	Component design and optimisation

NPSS	✗	Component design and optimisation
pyCycle	✓	Plug-in for OpenMDAO, system level optimisation

EngineSim is an open source Java-based applet developed by NASA Glenn Research Center[137]. This applet allows the user to design and analyse turbofan, turbojet, and ramjet engines.

EngineSim includes two operational modes, which are called the *design mode*, and the *test mode*. In the design mode the user can specify the design variables such as engine dimensions, pressure ratios, inlet performance, material characteristics, individual components efficiencies, temperature limits, and the design Mach and altitude conditions. The engine performance data used by other modules at the off-design conditions is obtained through the test mode for a frozen engine design, as schematically shown in Figure 4-6.
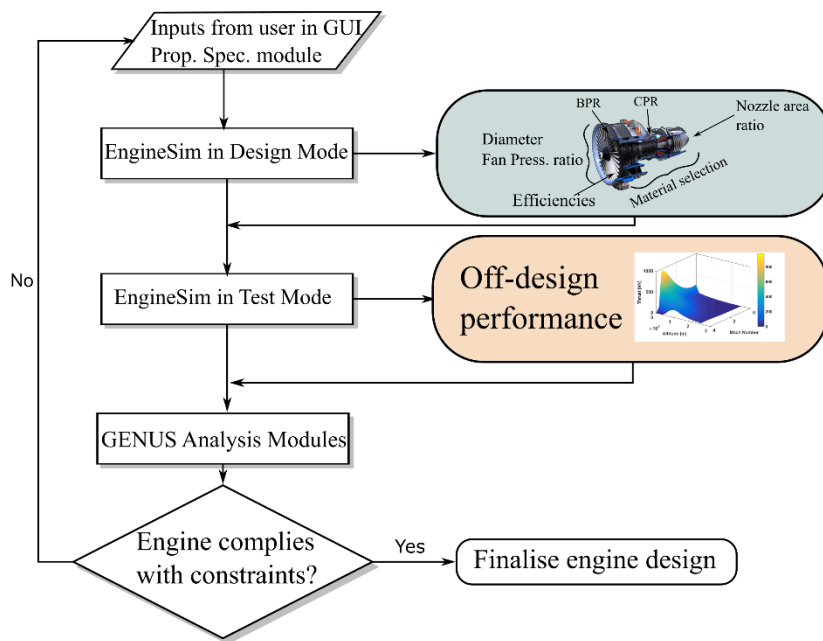
Figure 4-6 - EngineSim generic engine design procedure

The cycle analysis for turbojet engines given in Eqns. (4-6) to (4-22) is based on the numbering convention shown in Figure 4-7[138].
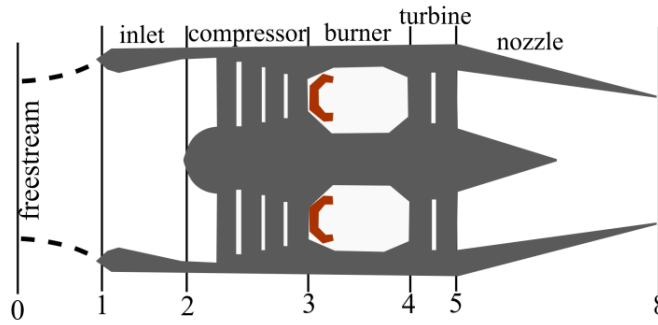
Figure 4-7 - EngineSim numbering convention

Starting with the isentropic total conditions calculated from the freestream:

$$\frac{T_{01}}{T_a} = 1 + \frac{\gamma - 1}{2} M^2 \qquad \text{(4-6)}$$

$$\frac{p_{01}}{p_a} = \left(\frac{T_{01}}{T_0}\right)^{\frac{\gamma}{\gamma - 1}} \qquad \text{(4-7)}$$

Where M is the freestream Mach number, γ is the specific heat ratio, p_a is the ambient static pressure, and T_a is the ambient static temperature. From the inlet to the compressor, the total temperature remains constant and for subsonic flight the pressure recovery is set as 1. The pressure loss is given as:

$$\frac{p_{02}}{p_{01}} = \begin{cases} 1, & M < 1 \\ 1.0 - 0.075(M - 1)^{1.35}, & 1 \le M \le 5 \end{cases} \qquad \text{(4-8)}$$

Pressure and temperature across the compressor are calculated as:

$$CPR = \frac{p_{03}}{p_{02}} = specified\ by\ user \qquad \text{(4-9)}$$

$$\frac{T_{03}}{T_{02}} = \frac{1}{\eta_c}\left[\left(\frac{p_{03}}{p_{02}}\right)^{\frac{\gamma - 1}{\gamma}} - 1\right] \qquad \text{(4-10)}$$

Assuming the burner is operating at its maximum temperature for a higher turbine entry temperature (TET), and thus higher efficiency:

$$T_4 = T_{04} = specified\ by\ user \qquad \text{(4-11)}$$

$$\frac{T_{04}}{T_{03}} = T_{04}\left(\frac{T_{02}}{T_{03}}\right)\left(\frac{1}{T_{01}}\right) \qquad \text{(4-12)}$$

68

$$\frac{p_{04}}{p_{03}} = specified\ by\ user \tag{4-13}$$

The ideal pressure ratio across the burner is equal to one; however the user may specify a value less than one to simulate losses.

The temperature and pressure across the turbine are then calculated as:

$$\frac{T_{05}}{T_{04}} = 1 - \frac{\left(\frac{T_{03}}{T_{02}} - 1\right)T_{01}}{T_{04}} \tag{4-14}$$

$$\frac{p_{05}}{p_{04}} = \left[1 - \frac{1}{\eta_t}\left(1 - \frac{T_{05}}{T_{04}}\right)\right]^{\frac{\gamma}{\gamma-1}} \tag{4-15}$$

The engine temperature ratio (ETR) and pressure ratio (EPR) can be calculated as:

$$ETR = \frac{T_{05}}{T_{04}}\frac{T_{04}}{T_{03}}\frac{T_{03}}{T_{02}} \tag{4-16}$$

$$EPR = \frac{p_{05}}{p_{04}}\frac{p_{04}}{p_{03}}\frac{p_{03}}{p_{02}} \tag{4-17}$$

The exit pressure at the nozzle is assumed to be the ambient pressure, and the nozzle flow is assumed as choked at the minimum area A_8. The exit velocity is then given by:

$$v_{exit} = \sqrt{2c_p T_{05}\eta_n\left[1 - \left(\frac{p_a}{p_{05}}\right)^{\frac{\gamma-1}{\gamma}}\right]} \tag{4-18}$$

The net thrust can be obtained from the freestream and exit velocities as:

$$\frac{F_n}{m_0} = v_{exit} - v_0 \tag{4-19}$$

The mass flow can be obtained by the choked nozzle condition as:

69

$$\frac{m_0\sqrt{\theta_t}}{\delta_t A_8} = \sqrt{\frac{\gamma}{R}} \frac{p_0}{\sqrt{T_0}} M \left[1 + \frac{\gamma - 1}{2}M^2\right]^{\frac{-(\gamma+1)}{2(\gamma-1)}} \qquad \textbf{(4-20)}$$

Where θ_t is the total temperature ratio, δ_t is the total pressure ratio, and R is the gas constant. The fuel to air ratio can be determined by:

$$f = \frac{\left(\frac{T_{04}}{T_{03}}\right) - 1}{\left(\frac{Q_R}{c_p T_{03}}\right) - \left(\frac{T_{04}}{T_{03}}\right)} \qquad \textbf{(4-21)}$$

Where Q_R is the fuel heating value in J/kg. Finally, the thrust specific fuel consumption is given by:

$$TSFC = \frac{f \cdot m_0}{F_n} \qquad \textbf{(4-22)}$$

Furthermore, the engine mass estimation is given by an idealised volume of the different engine components taking into account their diameter (d_i), length (L_i), and material density (ρ_i), as shown in Eq. (4-23), and Figure 4-8. However, this method has not been found to provide high accuracy. A comparison of EngineSim's mass prediction compared to an empirical regression mass estimation method (Raymer) is shown in Figure 4-9 for turbojets and turbofan engines.

$$M_{Engine} = \frac{\pi}{4}\sum_{i=0}^{n} \rho_i L_i d_i^2 \qquad \textbf{(4-23)}$$
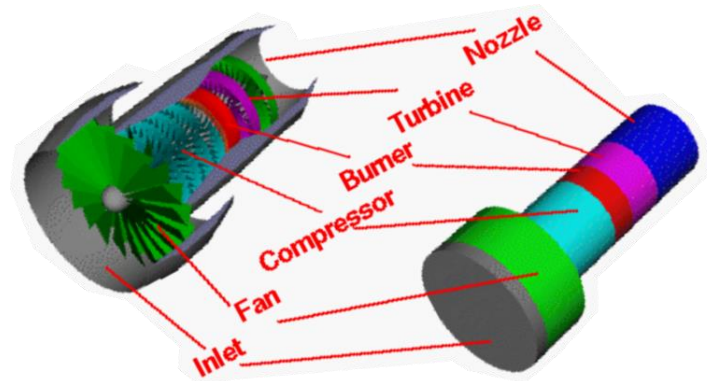
Figure 4-8 - EngineSim component idealization for weight calculation
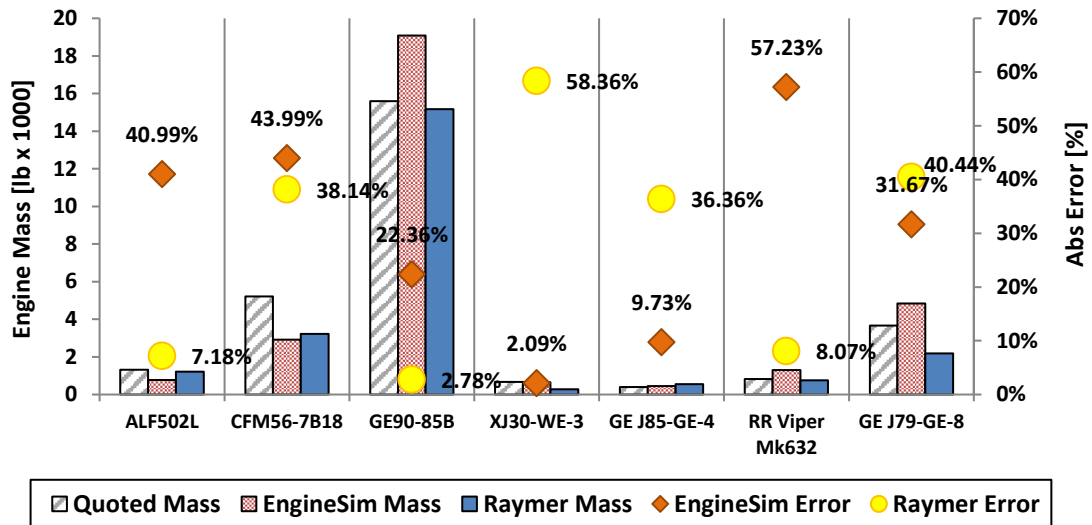
Figure 4-9 - Engine mass prediction comparison; EngineSim vs Raymer

Finally, Figure 4-10 shows the validation of EngineSim fully integrated into the GENUS framework for a GE-J79 engine in dry mode[139]. The main engine inputs for this validation were the engine diameter, compressor pressure ratio, compressor stages, and turbine stages[140]; the individual component efficiencies were modified in order to obtain a total engine efficiency of approximately 65%. The results show good agreement at various Mach and altitude conditions.
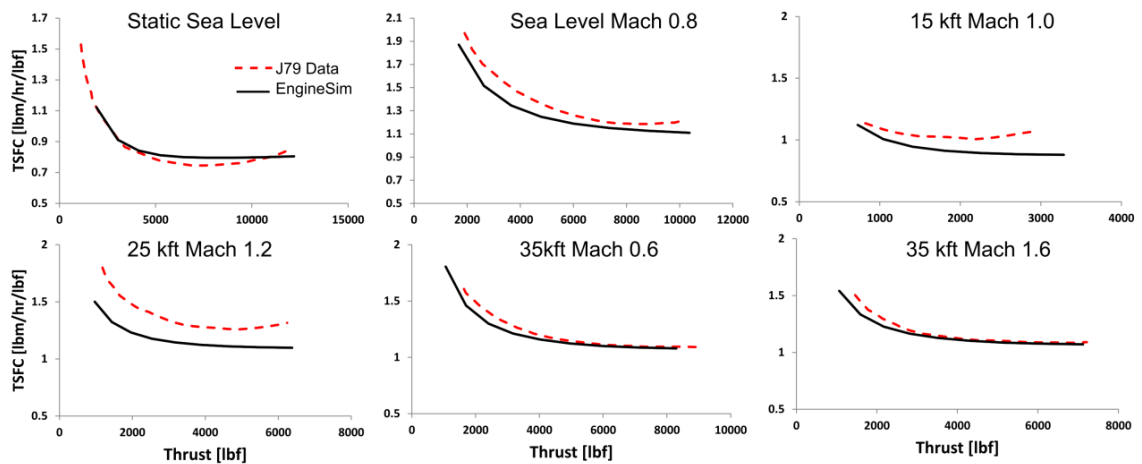
Figure 4-10 - EngineSim J79 engine validation in dry mode

4.5.2.3 Turbine-Based Combined Cycle Propulsion

During high speed operations, the propulsion system must be able to meet the mission requirements at a wide variety of conditions; from sea level static, to high-altitude, high-supersonic speeds. This is achieved through a turbine-based

71

combined cycle (TBCC) propulsion system that integrates a turbojet/turbofan engine with a ramjet combustor and nozzle. Common arrangements of TBCC architectures are shown in Figure 4-11. The tandem or co-axial architecture has been chosen as appropriate due to its reported lower mass and less restrictive integration into various aircraft configurations[141]. However, the complex mechanical and aerodynamic inlet and nozzle design are outside the scope of this research.
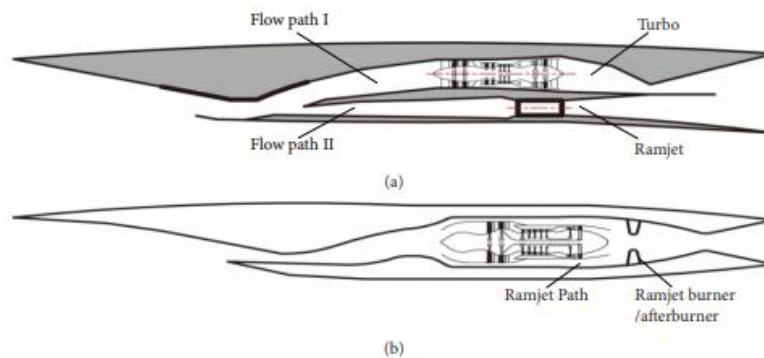
Figure 4-11 - Common TBCC architectures: (a) parallel, and (b) tandem

A key parameter of the combined propulsion systems is a smooth transition between the turbo/ram modes. Constant flow rates and thrust across the transition point are desirable in order to reduce performance penalties, as well avoiding recirculation across the turbine elements[142].

A simplified transition point has been estimated by modelling afterburning turbojet/turbofan engines and ramjet engines with equivalent inlet areas. The thrust surfaces shown in Figure 4-12 intersect at the Mach/Altitude transition points where the thrust outputs match, and therefore, the point where a smooth thrust transition can be achieved. It can be seen that the transition point depends only on Mach number, here estimated as $M \approx 2.5$, irrespective of altitude.
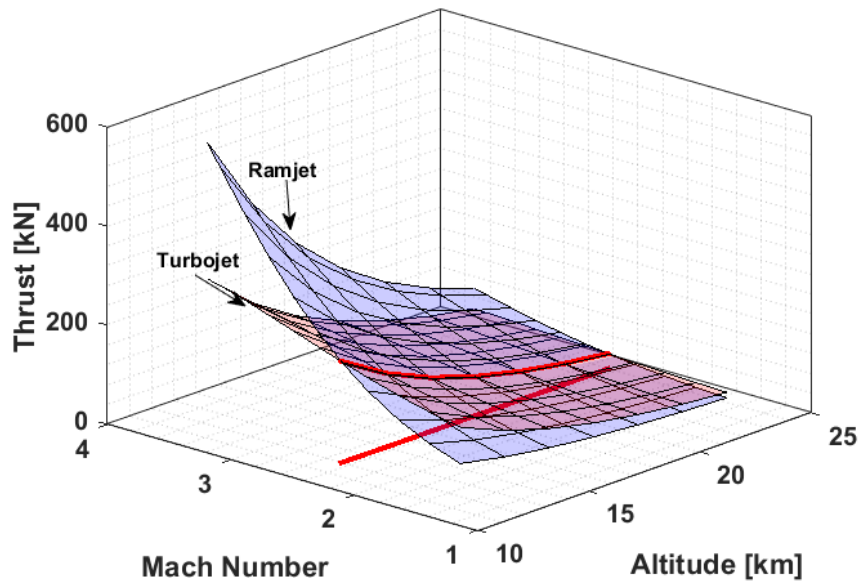
Figure 4-12 - Estimation of transition Mach number, turbojet-to-ramjet

A simple decision flag has been programmed into the *Turboramjet Powerplant object* in order to transition from turbo mode to ramjet mode, as schematically shown in Figure 4-13.
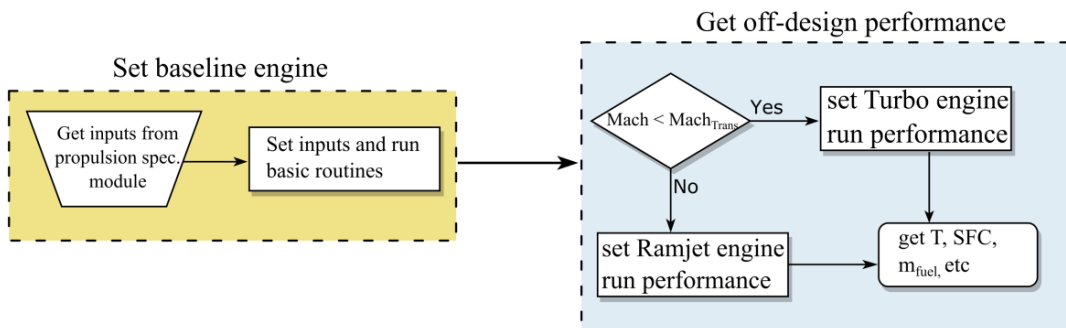
Figure 4-13 - Decision logic for turbo/ramjet modes

4.5.3 Inlet Sizing

Due to low-observability requirements, complex inlet shapes are often employed in order to avoid the reflection waves coming from the engine fan components. Intake and airframe integration for fighter/strike aircraft often follows these design practices[143]:

o Achieve low radar observability.

- Minimise flow field interference from other components such as landing gears, weapon carriage/anchoring, external fuel tanks, etc.
- Prevent boundary layer ingestion.
- Achieve uniform pressure recovery flow at a wide range of velocities.
- Good post-stall, high angle of attack behaviour.

Due to the complex aerodynamics of serpentine inlets, the detailed design is out of the scope of this research and inlets will only be sized for drag, thrust correction, and packaging purposes. The inlet size is a function of freestream Mach number, the assumed Mach number at the throat, and the maximum allowable Mach number at the engine front face. Throughout this research, a maximum throat Mach number of 0.6 and a maximum engine front face Mach number of 0.4 have been assumed, as shown in Figure 4-14. Using isentropic flow relations, Eq. (4-24), the inlet capture area is given by Eq. (4-25).

$$\frac{A}{A^*} = \frac{1}{M}\left[\frac{1 + 0.2M^2}{1.2}\right]^3 \tag{4-24}$$

$$\frac{A_0}{A_2} = \frac{\left(\frac{A}{A^*}\right)_0}{\left(\frac{A}{A^*}\right)_1} \cdot \frac{\left(\frac{A}{A^*}\right)_1}{\left(\frac{A}{A^*}\right)_2} \tag{4-25}$$
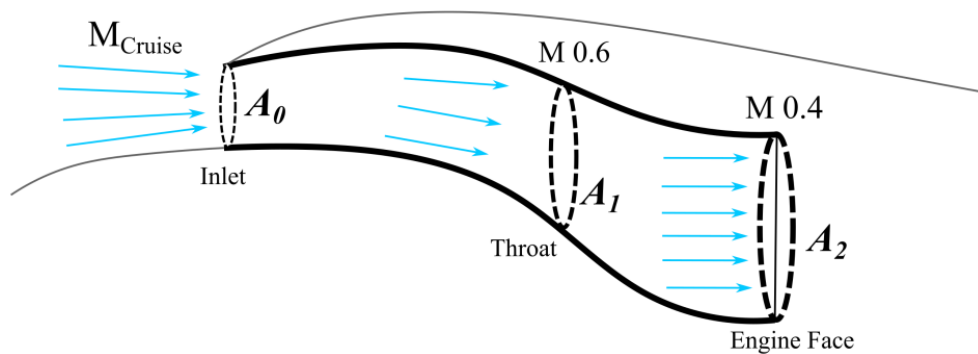
Figure 4-14 - Inlet flow conditions and sizing

Additional airflow is often required for secondary power, engine cooling, and bleed air, so an inlet area correction of approximately 20% is applied.

A simple thrust correction due to pressure losses is included via Eq. (4-26):

$$\frac{\Delta F}{F_0} = \frac{0.35 \cdot K \cdot M_\infty (1 - \eta_P) P_\infty}{q_\infty} \tag{4-26}$$

Where K is an engine dependent factor, commonly 1.5, P_∞ is the ambient pressure and q_∞ is the dynamic pressure both in Pascals, and the pressure recovery factor, η_P, can be estimated through MIL-Spec 5008B[144], Eq. (4-8), and Figure 4-15.
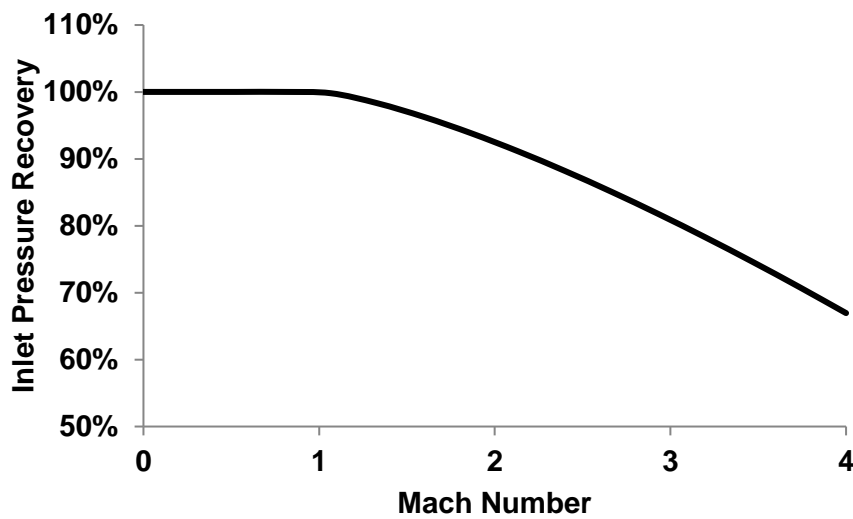
Figure 4-15 - Inlet pressure recovery at various Mach numbers

For high-supersonic flight, Nicolai[145, chap.15] establishes the pressure recovery as a function of the inlet type up to speeds of Mach 5.0. As seen from Figure 4-16, the isentropic spike inlet is the most efficient.
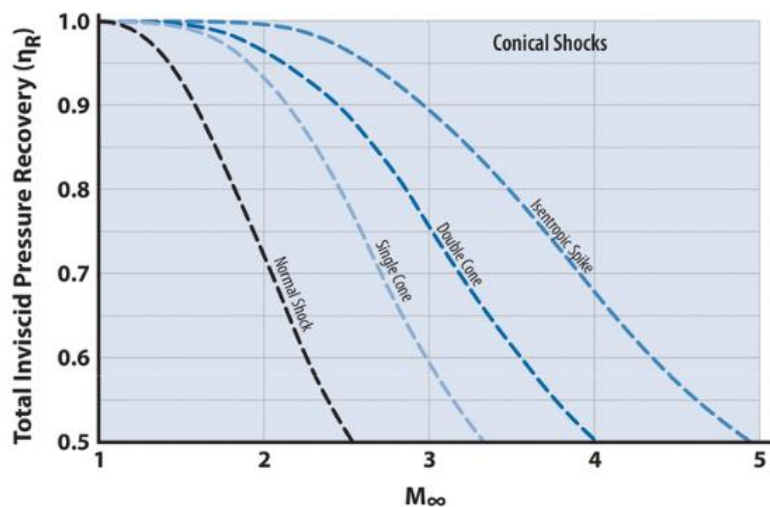
Figure 4-16 - Pressure recovery for conical shock systems

The inlet capture area is obtained through Eq. (4-27) where $\dot{m}_E$ is the engine airflow (kg/s), and $\dot{m}_S$ is the secondary air flow (kg/s) required for other systems like engine cooling, and $\left.A_{blb}\middle/A_C\right.$ is the correction factor due to boundary layer bleed[145, p.401].

$$A_C = \left(1 + \left.A_{blb}\middle/A_C\right.\right)\left(\frac{\dot{m}_E + \dot{m}_S}{g\rho_\infty V_\infty}\right)$$ **(4-27)**

However, due to the complex aerodynamics and mechanical system integration, a detailed design procedure for variable geometry inlets has not been integrated into the GENUS propulsion module.

4.6 Aerodynamics

The GENUS aerodynamics module allows for the aerodynamic characterisation of a flight vehicle through the combination of several analysis tools and fidelity levels and the use of *Coefficient Matrices* as the data objects shared by other modules, as schematically shown in Figure 4-17.

This approach is necessary due to the several design aspects and methods that affect aerodynamic characteristics such as the total drag build-up, or the total lift coming from different effects such as vortex or compression lift, as exemplified in Figure 4-18.
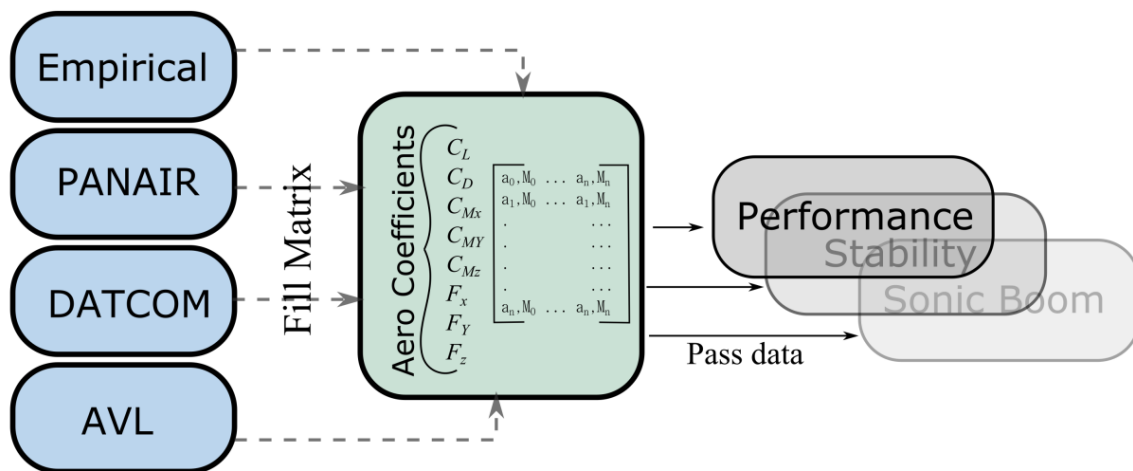
Figure 4-17 - Aerodynamic coefficients matrix
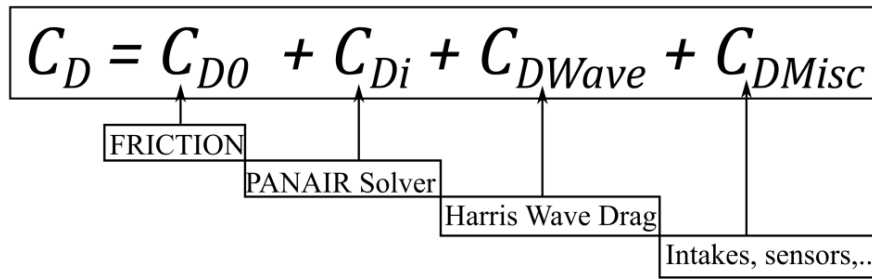
Figure 4-18 - Total drag build-up through a combination of analysis tools

4.6.1 Friction Drag

Skin friction and form drag calculations have been adapted from the FRICTION[146] code due to its parametric definition based on the geometric characteristics, the flexibility to include laminar to turbulent transitions, the inclusion of supersonic effects through the adiabatic wall recovery factor, and the flexibility to include form factors from various sources.

The total friction drag is obtained through Eq. (4-28), where the effects of flow turbulence are introduced via the laminar transition fraction F_{trans} shown in Eq. (4-29).

$$C_{D_0} = \sum_{i=1}^{N} \frac{FF_i S_{wet_i} C_{F_i}}{S_{ref}} \tag{4-28}$$

$$C_{F_i} = C_{F_{turb}} - F_{trans}\left[C_{F_{turb}} - C_{F_{lam}}\right] \tag{4-29}$$

Form factors are given in. Eqns. (4-30) and (4-31) for body components and lifting surfaces, from Torenbeek[147], chosen as conservative factors compared to other sources such as Hoerner and Raymer[148].

$$FF_{BodyComp} = 1 + 1.5\left(\frac{d}{l}\right)^{1.5} + 50\left(\frac{d}{l}\right)^{3} \tag{4-30}$$

$$FF_{LiftSurf} = 1 + 2.7\left(\frac{t}{c}\right) + 100\left(\frac{t}{c}\right)^{4} \tag{4-31}$$

Miscellaneous drag is added to account for external sensors, probes, and air intakes through empirical estimation methods[129, sect.12.5, 13.3].

4.6.2 Wave Drag

Compressibility effects must be accounted for during high subsonic and transonic flight segments, especially when operating beyond the drag divergence Mach number (M_{DD}), which is defined as the Mach number that results in a drag increase of 20 drag counts ($\Delta C_D = 0.002$). The local M_{DD} is obtained using the span-wise lift distribution (calculated through classical lifting-line theory), the wing geometry, and aerofoil factors as shown in Eq. (4-32).

$$K_{Aerofoil} = M_{DD} cos\Lambda_{0.5} + \frac{C_l(y)}{10 \cos^2 \Lambda_{0.5}} + \frac{t/c(y)}{cos\Lambda_{0.5}} \tag{4-32}$$

Where $K_{Aerofoil}$ ranges from 0.95 for supercritical aerofoils to 0.87 for regular aerofoils. The local critical Mach numbers and drag contributions are given in Eqns. (4-33) to (4-35)[148]. Subsonic wave drag is calculated only for the lifting surfaces.

$$M_{Crit}(y) = M_{DD}(y) - \sqrt[3]{\frac{0.1}{80}} \tag{4-33}$$

$$C_{d_{wave_{strip}}} = \begin{cases} 0, & M < M_{Crit} \\ 20(M - M_{Crit}(y))^4, & M \geq M_{Crit} \end{cases} \tag{4-34}$$

$$C_{D_{wave}} = \sum_{i=1}^{n} C_{d_{wave_{strip_i}}} \frac{S_{strip_i}}{S_{ref}} \tag{4-35}$$

At supersonic speeds, wave drag is calculated through the area rule procedure presented in the Harris wave drag routines[149]. The total wave drag is obtained via Eqns. (4-36) and (4-37) through the angles and rotation planes shown in Figure 4-19:

$$C_{D_{wave}}(\theta) = -\frac{1}{2\pi} \int_0^l \int_0^l A''(x_1)A''(x_2) \ln|x_1 - x_2| \, dx_1 dx_2 \tag{4-36}$$

$$C_{D_{wave}} = \frac{1}{2\pi} \int_0^{2\pi} C_{D_{wave}}(\theta)d\theta \tag{4-37}$$
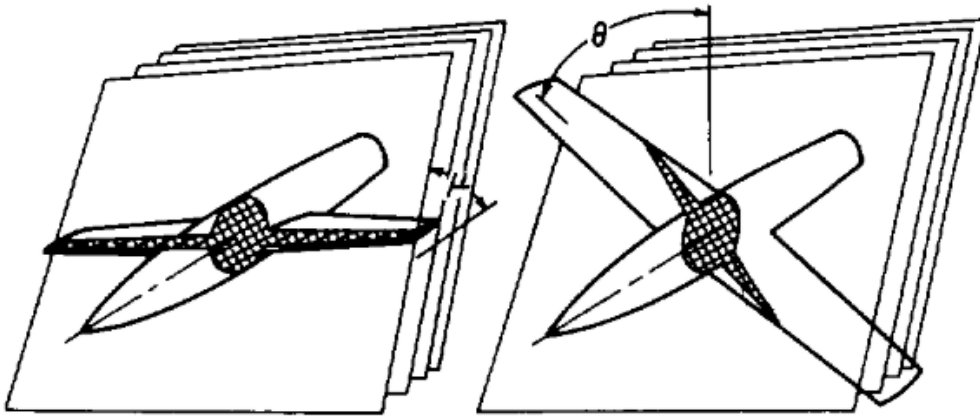
Figure 4-19 – Rotation angles for wave drag calculations: Mach angle (μ) rotated through the cone angles (θ)

4.6.3 PANAIR Aerodynamic Analysis

Due to the geometric choices for UCAV designs, and due to the wide variety of flight speed regimes to be investigated, a flexible and capable aerodynamic analysis tool was required. Several aerodynamic analysis tools were available in the GENUS framework prior to this research; these methods include empirical equations, Digital DATCOM, AVL (vortex lattice), and the Supersonic and Hypersonic Arbitrary Body Program (SHABP).

Digital DATCOM is not suitable to perform the main aerodynamic analysis due to its reliance on equivalent wing planforms and because its methods consist of a compendium of data mapped through simple semi-empirical relations. Similarly, AVL does not consider the effects of thickness and is limited to subsonic speeds, while SHABP is mainly used for hypersonic analysis.

Therefore, the panel method PANAIR was selected for its integration into the GENUS framework as the *default* aerodynamic analysis tool. PANAIR has been validated and applied to the aerodynamic analysis of fighter configurations[150], tailless UCAVs[151], the optimisation of fighter aircraft wing strakes[152], the ground effects of a lifting body[153], and even to the prediction of sonic boom intensity through the near-field pressure[154] and the lift distribution[155].

A comparison of the capabilities of the aerodynamic tools available in GENUS is shown in Table 4-3.

Table 4-3 - Aerodynamic Methods in GENUS

Method	Open Source	Arbitrary Geometry	Subsonic	Transonic	Supersonic
Digital DATCOM	✓	✗	✓	✓	✓
AVL	✓	✗	✓	✗	✗
SHABP	✓	✓	✗	✗	✓
PANAIR	✓	✓	✓	✓	✓

PANAIR was originally developed by Boeing and NASA; it is capable of performing aerodynamic analysis of arbitrary three-dimensional geometries up to Mach 4.0 by solving the Prandtl-Glauert equation, Eq. (4-38).

$$(1 - M_\infty^2)\phi_{xx} + \phi_{yy} + \phi_{zz} = 0 \qquad \textbf{(4-38)}$$

In order to derive Eq. (4-38) from the Navier-Stokes equations, the following flow assumptions have to be made[156]:

o   The viscosity terms have been eliminated

o   The flow is irrotational

o   Steady state conditions

o   Small perturbation approximation

Furthermore, PANAIR is not able to predict the local flow characteristics at transonic conditions, but it is capable of providing approximations of the total forces and moments. A comprehensive explanation of potential flow theory and its implementation in the PANAIR code is out of the scope of this research, for more details refer to the user manual[157].

The PANAIR solver (open source FORTRAN code obtained from PDAS[158]) has been integrated into the GENUS framework as a dynamic link library object (DLL) following the procedure shown schematically in Figure 4-20.
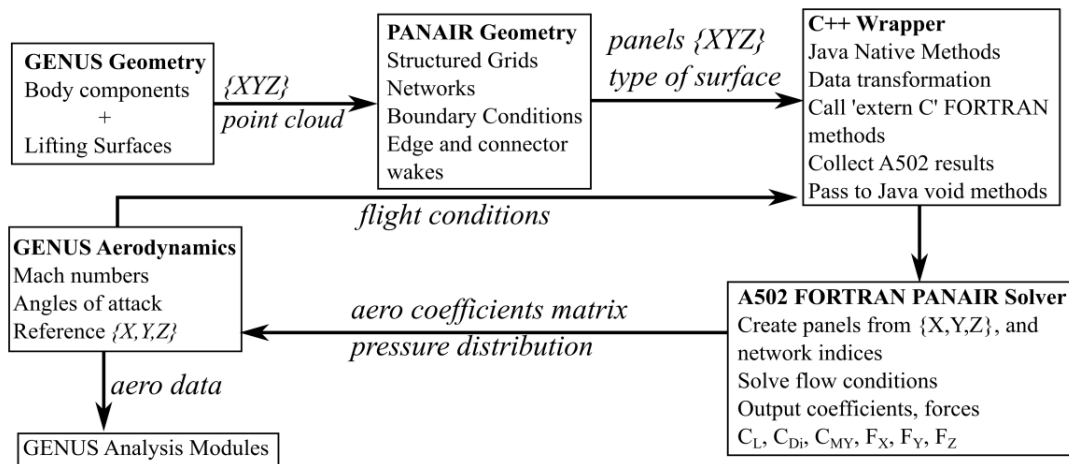
Figure 4-20 - PANAIR-GENUS interaction schematic

Panair requires the use of structured grids, with the various geometrical components divided into *networks.* Each network is composed by a grid of $N \times M$ points, where N and M represent the columns and rows. The order of the grid points must follow the right hand side rule with the surface normal vector pointing outwards. This is important for the setting of boundary conditions and edge alignment for thick, impermeable surfaces, where the mass flow through each panel is zero. Furthermore, the edges of contiguous networks must coincide in order to properly represent the flow and avoid geometrical and flow discontinuities which can result in erroneous pressure distributions. This *abutment* process is exemplified in Figure 4-21. A panelling algorithm was developed to automate the geometrical input process; details are provided in Appendix C.
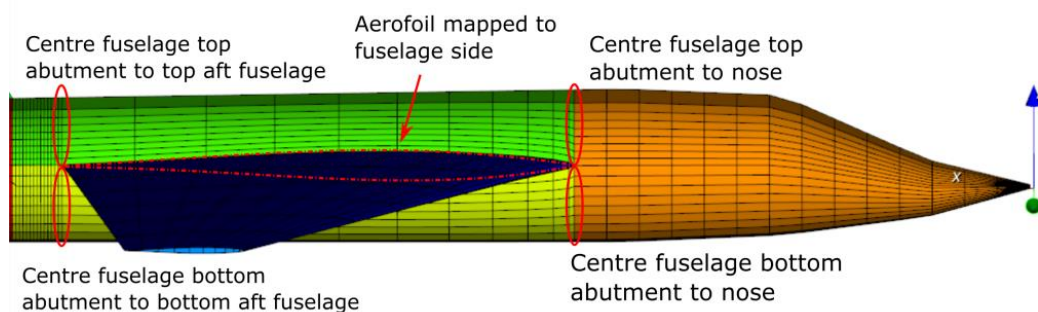
Figure 4-21 - Network edge abutments for a tube-and-wing geometry

Results have been validated against low speed wind tunnel data for a lambda-wing UCAV[159], shown in Figure 4-22, as well as against flight measurements for a Boeing 737 airliner[160]. Lift and drag coefficients agree well with experimental

81

results; however, PANAIR cannot account for the complex vortex interactions which results in pitch-up behaviour for UCAVs at moderate angles of attack.
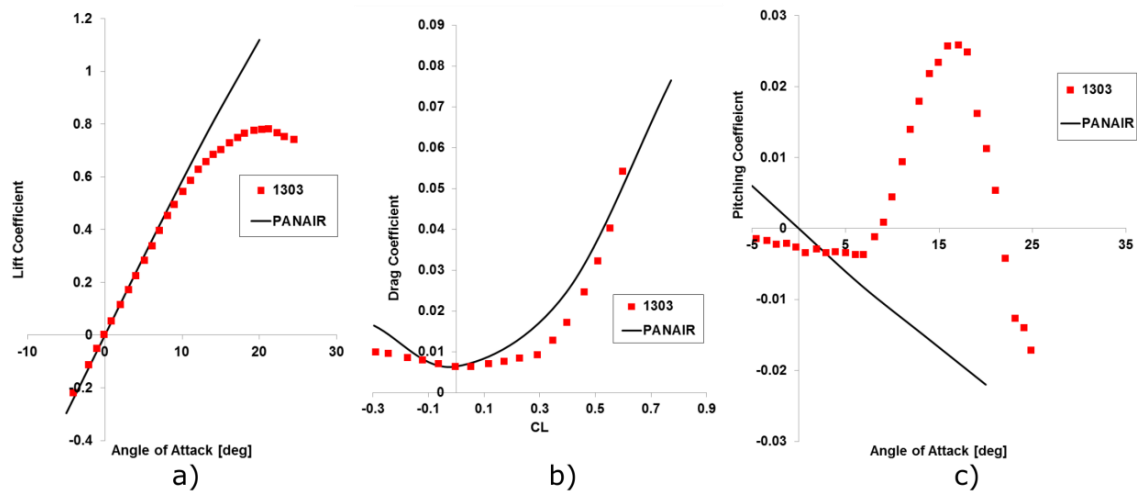
Figure 4-22 - Panair validation of 1303 UCAV low speed wind tunnel data (M = 0.3)

4.6.4 Aerodynamic Surrogate Model

Through the combination of the aforementioned aerodynamic analysis tools, a full aerodynamic characterisation is available at any given flight condition. The aerodynamic data can be interpolated between angle of attack, Mach number, and type of coefficient stored in the *Coefficients Matrix*, as schematically shown by the surrogate coefficient contours and data points in Figure 4-23.
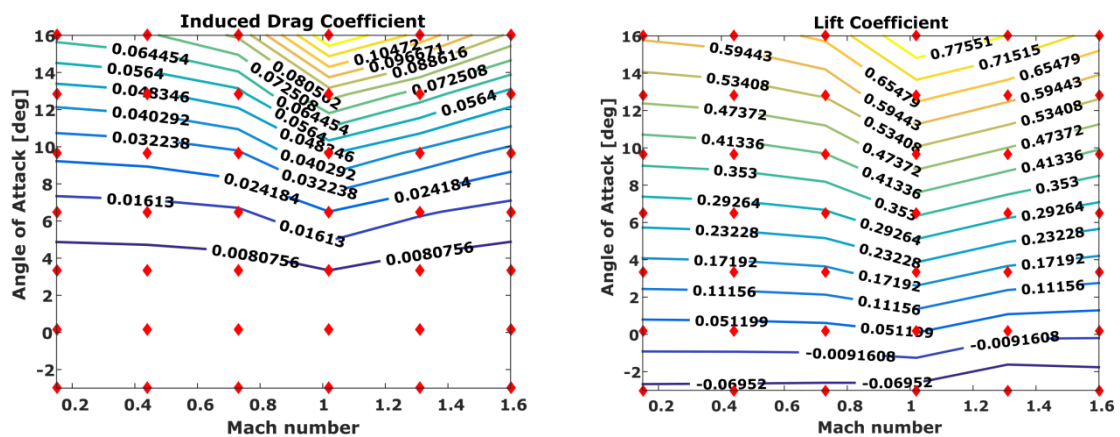
Figure 4-23 - Lift and induced drag coefficients surrogate models and data points

Furthermore, visualisation of pressure coefficients is available through an external post processing package called pyNastran, as shown in Figure 4-24. This tool is not integrated into the GENUS framework; however, the files required

for visualising the pressure coefficients are automatically generated by the Aerodynamic analysis module in GENUS.
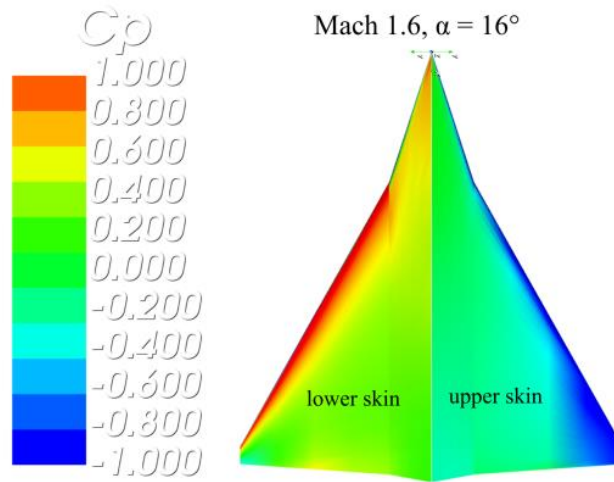
Figure 4-24 - Pressure coefficient visualisation in pyNastran

4.7 Performance

The performance module evaluates all mission segments, from take-off to landing. Additional mission constraints, such as manoeuvrability and point performance requirements can be added in this module.

4.7.1 Field Performance

4.7.1.1 Take-Off Performance on a Normal Runway

Normal take-off performance has been adapted from Lynn's TAKEOFF2.C code[161], which provides the balanced field length, shown in Figure 4-26. This code is based on the parametric take-off performance for jet propelled and vectored thrust aircraft by Krenkel and Salzman[162], complemented with an iterative solution for the balanced field length. The implementation of this code has been verified against a DC-9 take-off example available in the original source code with excellent agreement, as shown in Figure 4-25.

To account for wind effects, the take-off distance is multiplied by a headwind factor, Eq. (4-39)[163, chap.6].

$$hw_{factor} = \frac{0.7V_{TO} - V_{headwing}}{0.7V_{TO}} \tag{4-39}$$
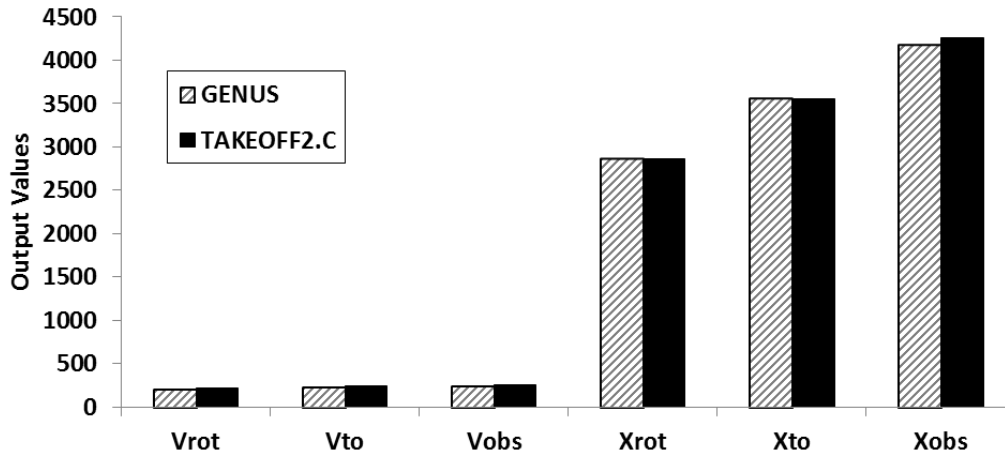
Figure 4-25 - Verification of take-off calculation
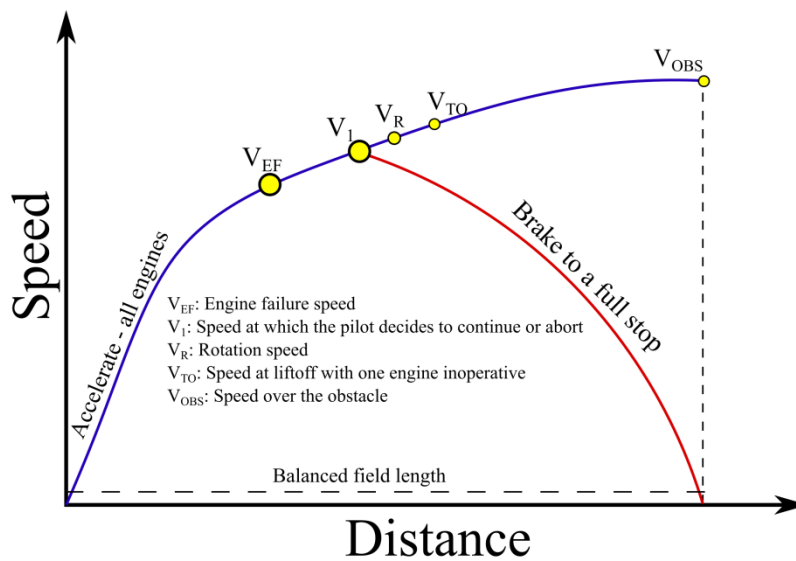
Figure 4-26 - Balanced field length

4.7.1.2 Catapult Assisted Take-Off

For any given class of aircraft carrier that offers catapult assisted take-off, the maximum catapult load can be calculated based on the catapult's cylinder diameter, maximum pressure, and estimated efficiency as:

$$F_{Cat} = \eta_{cat}\pi P \frac{D^2}{4} \tag{4-40}$$

This load acts as a booster thrust component that is idealised as acting aligned with the aircraft's longitudinal axis so that $\alpha_b = 0$. The overall take-off procedure is divided into an assisted ground roll, followed by an unassisted ground roll, and a transition to climb segment, as shown in Figure 4-27.
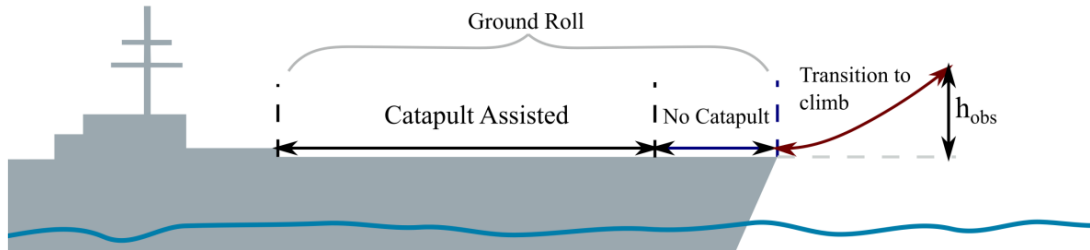
Figure 4-27 - Catapult assisted take-off segments

Using the forces shown in Figure 4-28, the equations of motion during the ground roll are given as[164, chap.10]:

$$
\begin{cases}
\dfrac{dV}{dt} = g\left\{\left[\dfrac{T\cos(\alpha_T) + T_b\cos(\alpha_b)}{W}\right] - \dfrac{D}{W} - \mu R - \sin(\Phi)\right\} \\[3mm]
R = g\left[\cos(\Phi) - \dfrac{L}{W} - \dfrac{T}{W}\sin(\alpha_T) - \dfrac{T_b}{W}\sin(\alpha_b)\right] \\[3mm]
\dfrac{dx}{dt} = V_{ground}
\end{cases}
\qquad \textbf{(4-41)}
$$

A numerical integration can be used by selecting adequate values of Δt during which the atmospheric, mass, propulsion and aerodynamic characteristics can be considered constant.
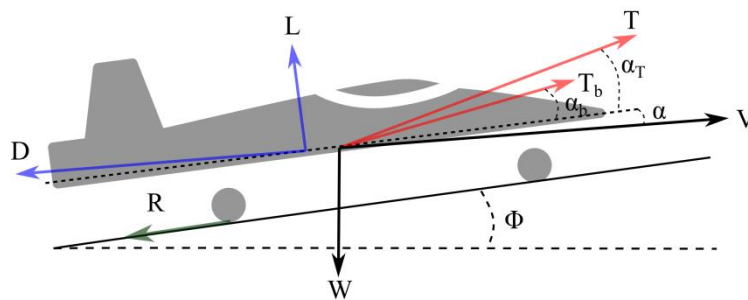
Figure 4-28 - Forces during ground roll

The transition to climb segment is divided into two sub-segments as follows:

1. A constant altitude acceleration from V_{LOF} (1.1V_{stall}) to V_2 (1.2V_{stall})
2. A constant speed circular arc (of radius R) from $\gamma=\Phi$ to γ_{climb} (Eq. (4-43))

The unassisted acceleration for sub-segment (1) is given by Eq. (4-42):

$$\frac{dV}{dt} = g\left[\frac{Tcos(\alpha + \alpha_T)}{W} - \frac{D}{W}\right] \tag{4-42}$$

$$\gamma_{climb} = \frac{T - D}{W} \tag{4-43}$$

The change in flight path angle for sub-segment (2) is given by Eq. (4-44):

$$\frac{d\gamma}{dt} = \frac{V}{g}\left[\frac{Tcos(\alpha + \alpha_T)}{W} + \frac{L}{W} - cos(\gamma)\right] \tag{4-44}$$

Finally, the horizontal and vertical distances are calculated as:

$$\frac{dx}{dt} = Vcos(\gamma) \tag{4-45}$$

$$\frac{dz}{dt} = Vsin(\gamma) \tag{4-46}$$

The transition segment ends when $\gamma = \gamma_{climb}$ or $h = h_{obstacle}$.

4.7.1.3 Ski Jump Take-Off

The ski jump take-off consists of a normal ground roll segment, followed by a ground roll on a circular arc at the ski ramp, followed by a final transition to climb segment described by a ballistic trajectory. The take-off distance is measured at the point where the vehicle clears the obstacle height, which must be added to the carrier's draught. The regular ground roll equations of motion are given by Eq. (4-41) with $T_b = 0$. The ground roll segment for the circular arc segment is given in Eq. (4-47):

$$\begin{cases} \frac{dV}{dt} = g\left\{\frac{Tcos(\alpha_T)}{W} - \frac{D}{W} - \mu R - sin(\Phi)\right\} \\ R_{friction} = g\left[\frac{WV^2}{R_{SR}} + cos(\Phi) - \frac{L}{W} - \frac{T}{W}sin(\alpha_T)\right] \\ \frac{d\Phi}{dt} = \frac{V}{R_{SR}} \\ x = R_{SR}cos(\Phi) \\ z = R_{SR}sin(\Phi) \end{cases} \tag{4-47}$$
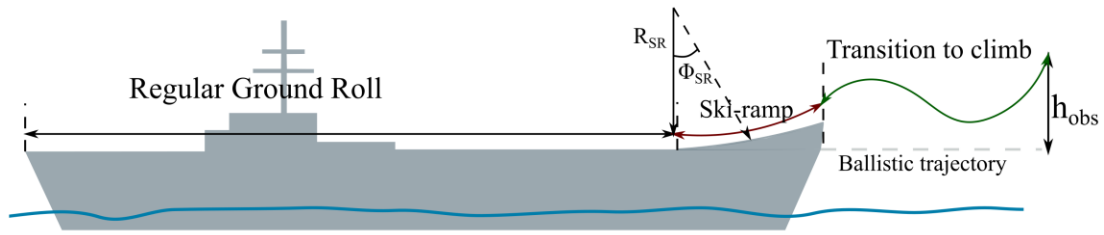
Figure 4-29 - Ski jump take-off segments

Finally, the equations of motion during the ballistic trajectory are given by Birckelbaw[165] as:

$$\begin{cases} \ddot{x} = g\left[\dfrac{T}{W}\cos(\alpha + \alpha_T + \gamma) - \dfrac{L}{W}\sin(\gamma) - \dfrac{D}{W}\cos(\gamma)\right] \\ \ddot{z} = g\left[\dfrac{T}{W}\sin(\alpha + \alpha_T + \gamma) - \dfrac{L}{W}\cos(\gamma) - \dfrac{D}{W}\sin(\gamma) - 1\right] \end{cases} \qquad \textbf{(4-48)}$$

A numerical integration can be adapted by selecting adequate values of *Δt* during which the atmospheric, mass, propulsion and aerodynamic characteristics can be considered constant. The flight path angle and angle of attack can be then calculated as:

$$\gamma_i = \tan^{-1}\left(\frac{V_{z_i}}{V_{x_i}}\right) \qquad \textbf{(4-49)}$$

$$\alpha_i = \theta_i - \gamma_i \qquad \textbf{(4-50)}$$

4.7.1.4 Landing

Landing performance is evaluated through a simple, empirical formulation given in Eq. (4-51)[166, sect.5.11.2], evaluated at 70% of the landing speed in order to account for an averaged deceleration.

$$s_L = \frac{1.69 W_{Ldg}^2}{g\rho S C_{L_{max}}[D + \mu(W_{Ldg} - L)]_{0.7V_L}} \qquad \textbf{(4-51)}$$

Friction coefficients during braking are given as *μ=0.4* for a dry runway and *μ=0.3* for wet or icy conditions.

In case of assisted landing by parachute, the additional parachute drag is calculated according to the type of parachute and its dimensions, as established by ESDU 09012[167] and Eq. (4-52).

$$\Delta C_{D_{Parachute}} = C_{D_0}^{Parachute} \frac{S_0}{S_{ref}}$$ **(4-52)**

4.7.2 Climb

Climb performance is evaluated through ESDU's energy height optimisation method[168,169], which offers minimum fuel-to-climb and minimum time-to-climb trajectories. This method makes use of energy height which represents the potential and kinetic energy at a given altitude and speed as shown in Eq. (4-53).

For a given energy height, the minimum time-to-climb trajectory is given by the speed/altitude pairs that maximises specific excess power, given in Eq. (4-54); a minimum fuel-to-climb trajectory is given by the speed/altitude pairs that minimise fuel specific energy, given by Eq. (4-55).

Minimum time-to-climb trajectories are shown in Figure 4-30 for a subsonic and a supersonic UCAV; the effect of transonic wave drag is evidenced by the specific excess power contour lines at speeds above Mach 0.9 for the subsonic climb case.

$$H_e = h + \frac{V^2}{2g}$$ **(4-53)**

$$P_s = V \left[\frac{T}{W} - \frac{q C_{D_0}}{W/S} - n^2 \frac{KW}{qS} \right]$$ **(4-54)**

$$\frac{df}{dH_e} = \frac{m_i g \cdot C}{V(T-D)}$$ **(4-55)**

$$C = T \cdot TSFC$$ **(4-56)**
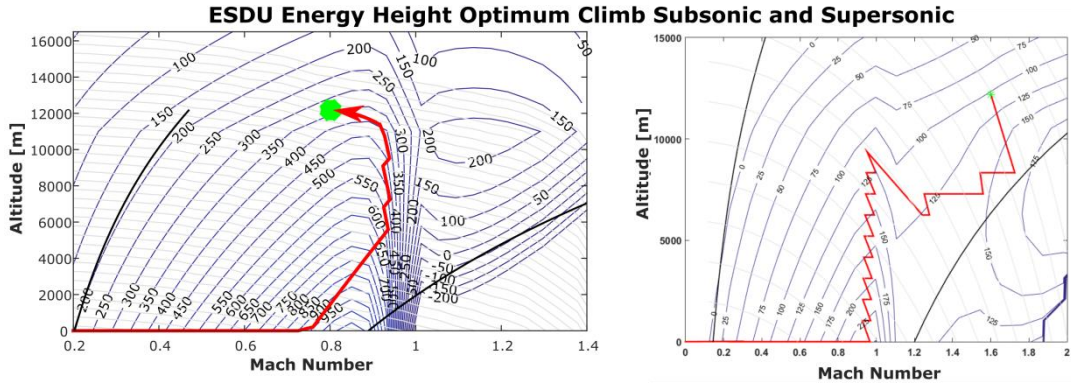
Figure 4-30 - Energy optimised climb trajectories

4.7.3 Cruise Segments

Three distinct cruise profiles are employed as required by the mission specifications. Fuel burn, speed, altitude, and attitude profiles are obtained through a numerical iteration[170].

4.7.3.1 Constant Airspeed and Constant Altitude

This cruise type requires that the attitude of the aircraft be varied through the segment, reducing lift coefficient and total lift produced as the aircraft loses weight due to fuel burn. Range is given by Eq. (4-57).

$$R = \frac{V}{gTSFC\sqrt{KC_{Dmin}}}\left[tan^{-1}\left(\frac{2\sqrt{K}}{\rho V^2 S\sqrt{C_{Dmin}}}W_i\right)\right.$$
$$\left. - tan^{-1}\left(\frac{2\sqrt{K}}{\rho V^2 S\sqrt{C_{Dmin}}}W_f\right)\right]$$

(4-57)

4.7.3.2 Constant Altitude and Constant Attitude

This cruise type requires that speed be varied through the segment, since the weight of the aircraft is decreasing, speed will also decrease. Range is given by Eq. (4-58).

$$R = \frac{1}{gTSFC}\frac{\sqrt{C_L}}{C_D}\frac{2\sqrt{2}}{\sqrt{\rho S}}\left(\sqrt{W_i} - \sqrt{W_f}\right)$$

(4-58)

4.7.3.3 Constant Airspeed and Constant Attitude

This cruise type is also known as cruise-climb. Since the weight of the aircraft is decreasing, the aircraft must climb to generate less lift as density decreases with altitude. Range is given by Eq. (4-59).

$$R = \frac{V}{gTSFC} \frac{C_L}{C_D} ln\left(\frac{W_i}{W_f}\right) \tag{4-59}$$

4.7.4 Descent

A descent method which is the reverse operation of a linearly varying Mach number, constant rate of climb can be used for non-time-critical missions where the mission range can be maximised under no time constraints; this descent should be performed at a minimum flight path angle, maximising the glide ratio. The fuel consumption during descent is low due to the engines operating at idle or near idle conditions; Howe estimates that the descent fuel consumption corresponds to 1% of the vehicle's gross mass[130, sect.7.4.4]. Given a constant descent angle γ, and for an altitude step ΔH, the time and fuel consumption are given by:

$$t_i = \frac{\Delta H}{V_{av_i}\sin(\gamma)} \tag{4-60}$$

$$fuel = \sum_{i=0}^{n} SFC_{idle}T_{idle}t_i \tag{4-61}$$

For time critical missions, where the majority of the flight should be carried out at the maximum speed, a descent manoeuvre that dissipates the maximum amount of energy in the least amount of time is required. This can be achieved by a non-steady turn at a high loading factor at the maximum dynamic pressure.

The manoeuvre is divided into segments of steady turn at constant flight path angle for an altitude change Δz, coupled to a non-steady turn at constant altitude for a Mach number change ΔM. During the steady turn, the equations of motion are given by Eq. (4-62), and by Eq. (4-63) for the non-steady turn[164, chap.9].

$$\begin{cases} \dfrac{dV}{dt} = 0 \\[2mm] \dfrac{d\gamma}{dt} = 0 \\[2mm] C_L = \dfrac{n_{max} W}{qS} \\[2mm] \sin(\gamma) = \dfrac{T - D}{W} \\[2mm] t_i = \dfrac{\sqrt{\Delta x^2 + \Delta z^2}}{V_i sin(\gamma)} \\[2mm] \dfrac{dx}{dt} = V cos(\gamma) \end{cases}$$

(4-62)

$$\begin{cases} \gamma = 0 \\[2mm] \dfrac{dz}{dt} = 0 \\[2mm] t_i = \dfrac{\Delta M_i \cdot a_{sound}}{g/W\,[T - D]} \\[2mm] \dfrac{dx}{dt} = V cos(\gamma) \end{cases}$$

(4-63)

A numerical integration can be performed by selecting appropriate values of time step Δt during which the aerodynamic, mass, propulsion, and atmospheric conditions can be considered constant. An example of this decent manoeuvre is shown in Figure 4-31 (generated by the performance analysis module).
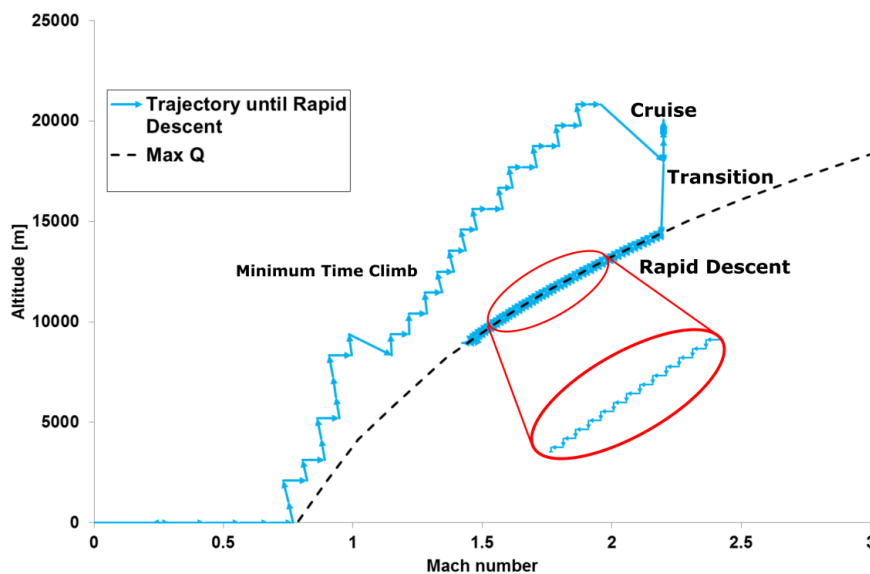
Figure 4-31 - Mission trajectory demonstrating rapid descent

4.7.5 Manoeuvrability

Point performance and manoeuvrability constraints are evaluated through vehicle characteristics such as thrust, power, wing loading, maximum lift coefficient, specific excess power, amongst others.

4.7.5.1 Instantaneous Turn Rate

Instantaneous turn rate requirements are evaluated through wing loading and maximum usable lift coefficient constraints, as shown in Eqns. (4-64) to (4-66).

$$\dot{\psi} = \frac{g\sqrt{n^2 - 1}}{V} \tag{4-64}$$

$$(W/S)_{max} = \frac{qC_{L_{Usable}}}{n_{Inst}k_{mass}} \tag{4-65}$$

$$k_{mass} = \frac{m_{@Manoeuvre}}{m_0} \tag{4-66}$$

4.7.5.2 Acceleration

Acceleration constraints are evaluated through the time required to transition from the initial speed to the final speed, at a given altitude and weight condition. The average acceleration, $\bar{a}$, available as a function of specific excess power, P_s, and instantaneous velocity, V, is given by Eq. (4-67); the resulting velocity after a time interval Δt is given by Eq. (4-68).

$$\bar{a} = \frac{gP_s}{V} \tag{4-67}$$

$$V_f = V_i + \Delta t \cdot \bar{a} \tag{4-68}$$

4.7.5.3 Sustained Turn Rate

Sustained turn rates are evaluated through the required thrust, which is equal to the generated drag shown in Eq. (4-69). The load factor obtained for a given turn requirement (n_{ST}) can be obtained from Eq. (4-64).

$$D_{SustTurn} = T_{Req} = qC_{D_0}S + \frac{K(n_{ST}W)^2}{qS} \tag{4-69}$$

The fuel consumption resulting from sustained turns is obtained through the turn radius, time and speed, and the thrust and specific fuel consumption at the specified Mach/Altitude/throttle condition, given in Eqns. (4-70) to (4-72).

$$R_{turn} = \frac{V^2}{g\sqrt{n^2 - 1}}$$ **(4-70)**

$$t_{turn} = \frac{2\pi N_{turns} R_{turn}}{V}$$ **(4-71)**

$$f_{turn} = T \cdot TSFC \cdot t_{turn}$$ **(4-72)**

Manoeuvrability constraints and capabilities are summarised in the Manoeuvring Diagram, which shows stall, maximum speed, maximum load factor, and specific excess power at a specified mass (percentage fuel and payload) and altitude condition, as exemplified in Figure 4-32.
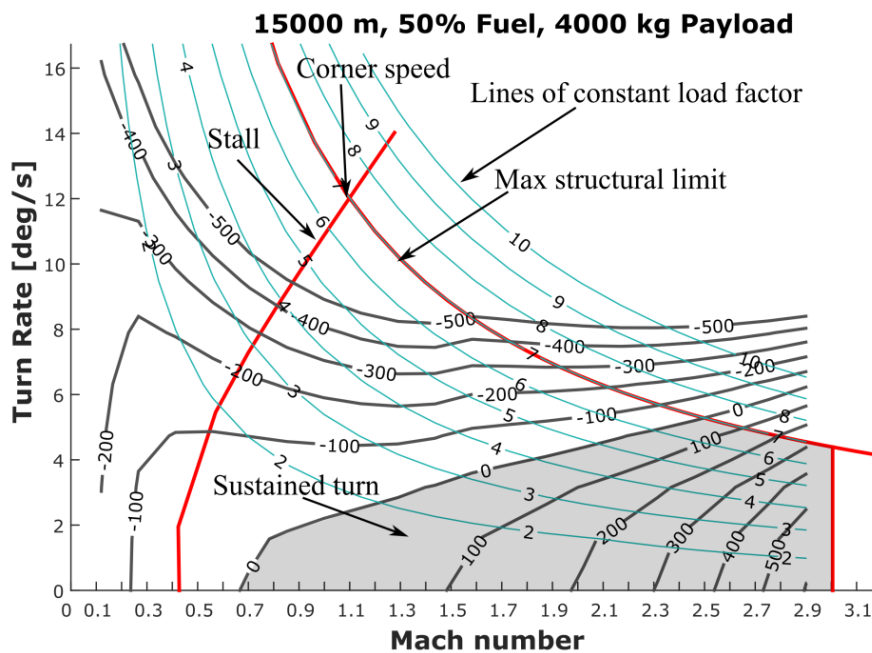
Figure 4-32 - Manoeuvre Diagram schematic

4.8 Packaging and Centre of Gravity

The main purpose of the packaging module is to calculate the location of the centre of gravity of the various mass components, and mass configurations of the vehicle (take-off mass, empty mass, 50% fuel, etc.). Within this module there are

subroutines to calculate essential characteristics such as wing fuel tank volume available, location and sizing of landing gear, and location and sizing of weapon bays depending on the payload choice; these subroutines will be explained in the sections below.

Furthermore, the packaging module has the capability to determine which elements can and should translate longitudinally and laterally in order to comply with centre of gravity ranges, desired locations, load constraints, volumetric constraints, and clash between components. This functionality is highly dependent on the definition of the mass breakdown components previously set in the Mass Breakdown module. The different components are declared as objects of the *mass component* sub-class, which is further divided into the sub-components shown in Figure 4-33. A series of parameters define each mass component, including the mass, a name, centre of gravity location (in global *{XYZ}* coordinates, if known or explicitly declared), a volume, a shape, and the dimensions depending on the declared shape. The pre-defined shapes include box, cylinder, sphere, conformal, and distributed. This division of components simplifies the input identification process within the packaging module.
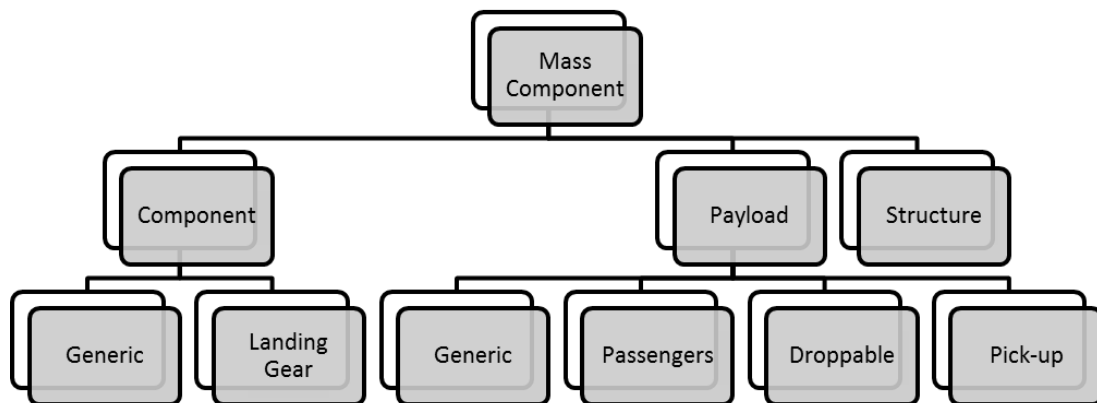
Figure 4-33 - Mass Components sub-class in GENUS

The flow chart in Figure 4-34 exemplifies the general execution procedure of the packaging module within a multidisciplinary design and analysis loop.

Clashes can be detected and resolved between components of explicitly defined geometric shapes such as boxes, cylinders, and spheres; and between these components and the outer shell of the vehicle. This action is performed through

a series of helper methods which compare the corner coordinates of the known component volumes against other coordinates obtained either from the geometry definition or the location of the other declared components.

A schematic of a UCAV packaging is exemplified in Figure 4-35 where the vehicle shows potential clashes between the weapon bays and the vehicle's outer skin and the landing gear enclosure volumes, as well as a partial clash between the wing fuel tank volume and the main landing gears. This last case can be handled by calculating the overlapping volume and subtracting it from the calculated wing fuel tanks. However, the rest of the cases need to be fully resolved, with no clashes found at the end of the design or optimisation loop.
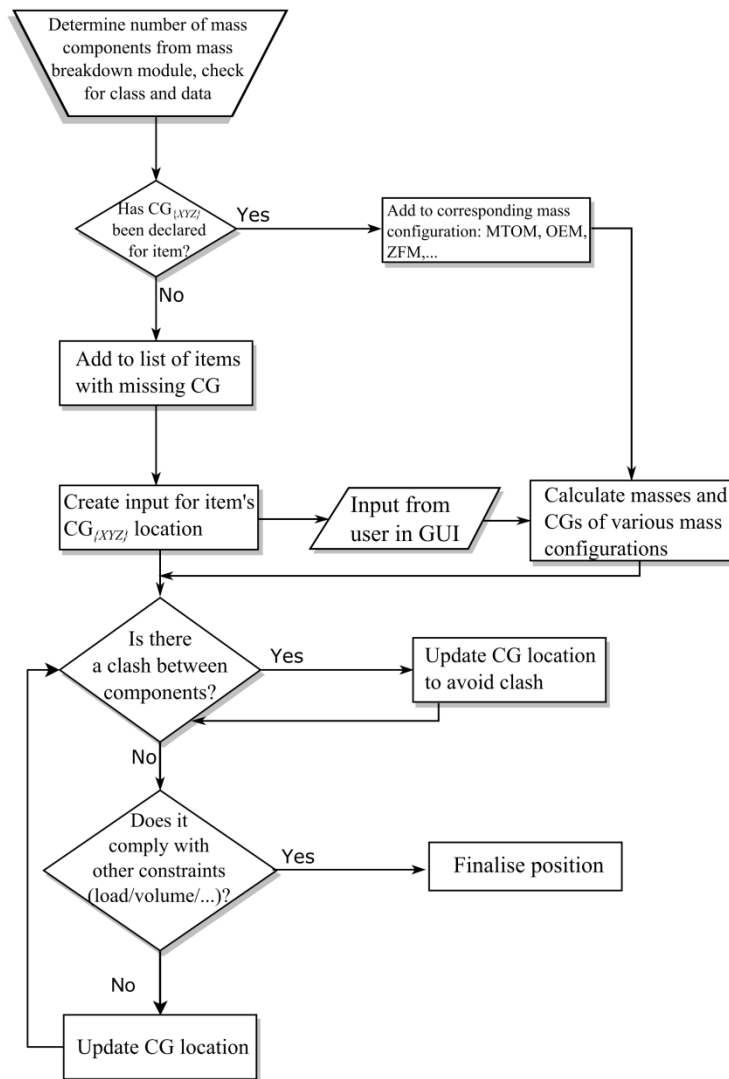
Figure 4-34 - Routine for locating items and resolving packaging issues
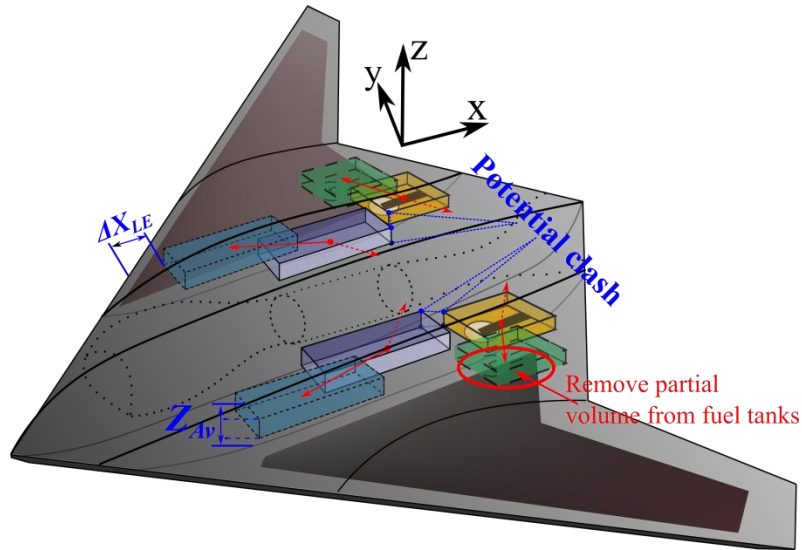
Figure 4-35 - Schematic of potential clashes in UCAV packaging

4.8.1 Wing Tank Volume

Wing tank volume calculations are performed via differential volumes, as shown in Figure 4-36, and Eqns. (4-73) and (4-74)[149]. The forward and aft wing tank limits are imposed through the assumed wing spar positions (user inputs).

$$\Delta v = \frac{\Delta y}{6} [\Delta x_1 (2\Delta z_1 + \Delta z_2) + \Delta x_2 (\Delta z_1 + 2\Delta z_2)] \tag{4-73}$$

$$\Delta z_j = \frac{1}{2} (z_j' + z_j'') \tag{4-74}$$
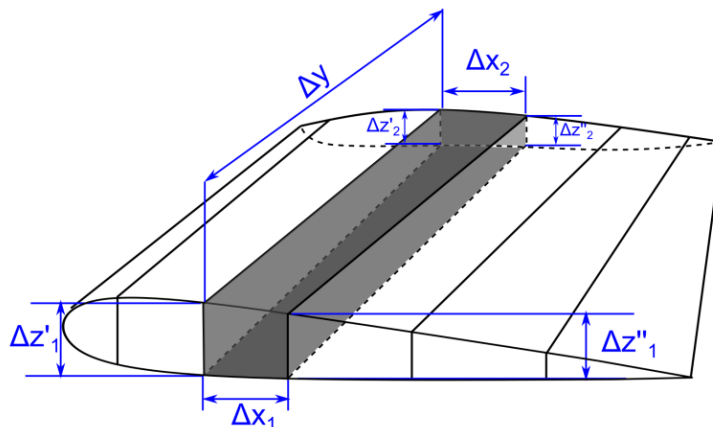
Figure 4-36 - Differential volume in a wing section

The total fuel volume is obtained as the sum of the differential volumes, multiplied by a correction factor ($f_{struc} \leq 1$) which accounts for the structural density, as shown in Eq. (4-75).

$$Vol_{fuel} = f_{struc} \sum_{i=1}^{n} \Delta v_i \tag{4-75}$$

This procedure can be applied to any area of a tailless configuration in order to represent complex, distributed fuel tank systems. The total fuel centre of gravity can then be obtained as:

$$X_{CG_{Fuel}} = \sum_{i=1}^{n} \frac{\rho_{fuel} \cdot v_i \cdot x_{cg_{fuel_i}}}{\rho_{fuel} \cdot v_i} \tag{4-76}$$

Where the local centre of gravity for the differential tanks is assumed to be at the geometric centroid of a frustum, given by Eq. (4-77), corrected for its overall location in the body axes system.

$$x_{cg_{fuel_i}} = \frac{h_i(A_{base_i} + 2\sqrt{A_{base_i}A_{top_i}} + 3A_{top_i})}{4(A_{base_i} + \sqrt{A_{base_i}A_{top_i}} + A_{top_i})} \tag{4-77}$$

4.8.2 Landing Gear Sizing and Positioning

Landing gear considerations have been limited to the typical tricycle configuration, with the main factors being the length of the landing gear to avoid a tail strike through the tipback angle, the overturn angle to avoid overturning during taxiing at sharp corners, and finally the maximum static loads allowed for the nose and main gears. The nose landing gear static load should remain within 8-20% for all CG conditions in order to provide sufficient compromise between steering and structural load. Static loads are given by Eqns. (4-78) and (4-79), and the schematic top and side views shown in Figure 4-37.

$$(Max\ static\ load)_{nose} = W\frac{M_f}{B} \tag{4-78}$$

$$(Min\ static\ load)_{nose} = W\frac{M_a}{B} \tag{4-79}$$
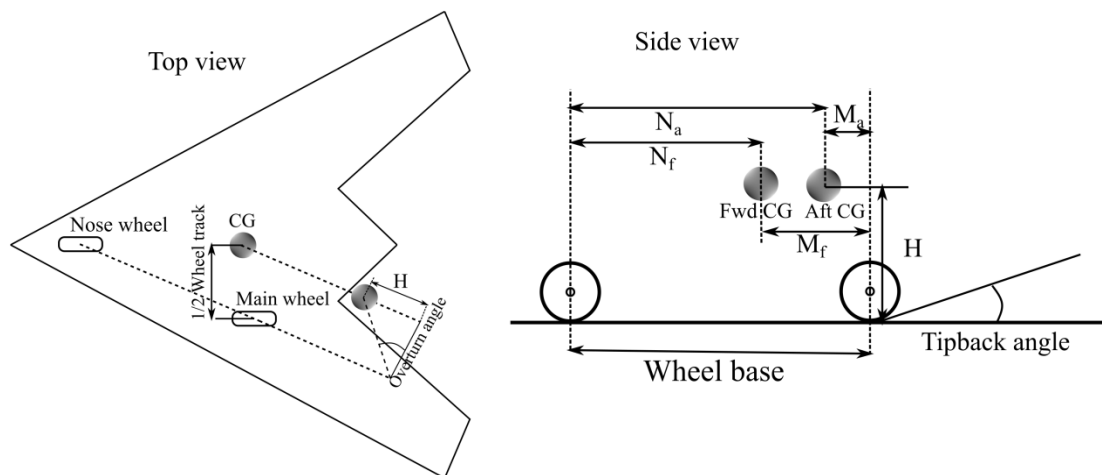
Figure 4-37 - Landing gear sizing and positioning schematics

An automatic *carrier-based* flag is used to set the maximum overturn and tipback angles according to Table 4-4[129, sect.11.2].

Table 4-4 - Landing gear sizing angles

Variation	Max Overturn Angle [deg]	Max Tipback Angle [deg]
Conventional	63	15
Carrier-based	54	25

4.8.3 Weapon Bay Sizing

The sizing of weapon bays is performed based on payload specifications, given that the payload dimensions are known. A database of commonly used weapons has been compiled. The number and dimensions of the weapon bays are obtained based on weapon(s) type, payload allowance, number of engines, and the overall vehicle geometry. The basic weapon bay dimensions follow Raymer's suggestions, as shown in Figure 4-38.
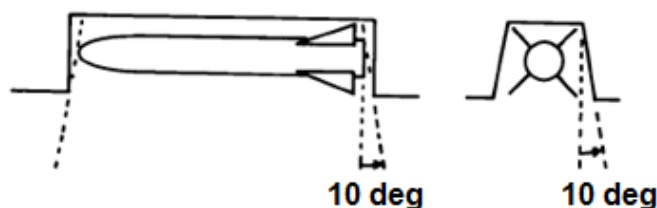
Figure 4-38 - Internal weapon bay sizing clearance

4.9 Stability and Control

Stability is evaluated for all user-defined flight conditions, where a flight condition is defined by the following flight characteristics:

$$flight_{cond} = f(Mass, Mach, Altitude, CG_{XYZ}, \alpha, \beta, Thrust)$$

Longitudinal static stability is constrained through the static margin, and control surface deflections required for achieving trim at all flight conditions. Static margin is a function of the neutral point and centre of gravity as given by Eq. (4-80).

$$K_n = \frac{x_{np} - x_{CG}}{\bar{c}} \tag{4-80}$$

The neutral point can be estimated from the geometry and the aerodynamic data as:

$$x_{np} = x_{ref} - \bar{c}\frac{C_{m_\alpha}}{C_{L_\alpha}} \tag{4-81}$$

Trim deflection is obtained as the deflection angle of some control effector for which the sum of moments about the aircraft's CG is zero, as given in Eq. (4-82). For the case of longitudinal trim, the moment axis is the lateral or Y axis.

$$\sum M_{y_{CG}} = \left(\frac{dC_{M_{ac}}}{d\delta_e}\right)\delta_e - \frac{x_w}{\bar{c}}\left[\left(\frac{dC_L}{d\alpha}\right)\alpha + \left(\frac{dC_L}{d\delta_e}\right)\delta_e\right] = 0 \tag{4-82}$$

Digital DATCOM has been implemented through the Java Native interface, as schematically shown in Figure 4-39, in order to automate the process of calculating the effect of symmetrical control effectors on lift and moment coefficients. DATCOM is also able to calculate trim automatically providing control effector deflections, and changes in lift, drag and moment coefficients.
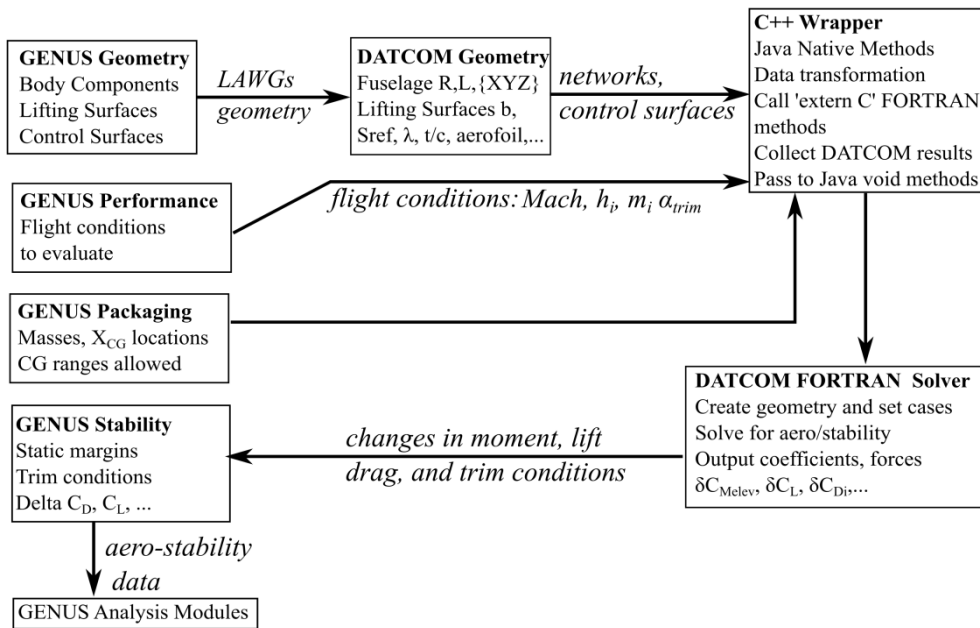
Figure 4-39 - DATCOM data inputs and outputs as implemented in GENUS

4.10 Stealth

As mentioned in §2.4.1, during the early stage of conceptual design studies, stealth considerations can most easily be addressed through the aspects relevant to susceptibility. These are, broadly, the electromagnetic, infrared, visual, and acoustic signatures.

Basic stealth considerations have been added to the GENUS framework as part of a special analysis module, so far limited to estimations of RCS, which is arguably the most relevant aspect of the electromagnetic signature. The estimation of the infrared signature remains as part of the future developments regarding stealth evaluations in GENUS.

4.10.1 Radar Cross Section

The term radar originates from the phrase *radio detection and ranging*, originally used during WWII. Radar cross section is a measure of the cross sectional area of a sphere that would reflect the same amount of energy as the actual target. The RCS signature is defined in relation to the incident and scattered fields in Eq. (4-83), and the unit conversion from dBsm to m^2 is given in Eq. (4-84). A typical

RCS scale equivalence, its meaning in terms of observability, and typical aircraft found in that RCS range are shown in Table 4-5.

$$\sigma = \lim_{r \to \infty} 4\pi r^2 \frac{|E_{scatt}|^2}{|E_{inc}|^2} \tag{4-83}$$

$$\sigma_{dBsm} = 10 \log_{10}(\sigma_{sm}) \tag{4-84}$$

Table 4-5 - RCS value scale and their observability

dBsm	20	10	0	-10	-20	-30	-40
m²	100.0	10.0	1.0	0.1	0.01	0.001	0.0001
Range	Conventional			Low-observable		Very LO	
Aircraft	Bombers, Fighter Aircraft			B-2, F-117		F-35, F-22	

The RCS of a complex object is a function of numerous aspects including its aspect, material, its angular orientation towards the radar, and the radar wavelength, amongst others. Generally, the RCS can be expressed as $\sigma_{pq}(\theta,\varphi)$, where p and q correspond to the incident and received polarisation, and θ and φ correspond to the spherical coordinate angles shown in Figure 4-40.
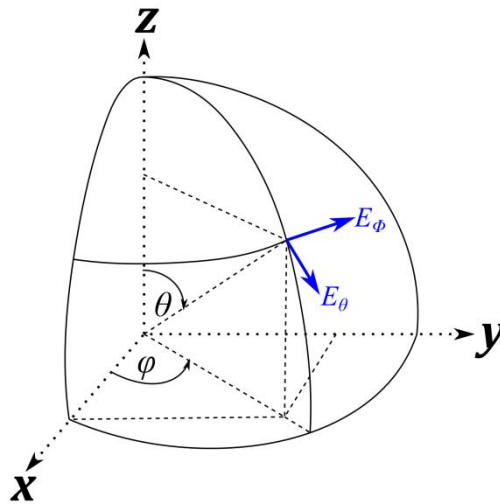
Figure 4-40 - Spherical coordinates system for RCS calculation

The most common numerical prediction methods for RCS include the method of moments (MOM), the finite difference method (FDM), geometric optics (GO), and physical optics (PO). The multilevel fast multipole method (MLFMM) can be applied to MOM to reduce the computational time. The theory behind each

method is beyond the scope of this research, for a comprehensive analysis see[171, chap.3].

Several numerical packages exist for calculating the RCS of a target or a stealth aircraft. However, most packages are integrated into other desktop design tools such as ANSYS. Table 4-6 compares various RCS codes in terms of their availability, geometric input and the solver method.

Table 4-6 - RCS code comparison

Code	Open Source	Geometry Input	Solver Method	Extra Features
RCSAnsys	✗	Detailed CAD	PO + GO	Part of ANSYS suite. Large structures.
CEMOne	✗	Detailed CAD	MLFMM	Part of Efield Software suite.
FEKO	✗	Detailed CAD	MLFMM + Large Element/PO	Computationally intensive.
POFACETS	✓	Triangular facets	PO	Freely available, simple inputs.

From the available numerical packages, POFACETS is the simplest one, which induces limitations to the analysis. However, the analysis method in POFACETS matches the level of fidelity in the geometric definition within GENUS, and it maintains the license-free philosophy of the framework. Therefore, RCS calculations in GENUS are limited to monostatic calculations derived from POFACETS[172,173], which have been translated from the original MATLAB format into Java routines.

Monostatic RCS means that the location of the transmitter and the receiver are the same, as opposed to bistatic or multistatic RCS where several transmitter/receiver locations are used, as shown in Figure 4-41.

a) monostatic   b) bistatic
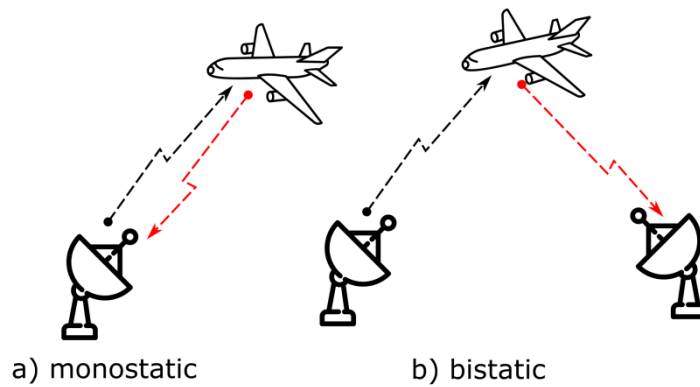
Figure 4-41 - Monostatic and bistatic radar arrangements

The PO method calculates RCS by approximating the induced surface current on the illuminated portion of the body as proportional to the incident magnetic field intensity. The total signature is obtained by superimposing the scattered field from all illuminated areas. Complex geometries can be represented by a collection of simple geometrical shapes, with triangular shapes being the most flexible for representing single and double curvature shapes, as seen by the triangular facet representation of complex targets in Figure 4-42[171, chap.6]. PO is a high-frequency approximation method that works best for electrically large objects, where the characteristic dimension of the body is many times larger than the incident wave length, also known as the optical region. Limitations to the PO method include the effect of surface waves, multiple reflections and edge diffractions, as well as the analysis of special scattering structures such as antennas and cavities.
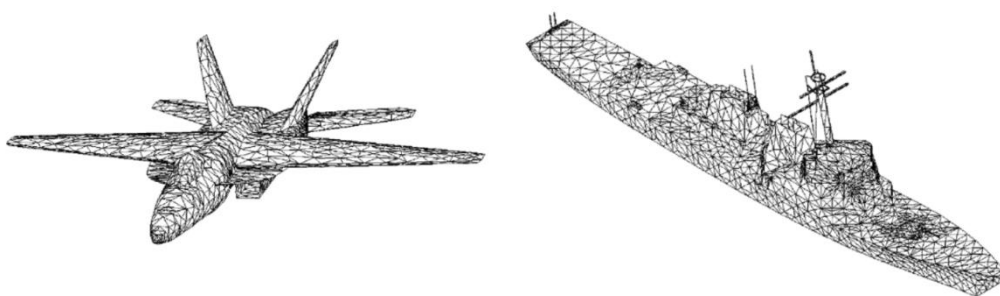
Figure 4-42 - Complex targets represented by triangular facets

Due to the restricted nature of defence information regarding the RCS of current and future fighter and UCAV designs, validation of the POFACETS calculations is difficult. However, estimations of the RCS for several aircraft and missiles have been reported by various sources, as exemplified in Figure 4-43.

a) F-5 aircraft   b) Low-observable aircraft

c) Generic aircraft target
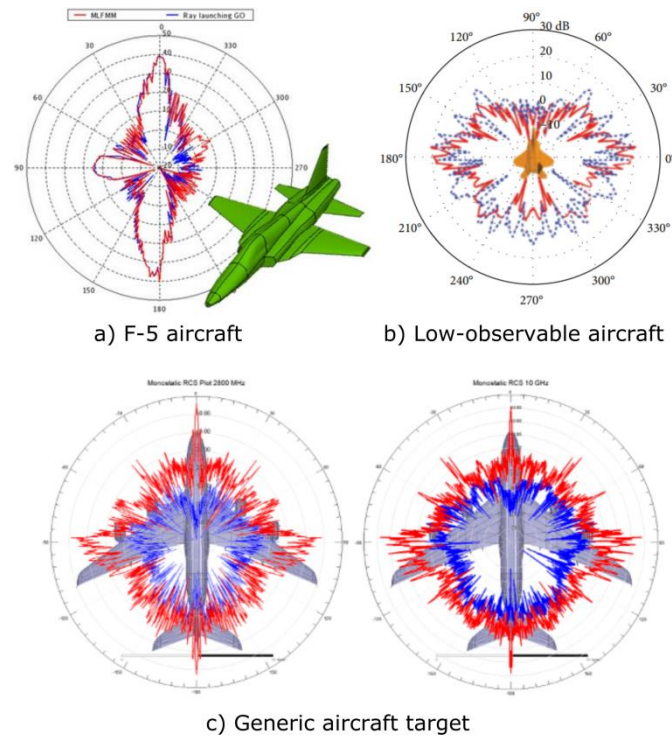
Figure 4-43 - Simulated RCS signatures for various aircraft[174,175]

Zikidis *et al.*[176] estimate the RCS of the F-35 as 0.001m^2 or -30 dBsm; however, they also mention the initial scepticism and criticism of the F-35 JSF programme, its shortcomings in performance and low-observability. This criticism partially originated as a consequence of the POFACETS results for the F-35's fuselage underside and axisymmetric nozzle reported by Air Power Australia. It shows vulnerability (RCS > -20 dBsm) and borderline low-observable performance (RCS > -30 dBsm) at most frequencies and angles. Very low-observability (RCS < -30 dBsm) was only found at high frequencies, specifically the X and Ku bands (8 to 16 GHz); the poorest performance was found at low frequencies[177]. These results also match the POFACETS data for the three-dimensional modelling of the F-35 geometry from two-dimensional drawings, assuming that RAM provides an RCS reduction of -10 dBsm[178], as shown in Figure 4-44.
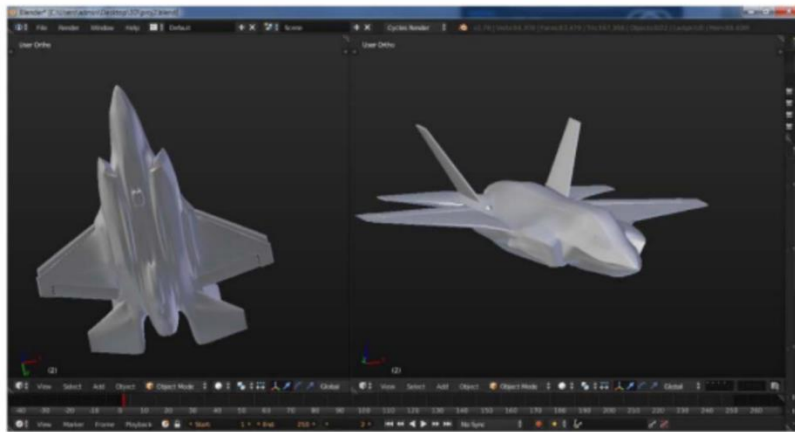
a) F-35 three-dimensional model from two-dimensional drawings
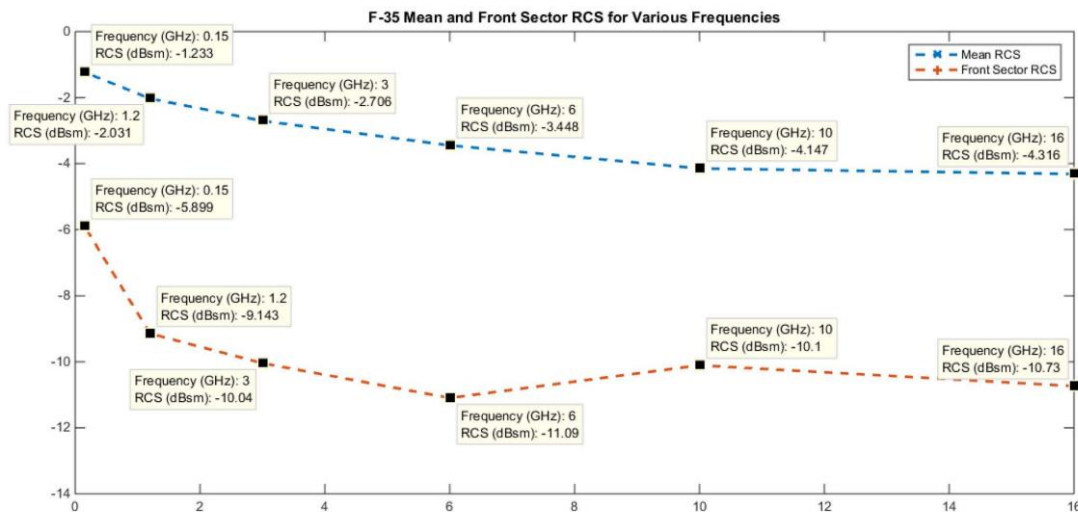
b) F-35 mean and front RCS vs frequency (no RAM)

Figure 4-44 - F-35 3D geometry and RCS using POFACETS

Having established the validity and applicability of the POFACETS code, a geometry conversion routine was developed in order to discretise the discrete geometry elements (body components and lifting surfaces) into triangular facets. The open source Java library QuickHull3D[179] has been used to automatically generate a series of three-dimensional convex hulls and perform Delaunay triangulations in order to simplify the code complexity, and to reduce development time. The geometry processing sequence is schematically shown in Figure 4-45. Additional details can be found in Appendix D.
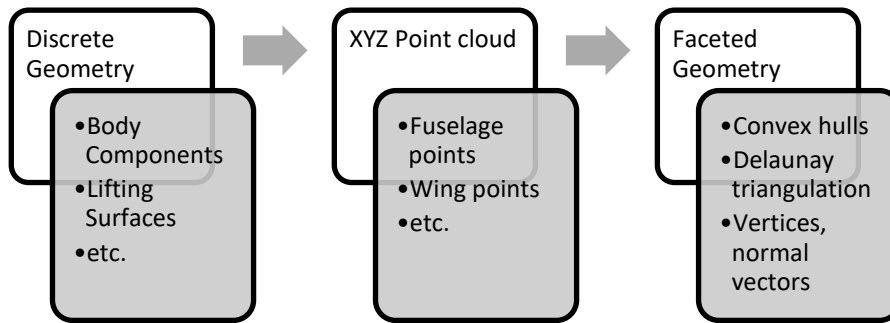
Figure 4-45 - Geometry processing for RCS calculation

The monostatic RCS in GENUS has been verified for clean, flying wing configurations assuming perfect electric conductor materials, with good agreement, as shown in Figure 4-46. Different radar absorbent materials can be incorporated into the analysis through the material's surface resistivity value R_s, where $R_s = 0$ means a perfect conductor, and as $R_s \to \infty$ the surface becomes transparent.
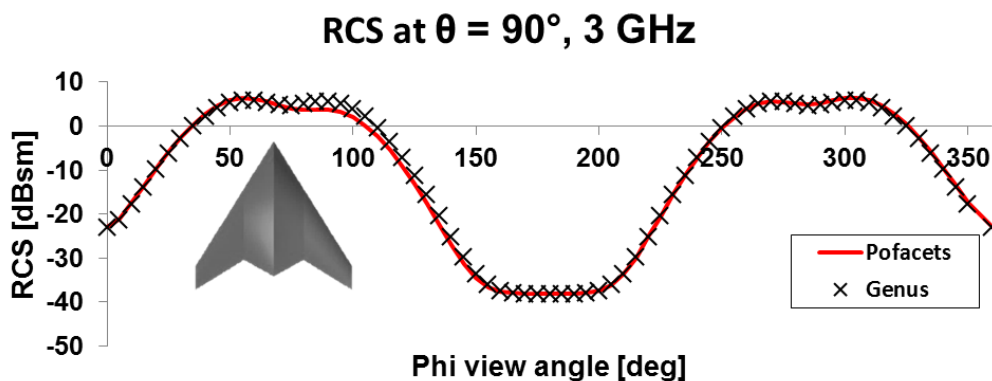
Figure 4-46 - Verification of monostatic RCS calculation in GENUS

The RCS module is fully integrated into the multidisciplinary design and analysis loop in GENUS, which allows to select the RCS as either the objective function or to include LO characteristics as part of the design space constraints. By selecting a range of θ and φ view angles, the designer can select maximum allowable values of radar signature. This constraint is applied to the clean geometries without taking into account cavities, control surface gaps, and intakes. An example of the radar signature at various θ and φ view angles, as well as a wing sweep design space exploration for a flying wing UCAV including a RCS constraint is shown in Figure 4-47.
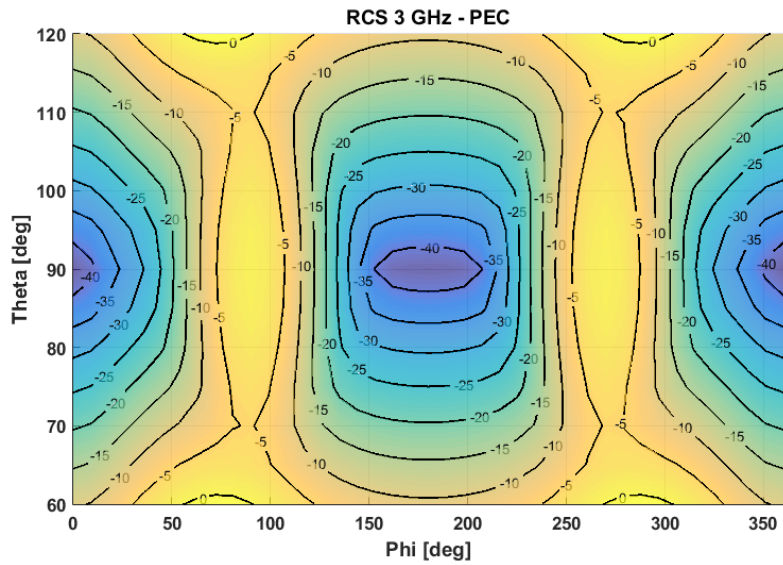
a) Monostatic RCS$_\varphi$ values at various θ and φ view angles
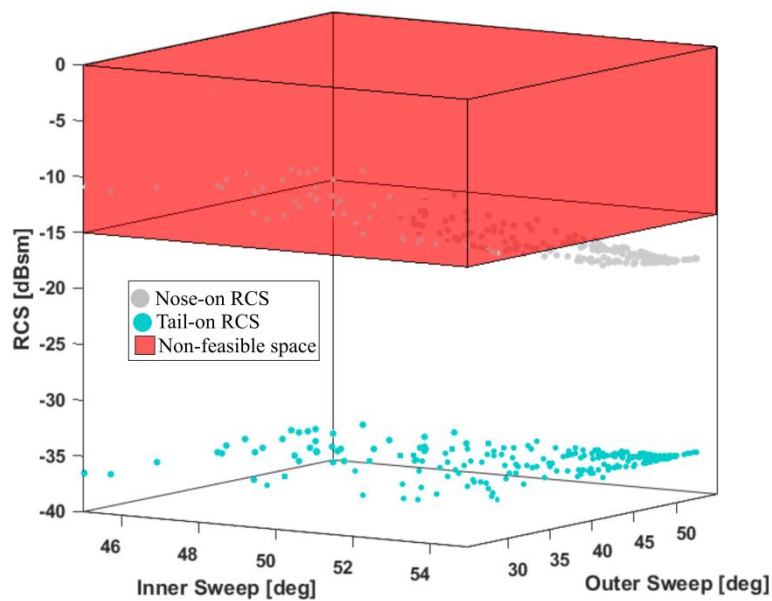
b) Sweep angle exploration incorporating RCS constraint

Figure 4-47 - RCS response at various view angles, and RCS constraint space

4.11 Vehicle Heat Balance and Thermal Management

For vehicles operating at high speeds, aerodynamic heating through direct compression of the flow or through friction presents additional design challenges. The high temperatures encountered during high speed flight can result in reduced structural strength, as well as system architecture constraints related to insulation of fuel or sensors.

The development of the aerodynamic heating module is part of the *special* GENUS modules. Table 4-7 compares several aerodynamic heating codes and packages. As can be seen, ZSTREAM requires a license and is part of the ZONAIR software package, relying on internal aerodynamic data for calculating aerothermal effects. SHABP mark 4.0 is an open source option that is only available in legacy FORTRAN code, incompatible with modern systems, and its implementation would require a complete re-structuring and re-writing of the methods available.

Table 4-7 - Aerodynamic heating code comparison

Code	Open Source	Method	Extra Features
ZSTREAM	✗	One-dimensional hypersonic boundary layer method	Dependent on ZONAIR aero data
SHABP mark4.0	✓	Data compendium, empirical methods	Not compatible with modern FORTRAN
ESDU	✓	Analytical, data compendium, empirical methods	Simple to implement through data tables

Therefore, the aerodynamic heating analysis has been developed following the empirical procedures provided in ESDU 69009[180], 69010[181], and 69012[182], simplified by neglecting the following aspects:

o Radiation from the hot gases around the nose of the vehicle (relevant only at very high Mach numbers, $M \geq 5$).
o Internal vehicle radiation and convection.
o Conduction along and through the skin (fuel heat transfer will be described in the thermal management system, §4.11.4).

This analysis also assumes the air is chemically stable and that the specific heat ratio (γ) and specific heat capacity (c_p) remain constant. Furthermore, the effect of leading edge radius will not be taken into account, and all wing segments will be considered as wedges, with semi-vertex angle φ as shown in Figure 4-48.
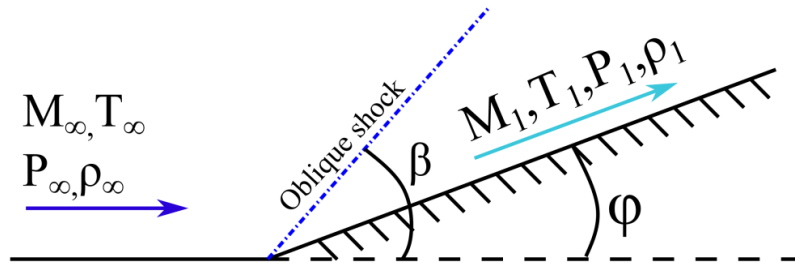
Figure 4-48 - Supersonic flow past a wedge

4.11.1 Aerodynamic Heating

For supersonic flow past a wedge with deflection angle φ, the oblique shock angle β can be found iteratively through Eq. (4-85).

$$tan\beta = \left[\left(\frac{\gamma+1}{2}\right)\left(\frac{M_\infty^2}{M_\infty^2 \sin^2\beta - 1}\right) - 1\right]^{-1} cot\varphi \qquad \textbf{(4-85)}$$

The Mach number downstream the oblique shock wave can be obtained as:

$$M_1^2 \sin^2(\beta - \varphi) = \frac{2 + (\gamma-1)M_\infty^2 \sin^2\beta}{2\gamma M_\infty^2 \sin^2\beta - (\gamma-1)} \qquad \textbf{(4-86)}$$

The rest of the downstream properties can be found through the isentropic relations as given by Eqns. (4-87) to (4-90).

$$T_1 = T_\infty \left[\frac{1 + \frac{\gamma-1}{2}M_\infty^2}{1 + \frac{\gamma-1}{2}M_1^2}\right] \qquad \textbf{(4-87)}$$

$$P_1 = P_\infty \left[\frac{\left(1 + \frac{\gamma-1}{2}M_\infty^2\right)^{\frac{\gamma}{\gamma-1}}}{\left(1 + \frac{\gamma-1}{2}M_1^2\right)^{\frac{\gamma}{\gamma-1}}}\right] \qquad \textbf{(4-88)}$$

$$\rho_1 = \frac{P_1}{RT_1} \qquad \textbf{(4-89)}$$

$$u_1 = M_1\sqrt{\gamma RT_1} \qquad \textbf{(4-90)}$$

The dynamic viscosity, μ, (kg/m/s) as a function of temperature (in K) is given in ESDU 73017[183] as:

$$\mu = \begin{cases} \mu_0 \left(\dfrac{T_0 + 110.4}{T + 110.4}\right)\left(\dfrac{T}{T_0}\right)^{3/2}, & 70 < T < 300\ K \\[2em] \dfrac{T^{0.5} \times 10^{-6}}{A_0 + A_1 s + A_2 s^2 + A_3 s^3 + A_4 s^4}, & T \geq 300\ K \end{cases} \tag{4-91}$$

Where

$\mu_0 = 17.956 \cdot 10^{-6}\ kg/ms$

$s = 100/T$

$A_0 = 0.552795$

$A_1 = 2.81089$

$A_2 = -13.5083$

$A_3 = 39.3531$

$A_4 = -41.4194$

The stagnation or total temperature is given by:

$$T_s = T_\infty \left(1 + \frac{\gamma - 1}{2} M_\infty^2\right) \tag{4-92}$$

The adiabatic wall temperature is always less than the stagnation temperature; therefore a recovery factor (r) is introduced to account for the fraction of the freestream dynamic temperature rise recovered at the wall. The adiabatic wall recovery temperature is then given by:

$$T_{wr} = T_1 \left[1 + r\frac{\gamma - 1}{2} M_1^2\right] \tag{4-93}$$

A constant value of 0.85 is acceptable for analyses at Mach numbers below 5.0 and for laminar boundary layers, while a recovery factor of 0.89 is used for fully turbulent boundary layers, or hypersonic speeds.

The local Stanton number (the ratio of heat transferred into a fluid to the thermal capacity of said fluid) in incompressible flow can be computed as a function of the boundary layer condition and the Reynolds number, Eq. (4-94), at any location x behind the oblique shock wave as given by Eq. (4-95).

$$Re_x = \frac{u_1 \rho_1 x}{\mu_1} \tag{4-94}$$

$$St_i = \begin{cases} 0.413 Re_x^{-1/2}, & laminar \\ 0.826 Re_x^{-1/2}, & turbulent \end{cases} \tag{4-95}$$

Where the boundary layer is considered turbulent if it meets the transition condition established in Eq. (4-96):

$$\log(Re_x) > [\log(Re_t) + C_M(M_{Local})] \tag{4-96}$$

The recommended transition values for different aircraft components are given in Table 4-8[184].

Table 4-8 - Boundary layer transition values

	$\log(Re_t)$	C_M
Fuselage	5.5	0.2
Wing, no sweep	5.5	0.2
Wing, with sweep	5.5	0.1

The overall Stanton number can be then corrected through ESDU 69010, fig. 2, interpolating between downstream temperature, downstream Mach number, and wall temperature ratios (T_w/T_{wr}), so that:

$$St = St_i \frac{St}{St_i} \tag{4-97}$$

Finally, the heat flux (W/m²) due to forced convection can be calculated as:

$$q_{aero} = St \rho_1 u_1 c_{p_{air}} (T_{wr} - T_w) \tag{4-98}$$

Where T_w can be set as the maximum material or structural temperature limit, or the equilibrium wall temperature.

4.11.2 Additional Heating Factors

The effects of solar irradiance on the overall heat balance of the vehicle have been included through the procedure given in ESDU 69015[185], where the total

solar heating is a function of the atmospheric conditions, location, altitude, time, and season, as schematically shown in Figure 4-49, and Eq. (4-99).
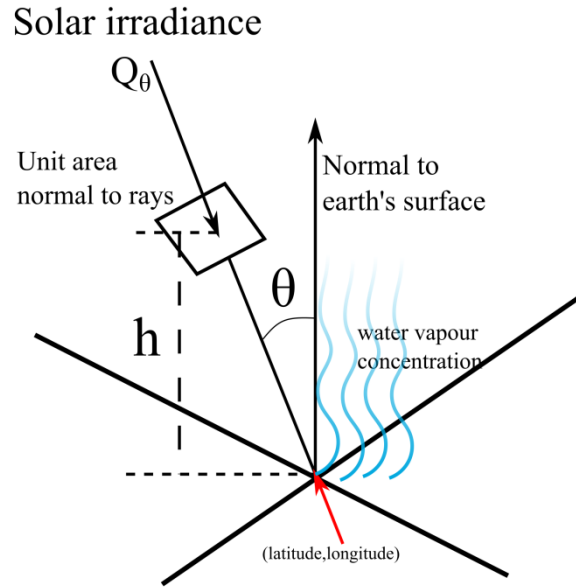
Figure 4-49 - Solar irradiance components

$$q_{sol} = \alpha_s Q_\theta \frac{S_{proj}}{S} \tag{4-99}$$

For the lower skin, the reflected solar irradiance from the ground should be considered with conservative assumptions such as no water vapour concentration to minimise heat dissipation. The heat transfer due to earth's reflection can be calculated as:

$$q_{earth} = \alpha_{earth} \alpha_s Q_e \left(1.75 - \frac{Q_N}{Q_e} \right) \frac{S_{proj}}{S} \tag{4-100}$$

The heat transfer by external radiation from the skin is given by:

$$q_{ext} = -\varepsilon_s B [T_w^4 - T_{amb}^4] \tag{4-101}$$

The heat transferred by the atmospheric radiation to the vehicle's skin is given by:

$$q_{atmos} = \alpha_s \varepsilon_G B T_1^4 \tag{4-102}$$

Absorptivity, emissivity, gas and material properties are given in Table 4-9.

Table 4-9 - Vehicle Heat Balance Constants

Parameter	Value	Unit
Stefan-Boltzman constant (B)	5.67×10^{-8}	W/m²K⁴
Gas constant (R)	287.041	J/kgK
Specific heat capacity of air ($c_{p_{air}}$)	1003.5	J/kgK
Heat capacity ratio of air (γ)	1.4	-
Emissivity of air (ε_G)	1	-
Average earth's albedo (α_{earth})	0.3	-
Solar constant (Q_e)	1360	W/m²
Average skin panel absorptivity (α_s)	0.8	-
Average skin emissivity (ε_s)	0.7	-
Specific heat capacity of Ti6Al4V material ($c_{p_{Ti}}$)	526.3	J/kgK
Specific heat capacity of Al7075 material ($c_{p_{Al}}$)	960	J/kgK

The heat dissipated from the avionics bay can be estimated through a power to weight ratio, the total mass of the system, and a thermal efficiency, such that the total heat load (W) is given by:

$$\dot{Q}_{avionics} = (1 - \eta_{thermal})\frac{P}{W}m_{avionics} \qquad \textbf{(4-103)}$$

4.11.3 Equilibrium temperature

Taking into account all the heating factors mentioned above, the heat balance equation for the skin can now be calculated as:

$$K_s\frac{dT_w}{dt} = q_{aero} + q_{ext} + q_{atmos} + q_{sol} + q_{earth} + q_{cooling} \qquad \textbf{(4-104)}$$

Where K_s depends on the material's specific heat capacity, density, and thickness, given by:

$$K_s = c_{p_s}\rho_s\tau_s \qquad \textbf{(4-105)}$$

The equilibrium wall temperature can be solved iteratively through an explicit numerical integration so that Eq. (4-104) becomes:

$$T_{w_{i+1}} = T_{w_i} + \frac{\Delta t}{K_s}(q_{aero} + q_{ext} + q_{atmos} + q_{sol} + q_{earth})$$ **(4-106)**

The heat flux resulting from stabilising the wall temperature at the limit or desired temperature can be then found through:

$$q_{cooling} = K_s(T_{w\,limit} - T_w)$$ **(4-107)**

The value of the explicit integration time step Δt has a large influence over the temperature convergence, and finding an appropriate value can be difficult. An acceptable value of $\Delta t = 5$ has been selected considering accuracy and run time, as shown in Figure 4-50.
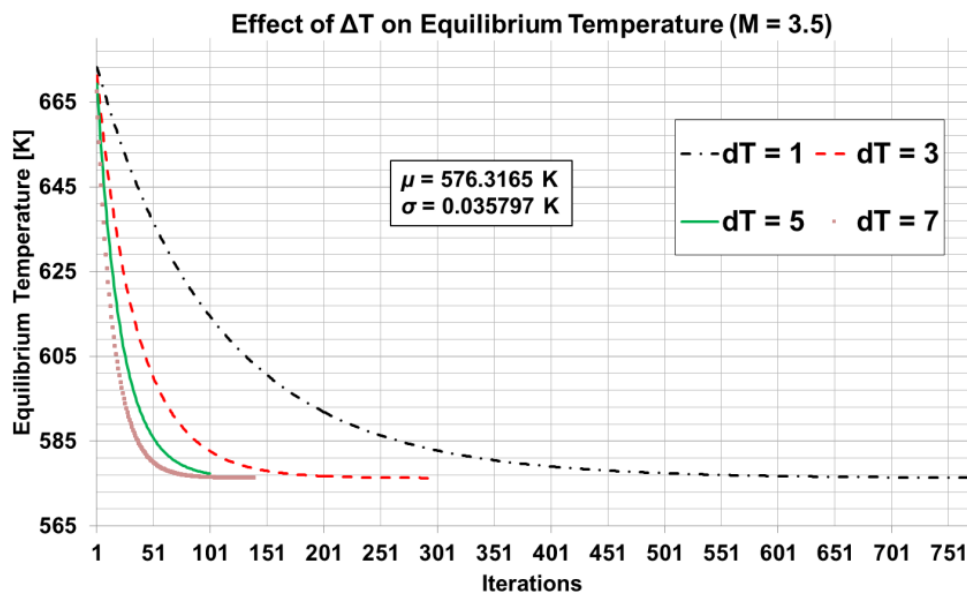
Figure 4-50 - Effect of Δt on equilibrium temperature convergence

Figure 4-51 shows the upper (right side) and the lower (left side) skin temperature distributions of a flying wing configuration at Mach 2.5, 3.0, and 3.5 (constant altitude of 17 km). It can be clearly seen that an increment of 0.5 in Mach number results in approximately a 100K increment for the maximum top skin temperature.

114
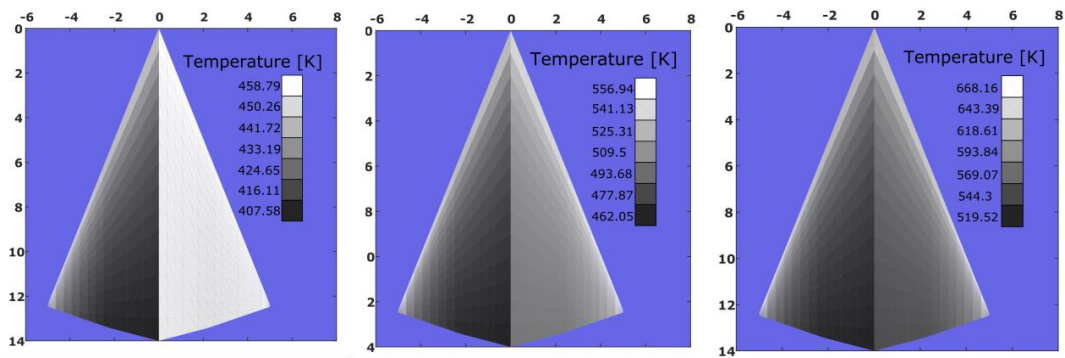
Figure 4-51 - Panel temperatures at different Mach numbers

4.11.4 Thermal Management System

Typical aircraft sizing methods are based on the mission and performance parameters such that the resulting gross weight and fuel consumption are a function of the required range and the overall flight envelope.

In the design of supersonic vehicles, thermal management demands can result in severe design constraints which require the implementation of a sophisticated thermal management system (TMS). The majority of thermal loads are associated with the propulsion system, the airframe loads due to aerodynamic heating, and to the avionics and ECS heat loads, as shown in Figure 4-52. A reasonable assumption for unmanned vehicles is to ignore the ECS loads since there is no passenger cabin.
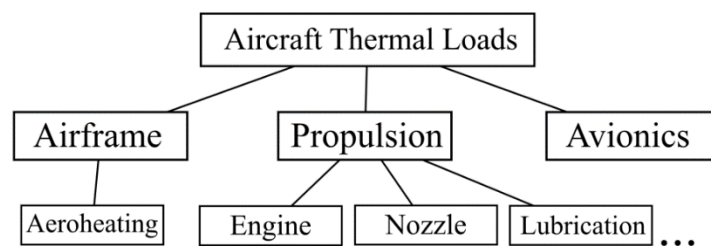
Figure 4-52 - Typical thermal loads[186]

An efficient solution to the TMS is to use the fuel as a heat sink prior to being burned by the engine. Various fuel thermal management systems (FTMS) architectures have been proposed and shown to have a noticeable influence over the optimum mission path of supersonic fighter aircraft[187], as well as having a significant impact on the vehicle sizing[188].

A simplified FTMS architecture consisting on an integral fuel tank with recirculation of unburned fuel is proposed here, as schematically shown in Figure 4-53. The main factors determining the performance of this system are: the fuel rate dictated by the engine requirements ($\dot{m}_{burned}$), the airborne heat loads ($\dot{Q}_{sink}$), the environmental heat loads ($\dot{Q}_{env}$), and the heat dissipated during recirculation ($\dot{Q}_{out}$).

In order to simplify the FTMS model, the following assumptions have been made:

o The heat generated by the fuel pumps and actuators has been ignored.

o The heat is instantaneously added and removed from the fuel.

o Fuel is spatially and chemically homogeneous.

o The mission segments are discretized into steady state segments where the heat loads are considered constant.

o The engine cooling system is considered as a distinct system for which a mass allowance is already included through the mass estimation.

o Infrared signature requirements are not prioritised, allowing a positive value of $\dot{Q}_{out}$.

o The reference fuel temperature is estimated as 20 °C (293 K), while the fuel temperature limit is 170 °C (443 K).
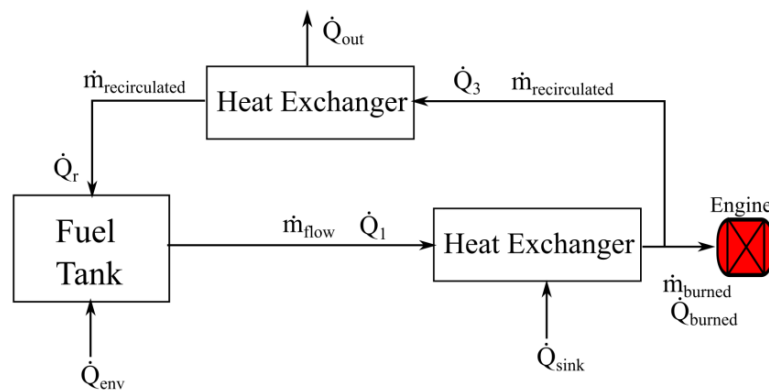
Figure 4-53 - Fuel thermal management system with recirculation

At moderate Mach numbers, the recirculation heat exchanger is typically a ram air device; however, at high Mach numbers ram air cannot be employed due to the high temperature flow surrounding the vehicle; therefore, a liquid or phase

changing coolant system is required. The heat dissipated by the recirculation heat exchanger can be calculated by Eq. (4-108).

$$\dot{Q}_{out} = \varepsilon_c \Delta T_{cool} \cdot \min(\dot{m}_{air}c_p, \dot{m}_r c_p, \dot{m}_{cool}c_{p_{cool}}) \qquad \text{(4-108)}$$

$$\dot{Q}_r = \frac{\dot{m}_r}{\dot{m}_{flow}}\left(\dot{Q}_1 + \dot{Q}_{sink}\right) - \dot{Q}_{out} \qquad \text{(4-109)}$$

Where ε_c is the heat exchanger's effectiveness, which depends on its type and area. The recirculated heat load $\dot{Q}_r$ is calculated through Eq. (4-109), and added to the airframe heat load $\dot{Q}_{env}$.

The system equation relating the temperature change in the fuel to the heat loads and fuel flow, as determined by Alyanak and Allison[188] is given as:

$$mc_v \frac{dT}{dt} = \dot{Q}_{env} + \left[1 - \frac{\dot{m}_{burned}}{\dot{m}_{flow}}\right]\dot{Q}_{sink} - \dot{Q}_{out} \qquad \text{(4-110)}$$

Where m is the total fuel in the tank, c_v is the specific heat at constant volume, and T is the temperature in the tank. An expression of the tank temperature can be found by setting the fuel mass as a function of the discretized mission segment's fuel burn and time as:

$$m(t) = m_i - \dot{m}_{burned_i}t_i \qquad \text{(4-111)}$$

So that the fuel temperature is obtained by the integration of Eq. (4-110) as:

$$T(t) = T_i + \int_{t_i}^{t_{i+1}} \frac{1}{m(t)c_v}\left(\dot{Q}_{env} + \left[1 - \frac{\dot{m}_{burned}}{\dot{m}_{flow}}\right]\dot{Q}_{sink} - \dot{Q}_{out}\right)dt \qquad \text{(4-112)}$$

$$k_T = \frac{1}{c_v}\left(\dot{Q}_{env} + \left[1 - \frac{\dot{m}_{burned}}{\dot{m}_{flow}}\right]\dot{Q}_{sink} - \dot{Q}_{out}\right) \qquad \text{(4-113)}$$

$$T(t) = T_i + k_T \int_{t_i}^{t_{i+1}} \frac{1}{m - \dot{m}_{burned}t}dt \qquad \text{(4-114)}$$

The thermal state metric for the FTMS, given by Eq. (4-113), is established so that if $k_T > 0$, the architecture cannot comply with the thermal needs; if $k_T < 0$, the

architecture has a thermal reserve; and if $k_T = 0$, the architecture is in thermal equilibrium. Finally, the explicit integration of Eq. (4-114) becomes:

$$T(t) = T_i + \frac{k_T}{\dot{m}_{burned}} ln \left(\frac{m - \dot{m}_{burned} t_i}{m - \dot{m}_{burned} t_{i+1}} \right) \qquad \textbf{(4-115)}$$

Where $m - \dot{m}_{burned} t_i$ is the fuel mass at the beginning of the mission segment and $m - \dot{m}_{burned} t_{i+1}$ is the fuel mass at the end of the mission segment. From this equation, a critical time can be calculated as the maximum thermal endurance of the system, where the fuel reaches its maximum allowed temperature, as given by:

$$t_{crit} = \frac{\dot{m}_{burned} t_i - m}{\dot{m}_{burned} \cdot e^{\frac{\dot{m}_{burned}\left(T_{crit} - T_{t=t_i}\right)}{k_T}}} + \frac{m}{\dot{m}_{burned}} \qquad \textbf{(4-116)}$$

The thermal endurance of a generic vehicle with an initial fuel mass of 8000 kg subjected to various environmental heat loads is shown in Figure 4-54. The effect of increasing environmental heat loads (aerodynamic heating) is shown, as well as the significant impact that thermal loads have on the sizing of supersonic vehicles, effectively limiting the mission endurance and resulting in unused fuel that needs to be carried through the mission.
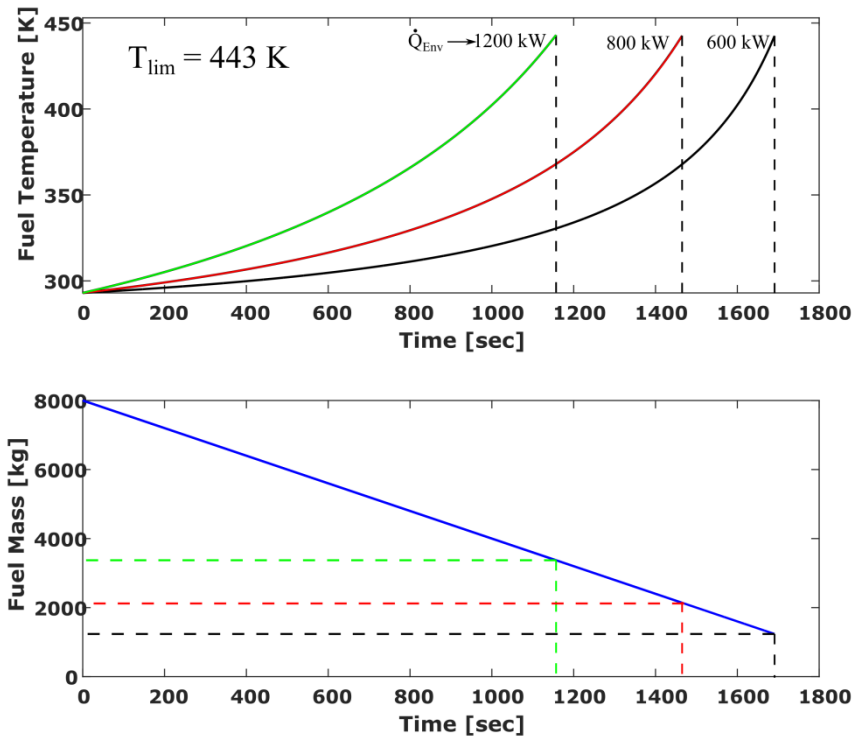
Figure 4-54 - Fuel temperature and residual fuel in the tank as a function of $\dot{Q}_{env}$

4.12 Cost Model

A simple Research, Development, Testing and Evaluation (RDT&E) cost model based on RAND DAPCA IV methods[189] has been included into the GENUS framework as a special module. This methodology consists of a few physical and operational characteristics of the vehicle, and has been well proven as valid for military aircraft by Nicolai[145, chap.24]. No operational of life cycle costs have been included in this model.

The cost estimation is divided into engineering hours, tooling hours, manufacture hours, quality control hours, development support cost, flight testing, manufacture materials, and engine production costs. The overall RDT&E cost evaluation requires educated assumptions on production numbers over the next five years (N_Q), as well as number of flight test aircraft (N_{test}). Equations (4-117) to (4-126) detail the cost modelling module.

$$H_{Engineering} = f_{adv} \cdot 5.18 M_{Empty}^{0.777} V_{Cruise}^{0.894} N_Q^{0.163} \qquad \textbf{(4-117)}$$

$$H_{Tooling} = f_{adv} \cdot 7.22 M_{Empty}^{0.777} V_{Cruise}^{0.696} N_Q^{0.263} \qquad \textbf{(4-118)}$$

$$H_{Manufacture} = f_{adv} \cdot 10.5 M_{Empty}^{0.82} V_{Cruise}^{0.484} N_Q^{0.641} \qquad \textbf{(4-119)}$$

$$H_{Quality} = 0.133 H_{Manufacture} \qquad \textbf{(4-120)}$$

$$C_{Development} = 67.4 M_{Empty}^{0.63} V_{Cruise}^{1.3} \qquad \textbf{(4-121)}$$

$$C_{FlightTest} = 1947 M_{Empty}^{0.325} V_{Cruise}^{0.822} N_{test}^{1.21} \qquad \textbf{(4-122)}$$

$$C_{Manuf-materials} = 31.2 M_{Empty}^{0.921} V_{Cruise}^{0.621} N_Q^{0.799} \qquad \textbf{(4-123)}$$

$$C_{Engine} = 3112(0.043 T_{SL} + 243.25 M_{max} + 0.969 TET - 2228) \qquad \textbf{(4-124)}$$

$$C_{avionics} = f_{adv} \cdot 16000 M_{Avionics} \qquad \textbf{(4-125)}$$

$$C_{RDTE} = R_E H_{Engineering} + R_T H_{Tooling} + R_M H_{Manufacture} + R_Q H_{Quality} \qquad \textbf{(4-126)}$$
$$+ C_{Development} + C_{FlightTest} + C_{Manuf-mat} + N_{Eng} C_{Engine}$$
$$+ C_{avionics}$$

A correction factor, f_{adv}, has been included in order to account for the use of advanced materials, manufacturing processes, and stealth related technology. A factor of 1.25 has been selected for engineering and avionics cost, 1.2 for tooling, and 1.5 for manufacturing. Additionally, to account for the cost of advanced avionics and software development costs of modern combat aircraft, a factor of 20,000 $/kg of avionics has been added to the total research and development cost.

Table 4-10 - Hourly rates for cost modelling

Role	Hourly rates
Engineering (R_E)	146 $
Tooling (R_T)	158 $
Manufacturing (R_M)	126 $
Quality Control (R_Q)	140 $

The hourly rates used through the cost calculations are given in Table 4-10, extrapolated for the year 2020, from Nicolai.

4.13 Summary

This chapter has introduced the methodologies selected and developed for the conceptual design and analysis of low-observable unmanned combat aerial vehicles, from fully subsonic regimes to high supersonic flight speeds.

It has been shown that the somewhat simple geometry definition allows for the introduction of geometrical rulings useful for RCS and supersonic flight through simple constraints. Mass estimations through empirical and semi-empirical relations have been validated against different UCAV designs available in the literature.

The development of the aerodynamic analysis module is composed of a multi-fidelity approach required to fully characterise the aerodynamic response at various flight conditions. This module makes use of a higher order panel method, PANAIR, for the analysis of arbitrary three-dimensional geometries from subsonic up to Mach 4.0.

The propulsion module includes a medium fidelity thermodynamic analysis of air breathing engines including afterburning and non-afterburning turbojets, turbofans, and ramjets. A combined turboramjet powerplant has been created through a simple transition condition from turbo to ramjet modes.

Through the flexibility of the mission module and the parametric mission definition available in the performance module, a wide variety of combat missions can be easily pre-set and evaluated. The mission performance evaluation includes every mission segment, from take-off to landing.

Stability considerations have been included through the wing-body trim analysis available in Digital DATCOM, with inputs being automatically transferred from the geometry, mission, and performance (flight conditions) modules.

Special modules include a physical optics approximation for RCS calculation, an aerothermodynamics module for aerodynamic heating and fuel thermal management system analysis, and a simple RDT&E cost estimation.

The integration of subsonic UCAV design methodologies into the GENUS framework, along with a framework validation exercise (Appendix E) have been published under the title *"Multidisciplinary analysis of subsonic stealth unmanned combat aerial vehicles"*, by the CEAS Aeronautical Journal (2019)[190].

The following chapters show the conceptual design studies and design space explorations for subsonic[191], moderately supersonic[192], and fully supersonic configurations (unpublished). The publications that resulted from these studies demonstrate confidence in these methodologies.

5 DESIGN AND ANALYSIS OF SUBSONIC STRIKE UCAVs

5.1 Introduction

Unmanned aircraft continue to expand their presence and relevance in the combat zone. It is therefore necessary to characterise the feasible operational limits imposed on certain classes of UCAVs, and while it may seem counterintuitive to evaluate subsonic strike configurations, this class of vehicles might have a vital role in the future of air combat, as stated by Stillion[193, chap.3], and as seen by the recent developments in unmanned *loyal wingmen* in various countries like the US, Australia and India[30,33,35].

As argued by Stillion, UCAVs need not follow the trends of the typical attributes of fighter aircraft, namely speed and manoeuvrability. To counter their limited performance, a combination of stealth, superiority by numbers, and advanced sensor and data fusion can counter advanced manned threats by enemy fighters, as envisioned in the joint operations depicted in Figure 5-1[193, chap.4]. This vision can be extended to ground strike aircraft, where UCAVs are likely to play significant roles in future S/DEAD missions.

This study explores the main performance trade-offs for subsonic, low-observable, tailless UCAV configurations that could potentially act as loyal wingmen and force multipliers to manned fighters. Low-observability design aspects are incorporated through shaping and system choices, but a more in-depth look at stealth needs to be carried out before drawing any conclusions. A typical Hi-Lo-Hi mission is evaluated for configurations of varying sweep angles and constant wing area; relevant mission parameters such as cruise Mach number, combat radius, and specific excess power (SEP) are varied in order to characterise the response space of such vehicles.
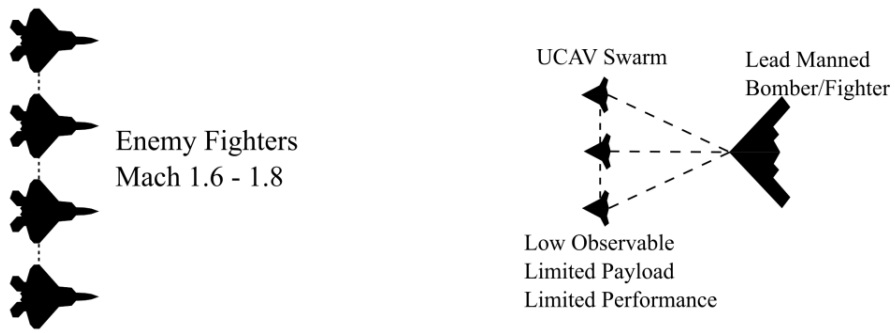
Figure 5-1 - Envisioned future aerial combat encounter

5.2 Mission Design

The mission profile follows a typical Hi-Lo-Hi ground strike, described by Figure 5-2, and the phases below. The minimum performance requirements are given in Table 5-1.

0-1	Warm up and take-off. Normal field performance is specified as <1500m
1-2	Minimum time to climb to cruise out Mach/Altitude
2-3	Cruise out segment (1440 km baseline)
3-4	Descent to ingress Mach/Altitude
4-5	Low altitude, high speed ingress (180 km at 0.8M/250m)
5-6	Payload delivery
6-7	Low altitude, high speed egress (180 km at 0.8M/250m)
7-8	Minimum time to climb to cruise Mach/Altitude
8-9	Cruise in segment (1440 km baseline)
9-10	Descent and land
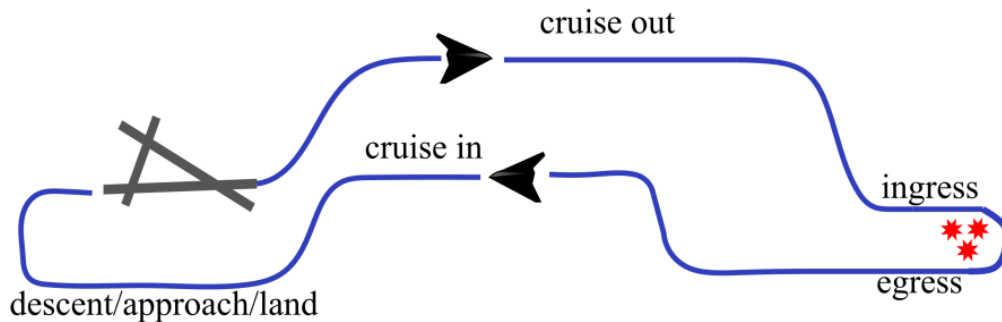
Figure 5-2 - Typical Hi-Lo-Hi strike mission diagram

Table 5-1 - Minimum performance requirements for subsonic ground strike

Payload	Internal 2xMk-84 JDAM ≈ 1850 kg
Field performance	Conventional take-off and landing ≤ 1500 m at SL
Specific Excess Power	≥ 60 m/s at 0.4M/1500 m
Instantaneous turn rate	20 deg/s at 0.7M/4500 m
Avionics mass	225 kg
Ferry Range	≥ 3000 km

5.3 Initial Assumptions and Baseline Design

In this study, the effects of operational and design constraints are evaluated through the selection of several UCAV configurations, with various leading edge sweep angles, for vehicles of constant wing area.

A straight leading edge lambda wing has been assumed due to its good aerodynamic efficiency and good compromise between its central length and span for easier systems integration[194]; carrier compatibility has not been considered during this study.

Figure 5-3 shows the baseline UCAV with a leading edge sweep angle of 57°, all internal engine and weapon bays, with a MTOM of 7822 kg, an OEM of 4845 kg, and a total fuel consumption of 1127 kg. The total vehicle length is 10.9 meters, with a wingspan of 12.8 meters, and wing area of 52.5 m^2. The sea level static thrust for the baseline configuration is 49.6 kN.

The major components have been sized and located through the mass estimation and packaging routines. The size and location of the weapon bays and the landing gear bays are a function of achieving acceptable CG locations and CG ranges, as well as acceptable maximum landing gear loads; interference checks between these components have also been carried out.

NACA63$_{a=1}$ aerofoils of varying thicknesses and a non-afterburning low bypass ratio turbofan engine have been assumed throughout this research. It is worth noting that for all trade studies, the engine bypass ratio, the fan and compressor pressure ratios, as well as the individual component efficiencies have been kept

constant, leaving only the overall engine diameter as the main thrust scaling factor.
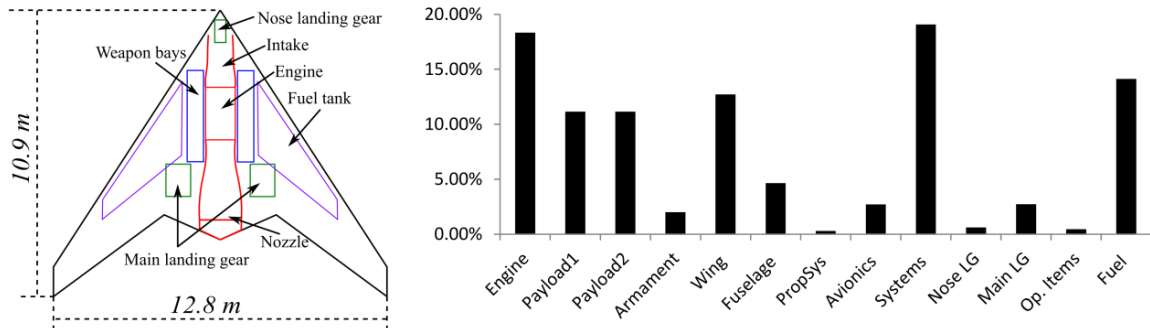
Figure 5-3 - Baseline UCAV design top view and mass breakdown

All results shown in the sections below have been obtained through an optimisation loop schematically shown in Figure 5-4. Packaging and stability constraints were checked in an external loop with relaxed constraints in order to reduce the complexity of the problem.
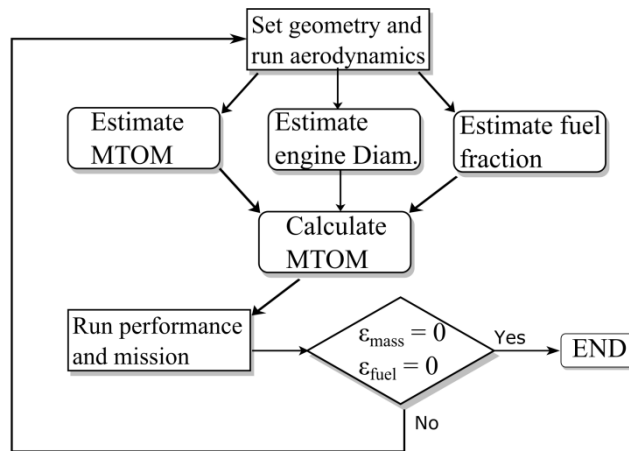
Figure 5-4 - Mass and fuel convergence loop

Due to the fact that detailed technical data is often not available in the open literature regarding UCAVs, additional work should be carried out in order to validate the results of the overall vehicle's masses, size, propulsion system characteristics, and general performance. The specific strategies required have been acknowledged as further work, and are mentioned in §9.2.

5.3.1 Leading Edge Sweep

The baseline mission requirements have been evaluated for configurations of varying leading edge sweep angles under constant wing area. Figure 5-5 (a) shows the take-off, empty, and fuel masses normalised with respect to the baseline configuration, as well as the normalised required sea level thrust. It can be seen that the masses and sea level thrust decrease as sweep increases, with a sharp increase in thrust for a leading edge sweep of 30°, which results in a large increase in fuel consumption. The total fuel consumption for a sweep angle of 65° shows a slight increase (+2.1 %) due to its very low aspect ratio (AR 1.9), resulting in an 18% reduction in aerodynamic efficiency during high altitude cruise segments when compared to the baseline.

The engine throttle settings for high-altitude cruise, low-altitude flight, and for the SEP requirement (0.4M/1500m) are shown in Figure 5-5 (b). It can be seen that for sweep angles higher than 30° the dominating constraint is SEP while at 30° sweep the engine is at full throttle during high-altitude cruise.

The drag build-up results shown in Figure 5-5 (c) and (d) for the high and low altitude cruise segments show that configurations with low sweep are dominated by induced drag at high altitudes (flown at max L/D, thus high C_L), while for sweep angles above 50°, the dominating drag component is the friction drag, with compressibility drag being practically negligible. During low-altitude, high-speed segments (low C_L) the induced drag is not relevant, while compressibility drag accounts for as much as 60% at low sweep values decreasing exponentially with respect to sweep. This behaviour is clearly seen in the Drag Divergence Mach number as a function of leading edge sweep angle shown in Figure 5-6.

The increase in fuel consumption at a leading sweep of 50° seen in Figure 5-5 (a) can be explained by the high-altitude cruise lift and drag coefficients (and thus L/D) shown in Figure 5-7, with an increase in cruise drag coefficient of 12% when compared to a sweep angle of 45°. Several attempts to reproduce this case have shown the same results which are not in line with the expected trends. The drag increment comes from an increase in induced drag and no significant reduction

127

in compressibility drag. Since the high-altitude cruise segments represent around 90% of the mission duration, this results in higher fuel consumption.
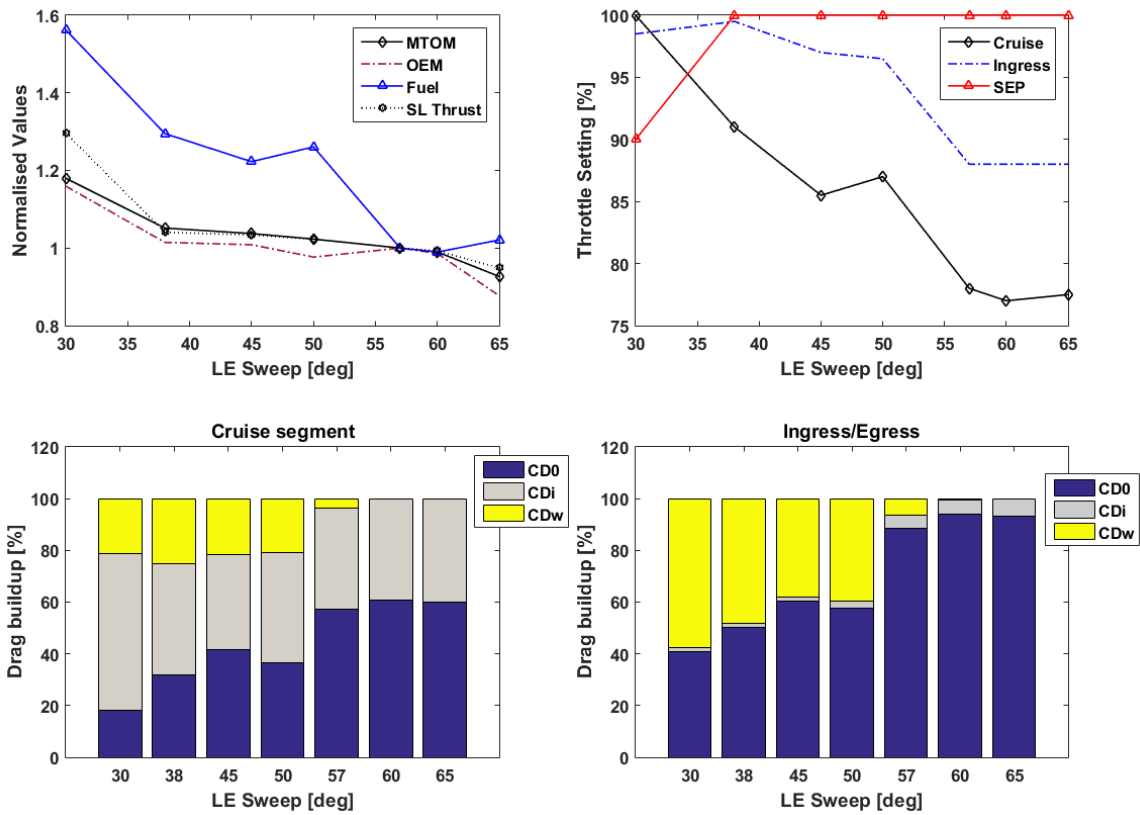
Figure 5-5 - Effects of leading edge sweep angle on gross, empty, and fuel masses, and drag build-up at cruise and ingress segments
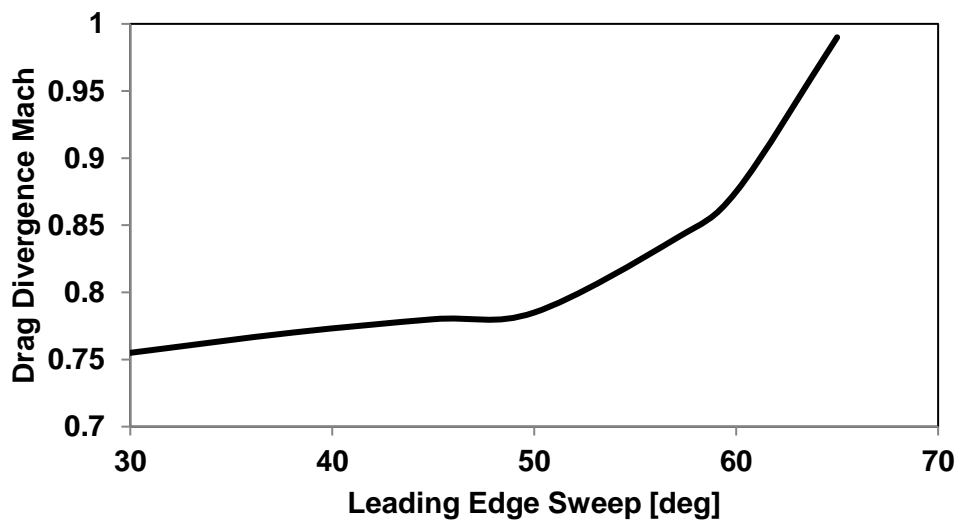
Figure 5-6 - Drag divergence Mach number vs leading sweep
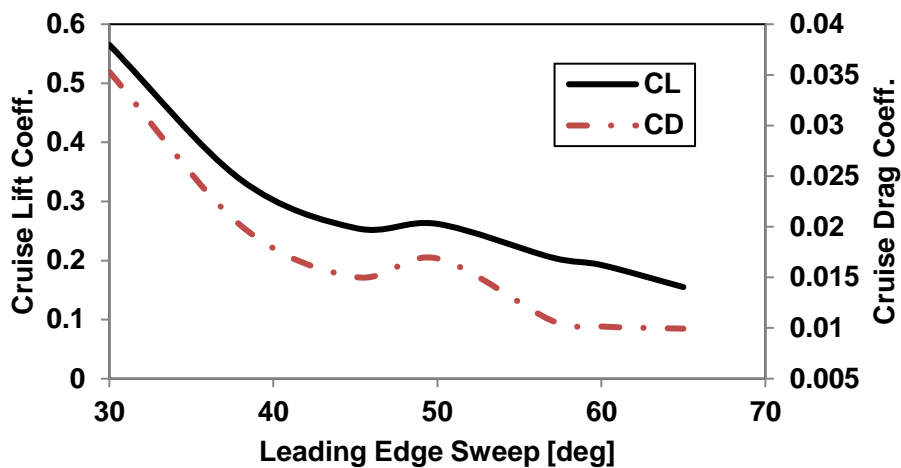
Figure 5-7 - Cruise lift and drag coefficients vs sweep

5.3.2 Cruise Mach number

Changes in high-altitude cruise Mach number have been investigated for all configurations for Mach numbers of 0.6 up to 0.9, while holding the rest of the requirements constant. Take-off, empty, and fuel masses, as well as sea level thrust values are shown in Figure 5-8 normalised with respect to the baseline configuration. No significant variations in all results are observed at Mach numbers below 0.8 for all sweep angles. This is due to the performance constraints imposed by the unchanged SEP requirements. At higher Mach numbers, mass and engine size growth clearly show exponential behaviour, and this trend is especially marked for configurations with sweep angles below 50°, for which no realistic solutions were found for Mach 0.9 due to prohibitively large engine sizes and fuel volume constraints. Results also show that the 65° sweep configuration remains unaffected by Mach number well into the transonic regime, thanks to the delay of compressibility drag shown before.

The achieved SEP values at 0.4M/1500m for all cruise Mach numbers and sweep angles are given by the shaded surface and the values in the colour bar in Figure 5-9, while the maximum throttle settings (%) during any of the cruise segments are given by the superimposed labelled contour lines. The areas shaded corresponding to the minimum SEP requirement value (60 m/s, dark blue), and where the throttle values are less than 100%, represent the design space dominated by the SEP requirement. Conversely, the areas showing achieved

SEP values larger than the required minimum and throttle settings close to or 100% are dominated by increases in thrust demands due to compressibility effects. As mentioned previously, no solutions were obtained for sweep angles below 50° at Mach number above 0.85 due to marked increases in engine diameter and total fuel consumption.
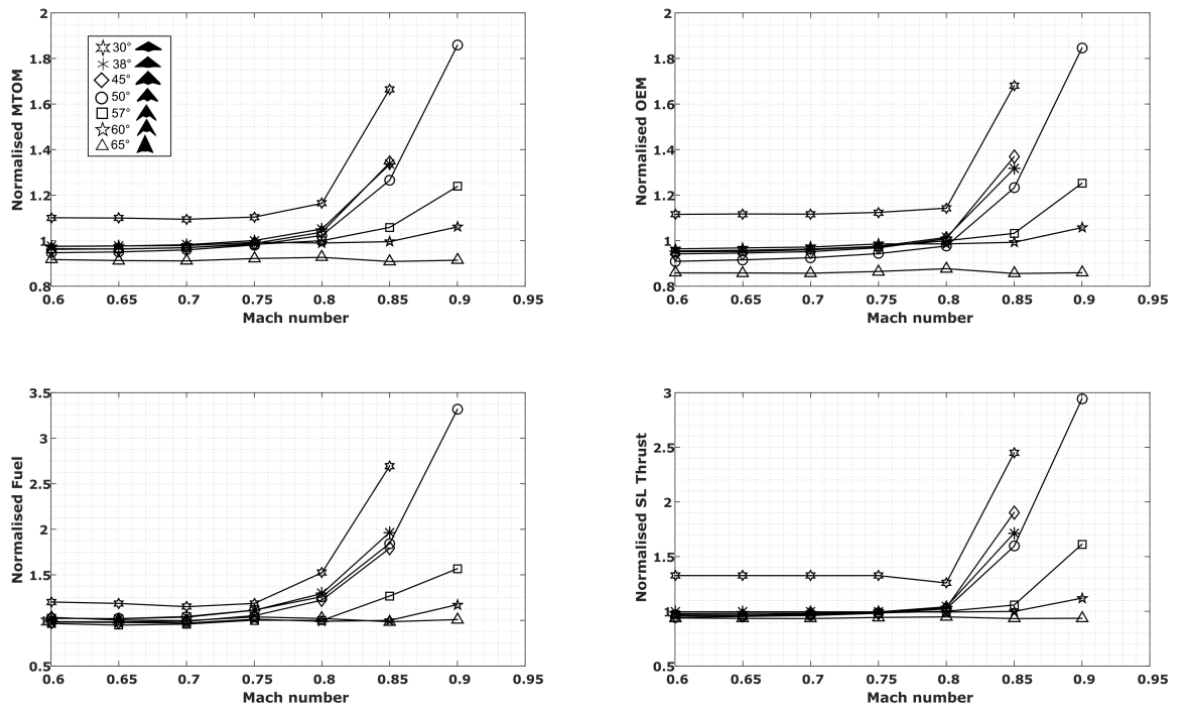
Figure 5-8 - Effect of cruise Mach number on vehicle's masses and engine sizing

Figure 5-10 shows the estimated Mach number at which the dominating constraint transitions from the SEP requirement to high or low altitude cruise thrust requirements.

5.3.3 Combat Radius

The effects of changes in combat radius have been investigated for all configurations up to a normalised combat radius value of 2.0 at a constant cruise Mach number of 0.8. Results in Figure 5-11 are shown normalised with respect to the baseline UCAV configuration.

Changes in take-off, empty, and fuel masses, as well as sea level thrust do not show a strong dependence on sweep angle. The overall mass growth responds to the initial fuel increase due to increased range, which prompts a slight increase

in engine size in order to comply with the SEP requirement, leading to increases in empty and take-off mass until a convergent solution is obtained. This trend is evidenced by the sea level thrust increase for a 30° sweep. This configuration achieved a higher SEP than the requirement, so engine growth is not observed before a 40% increase in combat radius.
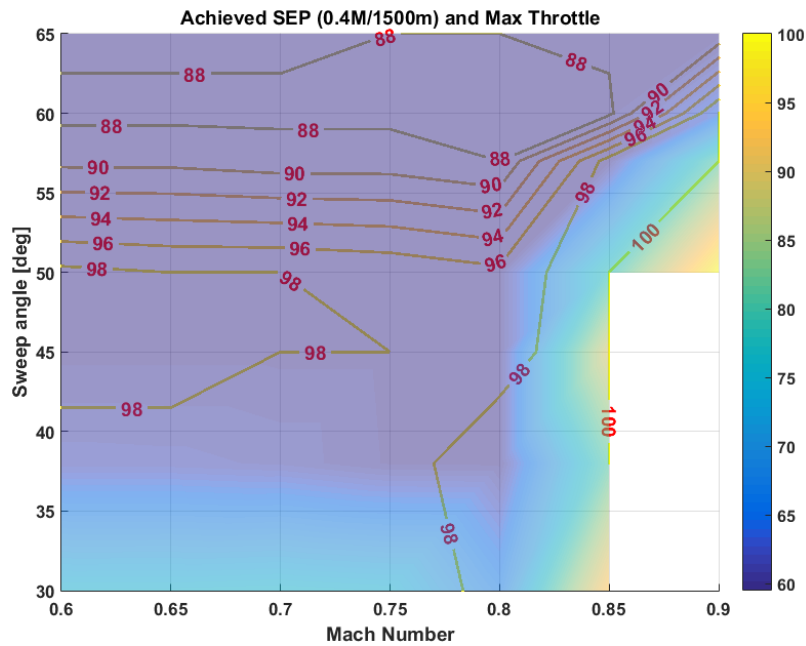
Figure 5-9 - Achieved SEP and maximum throttle for cruise Mach numbers
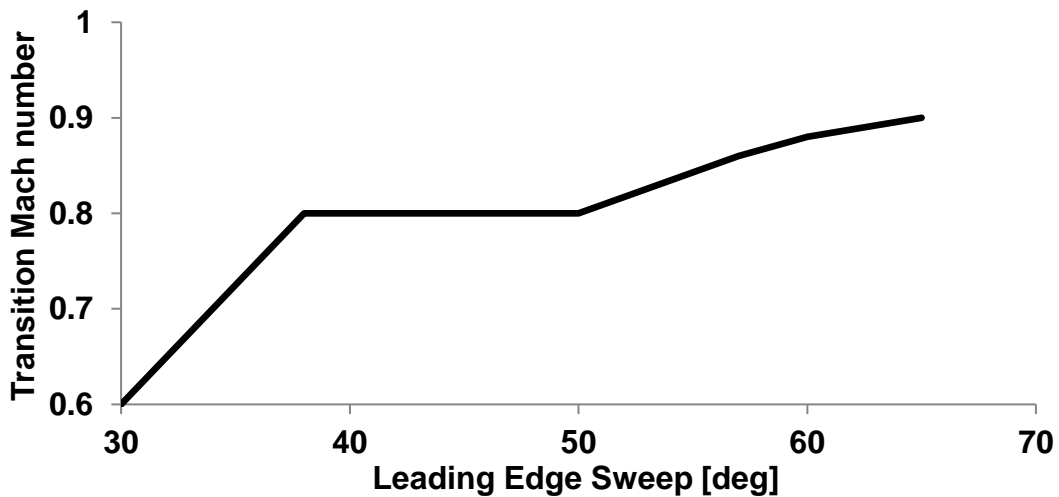
Figure 5-10 - Mach number at which the dominating constraint transitions from SEP to thrust requirements
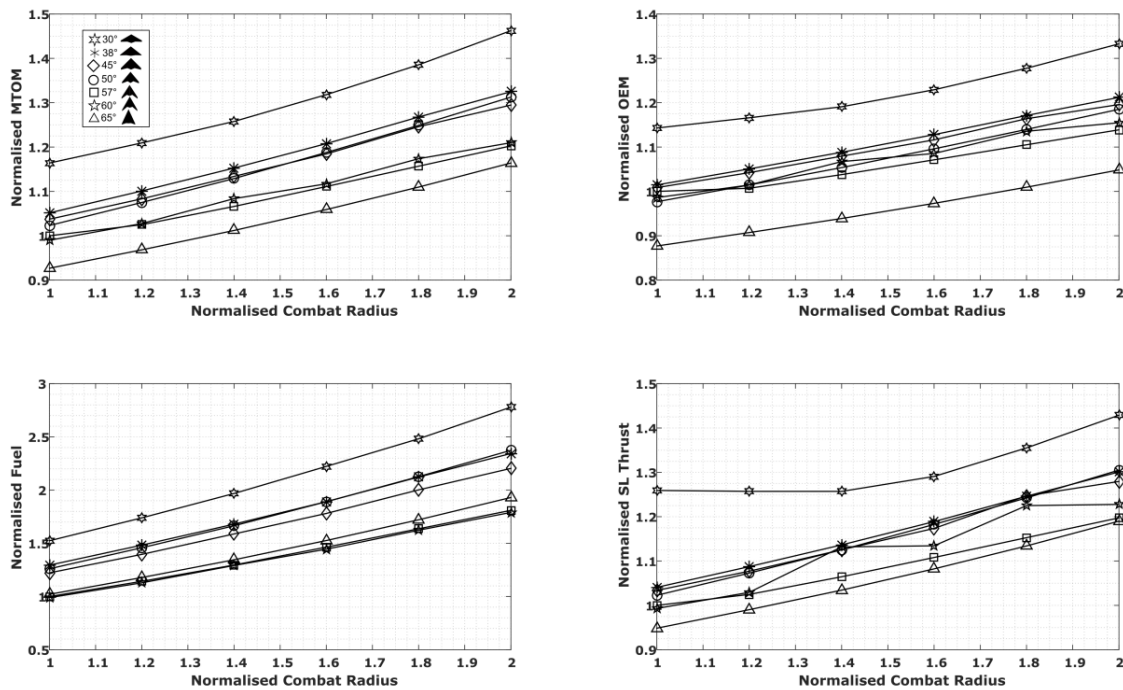
Figure 5-11 - Effect of combat radius on vehicle masses and engine sizing

5.3.4 Specific Excess Power

The results obtained thus far highlight the importance of specific excess power and its effect on the overall sizing of the configurations. Four configurations have been selected for investigating the effect of increasing SEP while maintaining the rest of the mission profile constant. Results shown in Figure 5-12 have been normalised with respect to each configuration's baseline results for clarity. It can be seen that an increase in SEP from 60 m/s to 100 m/s at 0.4M/1500m results in a sea level thrust increase between 90% and 100%, an increase in take-off mass of nearly 25%, an empty mass increase of approximately 35%, and a fuel consumption increase of 15%. Furthermore, the mass fraction of the engine increases from approximately 16% up to a value of 25%.
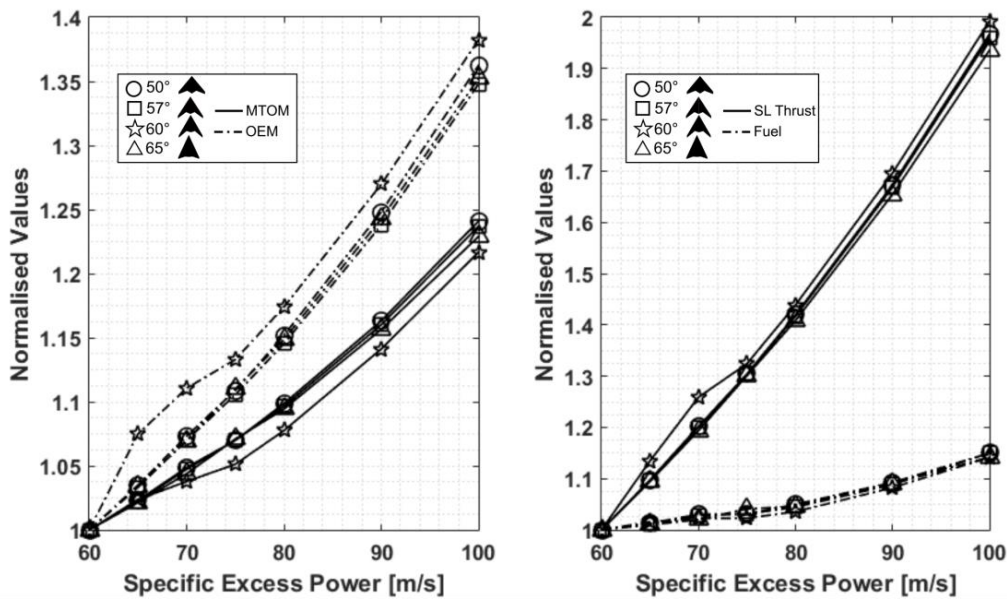
Figure 5-12 - Specific Excess Power requirement (at 0.4M/1500 m) effect on vehicle gross mass

5.3.5 Radar Cross Section

Finally, RCS results for clean configurations assuming the use of perfect electric conductor materials at a frequency corresponding to the S band (3 GHz), shown in Figure 5-13, also benefit the higher sweep configurations, especially for the range $\phi = [-30°, 30°]$. Results from the tail aspect ($\phi = 180°$) show no significant variation with respect to sweep.

These results can only represent a top-level indication of which configurations might outperform the rest, and a more detailed study including careful material choices, internal structural and systems arrangements, as well as a detailed inlet and exhaust geometries is required in order to draw any significant conclusions in terms of stealth.
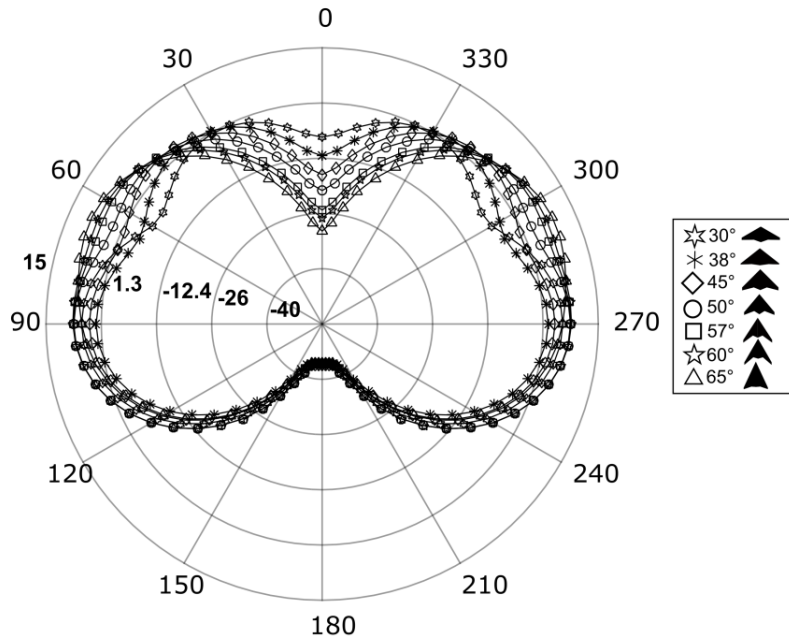
Figure 5-13 - RCS (PEC), S band (3 GHz), θ = 90° ϕ = [0°, 360°]

5.3.6 Cost

Variations in cost have been investigated through the basic RDT&E cost estimation model detailed in §4.12. Figure 5-14 shows the cost per aircraft (CPA) as a function of production number over a five year period, and CPA against normalised combat radius for a fixed production number. It can be seen that CPA decreases exponentially with respect to production number, as can be expected. Furthermore, it can be seen that CPA follows closely the engine growth trends reported for increases in combat radius (Figure 5-11).
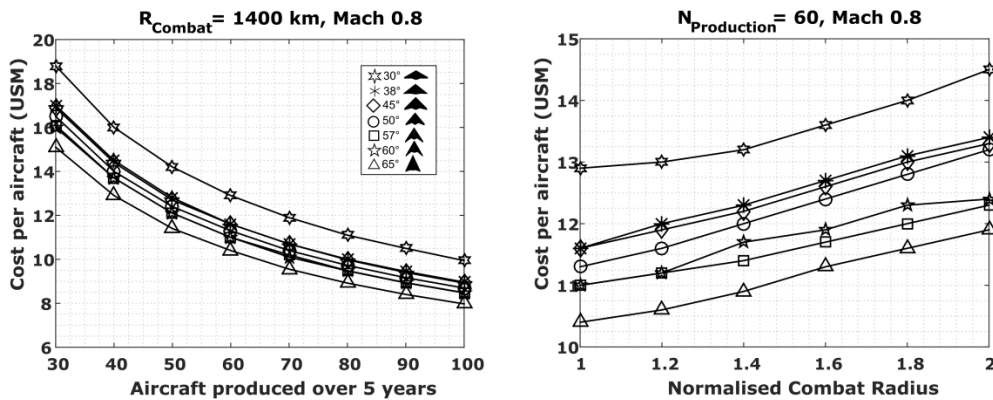
Figure 5-14 - Cost per aircraft against production number and combat radius

On closer examination, the cost of the aircraft has a higher correlation factor with the maximum take-off mass, when compared to the sea level thrust or the empty mass, as shown in Figure 5-15. More complete cost estimation methods that account for modern systems such as the cost of software development should be explored in the future.
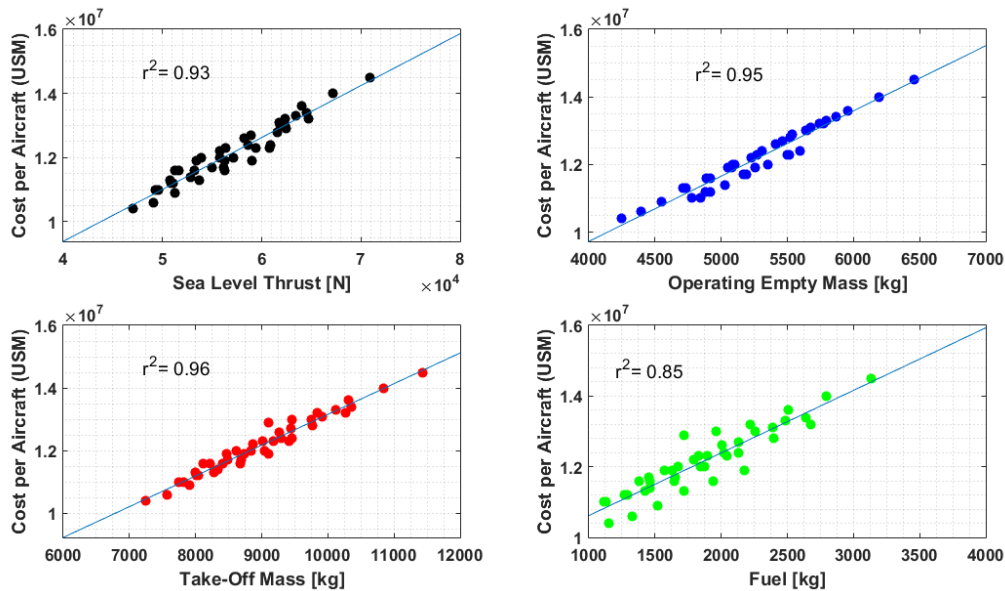
Figure 5-15 - Correlation between various parameters and cost per aircraft

5.3.7 Ferry Range

The ferry range requirement of at least 3000 km has been verified for all configurations. This mission can be flown at the most efficient Mach number and altitude. For a flight altitude of 12.2 km, all configurations can comply with the ferry range requirement, as shown by the contour lines in Figure 5-16.

5.4 Study summary

This study has introduced the importance of unmanned aerial vehicles in the future concept of aerial warfare, and their possible roles as force multipliers and 'loyal wingmen' in highly dynamic environments strongly influenced by the transformational challenges of fifth generation technologies.
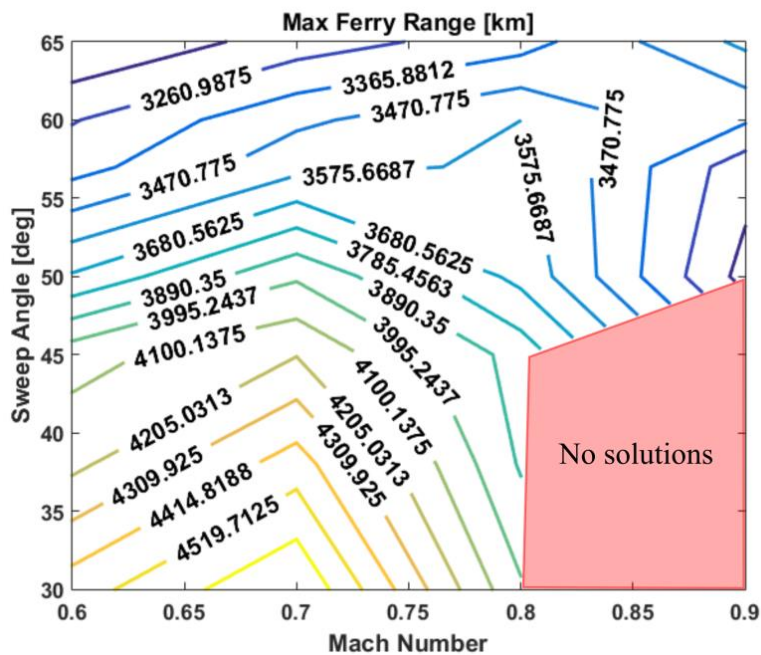
Figure 5-16 - Max ferry range contour at H = 12.2 km

A series of mission trade-off studies have been carried out for low-observable, tailless UCAVs performing subsonic Hi-Lo-Hi strike missions. A baseline lambda-wing UCAV configuration was designed through the GENUS framework. Subsequently, variations in leading edge sweep were investigated, from low sweep values (30°) to very high sweep angles (65°).

Results show that take-off, empty, and fuel masses decrease as sweep angle increases, mainly due to the delay of compressibility effects, and this reflects on the drag build-up at high and low altitude cruise segments. Furthermore, by investigating the effect of high-altitude cruise Mach number, it has been shown that the specific excess power requirement is the main engine sizing constraint even at high sweep angles, with an isolated case of low-altitude cruise thrust requirement as the sizing constraint for a sweep angle of 30°.

For the same reason, no significant mass reductions were observed for cruising at reduced Mach numbers while holding specific excess power requirements consistent with high speed ground strike and S/DEAD missions. The high increases in sea level thrust, take-off, empty, and fuel masses as a function of increasing specific excess power to levels equivalent to air combat missions

136

support the importance of this particular performance requirement and a well-balanced mission design.

Changes in the vehicle's characteristics with increases in combat radius do not show a strong dependence on leading edge sweep angle. The mass growth mechanism for increases in range behaves as follows: a mass increment due to the higher fuel consumption leads to an increase in engine size in order to comply with the specific excess power requirement, which leads to an increase in empty and take-off masses. This in turn leads to a new increase in fuel and the loop repeats until a convergent solution is found.

Top level RCS signatures also show favourable results for higher leading edge sweep angles, especially from a nose-on view range of [-30°, 30°], with no real variations of results from the tail-on aspect.

Initial results from the RDT&E cost study showed a close relationship between the sea level thrust and the cost per aircraft, as seen by the thrust requirement trends plotted against combat radius. Further analysis shows a higher cost correlation to the gross vehicle mass and the empty mass, compared to the sea level thrust. A more complete cost model is recommended to explore the effects of advanced software, and its offset on the cost correlations.

This study has been published under the title *"Impact of mission requirements on the design of low-observable UCAV configurations"* by Aircraft Engineering and Aerospace Technology (2019)[191].

6 FIFTH GENERATION UCAV DESIGN

6.1 Introduction

This chapter will introduce a potential mission, the conceptual and preliminary design efforts towards establishing a *5th generation UCAV* configuration. The main characteristics of such a platform are the capability to engage in strike and limited air combat, as well as enhancing the situational awareness in joint operations through a suite of advanced sensors and data fusion algorithms.

Similarly to Boeing's *Airpower Teaming System* loyal wingman UCAV, the expected performance of a 5th generation UCAV can be assumed to partially match that of current 5th generation multirole aircraft such as the F-35A.

6.2 Mission Design

This mission combines Hi-Lo-Hi ground strike requirements with limited air combat requirements and supersonic capabilities adapted from a generic air superiority mission[195, sect.1.11]. The mission is described by the following phases:

0-1	Warm up and take-off. Normal field performance is specified as <1500m
1-2	Minimum time to climb to cruise out Mach/Altitude
2-3	Cruise out segment at 0.8M/12km (1090 km baseline)
3-4	Descent to ingress Mach/Altitude
4-5	Low altitude, high speed ingress (80 km at 0.9M/250m)
5-6	Ground strike payload delivery
6-7	Low altitude, high speed egress (80 km at 0.9M/250m)
7-8	Minimum time to climb to supersonic cruise Mach/Altitude
8-9	Supersonic dash (50 km) segment at 1.5M/9.5km, sustained supersonic turn and release of air-to-air payload
9-10	Climb to subsonic cruise Mach/Altitude
10-11	Cruise in segment at 0.8M/12km (1040 km baseline)
11-12	Descent and land
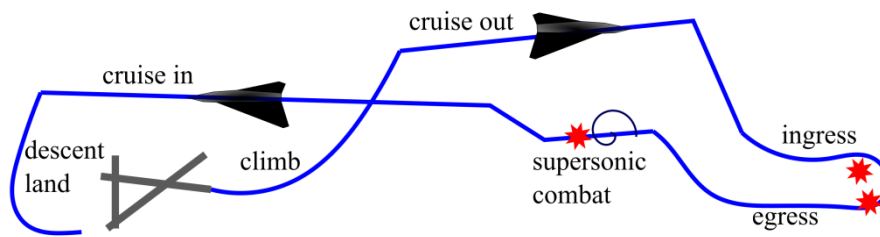
Figure 6-1 - 5th generation UCAV mission diagram

The minimum performance requirements are given in Table 6-1.

Table 6-1 – Minimum performance requirements for 5th generation UCAV

Payload	Fully Internal, 2 air-to-surface + 2 air-to-air, ~2030 kg
Field performance	Conventional take-off and landing ≤ 1500 m at SL
Ceiling	Above 15 km
Supercruise	1.5M/9.5 km
Maximum Speed	1.6M/9.5 km
Instantaneous turn	+7.5, 0.75M/4500 m
SEP (1g)	120 m/s, 0.8M/4.5 km, 50% fuel, 180 kg payload
Acceleration	Mach 0.8 to 1.2 in < 60 seconds, 9.5 km, max power
Sustained Turn	+5g at 1.5M/9.5 km, 25% fuel, 180 kg payload
Avionics	Advanced sensor package, 300 kg allowance
Stealth	Very low signature, 200 kg allowance

6.3 Initial Design Assumptions

Continuing with the choice of very low-observable designs, this concept will be based on a tailless aircraft with all internal weapon bays, a central buried engine, and a choice of low-observable intake and exhaust design. The weapon bay arrangement will follow the size and general arrangement of the F-35 JSF in stealth mode, as shown in Figure 6-2; payload flexibility studies will be considered in future design iterations.
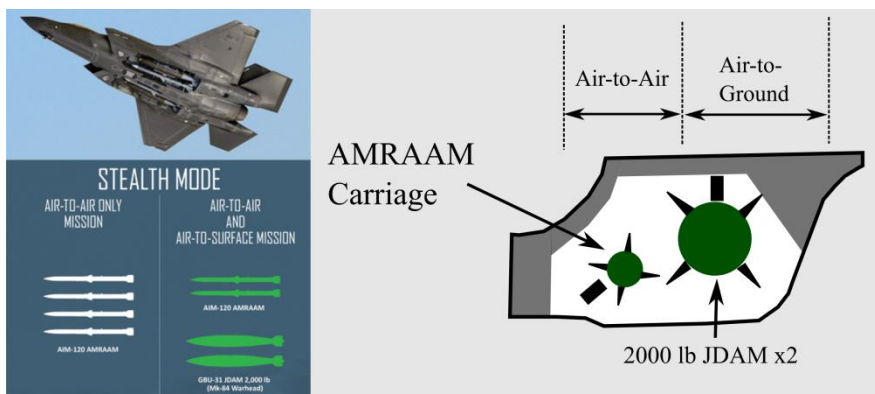
Figure 6-2 - Weapon bay arrangement in F35 stealth mode (Source: f35.com)

An initial parametric analysis has been carried out with low-fidelity tools and estimates in order to obtain wing and thrust loadings. The initial design point is shown in Figure 6-3 along some subsonic UCAVs and the F-35A, with a wing loading 3470 N/m^2 and a thrust loading 0.71. The take-off mass has been estimated as ~18000 kg, resulting in a wing area of 50.5 m^2 and a sea level thrust of 125 kN.
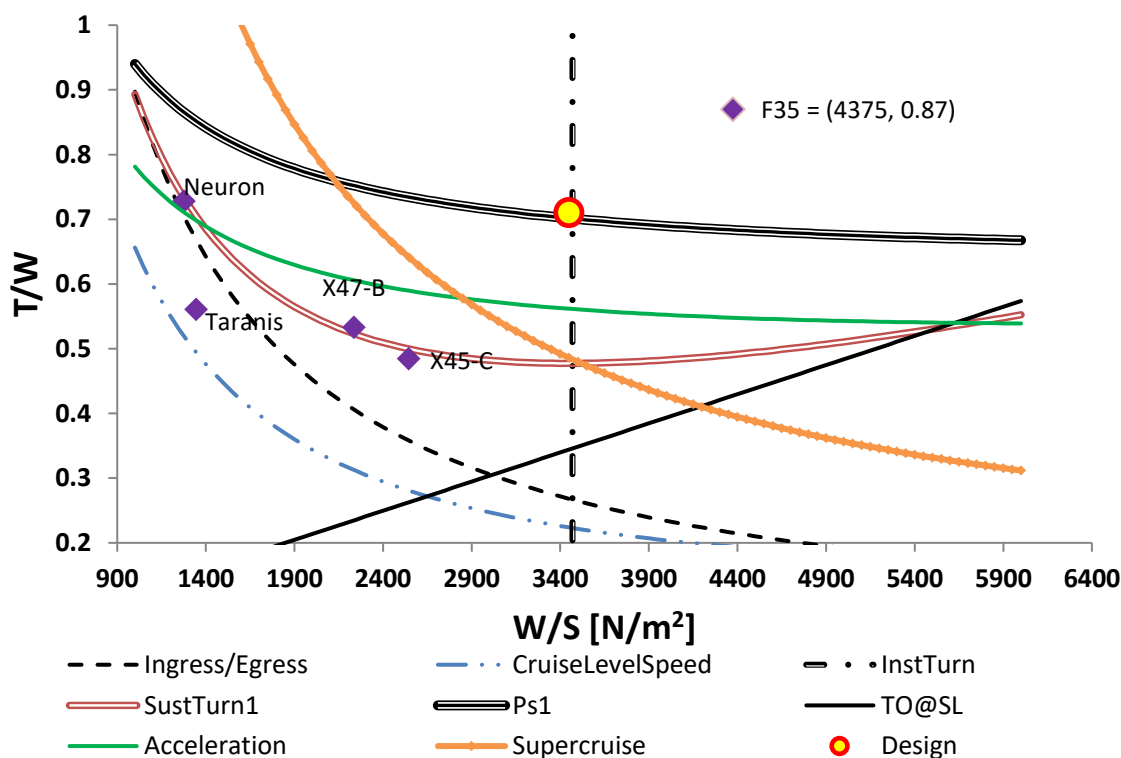
Figure 6-3 - Initial parametric analysis for 5th gen. UCAV

A double delta configuration has been selected as the baseline geometry. The central wing section will act as a fuselage-type component housing the engine, avionics, weapon bays, and landing gears for the most part, while the outer wing will contain the fuel. A simple top-view schematic of a packaged configuration as well as a size comparison against and F-35A is shown in Figure 6-4.

A high sweep angle at the central wing section (fixed at 72°) allows for a longer configuration which will reduce supersonic wave drag and allow for a better integration of the intake and other systems. The minimum sweep angle at the outer wing for maintaining subsonic leading edges through the entire geometry has been calculated as 48°. However, as seen by previous studies, the effects of subsonic wave drag are reduced by increasing sweep angle and higher sweeps will be investigated.
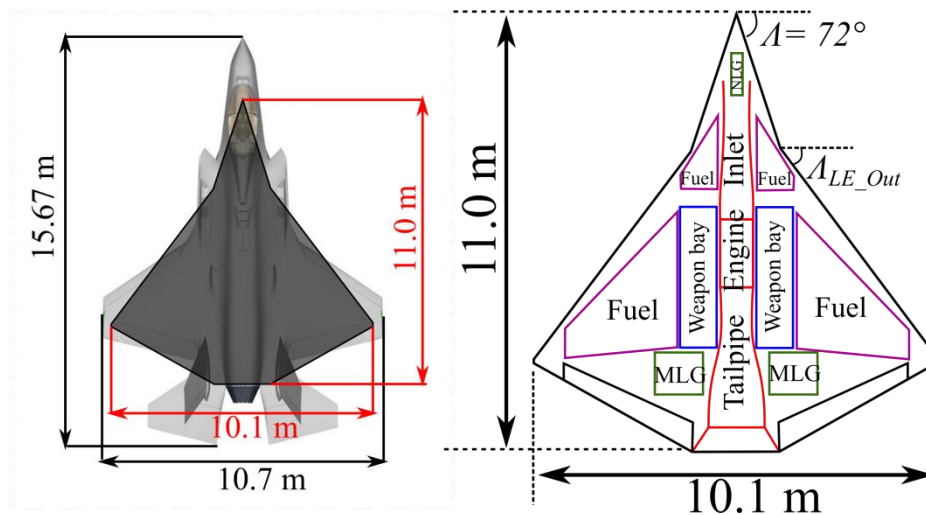
Figure 6-4 – Top view schematic of a 5th generation UCAV

A simple afterburning turbojet engine has been initially selected; NACA 63 aerofoils of varying thicknesses have been assumed for the outer wing, while a modified biconvex aerofoil of 10% thickness has been assumed for the central aerofoil, with a linear interpolation in between central and outer wing.

6.4 Design Trade-off Studies

The initial take-off mass estimate of 18000 kg has been challenged through a set of initial geometries and trade studies for outer wing sweep angles and aerofoil thickness-to-chord ratios; the initial results show that significantly lower take-off

masses, in the range of 10000 to 13000 kg can be obtained. The initial design trade studies shown in the following sections have been obtained through a convergence loop using the gradient-based optimiser. The geometry and aerodynamics are fixed, and the optimiser has been used to find the right value of take-off mass, fuel mass, and engine size.

The outer wing leading edge sweep angle and thickness-to-chord ratio trade studies show potential minima close to a leading edge sweep of 60° and very low thickness ratios of approximately 4-5%, as shown by the contour lines in Figure 6-5. The red bars in the figures indicate the actual GENUS data while the rest of the response data have been extrapolated with polynomial response functions for masses as a function of sweep and thickness ratio respectively, so that the masses are given in function form as:

$$m_i = f(\Lambda_{LE}) \cdot g\left(\frac{t}{c}\right)_i \tag{6-1}$$
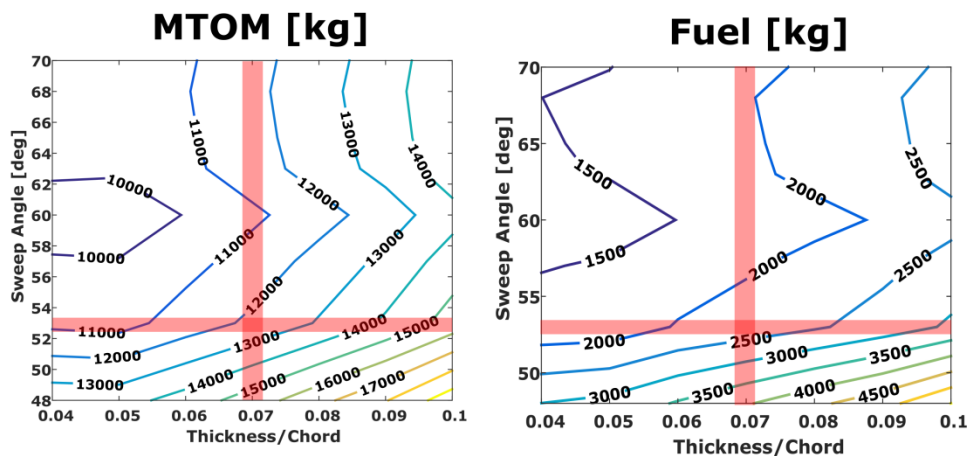
Figure 6-5 - Take-off and fuel mass response contours as a function of outer wing sweep and thickness ratio

Figure 6-6 shows the volumetric fuel constraint as a function of thickness ratios for a fixed sweep angle. The fuel volume constraint has been calculated for the available fuel volume in the outer wing, after the wing kink and the outer edge of the weapon bays. As can be seen in Figure 6-6, sufficient fuel volume exists for aerofoils with a thickness ratio of 5%, increasing with thickness ratio with a maximum fuel surplus for aerofoils with 8% thickness ratio. Increasing the thickness of the aerofoil further leads to large increases in drag, especially for the

transconic and supersonic segments, leading to an engine size increase and higher fuel consumption.

Due to the already existing packaging challenges for a tailless configuration, and added to the high loading factors, a minimum thickness-to-chord ratio of 7% has been chosen for sufficient structural depth and acceptable fuel volume allowance. Future design iterations might challenge this value through performance considerations, aerodynamic improvements, and actuator packaging issues.
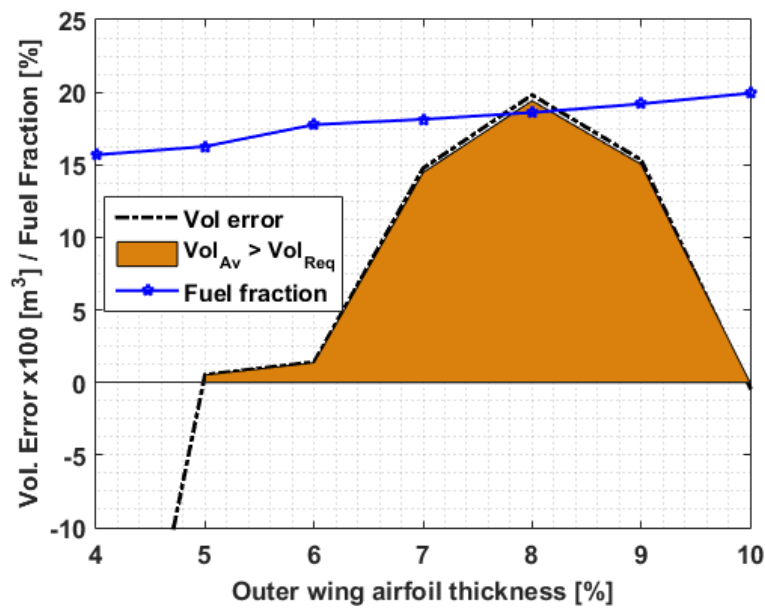
Figure 6-6 - Wing fuel tank volume constraint vs thickness ratio

The effect of outer wing dihedral (or anhedral) has been investigated for a range of $\Gamma_{Out} = [-5°, 5°]$. No noticeable effects were observed for take-off, empty, or fuel masses, aerodynamic efficiency at cruise Mach number or sea level thrust.

6.4.1 Aerofoil Selection

Due to the combination of long subsonic segments, short supersonic segments, and performance requirements equivalent to those of combat aircraft, subsonic, transonic, and fully supersonic aerofoils have been investigated and their effects quantified. These studies were carried at a fixed outer wing sweep and thickness-to-chord ratio of 7% (except for the supercritical aerofoil with a 6% thickness ratio).

The results for the fuel consumption during each mission segment are shown in Figure 6-7. As can be expected, typical subsonic aerofoils (NACA4 and NACA5) show the highest fuel consumption, followed by a transonic NACA6 aerofoil and the fully supersonic biconvex aerofoil. The lowest fuel consumption is achieved by a supercritical aerofoil SC(2)-0406, with lift coefficient 0.4 and thickness ratio of 6%. Fuel increments compared to the SC(2)-0406 aerofoil are shown in Figure 6-8.
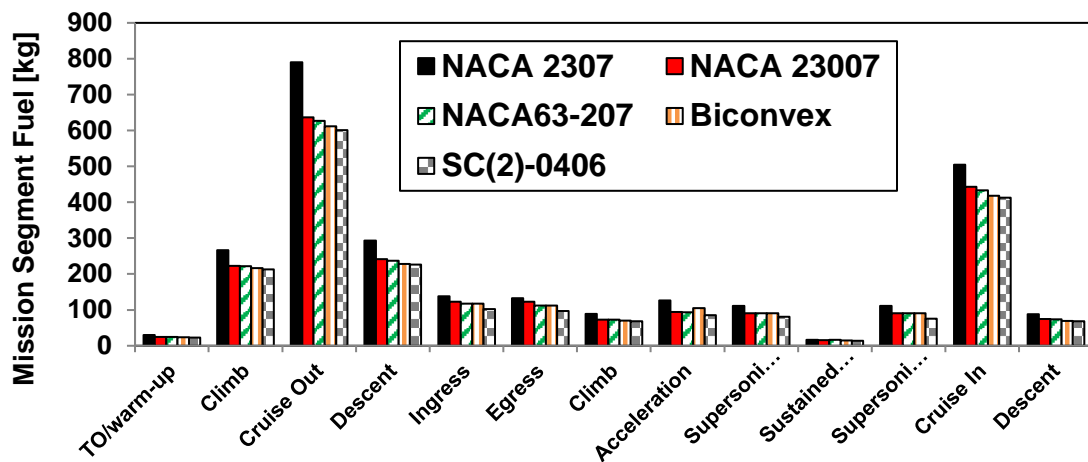
Figure 6-7 - Mission fuel consumption for various aerofoils
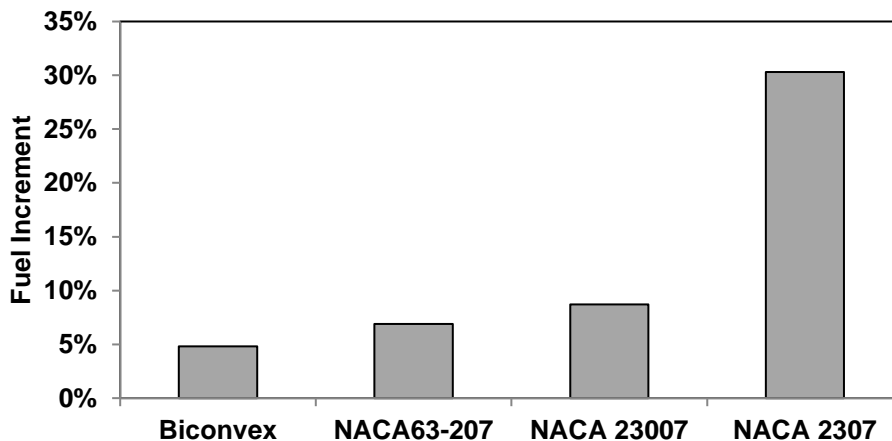
Figure 6-8 - Fuel increment as a function of outer wing aerofoil

The drag polar for all aerofoils at high subsonic, transonic, and supersonic speeds are shown in Figure 6-9; these results are the output from PANAIR aerodynamics, complemented with friction and wave drag methods in GENUS. It can be seen that at Mach 0.8 and low lift coefficients, there is no significant difference in drag coefficient, however at large lift coefficients the NACA4 aerofoil shows a large

144

drag increase. At transonic speeds, the most noticeable effect is the elimination of compressibility drag thanks to the supercritical aerofoil, resulting in a very marked drag reduction; the NACA6 and Biconvex aerofoils perform better than NACA4 and NACA5 aerofoils. The most striking result is the supercritical aerofoil outperforming the biconvex aerofoil at Mach 1.5 and lift coefficients less than 0.15.

In summary, for a fixed sweep angle, the supercritical aerofoil outperforms all other choices and results in a configuration with a gross mass reduction of 5%, and a total fuel consumption reduction of 6.9% compared to the baseline NACA6 aerofoil.
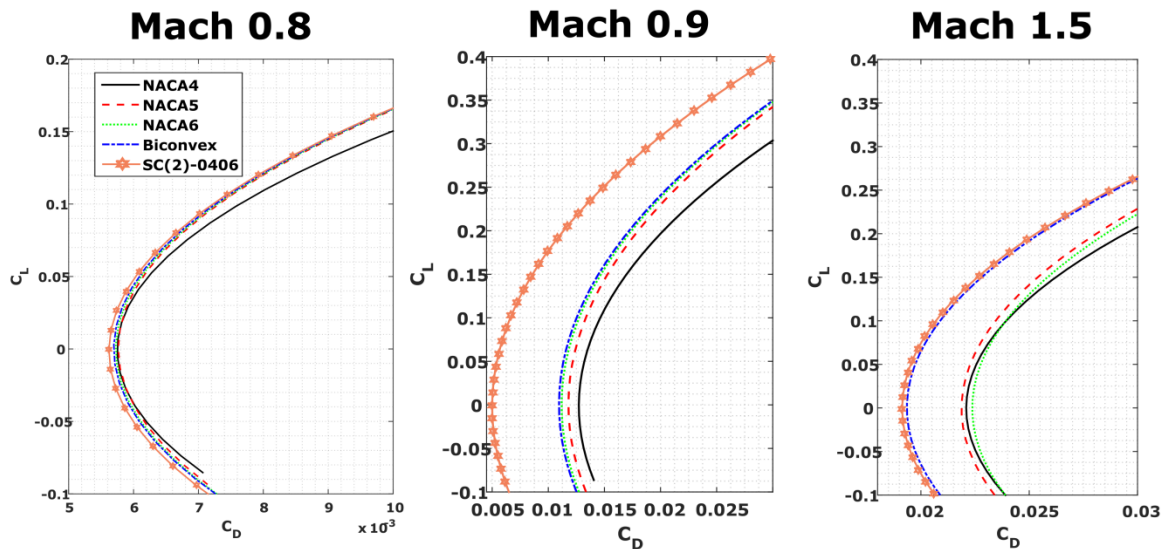
Figure 6-9 - Drag polar at subsonic, transonic, and supersonic speeds

6.4.2 Engine Bypass Ratio

The original turbojet engine choice has been challenged by investigating the effect of bypass ratio for afterburning turbofans. This choice will impact many aspects of the design like fuel consumption, systems integration, cost, and low-observability through the infrared signature.

The results shown in Figure 6-10 have been normalised against the afterburning turbojet (bypass ratio 0) data for a fixed sweep and thickness ratio. As shown by Figure 6-10 (a), no significant fuel mass reductions are achieved with bypass ratios below 0.5; the minimum fuel was achieved at a bypass ratio of 0.7 with a

fuel decrease of 7.5%. Despite the fuel savings, the increase in engine and propulsion system mass results in overall heavier design solutions, as shown by the engine mass fraction as a function of bypass ratio in Figure 6-10 (b).
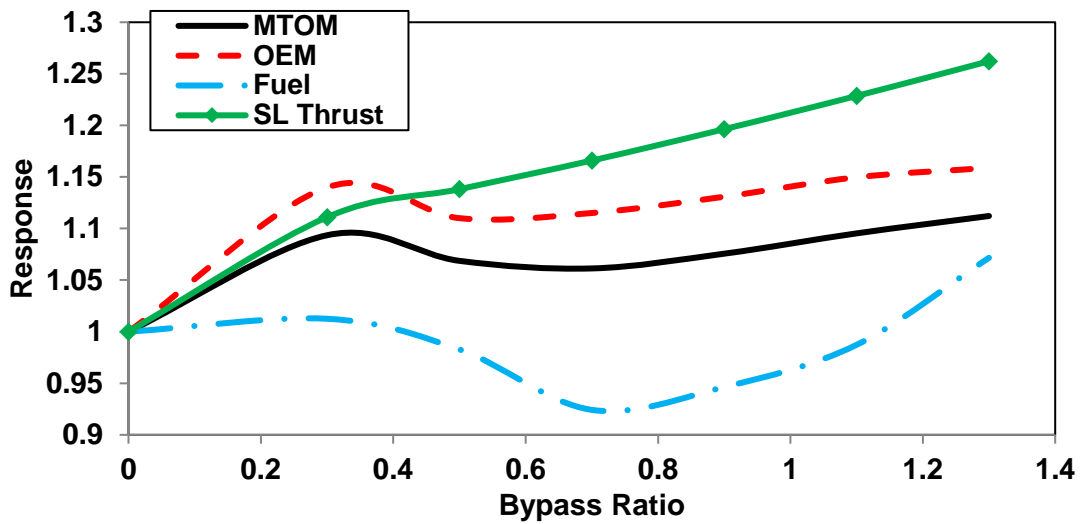
a) Changes in take-off, empty, and fuel masses, and SL thrust
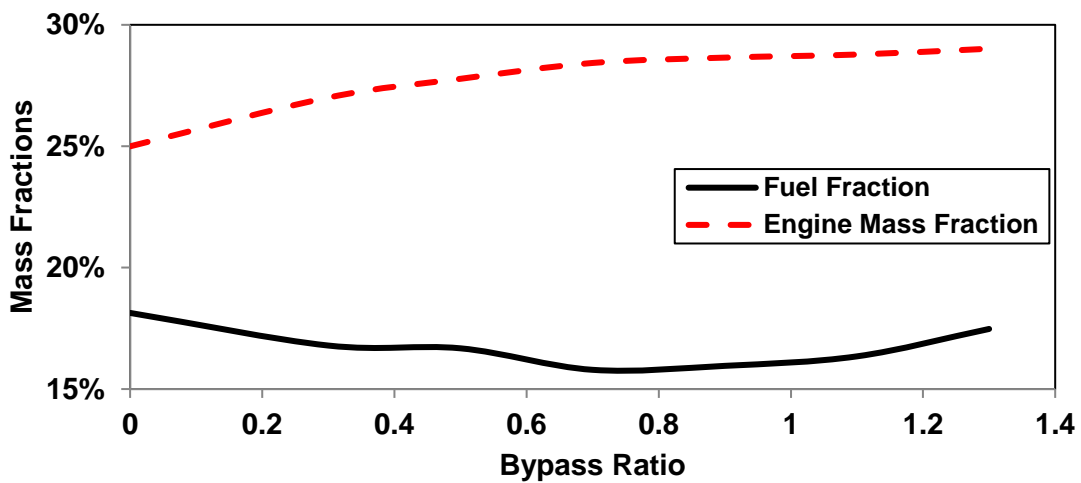
b) Fuel and engine mass fractions with bypass ratio

Figure 6-10 - Effect of engine bypass ratio

For the baseline concept a simple afterburning turbojet has been found to provide the lightest solutions. This choice also offers the lowest RDT&E cost, as it has been shown to be highly dependent on engine mass and thrust requirements.

The higher exhaust temperatures produced by an afterburning turbojet, and the corresponding increase in infrared signatures, can be offset by the design of a

high aspect ratio exhaust, careful material selection and geometric masking of the hot structural components.

6.5 Multivariate Optimisation

The GENUS genetic and gradient-based optimisers have been used in hybrid mode to converge on a low mass solution through multivariate optimisation, having chosen several design characteristics such as outer wing aerofoil, thickness-to-chord ratio, and engine type and bypass ratio.

The optimisation problem is formally defined as follows:

$$\text{minimise: } f(\bar{x}) = MTOM \tag{6-2}$$

Where the input variable vector is defined as:

$$\bar{x} = (\Lambda_{LE\,Outer}, b_{Outer}, C_{Root}, \lambda_{Outer}, Fuel_{frac}, D_{Eng}) \tag{6-3}$$

Subject to:

$$h_0(\bar{x}) = \frac{|MTOM_{Calc} - MTOM_{Est}|}{MTOM_{Est}} = 0 \tag{6-4}$$

$$h_1(\bar{x}) = \frac{|Fuel_{Calc} - Fuel_{Est}|}{Fuel_{Est}} = 0 \tag{6-5}$$

$$g_0(\bar{x}) = \frac{V_{fuel\,Req} - V_{fuel\,Av}}{V_{fuel\,Req}} \leq 0 \tag{6-6}$$

$$g_1(\bar{x}) = t_{Accel\,Ach} - t_{Accel\,Req} \leq 0 \tag{6-7}$$

$$g_2(\bar{x}) = SEP_{Req} - SEP_{Ach} \leq 0 \tag{6-8}$$

$$g_3(\bar{x}) = T_{SusTurn\,Req} - T_{SusTurn\,Av} \leq 0 \tag{6-9}$$

$$g_4(\bar{x}) = T_{Cruise\,Req} - T_{Cruise\,Av} \leq 0 \tag{6-10}$$

Additionally, the internal components' longitudinal and lateral positions have been checked for clashes, and acceptable CG margins for achieving a longitudinal static margin at all flight conditions within the range $K_n = [-15\%, 15\%]$.

The upper and lower bounds of the input variables are specified in Table 6-2.

Table 6-2 - Input variables bounds for multivariate optimisation

Input Variable	Lower Bound	Upper Bound
Outer wing sweep $\Lambda_{LE_{Outer}}$ [deg]	45	70
Outer wing span b_{Outer} [m]	2.9	4.0
Root Chord C_{Root} [m]	10.5	12
Outer taper ratio $\lambda_{Outer} = C_{Kink}/C_{Out}$ [-]	0.01	0.4
Fuel fraction [%]	15	40
Engine diameter D_{Eng} [m]	0.5	1.2
Component positions	Component dependent	

The evolutionary histories for all input variables as well as the take-off mass error, fuel volume error and fuel mass error are shown in the form of parallel coordinates in Figure 6-11. It can be seen that after only 10 generations all variables have mostly converged to their final values. Little variation is observed between Generations 10 and 20, and whatever difference there exists is due to the random mutations inherent to the genetic algorithm. The input variable values after genetic optimisation are given in Table 6-3.

Table 6-3 - Input variables after genetic optimisation

Input Variable	Final Value
Estimated Take-off mass $M_{0_{Est}}$ [kg]	11861.6
Outer wing sweep $\Lambda_{LE_{Outer}}$ [deg]	60.61
Outer wing span b_{Outer} [m]	3.88
Root Chord C_{Root} [m]	11.2
Outer taper ratio $\lambda_{Outer} = C_{Kink}/C_{Out}$ [-]	0.06
Fuel fraction [%]	16.5
Engine diameter D_{Eng} [m]	0.76
MTOM Error [%]	1.25

Fuel Vol Error [%]	-0.65
Fuel Mass Error [%]	0.008
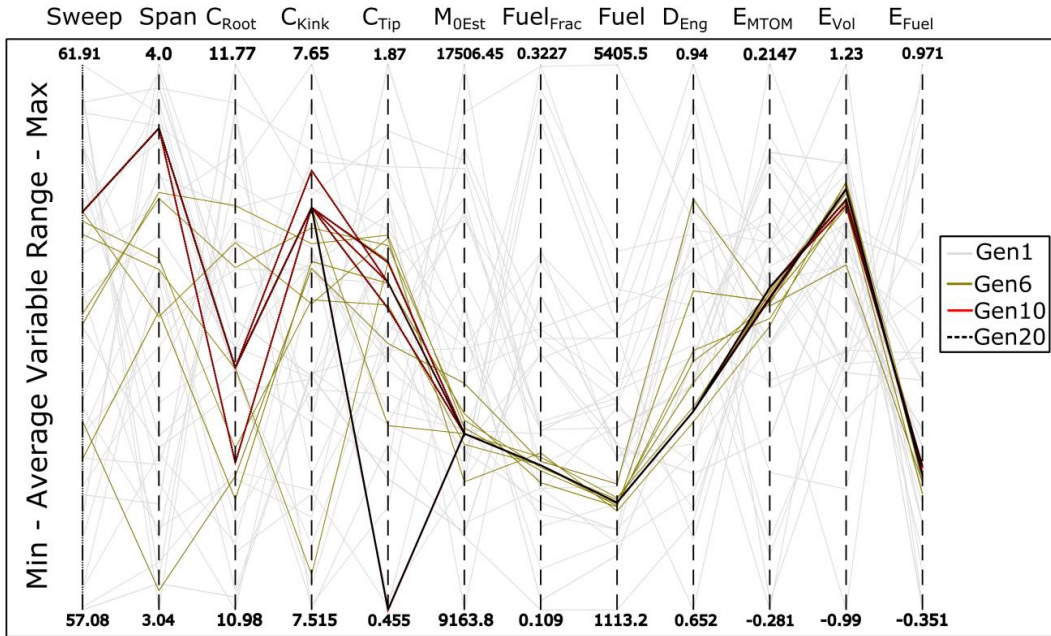
Figure 6-11 - Parallel coordinate graph for inputs and 3 constraints
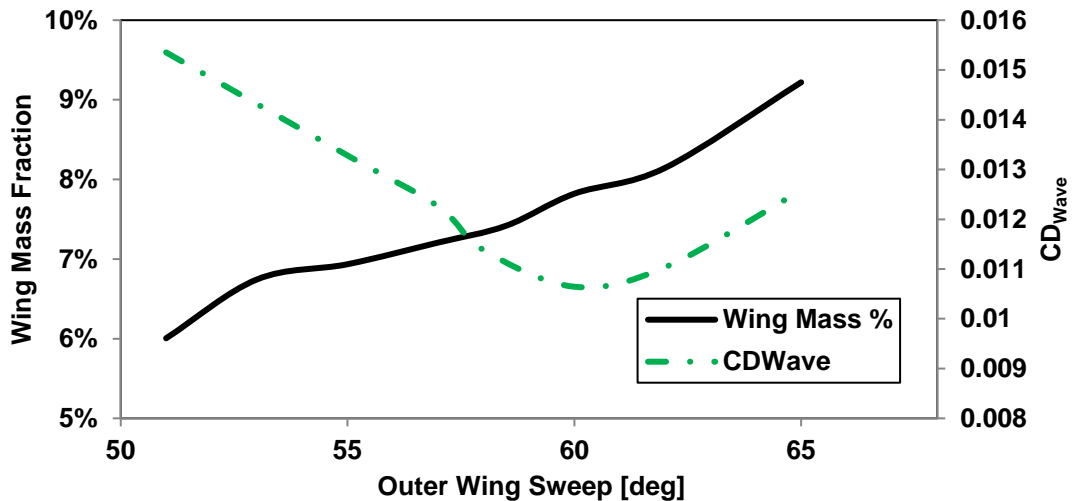
Figure 6-12 - Wing mass fraction and supersonic wave drag (M1.5) vs sweep

The relatively high outer wing sweep was selected by the optimiser due to the wave drag behaviour observed in Figure 6-12, despite the wing structural mass increment as a function of sweep.

After the quick convergence of the genetic algorithm, the LSGRG2 gradient-based optimiser was automatically selected by the GENUS framework, and

several design variables were refined. This second process resulted in a reduction in wing area in order to improve turning performance, and a slight increase in engine diameter, leading to an increase in fuel of 379 kg. Overall, a mass reduction of 70 kg was achieved by this further design convergence.

The main engine sizing constraints were found to be the supersonic thrust requirement, as well as the sustained turn thrust, as shown in Figure 6-13. The acceleration time requirement of 60s was not found to be restrictive and it can be reduced to 30s, as shown by the acceleration profile in Figure 6-14. The acceleration profile shows a change in slope at Mach 1.0, which is expected due to the increase in drag from the supersonic wave drag component. Furthermore, a SEP of 147 m/s at 1g, 0.8M/4.5 km, 50% fuel, and 180 kg payload was achieved, surpassing the requirement.
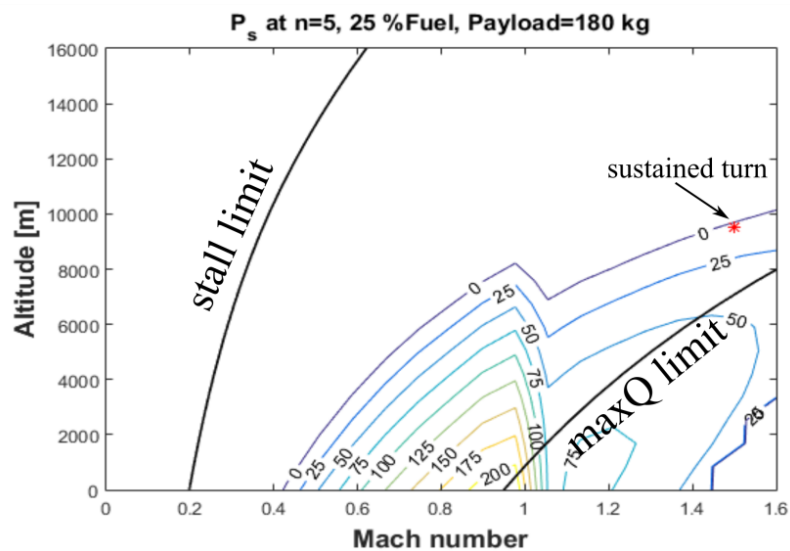
Figure 6-13 - Specific excess power map for sustained turn conditions
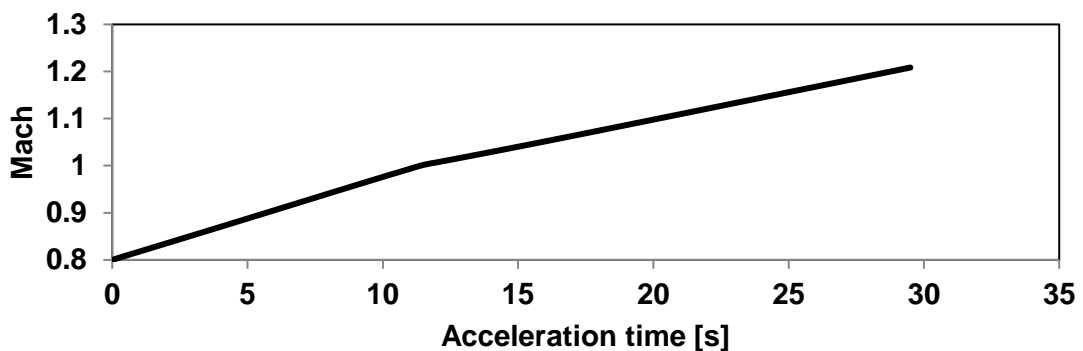
Figure 6-14 - Acceleration Mach profile

150

A top view schematic of the final geometry, the arrangement of the internal components, and a mass breakdown are shown in Figure 6-15. The total wingspan is 8.9 m, with a central chord of 11.2 m, a reference wing area of 47.73 m^2, a take-off mass of 11791 kg and a total fuel consumption of 2336 kg. The sea level thrust is 93 kN in dry mode, and 112 kN in afterburner mode. The final thrust loading is 0.8, and the wing loading is 2423 N/m^2.
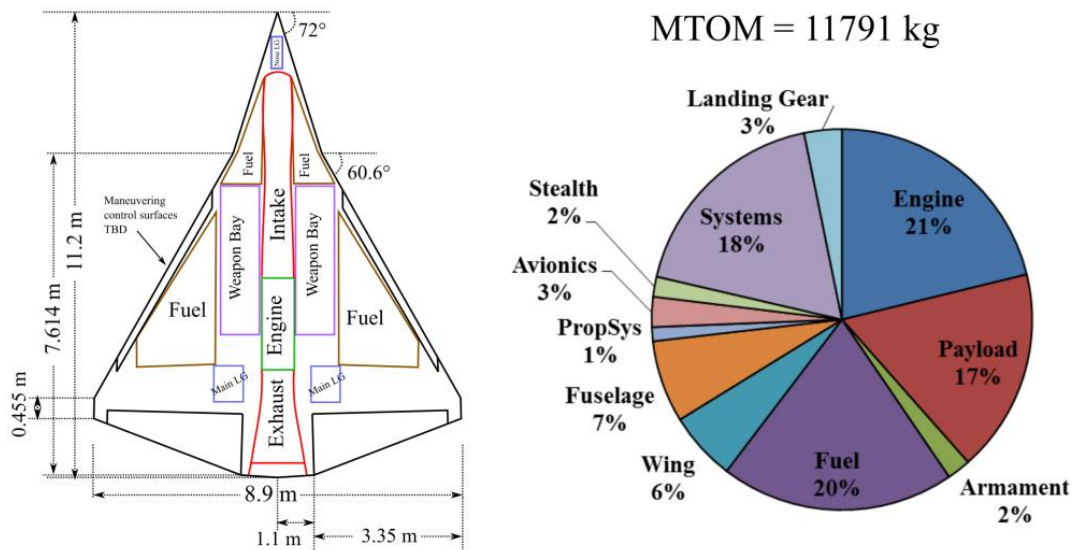
Figure 6-15 - Final UCAV characteristics and mass breakdown

The weapon bays have maximum dimensions of 3.56 m in length, 0.94 m in width and 0.6 m in height, to be refined during the preliminary design studies. Also schematically shown are the low-observable intake and exhaust designs. These components have not been designed in detail and will also be refined through subsequent studies.

From the mass breakdown, it can be seen that the engine and propulsion systems make up more than 20% of the gross mass, followed by the fuel, the structural components, the various systems, and finally the payload.

The aerodynamic characteristics are given in Figure 6-16 to Figure 6-18, while the specific excess power map compared to non-official data for two fighters[196] is shown in Figure 6-19 (F-22 data is given at a heavier payload and fuel condition than F-35 or UCAV data).
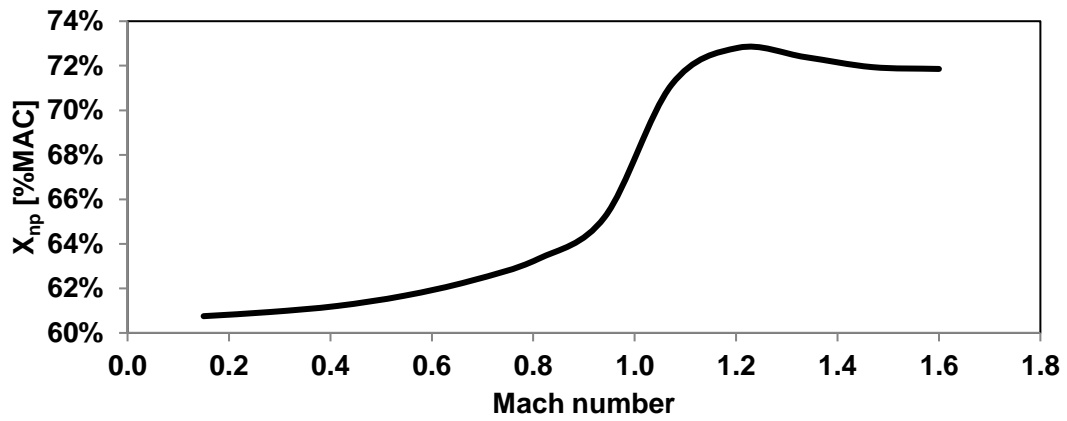
Figure 6-16 - Neutral point vs Mach number
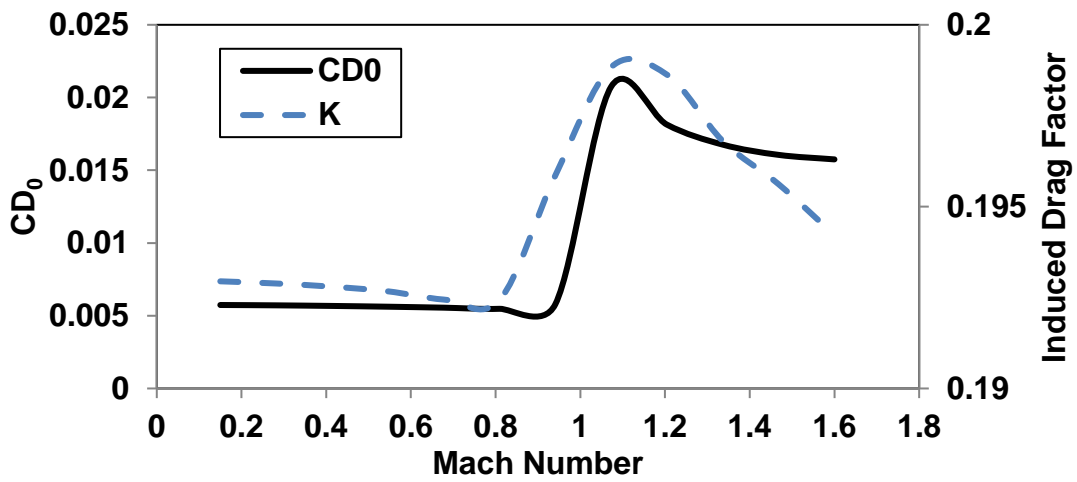
Figure 6-17 - Zero-Lift drag coefficient and induced drag factor vs Mach number
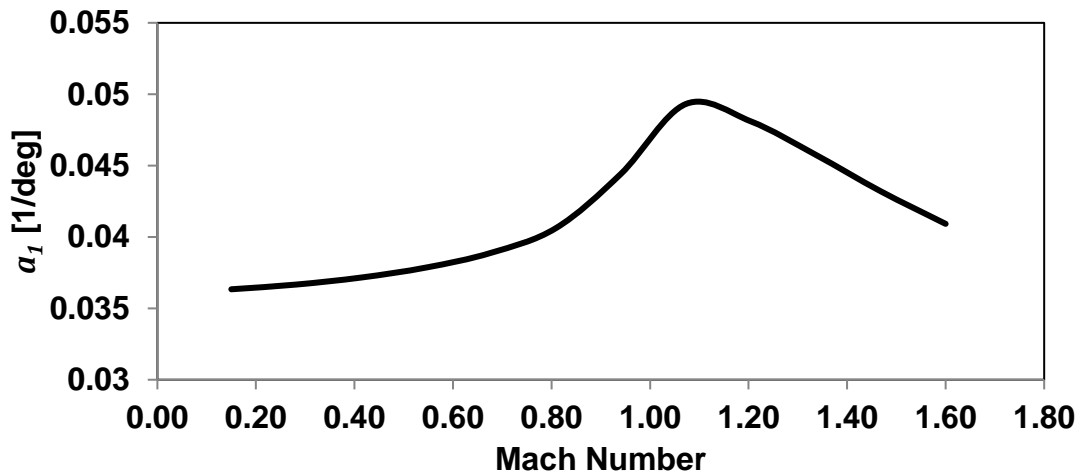
Figure 6-18 - Lift curve slope vs Mach number
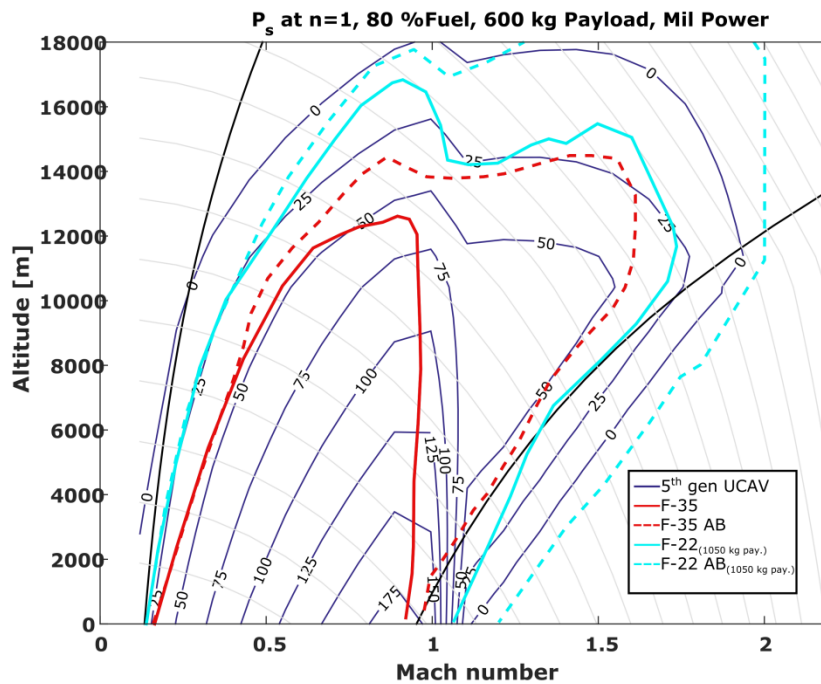
Figure 6-19 - Specific Excess Power map at 80% fuel and 600 kg payload

A full mission profile is shown in Figure 6-20. Altitude in km, vehicle mass in tonnes, and angle of attack in degrees are to be read against the left vertical axis, while Mach number is shown in the secondary vertical axis on the right. High angles of attack are experienced during the minimum time-to-climb segments, with potential challenges to maintain longitudinal control.
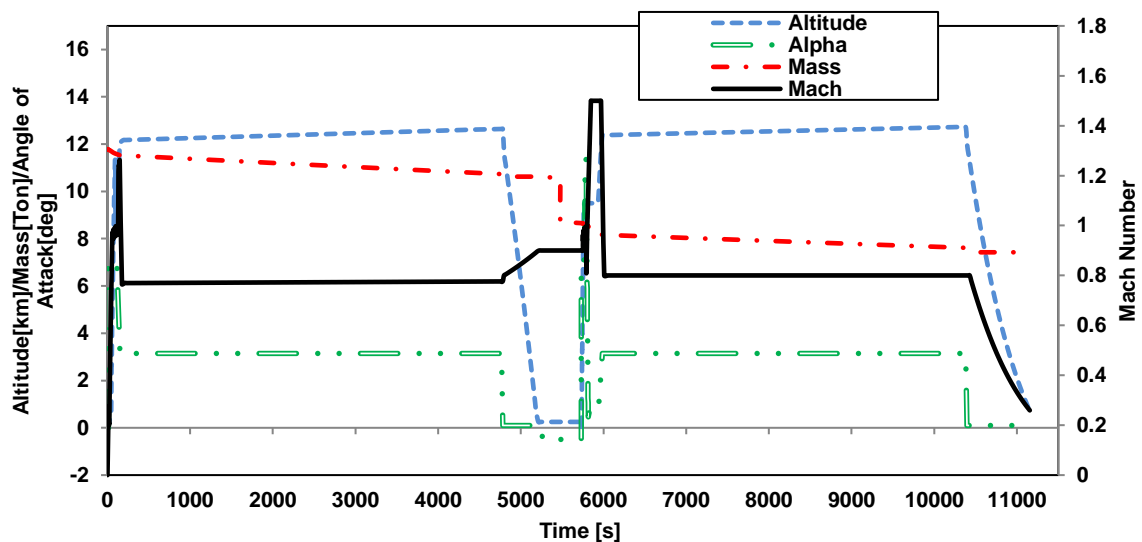
Figure 6-20 - Mach, mass, altitude, and angle of attack throughout the mission

Through the packaging and CG module in GENUS, four potential fuel tank areas have been identified and sized, as schematically shown in Figure 6-15. The total fuel volume available exceeds the fuel consumption needs by 22%, allowing a total of 2851 kg of fuel carried internally. The aft fuel tanks can accommodate up to 73% of the nominal mission fuel, while the forward tanks can accommodate 49% of the nominal mission fuel.

This fuel tank arrangement allows for flexibility in terms of CG control and longitudinal trim. The CG excursions as a function of fuel consumption and fuel scheduling for a ferry mission and a nominal mission are shown in Figure 6-21. The desired fuel CG locations through time can be calculated for maintaining a particular static margin, as shown in Figure 6-22, however not all fuel CG locations are feasible.
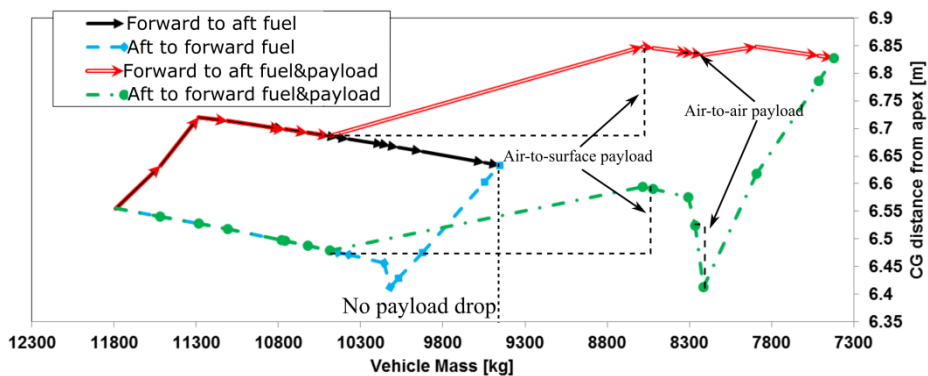
Figure 6-21 - CG excursion due to fuel scheduling and payload drop
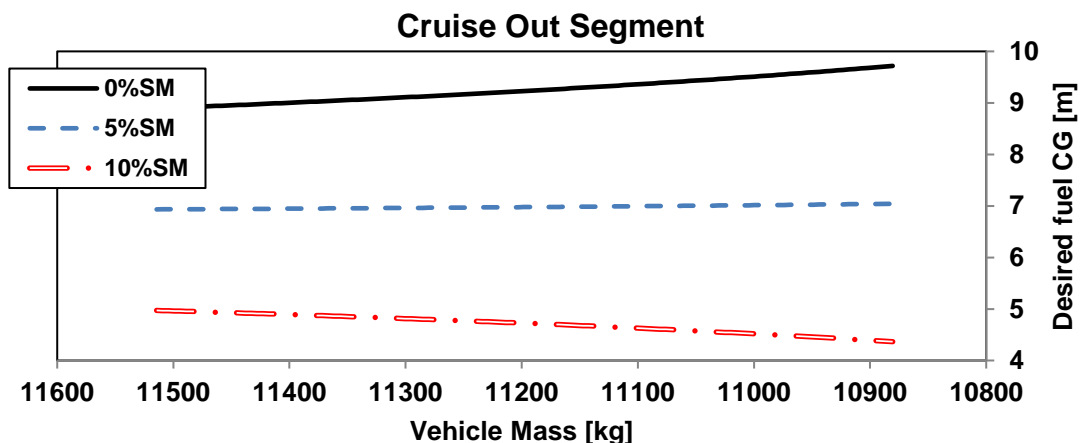
Figure 6-22 - Desired fuel CG to maintain a static margin

As mentioned previously in §5.3, additional work should be carried out in order to validate the results of the overall vehicle's masses, size, propulsion system characteristics, and general performance. The specific strategies required have been acknowledged as further work, and are mentioned in §9.2.

6.6 Summary of conceptual design studies

Following the trend of more capable UCAVs and loyal wingmen acting in highly coordinated operations, a potential mission for what is being referred to as a 5th generation UCAV was introduced. Subsequently, the GENUS framework has been used to perform several trade-off studies and multivariate optimisation for a low-observable, tailless configuration with internal payload and a central buried engine.

Aerofoil selection has been completed through a comparison of typical subsonic aerofoils against transonic and fully supersonic aerofoils. A supercritical aerofoil demonstrated a significant drag reduction during transonic and supersonic flight compared to other subsonic and supersonic aerofoils, resulting in fuel savings.

Furthermore, afterburning turbofans of varying bypass ratios have been compared to an afterburning turbojet engine. Results show that while fuel consumption decreases reaching a minimum value with a bypass ratio of 0.7, the heavier powerplant and propulsion systems do not result in overall mass reductions. Sea level thrust requirements also increase with increases in bypass ratio, thus so does the cost of the vehicle. For this reason, a simple afterburning turbojet has been selected as the powerplant at this stage of the design.

Finally, multivariate optimisation has been carried out through a genetic algorithm and a robust gradient-based optimiser. A quick convergence after only 20 generations was achieved by the genetic optimiser; however, several design characteristics were later refined by the gradient-based optimiser. The wing area was reduced by 8.25% to improve turning performance, and the engine diameter and fuel increased slightly in order to comply with supersonic cruise and sustained turn requirements at supersonic speeds.

The specific excess power maps show that the thrust modelling or the drag prediction might be optimistic. However, the validity of the fighter data being used to compare the UCAV values cannot be guaranteed; nevertheless, the overall SEP trend values seem in line with the much lighter UCAV configuration, and the relatively high sea level thrust mandated by manoeuvrability constraints. The preliminary engine selection might help define this performance criterion more realistically.

In terms of stability, the static margin was limited to -15% to +15% during all flight conditions. Trim was checked for trailing edge devices located on the outer wing with a chord ratio of 20%, all deflections were found to be within the -20°/+20° range. Future studies will determine the leading edge control surfaces for improved performance and control, as well as the design of lateral control means, which are not trivial.

Low-observability criteria will be tested during preliminary design studies as the geometry, packaging, structural arrangement, and system architecture are developed in more detail. As of now, it is assumed that the vehicle will comply with the very low-observable requirements due to its inherent low-observable platform, high sweeps, and fully internal components.

6.7 Preliminary Design Studies

Starting from the conceptual design characteristics presented in the sections above, a set of technical specifications were compiled for the purpose of preliminary design studies. The main preliminary design tasks are:

1. *Structural concept*: allocation of the main structural elements, sizing and design of weapon bays and landing gears.
2. *Systems architecture*: definition of electrical, power generation, and actuation systems following a more-electric aircraft philosophy.
3. *Engine selection and packaging*: definition of an off-the-shelf engine and its integration.

156

4. *Low-observability*: definition a detailed surface model, intake and exhaust design, and development of a methodology for consistent low-observability analyses including radar and infrared signature.

5. *Avionics*: requirements and systems definition for highly cooperative operations between 5th and 6th generation manned/unmanned aircraft.

6.7.1 Structural Concept

The structural concept has been developed by Sleightholme[197] within the confines of a general structural arrangement following the identification of the main load cases. Load magnitudes were not calculated due to time constraints and a lack of clear certification process. However, certification was considered and it is likely to follow an *ad hoc* approach, with potentially thousands of certification requirements from both Def-Stan 00-970 Part 1 and Part 9.

The main load cases considered for the structural concept are inertial loads, aerodynamic loads, and ground loads. For the inertial loads, distributed and localised components were identified, and the distributed mass was assumed to be spread equally over the UCAV wing area. Aerodynamically, the longitudinal load has been assumed as equivalent to the load of an aerofoil with a flap section following Howe's procedure and verified with XFOIL. The span-wise distribution assumes a simple Schrenk lift distribution. The mass distribution in the longitudinal and lateral directions, as well as the 1g shear force and bending moment diagrams are shown in Figure 6-23.

A continuous structure from wing tip to wing tip has been adopted as potentially offering the highest strength. The longitudinal position of the frames was obtained as a function of the main discrete load elements such as nose and main landing gears, weapon bay edges, and the attachment points of the engine. Due to the high sweep angle, low thickness value, and high load factors, the wing follows a multi-spar design. At this stage, it was decided to only add spars that would terminate at a frame to which they could be joined.

The rib layout was selected in order to reinforce the main cut-outs, as well as location of control surface hinges. The exact number of ribs requires a more

detailed load analysis. To ensure sufficient strength in the longitudinal direction, especially close to the engine inertial loads, two longerons have been added at the height of the engine attachments.

Finally, the control surface structure has been assumed as a spar-ribs combination; however, a full-depth honeycomb option could be explored. The complete structural layout is summarised in Figure 6-24.

a) Lateral mass distribution

b) Longitudinal mass distribution

c) Lateral Shear Force diagram

d) Longitudinal Shear Force diagram

e) Lateral Bending Moment diagram

f) Longitudinal Bending Moment diagram
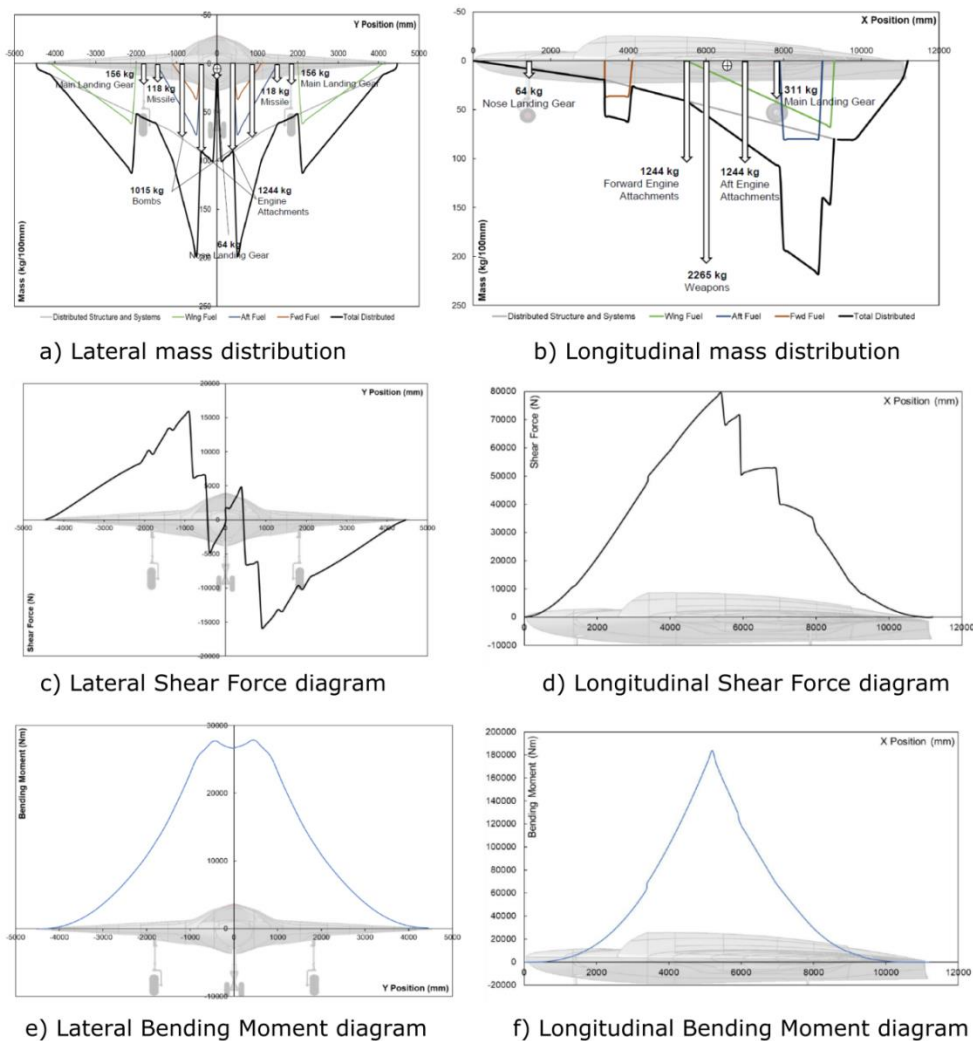
Figure 6-23 - Shear force and bending moment diagrams[197]

Maintenance has been considered primarily for the engine. It has been determined that no fixed structure should be placed under the engine door, and only a removable link is to be placed under the engine.

The material selection assumes a high degree of composite material usage, both for structural and mass saving and for low-observability constraints. Aerospace grade alloys and aluminium are used for the areas with high thermal loads, specifically around the engine, exhaust, the leading edges and the vehicle's nose.

A particular challenge for the structural arrangement and the packaging of systems relates to the operations at extended ranges, due to the majority of targets would not be within the defined range from UK bases. Three options for extending the range were identified; these include aerial refuelling, carrier-based capability, and sea or air transport.
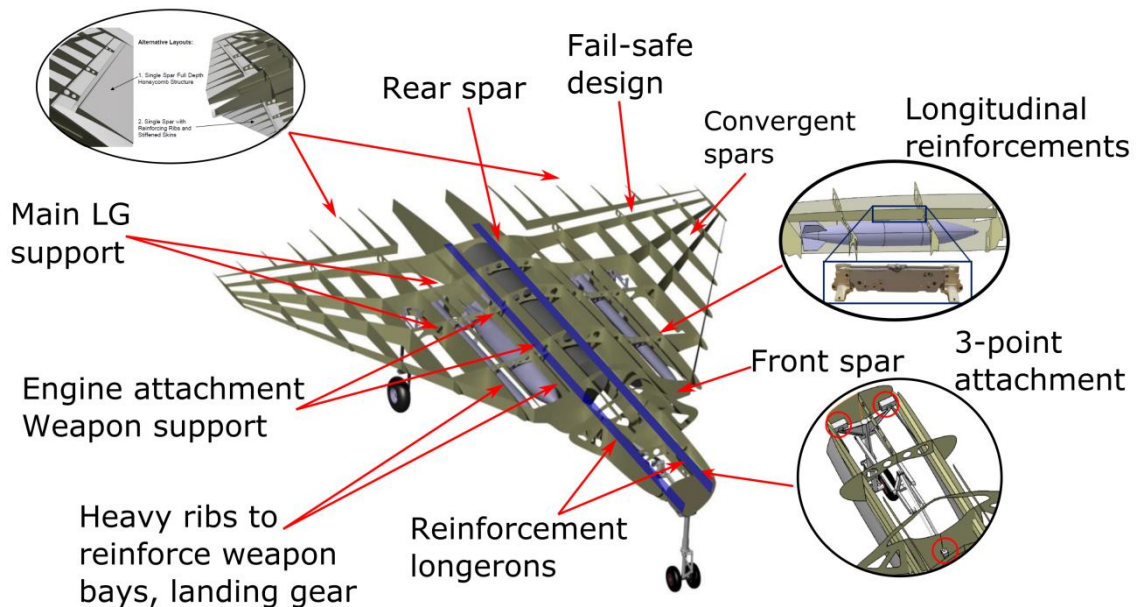
Figure 6-24 - UCAV complete structural arrangement (adapted from Sleightholme[197]**)**

Aerial refuelling does not pose significant structural challenges but it might impose system challenges. Carrier-based operations will impact the landing gear design and mass due to the higher loads. However, the UK aircraft carriers do not include ramps or catapults, and are only prepared for STOVL aircraft. To comply with this requirement would require a complete redesign of the propulsion system. Therefore, sea and aerial transport are the only viable options for locating the UCAV in the required area. Sea transport does not impose significant challenges due to the dimensions of the UCAV. Aerial transport requires the UCAV's outer wings to be either folded or removed for transport. Due to the

continuous elevon structure, the wing fold cannot comply with the maximum cargo width (5.48 m) for the standard C-17 aircraft used by the UK armed forces, as shown in Figure 6-25 (left). This requirement might dictate a change on the control surface's configuration and structure. Removing the wings could be another solution, with suboptimal operational and maintenance implications.
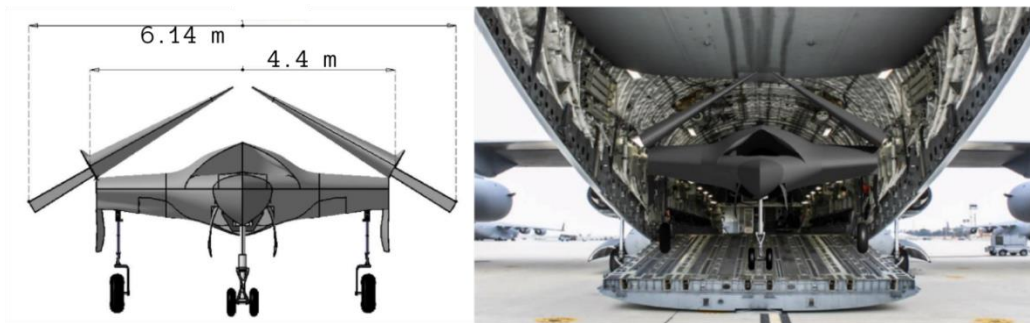
Figure 6-25 - Wing fold issues for aerial transportation inside a C-17 aircraft[197]

To conclude, the final recommendations from the structural designer include the following:

o Refinement of the flight envelope requirements.

o Aerodynamic considerations including washout and aerofoil changes.

o Reducing the payload size and mass would simplify the packaging and structural arrangement.

o Wing fold mechanism for aerial transportation requires control surface changes, it is recommended to split the elevons into inner flaperons and outer elevons.

6.7.2 Nose Landing Gear, Engine Selection, and Fuel System

Preliminary design and packaging of the nose landing gear (NLG), fuel system, engine selection and integration, and design of the intake and exhaust have been undertaken by Catala[198].

The initial layout of the NLG consists of a dual wheel configuration that retracts backwards. The dual wheels reduce the tyre size and ease the structural integration inside the already limited nose of the UCAV geometry. Loads have been analysed for various mass and CG positions according to the fuel scheduling limits, with the highest load found at the MTOM, with a 10% load. The

backward retraction has some drawbacks regarding the safety and reliability of the system, potentially not being able to extend due to gravity in the case of actuator failure. This configuration was chosen purely based on packaging constraints. No brake is integrated into the NLG.

Basic system design has been considered through the integration of an oleo-pneumatic shock absorber, and a rack and pinion steering system. The retraction mechanism has been adapted from a study of the Dassault's Neuron, the BAE Taranis and the Northrup Grumman X-47B retracting systems, as well as the NLG door designs. Figure 6-26 shows the NLG in extended and retracted positions, as well as its integration into the UCAV's nose.
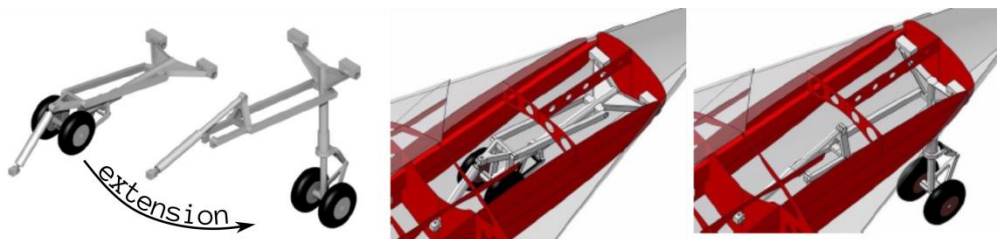
Figure 6-26 - Nose landing gear design and integration (adapted from Catala[198]**)**

For the engine selection and integration, various off-the-shelf low bypass ratio afterburning turbofan and turbojets were analysed and characterised in terms of their thrust-to-weight ratios in dry and reheat modes. Furthermore, these data were matched to the thrust requirements during several critical mission segments. A simple scaling factor for the maximum allowable engine weight was applied, and these data were compiled into the green-blue feasible zones. It can be seen in Figure 6-27 that the only engine able to comply with dry, reheat, and weight constraints is the Safran M88-3 turbojet engine.

The intake integration and design challenges relate mainly to the need for acceptable performance at both subsonic and supersonic segments. The inlet capture and throat areas have been sized for subsonic cruise through the conservation of total airflow, assuming a maximum air speed at the engine face of Mach 0.4, and a maximum air speed at the throat of Mach 0.6. The possibility of a variable geometry intake through a movable lip was considered for supersonic operations; however, this design is not reflected in the CAD and no

estimations of its cost and performance penalties were performed. The possibility of a divertless supersonic inlet (DSI) was not considered at this stage of the design.

a) Dry thrust vs weight   b) Reheat thrust vs weight
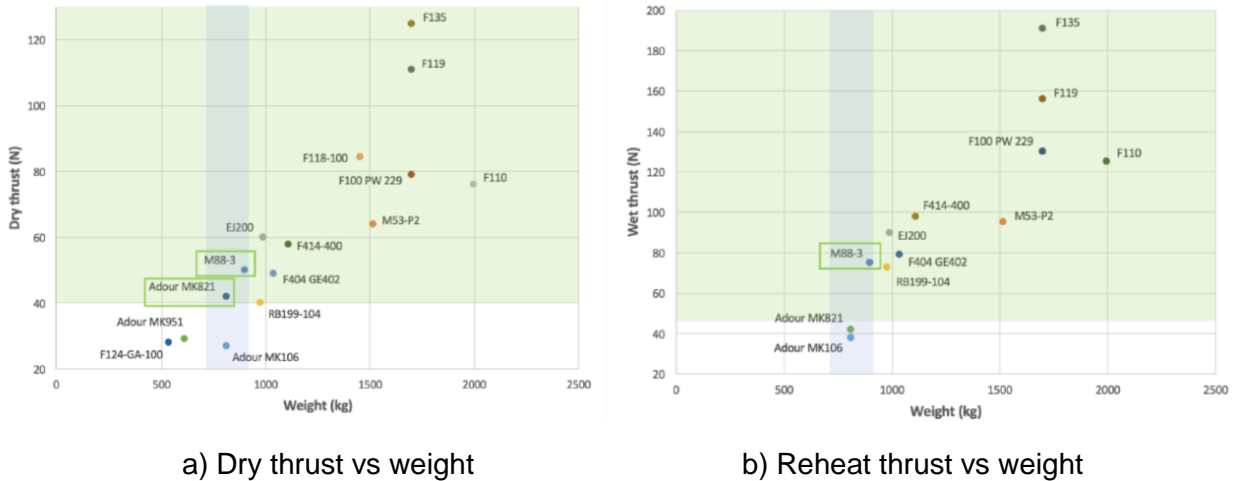
Figure 6-27 - Off-the-shelf engine selection charts[198]

In order to keep the engine operating at its maximum efficiency under various flight speeds, a variable geometry nozzle is most likely required. The integration of such a system is a challenge for this configuration not only because of the planform choices, but also due to the low-observability criteria that is being prioritised throughout the design. No thrust vectoring was specified by the conceptual design; therefore, a flat nozzle was designed with a serpentine exhaust to maintain low RCS and infrared signatures. Future design iterations might consider a complete re-design of the exhaust-nozzle geometry, and its effect on the trailing edge control of the vehicle, as seen in Figure 6-28, which includes the possibility of thrust vectoring for improved manoeuvrability and take-off performance, which will prove essential during potential carrier-based operations.

The design of the fuel system is complex not only because of the purpose of the vehicle and the inherent risks it is exposed to, but also due to the inherently unstable configuration which requires CG control through trim tanks. The majority of the fuel is carried in the outer wing portions, but two frontal trim tanks are used to accommodate mission fuel and to provide CG control. The major wing tanks have been divided into two independent tanks, with shut-off valves connecting

them. Furthermore, the fuel system is designed to connect to potential additional fuel tanks carried in the weapon bays for ferry missions. Fuel jettison valves are located at each wing tip in case of miscellaneous failure, shortened missions, or emergency landings at a mass higher than the maximum landing mass.
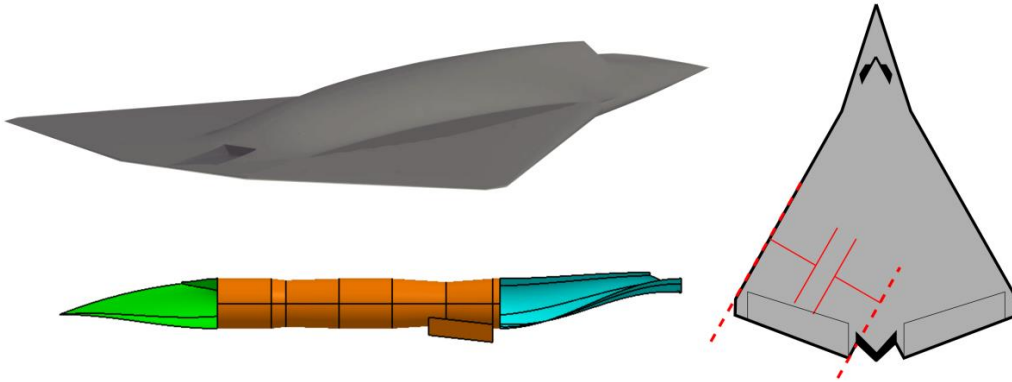
Figure 6-28 - Isometric and lateral view of the exhaust-nozzle system, and a potential nozzle design based on BAE Taranis (adapted from Catala[198])

The fuel system incorporates an On-Board Inert Gas Generation System (OBIGGS) in order to eliminate the risk of fuel ignition inside the tanks due to the presence of oxygen. Finally, an Integrated Power Pack (IPP) system that replaces the conventional APU has been used due to its compact size and lightweight. The complete fuel system architecture is shown in Figure 6-29. The main fuel pumps, valves, and pipes have been sized obtaining a total system mass of 82 kg.

Finally, a 'fully' packaged UCAV is shown in Figure 6-30 including the various antennas and avionics components. The detailed design of the weapon bay doors and landing gear doors has not been carried out at this stage.

6.7.3 Main Landing Gear and Airframe Systems

Airframe and power systems, as well as the structural design of the main landing gear (MLG) and its doors, payload integration, and weapon bay doors have been carried out by Mangion[199].
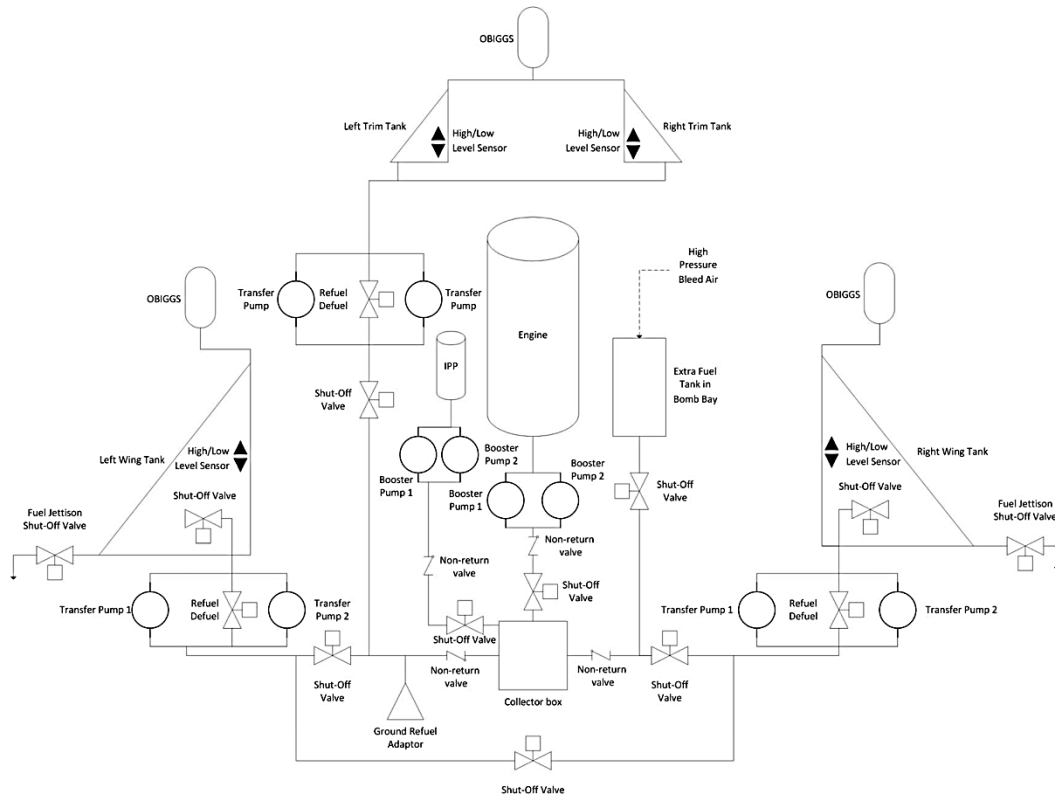
Figure 6-29 - Fuel system architecture diagram[198]
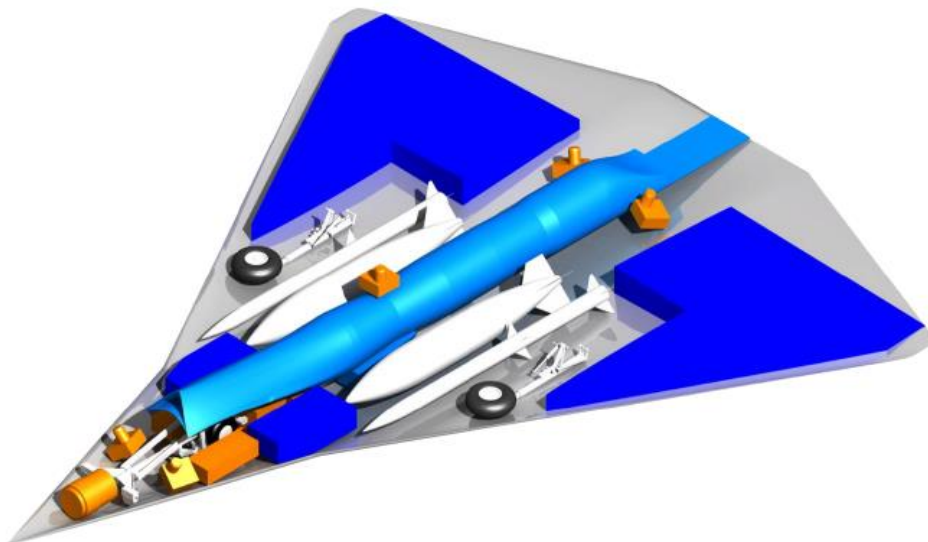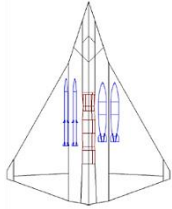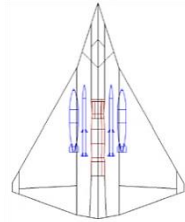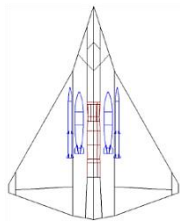
Figure 6-30 - Fully packaged UCAV[198]

The conceptual design specifications relating to the inclusion of two AIM-132 missiles was challenged due to the fact that most uses of the AIM-132 missile have been developed for external carrying and launching. In their place, two AIM-120 Advanced Medium Range Air-to-Air Missiles (AMRAAM) are proposed, despite being 80 cm longer.

Three payload storage configurations have been explored; their advantages and drawbacks are summarised in Table 6-4, adapted from Mangion[199].

Table 6-4 - Payload Integration Configurations

Configuration	Advantages	Disadvantages
Asymmetric	None identified	Obvious asymmetry creates complex structural arrangement, difficulties for take-off, landing, manoeuvring.
Bombs Outboard	The longer elements are located closer to the centreline, which is naturally longer. This configuration might simplify the wing structure. More flexibility for locating the bombs near the longitudinal CG of the aircraft	Harder to reinforce the weapon bay structure. Large bending moments transferred to the fuselage frames due to the longer lateral arm of the heavier bombs. Harder to integrate in the thinner aerofoil for the outer wing, severe geometric/aerodynamic impact.
Bombs Inboard	Heavier items located closer to the aircraft's CG; improved manoeuvrability and reduced structural reinforcement due to the diminished bending moments and shear applied to other structural components.	Severe interference between the weapon bay and outer wing structure due to the longer bay required.

The third configuration, or *bombs inboard*, has been chosen as the standard payload arrangement by the designer for its better CG control and lighter structure. The weapon bay dimensions have been calculated as 3.82 m in length and 1.18 m minimal width. The release mechanisms for each weapon type have been considered and decided upon; the bomb will use a NATO standard *Bomb Rack Unit* (BRU), while the missile will employ the *LAU/142-A* AMRAAM Vertical Eject Launcher, the same mechanism employed in the F-22 weapon bay. Both ejectors are shown in Figure 6-31. These choices avoid the use of any pyrotechnical systems, and are intended to provide sufficient ejection force to

avoid fly-back behaviours and the potential collision of the payload with the UCAV geometry.
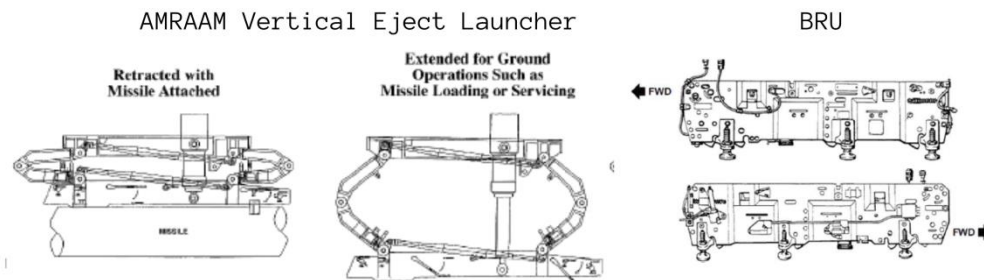
Figure 6-31 - Weapon launchers for missiles and smart bombs[199]

The complex aero-acoustic environment found in an open cavity, especially that at supersonic speeds, has been identified by the designer as a critical design case for the weapon bays structural and system arrangement. However, due to the complexity of the analysis (often involving high-fidelity CFD and experimental data) this issue has not fed into the design of the weapon bays or the weapon bay doors. Two potential solutions were identified: (1) locating control surfaces in the vicinity of the weapon bays in order to have better control of the flow; and (2) changes to the weapon bay geometry for reduced acoustic vibrations (which can reach up to 180 dB and can damage the structure of the UCAV). Finally, the weapon bay doors layout consists of two split doors with saw toothed edges for reduced radar signature.

For the MLG design, a theoretical constraint analysis was performed including a tip-back angle clearance angle of 20°, a maximum turnover angle of 63°, roll clearance angles of 7° and 20° which were found not to be relevant due to the low aspect ratio of the UCAV, and finally the maximum static loads for the NLG between 8% and 15%.

Due to concerns from the structural designer, an alternative suggestion for the MLG's longitudinal position has been suggested in order to attach it to the engine frame, which is one of the most solid structural components in the *fuselage* section; this change in position is reflected in Figure 6-32.

The designer has agreed that this new location has structural advantages; however, the decision has been made not to relocate the main gear due to the following drawbacks:

o The lean back angle between the most aft CG position and the touch-down point of the MLG changes from 15° to 40°, inducing severe penalties for the take-off performance.

o Landing performance is affected due to the longer wheel track, inducing higher shock loads at the NLG after touch-down. This could affect the sizing and the structure of the NLG.

o The static load of the NLG has increased from 8.5% at the MTOM condition, to 21% also at the MTOM. This is beyond the recommended load range for safe operations.
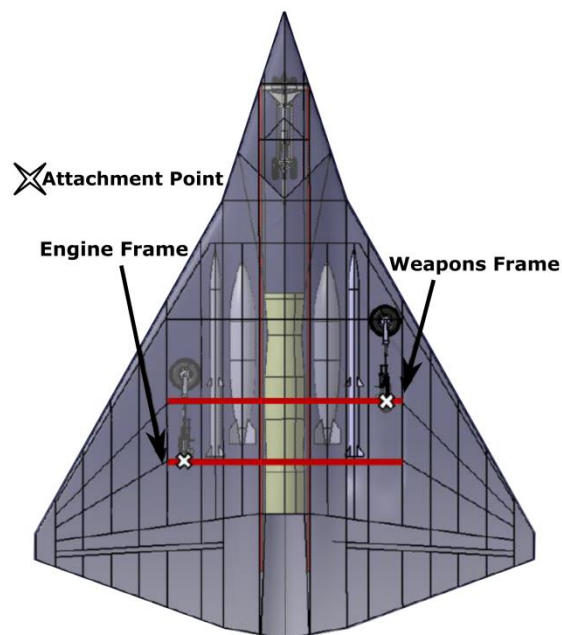
Figure 6-32 - 'Optimal' (right) and alternative (left) MLG position (adapted from Mangion[199])

Tyres have been sized according to conventional guidelines; the wheel structure has been selected as bowl type despite its reduced stiffness when compared to an '*A*' frame wheel in order to house the braking system, which has been sized for rejected take-off, 5, 100, and 250 stops to allow for system wear. The required dimensions were found to fit inside the MLG wheel system.

Also shown in Figure 6-32 is the forward retraction of the MLG; this has been selected mainly due to packaging constraints affecting the wing fuel tanks, as well as the optimal position of the landing gear previously determined. However, forward retraction requires the rotation of the tyre by 90° in order to fit into the thin wing section without severely compromising the external geometry and thus the radar signature. Finally, a single door has been designed with saw toothed edges for reduced radar signature. The final CAD of the MLG assembly (except for the detailed saw toothed geometry) is shown in Figure 6-33.
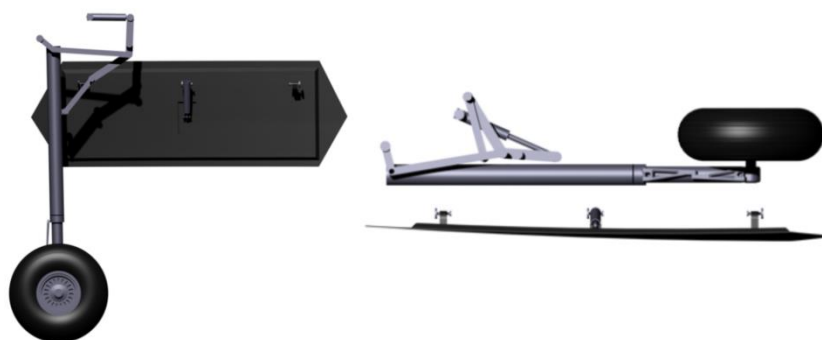
Figure 6-33 - Main Landing Gear and door CAD[(199)]

An initial qualitative design of the actuation system has been carried out by the designer; qualitative mainly due to the lack of data on the airframe loads. Classical actuation systems have been discarded and new technologies corresponding to the More Electric Aircraft (MEA) and Power-by-Wire philosophies have been considered. These philosophies revolve around increased safety and reliability, as well as reduced power consumption, acting through power-on-demand controls, meaning the systems do not consume power unless activated, unlike classical actuation systems. The two main types of architectures consider are Electrohydrostatic actuators (EHA), and Electromechanical actuators (EMA).

EHA are capable of generating the hydraulic pressure and force required to move the actuator locally. Hydraulic pumps, valves, and reservoirs are contained within the actuator itself, complemented with an electric motor and solid state electronics to regulate the temperature and pressure of the working fluid.

EMA vary from EHA in that they do not make use of hydraulic fluid, and instead the self-contained electric motor is used to drive a reduction gear for the actuator motion. A classical centralised hydraulic actuation system (CHA) is compared in Table 6-5 to EHA and EMA systems.

Table 6-5 - Actuation system comparison[199]

Criterion	CHA	EHA	EMA
Power requirements	High	Low	Low
Latency	Moderate (depending on routing)	Low (power-on-demand)	Low (power-on-demand)
Volume	High (pipes + redundancy)	Moderate	Low
Efficiency	Low	High	High
Torque/Mass ratio	Low	Moderate	High
Overheating	Low	Moderate	High
Safety	High (redundancy)	High (system independence)	Low (jamming risk)
Type of control surfaces	Primary and secondary	Primary and secondary	Secondary

The complete actuation architecture is shown in Figure 6-34. A combination of EHA and EMA has been selected depending on the surface to actuate. Fault analyses have not been performed and the number of actuators per surface have not been yet determined. Spoilers are shown but their location, or in fact the need for them, has not been fully determined at this stage of the design. However, since they are considered secondary control surfaces, they have been assigned an EMA through a simple Lead Screw Actuator (LSA), same as the leading edge control surfaces.

Due to the complex power demand of the actuation system, the equipment of the UCAV with state of the art avionics, and the potential inclusion of electronic

countermeasures, a high voltage Power and Thermal Management System (PTMS) has been proposed by the designer.
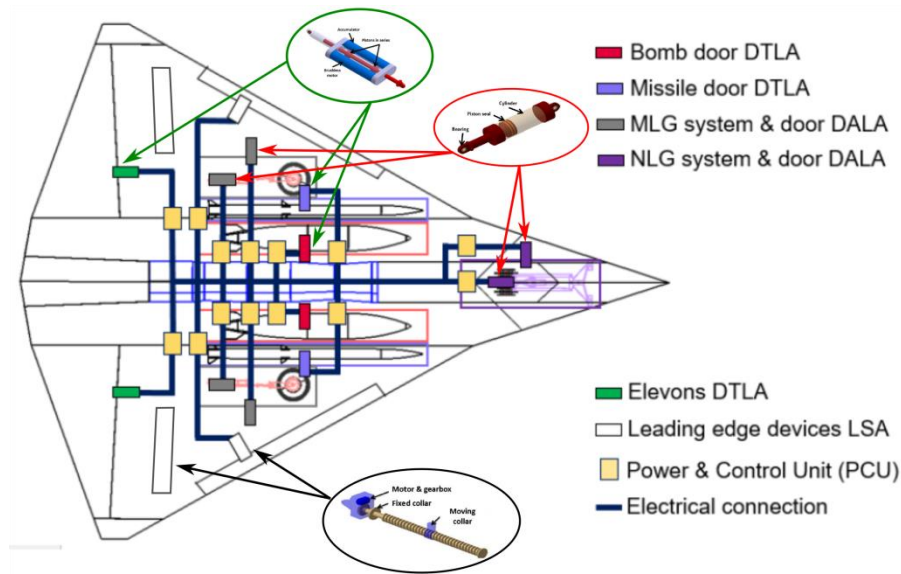
Figure 6-34 - Actuation system architecture (adapted from Mangion[199]**)**

The main electrical load has been identified as 270 VDC under High Voltage (HV) architecture, rather than a High Current (HC) set-up, as summarised by Table 6-6. Furthermore, direct current architecture has been chosen over an alternate current one because of its improved stealth (low electromagnetic interference), and compact packaging (simple control devices, low number of components).

Table 6-6 - Power architecture comparison[199]

Configuration	Advantages	Disadvantages
HV	Low current, small cable diameter (lighter).	Low commonality with current avionics and electrical systems. Probability of arcing.
HC	High commonality with current avionics and electrical systems	Heavier wiring, large heat dissipation, and high electromagnetic interference.

The secondary power channel has been identified as a conventional 28 VDC to power medium power navigation (Tactical Air Navigation, Traffic Collision Avoidance, and Flight Management) and communication (Peer-to-Peer, Master-Slave, and Identification Friend or Foe). Finally, to comply with MIL-STD-1760

Aircraft / Store Electrical Interconnection Systems standard, the weapon's electrical and power system must be connected to an alternate current input for the correct data sharing of guidance and targeting. Therefore, a tertiary electrical load channel has been identified as the medium power 115 VAC.

The main power generating unit consists of a Permanent Magnet Generator (PMG) coupled to the engine's gearbox which will produce 3-phase 115 VAC. Instead of using the cumbersome and heavy Constant Speed Drive (CSD) hydraulic units to convert the power output from variable to constant frequency, state of the art solid state power controllers, more specifically, Transformer Rectifier Units (TRU) will be employed coupled to 'ripple filters' in order to obtain a clean 270 VDC output from the 115 VAC generator. Figure 6-35 summarises the different electrical zones on the UCAV as well as the architecture for the power generating system, redundancy has been provided through two independent generators.
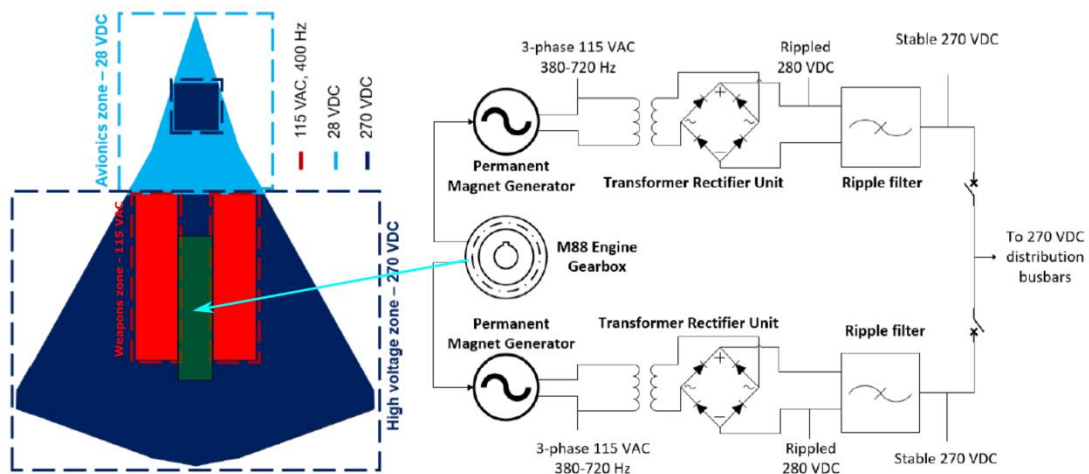
Figure 6-35 - Electrical load zones and power generating system schematic (adapted from Mangion[199])

The UCAV will also be equipped with an Integrated Power Pack (IPP) to replace the conventional APU. This system consists of a small turbine which can provide auxiliary and emergency power by burning the UCAV's fuel supply, as well as engine starting during nominal and emergency power-up, and finally it is able to cool the avionics by circulating cooled bleed air from the main engine. Furthermore, the UCAV will be equipped with an independent Uninterruptible

Power Supply (UPS) lithium-ion 270 VDC battery connected to the flight-critical distribution circuit to prevent catastrophic failure by providing surge suppression.

In order to design the electrical distribution system, the human-centric 'vital' and 'essential' system classification has been challenged and replaced by an unmanned relevant description, summarised in Table 6-7 as the 'essential' and 'non-essential' electrically powered UCAV systems. Redundancy has been provided by two independent electrical busbars, and a series of circuit breakers that re-direct the electrical power to the essential systems in case of an emergency; provisions for external power during ground operations have also been considered. The electrical power system architecture is summarised in Figure 6-36.

Table 6-7 - Electrically powered UCAV systems classification[199]

Essential	Non-essential
Communication and navigation avionics	Offensive and defensive avionics
PTMS	IPS
Flight control systems/actuators	Weapon bays systems/actuators
Landing gear systems/actuators	-
Fuel System	-

Concerning the thermal aspects of the PTMS, the designer has identified two main heat loads, those being the electrical losses from high power avionics and airframe systems, and the kinetic heating due to friction. Two flight segments have been evaluated, namely the high altitude subsonic cruise (0.8M/12km), and the supersonic dash segment (1.5M/9.5km). The avionics and electrical power system efficiency has been estimated as 50% for a conservative analysis. An estimate of 20 kW total power consumption has been given by the avionics system designer, meaning a heat load of 10 kW. A simplified cabin heat balance analysis, Eq. (6-11), has been performed at these two flight segments. The assumed avionics temperature, T_{cabin}, is 21 °C.

$$Q_{inlet}C_p(T_{inlet} - T_{exit}) - U_{wall}A_{wall}(T_{cabin} - T_{skin}) + H_{avionics} = 0 \qquad \textbf{(6-11)}$$

Bleed air from the inlet has been estimated as 5% during the subsonic segment and 3% during the supersonic dash.
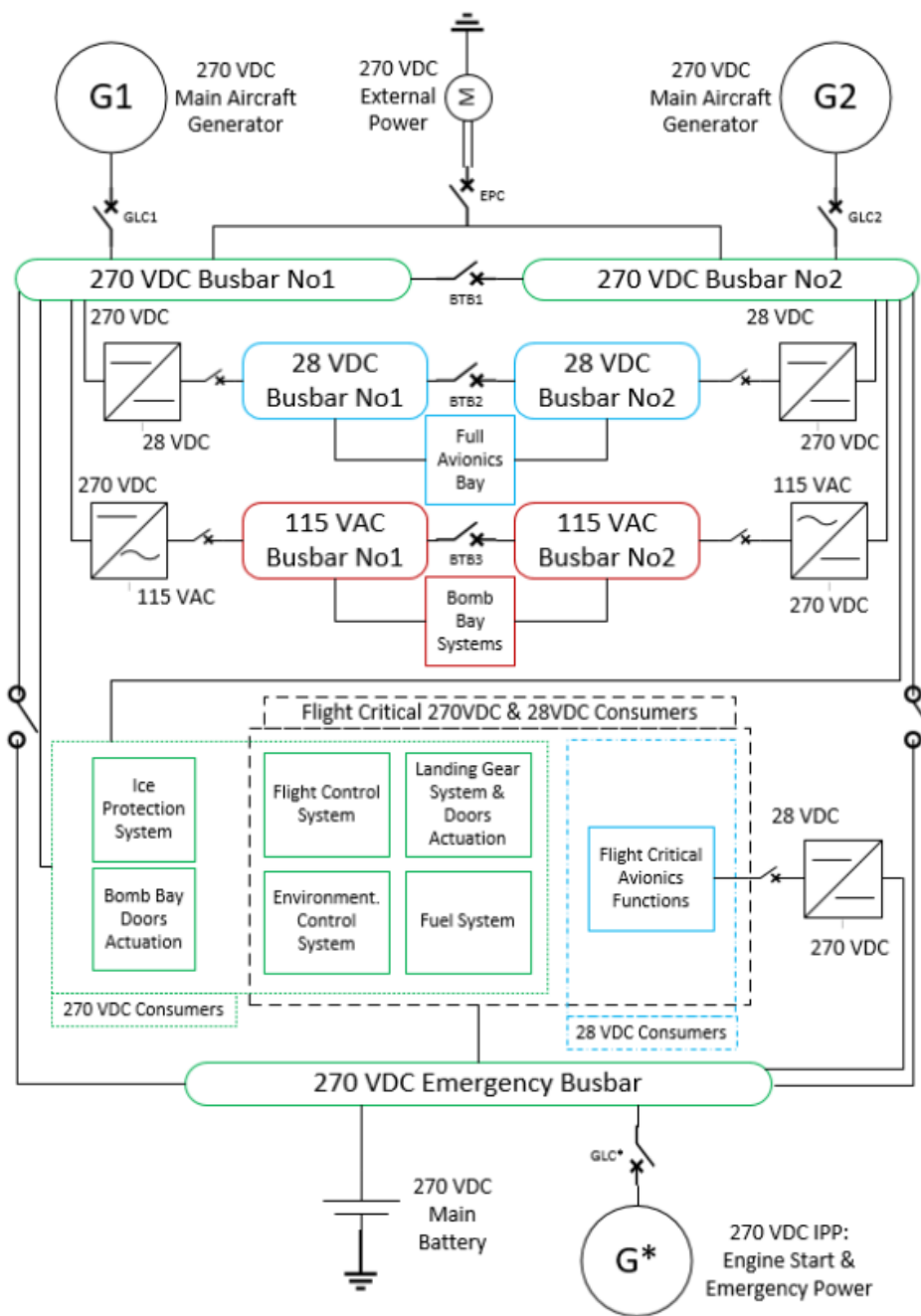
Figure 6-36 - Electrical distribution architecture[199]

During supersonic flight a cooling air flow of -30 °C is required to stabilise the avionics at 21 °C, while at subsonic flight the required air flow temperature is 13 °C. This analysis assumes steady state conditions, so it might not be applicable

to the supersonic segment, which lasts around 2 minutes; the subsonic segment lasts around 73 minutes and can be considered as steady conditions.

The integrated PTMS has three operational modes: (1) starter mode; (2) cooling mode, and; (3) emergency mode. On starter mode, the following actions occur:

o The IPP machinery starts rotation through 270 VDC battery or external power

o The IPP will begin to burn fuel to sustain rotation, and start the PMG

o When the IPP reaches nominal rotation, the PMG will produce electricity to power the essential avionics, the engine's fuel pumps and starter; the cycle ends when the main engine reaches self-sustaining rotation

During cooling mode, the PTMS performs the following actions:

o Redirected bleed air from the main engine's compressor is used to drive the IPP's power turbine (PT)

o Further air cooling and expansion takes place through a ram air heat exchanger located in the main engine's bypass flow

o Air is redirected to pass through the IPP's cooling turbine (CT). This air is available to cool avionics and other airframe systems

o The engine's PMG are cooled through a fuel heat exchanger

During emergency mode, the PTMS performs the following actions:

o The IPP intake and exhaust doors will open; fuel will be directed to the IPP's combustion chamber in order to produce electricity through its PMG

o In conjunction with the 270 VDC battery, the electric power from the IPP will be redirected to the 270 VDC emergency busbar

o An emergency electrical supply has been included for the attempted restart of the main engine through the IPP's PMG

The functional diagrams for each operational mode are presented in Figure 6-37
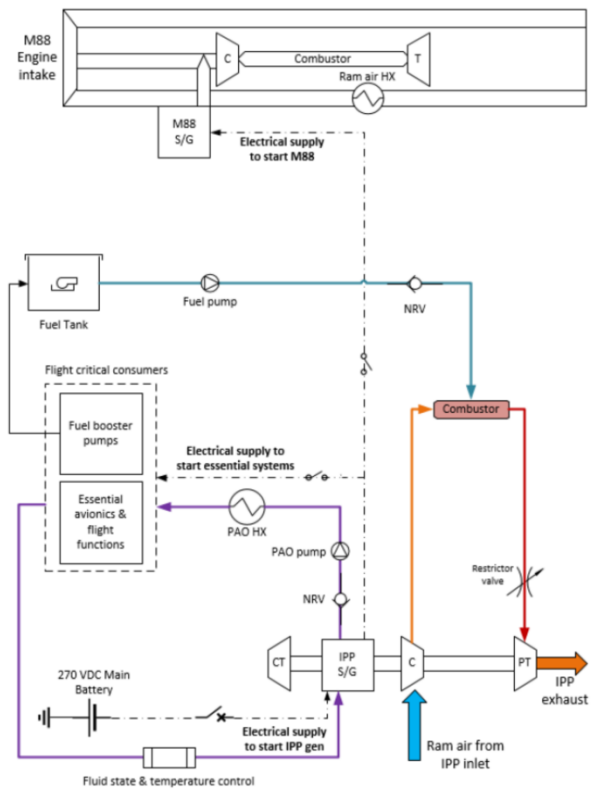
a) PTMS Starting Mode   b) PTMS Cooling Mode   c) PTMS Emergency Mode
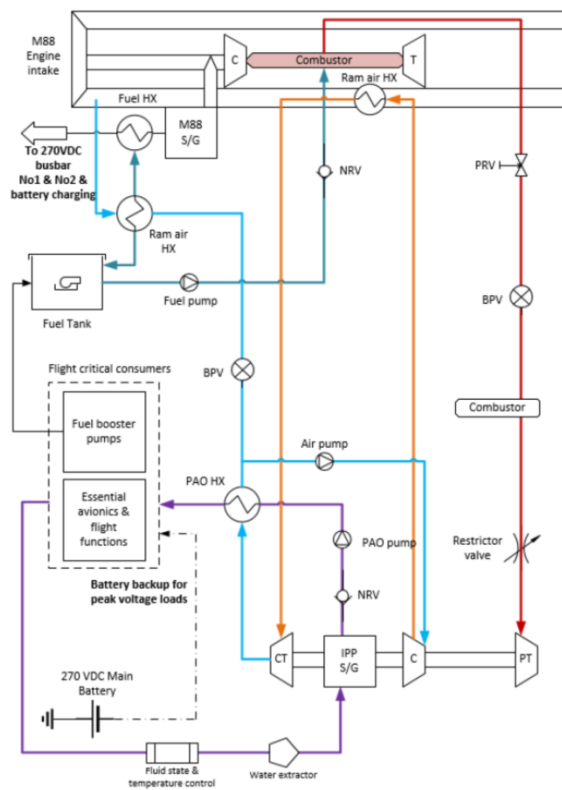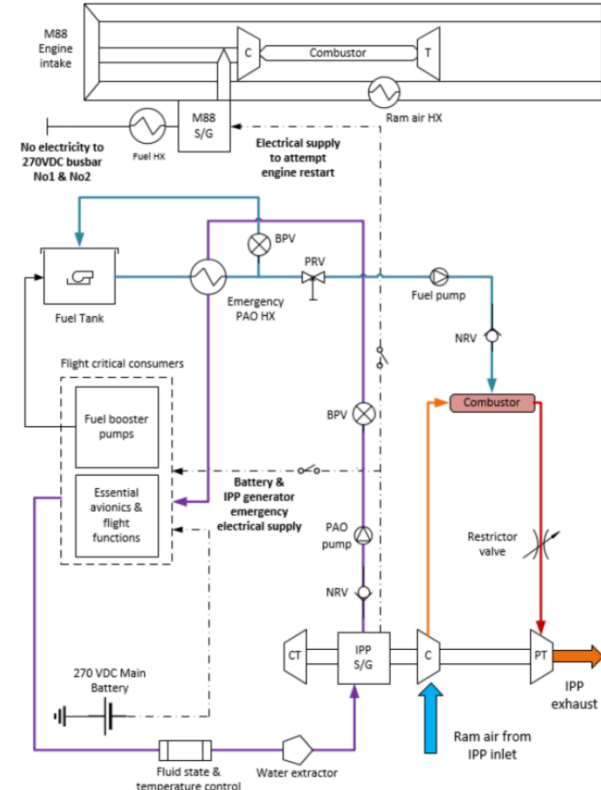
Figure 6-37 - PTMS System architecture in starter, cooling, and emergency modes (adapted from Mangion[199])

6.7.4 Low-observability

Low-observability analyses for a tailless 6th generation fighter geometry and the 5th generation UCAV has been carried out by Chaillous[200]. These analyses make use of the POFACETS code for estimating the RCS of a complex geometry. Due to the concurrent development of the various aspects of both fighter and UCAV geometries, the effect of RAM were considered, and a purely geometric analysis was conducted. A correction factor was applied to the obtained results due to a calibration against the mean RCS value of the F-35 reported by the USAF at ±15° elevation (θ) and ±45° azimuth (φ).

The effect of a rounded nose has been investigated for a conventional airliner, the F-35 model, and the UCAV geometry, showing that a pointed nose can reduce the wave reflection in monostatic case. Similarly, for the 6th generation fighter the effect of vertical tail planes has been evaluated. Results in Figure 6-38 show the very low RCS levels of the UCAV and the tailless fighter. However, results for the A340 geometry are not symmetric over the $\varphi=0°$ axis, and the results of the 6th gen fighter for the tail evaluation are also not symmetrical about the $\varphi=180°$ axis, raising questions about the validity of the geometries used.

a) Effect of rounded vs pointed nose   b) Effect of vertical tails
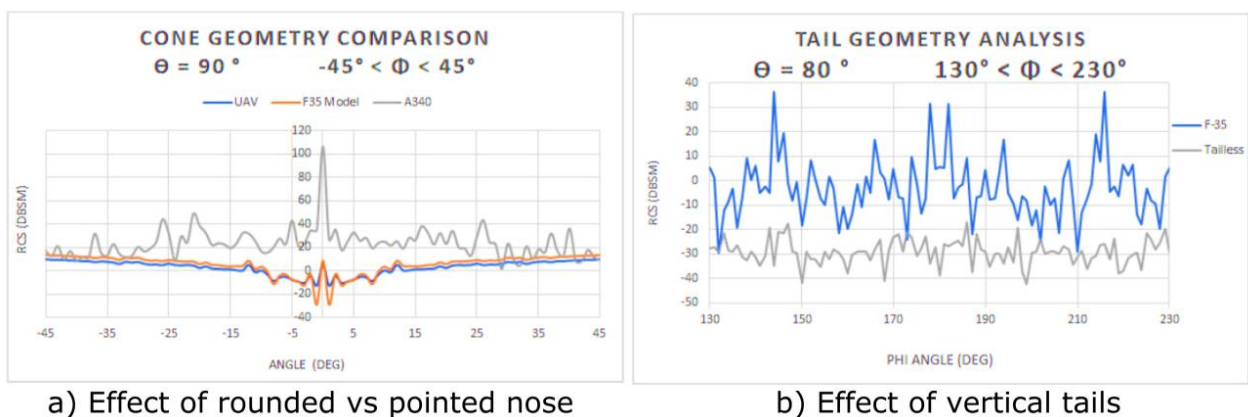
Figure 6-38 - Effects of nose roundness and vertical tails on RCS[200]

The effect of trailing edge geometry has also been investigated by comparing a trailing edge section with the same angles as the F-117, a straight trailing edge, and the UCAV geometry. Results in Figure 6-39 show a reflection peak at a view angle perpendicular to the trailing edge, with the UCAV showing a large peak

from the tail-on aspect. This geometry does not include the exhaust geometry, and no real conclusion can be extracted from these results.
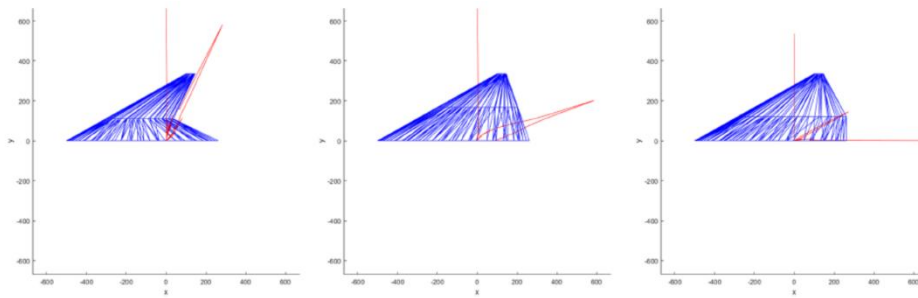
a) Trailing edge geometries
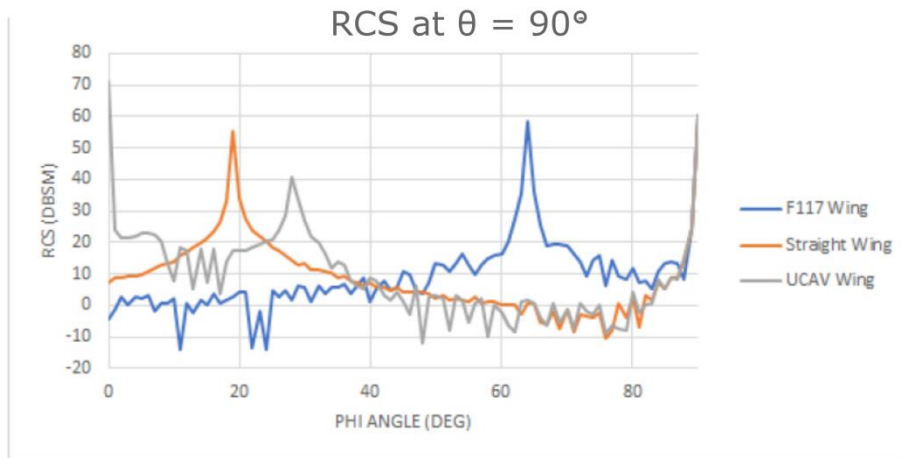
b) RCS results for various TE geometries

Figure 6-39 - Effect of TE on RCS reflection (adapted from Chaillous[(200)])
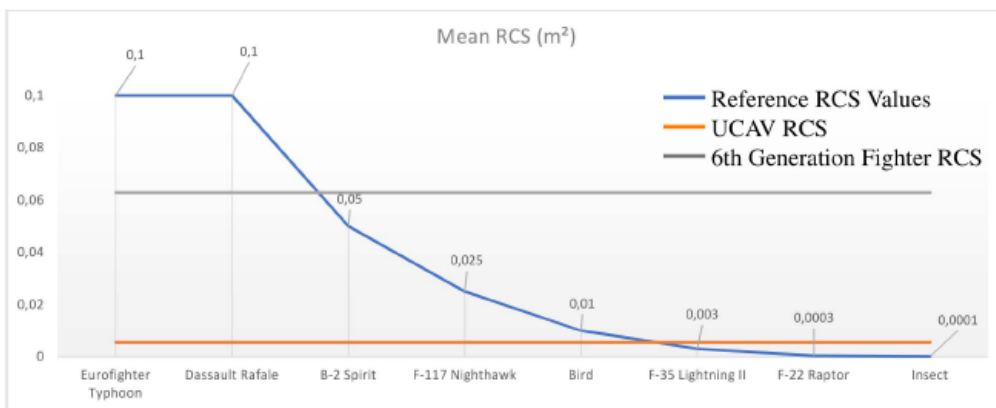
Figure 6-40 Nose-on RCS comparison for UCAV, 6th generation fighter, and other aircraft[(200)]

Nose-on RCS results for all the configurations evaluated in this study are summarised in Figure 6-40. It can be seen that the UCAV has a similar signature

177

to the F-35, while the 6th generation fighter shows a much higher RCS. The exact reasons for this result have not been determined.

Due to time constraints, there was no opportunity to develop an infrared signature estimation methodology.

To conclude, a top-level basic estimate of the RCS of a 5th generation UCAV geometry has been obtained and results show similar low-observability levels as the F-35 geometry. A series of material assumptions and correction factors were used that raise questions about the validity of the results. Furthermore, even though the serpentine inlet has been notionally integrated into the design, the effects of changes in the inlet geometry have not been carried out. Complete obstruction of the engine face has not been achieved for all viewing angles, which is partially due to the tight packaging constraints inherent to this design.

6.7.5 Avionics

The avionics system design for a 6th generation fighter and a 5th generation UCAV has been carried out by Moraillon[201].

The main philosophy for the development of the avionics systems requirements and equipment follows the *systems of systems and network-centric warfare*, which aims to enable and enhance situational awareness, target assessment and distributed weapon assignment through the integration of multiple services into a single joint command. This way, aircraft are able to engage targets without ever detecting them, increasing mission effectiveness while limiting exposition to enemy threats. An example of such a scenario is shown in Figure 6-41 in terms of detection ranges of early warning aircraft, friendly and enemy fighters.

The recent advances of modern avionics systems has greatly improved the accuracy and data processing capabilities of components, while continue to drive their miniaturisation. Thanks to these computing enhancements, future systems will include new techniques like machine learning and artificial intelligence. Another characteristic of current and future avionics systems is *data fusion*. This means that the data generated by different sensors is combined in a way that increases the situational awareness of the pilot or operator, with an increased

accuracy due to cross-checks across multiple sensors, a reduced pilot/operator work-load, and finally, a high degree of task automation.
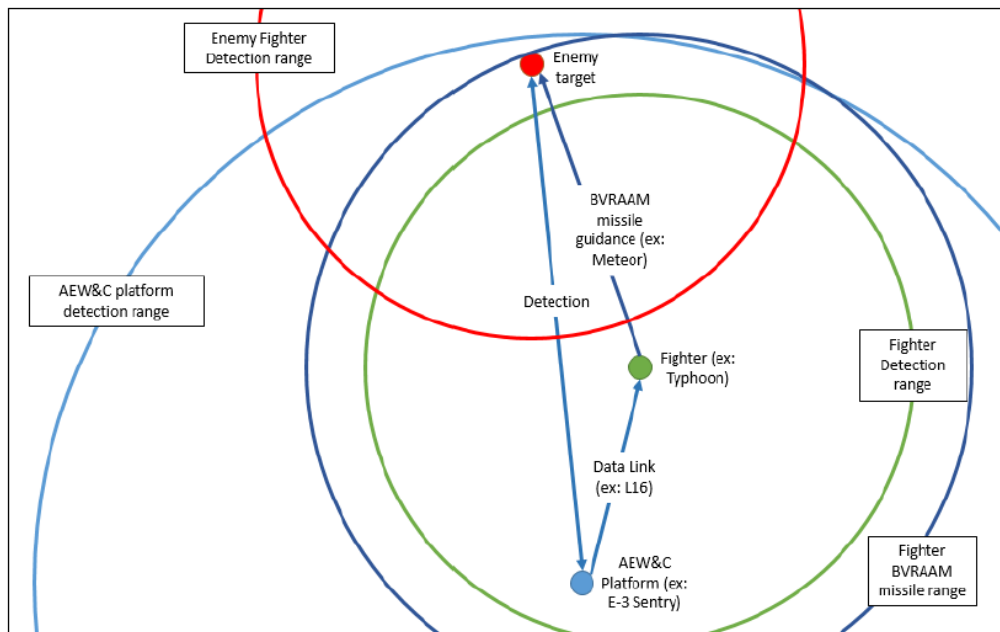
Figure 6-41 - Network centric warfare tactical scenario[201]

The designer has decided to include a high degree of commonality between the fighter and the UCAV configurations, which would help reduce development costs, ease maintenance and replacement of shared modules. Only the UCAV relevant avionics systems will be mentioned hereafter.

The main avionics architecture has been divided into five sub-groups:

1. Control station systems: displays and communications with UCAV.
2. Avionics systems: communications, navigation and flight management system.
3. Mission systems: all sensors integrated into the aircraft, electronic warfare sensors and mission computing modules.
4. Weapons system: interface between weapons and the aircraft.
5. Vehicle systems: propulsion system, fuel system, electrics, and flight control.

Three data buses are used to connect all the sub-groups together, these are:

1. Main data bus consisting on a fibre optics channel technology. This channel connects all avionics, sensors and defensive sub-systems, achieving data rates as high as 1+ GB/s.
2. IVHM data bus consisting on the widespread IEEE 1394b. This data bus connects the flight control system, hydraulic and electric systems sensors.
3. Weapons data bus based on the MIL-STD-1760, ensuring high integrity of data between the aircraft and the weapons.

Communication between the ground control station (GCS) and the UCAV can take place through a line-of-sight Ku-band datalink with a range of 200 km, or SATCOM for beyond line-of-sight operations.

An Integrated Navigation System that fuses Global Navigation Satellite Systems (GNSS) and Inertial Navigation sensors has been integrated into a triple redundant Flight Management System (FMS), as shown by the diagram in Figure 6-42.
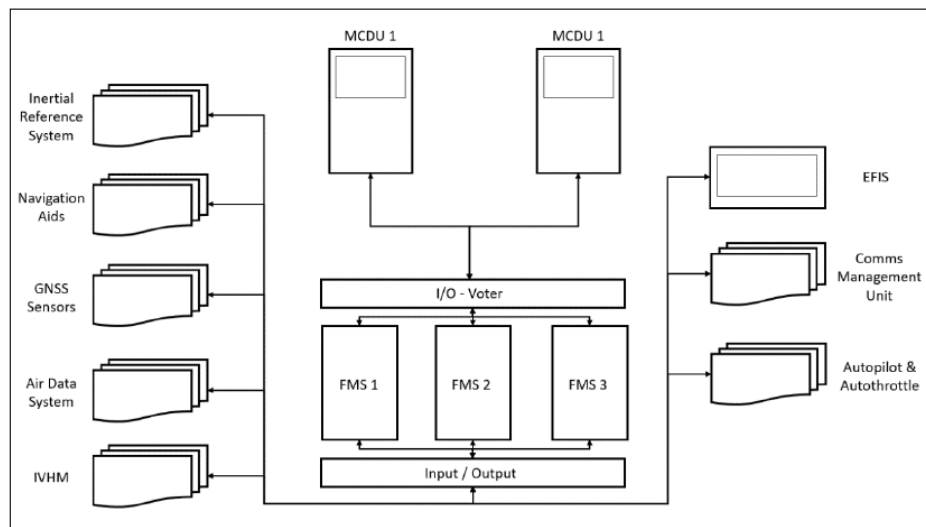
Figure 6-42 - Triple redundant FMS[201]

In terms of identification sensors, the UCAV will be equipped with ATC Mode S for airborne collision avoidance, ADS/A and ADS/B for oceanic and overland crossings navigation, and finally, IFF MK XII military transponders for identification of allied and enemy platforms.

One of the most problematic aspects of the UCAV avionics systems or sub-systems relates to the Integrated Hazard Detection and Avoidance System (IHDAS), part of the Communication, Navigation and Identification (CNI) system. This system has a strong relation to the level of automation intended during unmanned operations. A top-level IHDAS architecture has been proposed for the 6th generation fighter as shown in Figure 6-43. Unmanned aircraft automation levels are still a uncertain, with strong support and opposition on both ends of the spectrum, from remotely operated to fully autonomous decision-making machines. However, if the UCAV is intended to operate in highly cooperative joint operations under the command of one or more manned bomber/fighters, a high degree of autonomy will be required, which in turn might require full-authority detect and avoid capabilities within the UCAV systems.
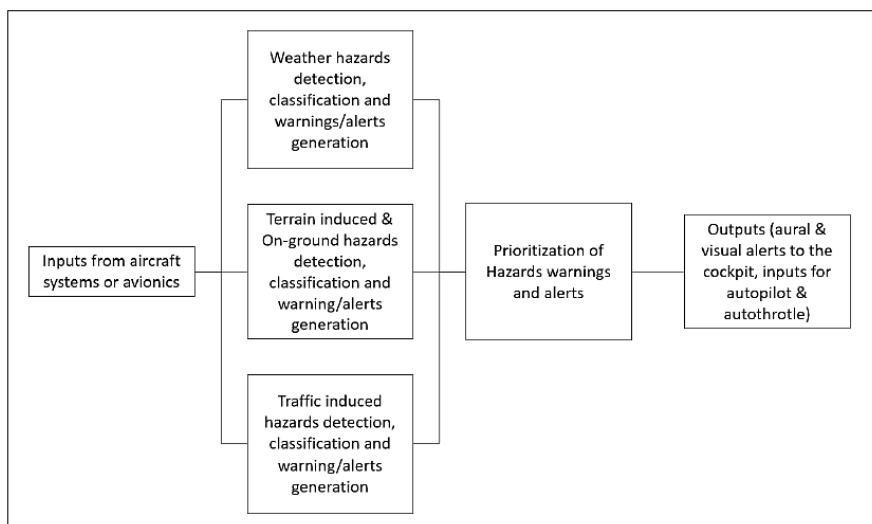
Figure 6-43 - IHDAS top-level architecture[201]

The avionic systems component locations are shown schematically in Figure 6-44, and in the CAD packaging images in Figure 6-45. A description of the sensors will be given below:

Radar: The radar consists of an Active Electronically Scanned Array (AESA) system. Initially intended to be the same as component as the fighter, but due to size restrictions the diameter has been reduced by two, which results in a surface area and emitting power reduction by a factor of four. If more power is required

after a more detailed evaluation, a potential solution consists of adding conformal AESA antennas.

Number	System	Type	Elements	Band (GHz)	Functions
1	Radar, EW, CNI	WBSA	300	6-12	A/A & A/G radar, RWR, ECM,SA, Passive Targeting, CHBDL, Weapon Data Link
2 & 3	EW,CNI	WBSA	200	6-18	RWR, ECM, SA, Passive Targeting, CHBDL
4 to 6	EW,CNI	WBSA	64	2-6	RWR,ECM,SA,Data Link, MLS
7 & 8	EW	Spiral	1	2-18	RWR,ECM receiver
9 to 12	CNI	MASA	8	0.2-2	UHF, GPS, ILS glideslope, JTIDS, TACAN, IFF Receiver, TCAS
13 & 14	CNI	MASA	8	0.2-2	IFF Interrogator
15 & 16	Radar, EW	MASA	8	0.2-2	RWR, SA, ECM, SAS
17 & 18	EW, CNI	MTL	1	0.03-0.2	VHF, SINCGARS
19 & 20	EW, CNI	MTL	1	0.03-0.2	VOR, ILS localizer, SINCGARS,
21 & 22	CNI	MTL	1	0.002-0.03	HF, L11

Figure 6-44 - Antenna positioning in UCAV design (adapted from Moraillon[201])

a) Integration of avionics components - isometric view

b) Bottom and top views of antenna locations
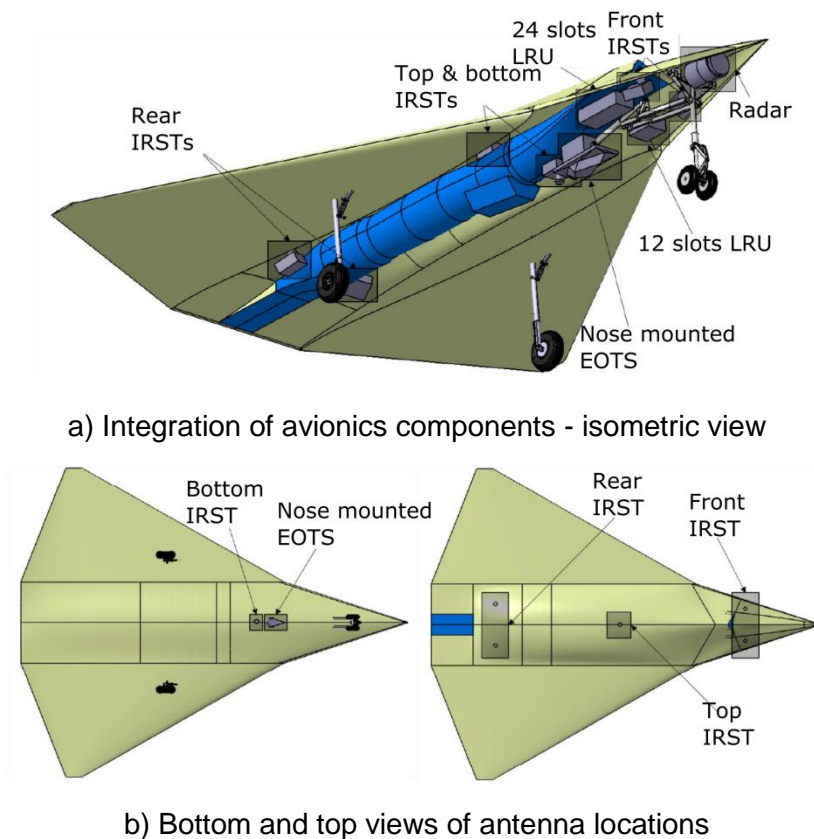
Figure 6-45 - Packaging of avionics components (adapted from Moraillon[201])

EW and EO suites: This sensor is based around the Electro-optical Targeting System (EOTS) found in the F-35, developed by Lockheed Martin. The capabilities of this system include forward-looking infrared, laser designator, TV imaging and laser spot tracker, as well as full coverage infrared search and track (IRST) and missile approach warning all around the aircraft.

Lastly, regarding the design of the control station (CS), the designer recommends adopting the single-pilot layout recently demonstrated by General Atomics for the operation of the MQ-9 Reaper fleet. However, there is a trade-off between the location of the CS and the latency of the communications, with a latency of 1-1.2 seconds via SATCOM, in case of remote operation from a location far from the operational theatre. Local CS may reduce latency through radio data-links, or an airborne CS can be adapted through early warning aircraft such as the C2 platform. A final and more advanced solution would be to directly monitor the UCAV through nearby 6th generation fighters. This solution would require high degrees of autonomy on the UCAV side, which might not be a feasible solution within the next 5-10 years.

6.7.6 Summary of Preliminary Design Studies

Through a series of preliminary design studies, the feasibility of what is being referred to as a 5th generation UCAV has been explored. Even though the designers have worked in conjunction as much as possible, some discrepancies remain which require further design efforts.

The structural concept has been completed in a qualitative and schematic way without a complete definition of the aerodynamic or inertial loads. The presented structure represents the minimal structural elements required to carry and transmit the load *types*. A more detailed analysis might reveal a different structural arrangement and distribution, especially around the weapon bay areas. Structural and packaging issues have also been identified for the main landing gear, specifically its longitudinal position and structural attachment. A somewhat complex wheel rotation system has been included for the MLG due to the limited storage volume.

Payload integration resulted in complex arrangement due to the large size of the intended weapons to be carried. General recommendations include a re-evaluation of the selected payload in order to improve the structural arrangement and packaging of the UCAV.

The engine integration study has shown that an off-the-shelf option exists to satisfy the thrust requirements during the most demanding mission segments. However, detailed performance studies have not been carried out, and higher fidelity aerodynamic data are required in order to draw any definite conclusions in this regard. Moreover, an aerodynamic optimisation to improve performance and stability is required in order to determine the span-wise twist and optimal aerofoil shapes. Several packaging aspects remain unresolved, including the detailed sizing of the gearbox for power generation, and the packaging of secondary engine systems. The initial analysis concludes that there is enough space for all considered systems thus far; however, the intake and exhaust design requires further work for improved stealth, performance, and packaging.

The airframe and power systems design has followed a more electric and power-by-wire philosophy. A series of electrohydrostatic and electromechanical actuators have been used for primary and secondary surfaces. Furthermore, typical APU architectures have been replaced by and Integrated Power Pack, solid state electronics, and a Power and Thermal Management System in order to generate and distribute a primary high voltage power supply, and manage the thermal needs of the UCAV during subsonic and supersonic flight. Redundancy has been achieved through two independent electrical supply busbars, and an emergency supply procedure.

Low-observability studies have confirmed the relevance of smooth surfaces, including the sharp UCAV nose and the reduction in signature by removing tail plane surfaces. However, the effects of the intake geometry and material choices have not been explored due to the low maturity of the CAD available at this stage of the design efforts.

The avionics system design has sought to provide with high degrees of commonality between a 6th generation fighter design and the proposed 5th

generation UCAV. The main philosophy for the design of this system was the network centric operations envisioned in the future aerial warfare. Mechanical radars have been replaced by electronical scan array radars for increased flexibility and accuracy with reduced mechanical complexity. State of the art electro-optical targeting systems have been integrated following the F-35's design, which provides with an all-around the aircraft vision and warning systems. The packaging of the avionic components has been achieved but several restrictions have been found due to the compact UCAV geometry, specifically the reduction in the radar area and the inherent reduction in its capabilities. Conformal antennas could be added if further analysis shows the frontal antenna cannot comply with the requirements.

The most pressing question that remains for the avionics system design relates to the degree of automation included in the UCAV operations. This will have a major impact on the identification, avoidance, and engagement of other manned and unmanned aircraft, as well as the design and deployment of control stations, including ground-based control stations and potential airborne solutions.

Final recommendations on the conceptual and preliminary design of a 5th generation UCAV include the following:

o An explicit declaration of the operational envelope, including maximum speeds and altitudes

o Aerodynamic optimisation of the twist distribution and potential aerofoil changes to improve stability (reflex aerofoils)

o A complete characterisation of the inertial and aerodynamic loads

o A revision of the payload selection for easier packaging integration and improved structural integrity

o Improved design of low-observable features, including the intake and exhaust/nozzle

o Explicit definition of acceptable/autonomy levels for a more detailed avionic system evaluation

7 SUPERSONIC UNMANNED AERIAL VEHICLES

7.1 Introduction

Military authorities all around the globe are currently seeking transformational capabilities aiming towards entire fifth generation forces, not just aircraft. This challenge can be addressed through several technologies, one being the creation of unmanned aircraft capable of operating in co-operative, network centric scenarios, along with current fifth generation fighters, legacy fighters, and possible sixth generation aircraft. Besides high performance requirements, such as supercruise and large normal acceleration turns, low-observability is also desirable in order to produce effective and survivable platforms. Therefore, supersonic tailless UCAVs are ideal candidates for addressing these needs.

Furthermore, high supersonic (M 3+) aircraft can provide a significant advantage, especially in *first day of war* operations, where time critical and high value targets (HVT) are to be engaged.

This section presents the conceptual design studies carried out in order to establish feasible concepts to meet this transformational challenge.

7.2 Deep Interdiction UCAV

This mission aims to develop a platform that can effectively deliver precision guided tactical weapons at a long range and supersonic speeds, and that can be deployed with minimum support to regional conflicts, with a starting service date around the year 2030.

The mission requirements are based on the RFP published by AIAA's design competition in 2001/2002, as shown in Jenkinson's design exercise[202, chap.8], which will be used to establish baseline design assumptions. Several requirements have been modified to more closely resemble the capabilities and sizes of potential UCAV platforms performing similar roles, as well as to reflect a more appropriate service entry date.

7.2.1 Mission Design

The interdiction mission (Hi-Hi-Hi) is described in Figure 7-1, and the mission phases below, while the original and modified requirements are given in Table 7-1.

0-1   Warm up and take-off. Normal field performance is specified as <2500m

1-2   Minimum time to climb to supercruise altitude (12.2 km)

2-3   Supercruise to conflict area (M 1.6)

3-4   Climb to 15 km and accelerate

4-5   Dash to target (M 2.0)

5-6   Turn and weapon release

6-7   Dash out (M 2.0)

7-8   Descend to supercruise altitude (12.2 km)

8-9   Supercruise to return (M 1.6)

9-10   Descent and landing

Table 7-1 - Deep Interdiction Mission Requirements

Requirement	Original	Modified
Supercruise segments (each)	1852 km	1500 km
Dash segments (each)	1390 km	900
Field Performance	All weather capability, including icy runways (8000 ft/2440 m)	
Max. Payload	~6200 kg	~4000 kg (Four 2000 lb JDAM + two AIM-120)
Structural limits	+7/-3 g with 50% fuel	
Maximum dynamic pressure	103 kPa	
Subsonic static margin limits	+10/-30 %	
SEP (1g) mil power, M 2.0/15 km (50% fuel, 100% payload)	0 m/s	
SEP (1g) max power, M 2.0/15 km (50% fuel, 100% payload)	60 m/s	

SEP (2g) max power, M 2.0/15 km (50% fuel, 100% payload)	0 m/s	
Max. instantaneous turn rate M 0.9/4.5 km (50% fuel)	8°/s	
RCS signature ($\theta = 90, \phi = 0, S\ band\ 3\ GHz$)	-13 dB	-30 dB
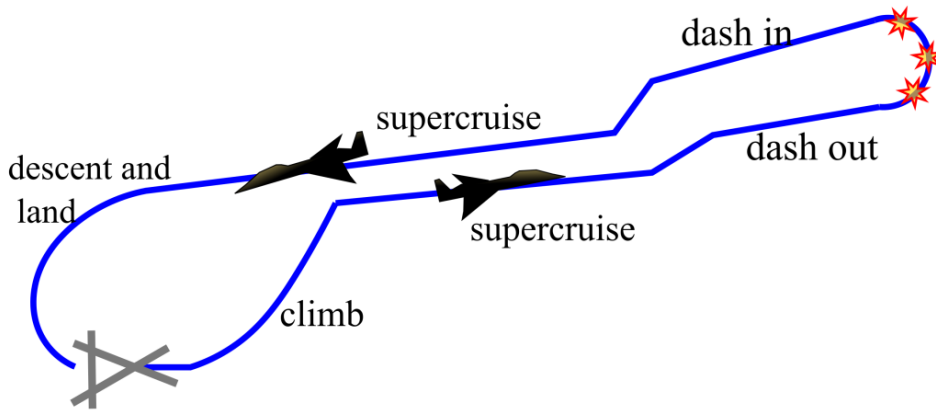
Figure 7-1 - Deep Interdiction mission diagram

7.2.2 Initial Design Assumptions

The central focus of this design should be minimising wave drag at supersonic speeds. In order to achieve this, a smooth area distribution should be achieved, as well as a long and slender configuration, as shown by the empirical wave drag rise in Eq. (7-1).

$$\Delta C_{D_{wave}} = \frac{14.14 \left[\frac{A_{Max}}{L}\right]^2}{S_{ref}}$$

(7-1)

Furthermore, the wing leading edge should be kept inside the Mach cone, which limits the span and sweep angle ($\Lambda_{LE} \geq 90 - \mu$), as given by the Mach angle, such that:

$$\mu = \sin^{-1}(1/M_\infty) \quad \text{For a cruise Mach number of 2.0: } \mu = 30°$$

Therefore, a wing leading edge sweep greater than 60° is required for a subsonic leading edge; subsonic or transonic aerofoils can be then used to reduce drag and fuel consumption.

189

Additionally, in order to maintain low-observability, a tailless configuration has been chosen, with all internal payload, as well as low-observable intakes and exhausts. Variable intake geometry has been taken into account for the mass prediction, but the detailed geometry, internal aerodynamics, and actuation system will not be addressed.

An initial wing loading of 3820 N/m^2 has been chosen as a compromise between strike and bomber aircraft; a thrust loading of 0.6 (sea level, dry) and a payload ratio of 15% have been estimated. These estimates yield a take-off mass of 26700 kg, a wing area of 68.6 m^2, and a sea level thrust of 157 kN. Furthermore, an initial estimate of 30% fuel fraction results in 8010 kg of fuel.

A simple analysis of delta and double delta wing geometries shows that for equal spans, a double delta configuration will result in generally longer centreline chords, reducing wave drag. Furthermore, increasing the taper ratio of the central wing section ($\lambda_1 = C_1/C_0$) and decreasing the central span ratio ($\gamma_1 = b_0/b_{total}$) will result in longer configurations as shown in Figure 7-2 (values shown for a fixed wing area of 68.6 m^2), and responding to Eq. (7-2):

$$C_0 = \frac{2S_{ref}}{b[\lambda_1(1 - \gamma_1) + \gamma_1(1 + \lambda_1)]} \qquad \textbf{(7-2)}$$
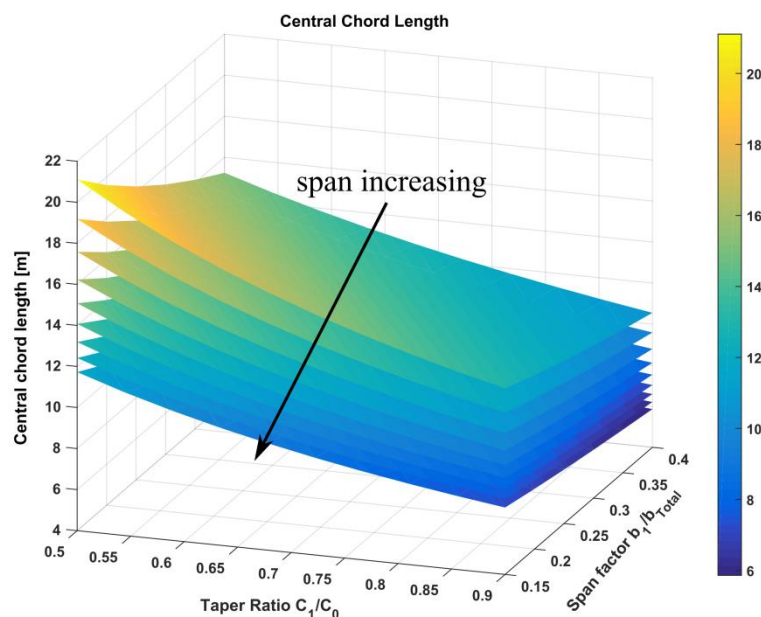
Figure 7-2 - Central chord length as a function of taper and span ratios

Long and slender configurations are achieved with low values of span ratio and high taper ratios. Low spans, and reduced outer wing chords will have an impact in aerodynamic efficiency, and fuel volume, which result in contradictory design preferences.

Another important geometric constraint is that of maintaining subsonic flow conditions at the leading edge in order to reduce drag and fuel consumption.
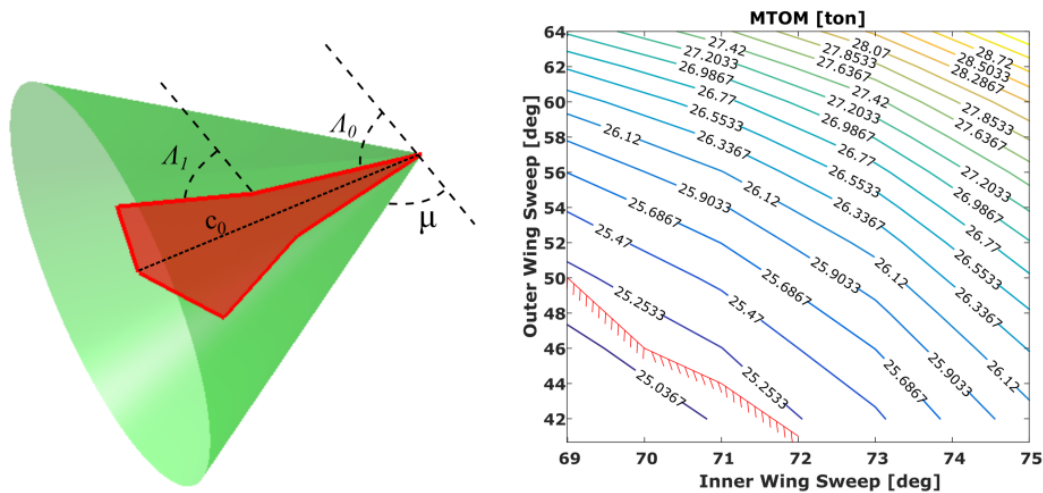
Figure 7-3 - Subsonic leading edge constraint (hatched line)

Choosing a large leading edge sweep angle for the central wing section allows for sweep values on the outer wing less than 60° while retaining the subsonic leading edge condition, as shown in the right hand side of Figure 7-3. Low sweep values also reduce the wing structural mass penalty, but increase transonic and supersonic drag.

Furthermore, the high payload requirements translate into stringent volumetric and packaging constraints, especially affecting the central wing section, and the fuel tanks arrangement. The weapon bay dimensions depend on the choice of weapons abreast, as given in Table 7-2.

Table 7-2 - Weapon bay dimensions

Weapons abreast	Length [m]	Width [m]	Height [m]
4	3.9	3.2	0.8
2	7.0	1.6	0.8

Based on the estimated wing area, and choosing values of the central wing section taper and span ratio, 0.65 and 0.2 respectively, to maximise the central chord length without excessively limiting the central wing section volume available for payload and propulsion systems, resulted in a configuration with a total wingspan of 12 m, a centreline chord of 13 m, and a wing kink chord of 8.51 m, with a tip chord of 0.1 m. The centre wing has a leading edge sweep angle of 75° with a total semi-span of 1.2 m, while the outer wing has a leading edge sweep angle of 60° and a semi-span of 4.8 m, which satisfies the subsonic leading edge constraint for all wing sections.

Furthermore, the central wing section acts a pseudo-fuselage, while the outer wing uses a supercritical aerofoil with design lift coefficient of 0.4 and a thickness of 6%. Finally, two afterburning turbofans based on the GE F404-402 have been assumed and located over the weapon bays on 2 body component nacelle objects in order to properly account for the wave drag and volume distribution at supersonic speeds; this configuration is schematically shown in Figure 7-4.

An initial convergence check using the GENUS optimisers was carried out in order to obtain the characteristics of the aircraft. During this loop the geometry remained fixed. The resulting MTOM is 23473 kg, with an OEM of 13890 kg, and a total fuel consumption of 5580 kg. The nose-on RCS signature $(\theta = 90°, \phi = 0°)$ for a perfect electric conductor material is -30.29 dBsm.

Due to the large volumetric requirements resulting from the large payload, and the required fuel consumption, it was determined that the vehicle's dimensions were insufficient to comply with volumetric constraints, specifically the available fuel tank volume. Furthermore, unresolvable clashes were found between the landing gear and the weapon bays due to the limited central chord length and central wing section span. An acceptable CG range, static margin, and trim for all flight conditions were not found, again pointing towards a revised vehicle sizing. The original wing loading value of 3820 N/m^2 has been found to be too restrictive, due to the fact that the central wing section is acting as a fuselage and the additional volume usually provided by a conventional fuselage is not available.
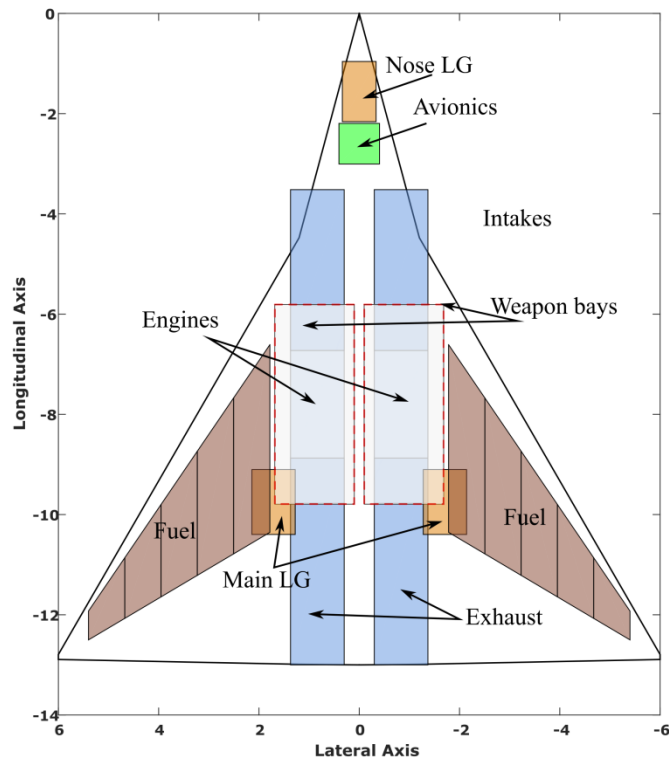
Figure 7-4 - Non-compliant initial UCAV with packaging

A revised baseline configuration has been resized by first imposing the central wing section geometry as a function of packaging constraints, mainly coming from the selection of the 4-abreast weapon selection, resulting in a central span of 3.6 m, and a total centreline length of 17 m.

Subsequently, the LSGRG2 gradient-based optimiser was then used to size the outer wing chord and outer wing span at a fixed sweep angle of 60°, with input variables and constraints given in Table 7-3, and with the take-off mass as the objective function.

Table 7-3 - Interdiction UCAV baseline sizing optimiser data

Input Variable	Lower Bound	Upper Bound
Outer wing λ_1	0.5	0.65
Outer wing semi-span	3 m	5 m
Estimated Take-Off Mass	15000 kg	35000 kg
Estimated Fuel Fraction	15%	35%
Engine Diameter	0.8 m	1.2 m

Constraints	
Fuel Volume	$Vol_{Av} \geq Vol_{Req}$
Subsonic Leading Edges	$\{XYZ\}_{LE_i} < \{XYZ\}_{MachCone}$
Mass Error	$\|MTOM_{Calc} - MTOM_{Est}\| \leq 1E\text{-}4$
Fuel Error	$\|Fuel_{Calc} - Fuel_{Est}\| \leq 1E\text{-}4$
SEP Errors	$Ps_{Av_i} \geq Ps_{Req_i}$
Thrust Errors	$T_{Av_i} \geq T_{Req_i}$

The resulting outer wing taper ratio is 0.6, meaning an outer wing chord of 10.2 m, and an outer wing span of 4.0 m. The total wing area is 90.23 m^2, with an outer wing area of 78.3 m^2. The overall aspect ratio is 1.486.
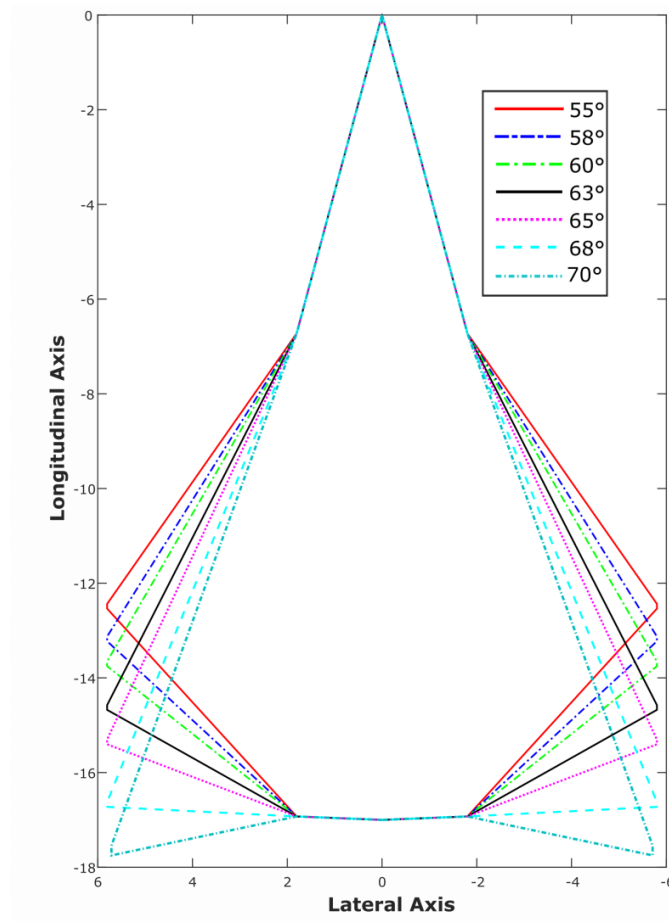
Figure 7-5 - Configurations with varying outer wing sweep

Outer wing sweep angles ranging from 55° up to 70° (top views given in Figure 7-5) were investigated to quantify the effects of wing structural mass penalty, reduced wave drag, and changes in the RCS signature.

From the results shown in Figure 7-6, fuel ratio is inversely proportional to sweep angle due to reduced wave drag at supersonic speeds (Figure 7-7), while the wing structural mass increases as sweep increases. At high sweep angles (> 65°) the wing structural mass penalty results in higher empty mass, leading to an increase in engine size and fuel consumption. This can be seen by the sharp increase in take-off mass, as well as the plateauing of fuel fraction.

The dominating constraints for all configurations were the specific excess power requirement of 60 m/s at Mach 2.0 and 15 km altitude, with 50% fuel, 100% payload and afterburner on; the fuel volume required, and the engine throttle at dash Mach number.
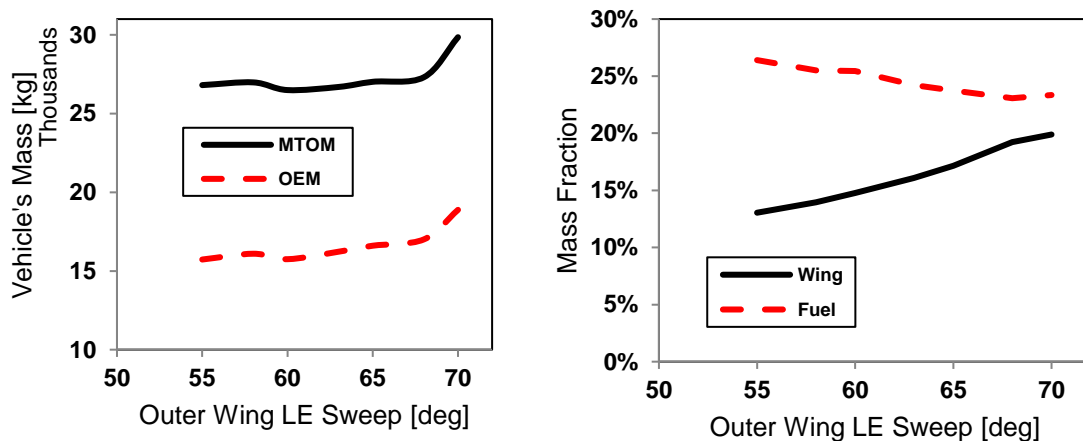
a) Take-off and empty masses against wing sweep angle

b) Fuel fraction and wing mass fraction against wing sweep angles

Figure 7-6 - Effects of outer wing sweep on vehicle's masses

Another aspect to consider is the trailing edge sweep angle and control surface effectiveness. Similar studies suggest limiting trailing edge sweep angle to a maximum of 30° forward. As shown in Figure 7-8, this limits the selection to configurations with leading edge sweep angles higher than 62°. This trend is also beneficial to RCS signature, since configurations with sweep angles less than 60° do not comply with the set requirement of -30 dBsm.
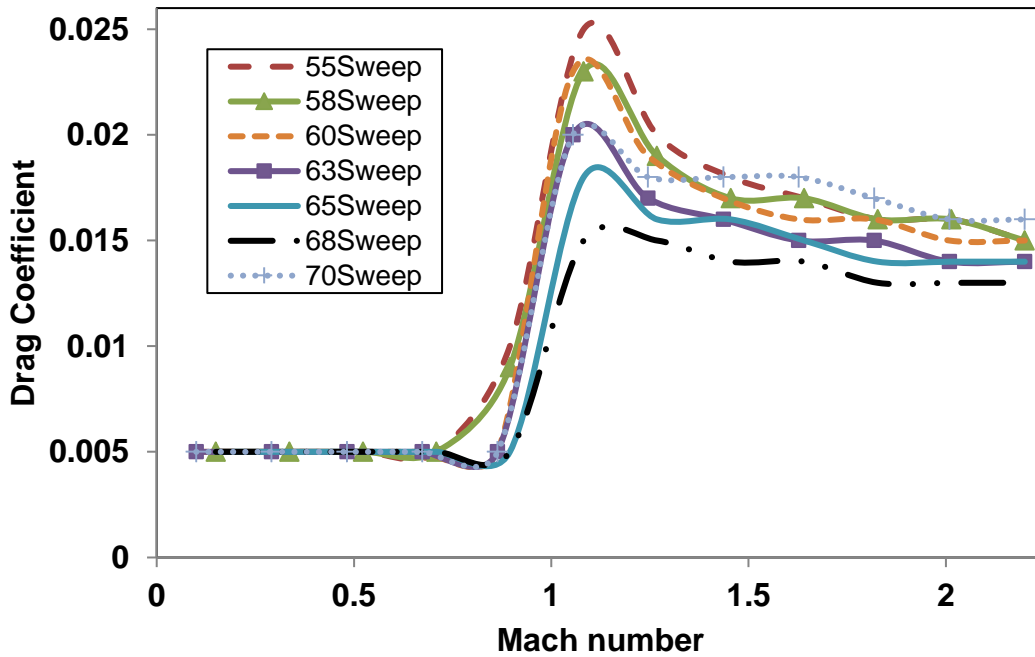
Figure 7-7 - Drag coefficient as a function of outer wing sweep angle
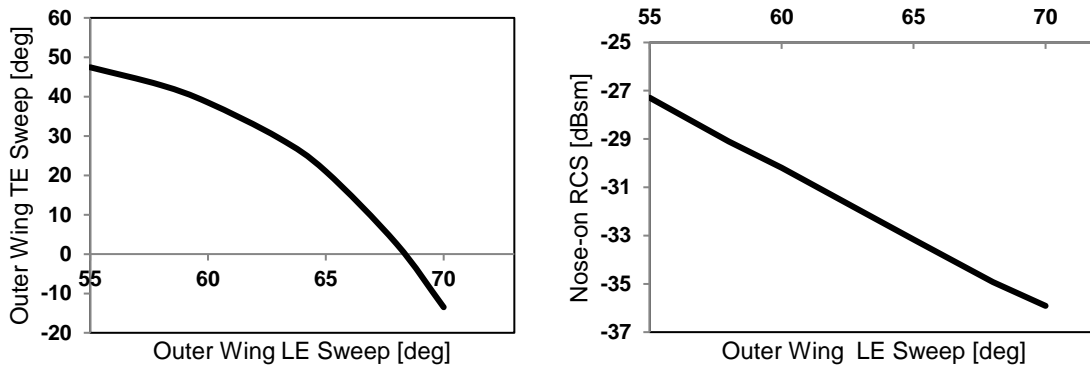
a) LE and TE sweep angles

b) Nose-on RCS signature vs sweep

Figure 7-8 - Trailing edge sweep and RCS signature as a function of leading edge sweep

Considering all of the above design criteria, the final baseline configuration results in an outer wing sweep of 63°, a trailing edge sweep (forward) of 29.5°, a take-off mass of 26690 kg, an empty mass of 16224 kg, a total fuel consumption of 6465 kg. The sea level (dry) thrust loading is 0.588, with a wing loading of 3343 N/m² when considering only the outer wing area.

A comparison of the initial design assumptions and the baseline design characteristics is given in Table 7-4. It has been found that a payload ratio of 15%

is an accurate estimate, while the initial fuel fraction was reduced by 5.5%. Similarly the sea level thrust was reduced by 7.6%. The largest difference is a wing area increase of 31.5%, mainly due to packaging and fuel volume constraints.

Table 7-4 - Comparison of initial assumptions and final results

Design Parameter	Initial Assumption	Final Result
Take-off Mass	26700 kg	26690 kg
Payload fraction	15%	15%
Fuel fraction	30 %	24 %
Thrust loading	0.6	0.588
SL Thrust	157 kN	154 kN
Wing loading (outer wing)	3820 N/m^2	3343 N/m^2
Wing area	68.6 m^2	90.23 m^2

A top-level mass breakdown is given in Figure 7-9, compared to a manned aircraft designed for a similar mission, as presented by Jenkinson[202, chap.8]. The much higher fuel fraction on the manned version is partly a result of the originally longer range and payload (lower payload mass fraction), and partly due to the fuel increase due to the larger engines and higher overall mass of the manned aircraft, with an estimated MTOM of 51400 kg. It can be seen that the propulsion mass fraction is equivalent in both configurations, and that the systems and structures form a larger portion of the overall mass for the UCAV, with 41% compared to 24% for the manned aircraft.

As mentioned previously, the dominating constraint was found to be the specific excess power requirement of 60 m/s at Mach 2.0 and 15 km altitude, with 50% fuel and 100% payload, this value corresponds to sustained turn values of ~4.5g, as shown by the manoeuvring diagram in Figure 7-10. Sufficient thrust was obtained during the cruise segments, with a throttle setting of 93% in dry mode during the supercruise segments, and a 97% throttle, also in dry mode, during the dash segments. Figure 7-11 (a) shows the drag envelope (shaded area, limited to 100 kN) imposed on the thrust contour (top), and Figure 7-11 (b) shows

the specific excess power maps at 1g and 2g conditions. It can be clearly seen that these mission requirements can be met by the baseline configuration.

a) UCAV   b) Manned
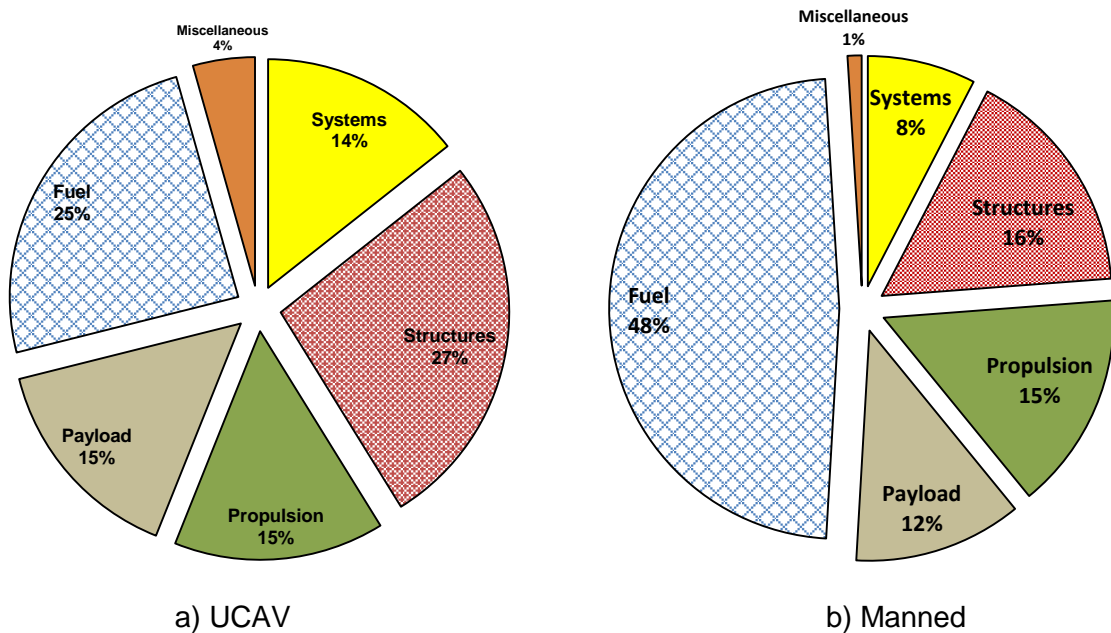
Figure 7-9 - Mass breakdown comparison of UCAV and manned aircraft

After the main vehicle characteristics were obtained, a secondary optimisation loop was performed in order to improve the packaging and CG range, as well as the static margin during the main cruise segments. Table 7-5 shows the input variables and constraints applied during this loop.

The results of the packaging and CG optimisation are shown schematically in Figure 7-12, and the CG translation and static margin during the main cruise segments are shown in Figure 7-13. A minimum static margin of -6.3% occurs during the dash in segment, which is well within the requirement limits.

Fuel scheduling has not been fully explored at this stage of the design, and as seen from three-view schematics in Figure 7-12, there are potential locations for additional trim tanks, specifically behind the main landing gear bays.
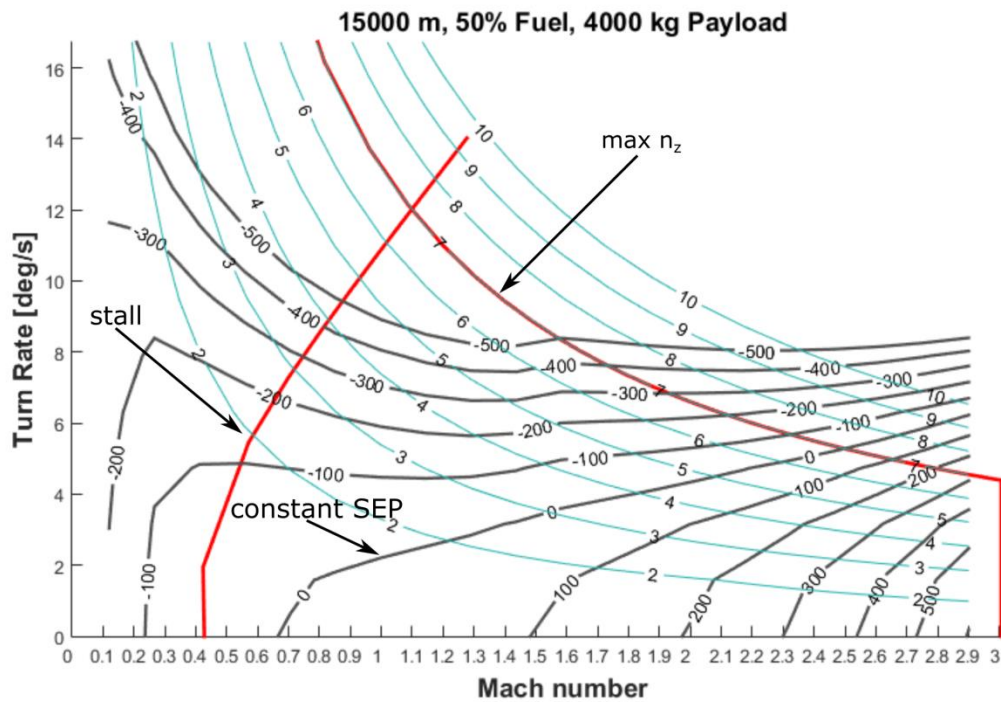
Figure 7-10 - Manoeuvring diagram during dash segment

Table 7-5 - Packaging and CG optimisation inputs

Input Variable	Lower Bound	Upper Bound
Engine CG	11.05 m	12.75 m
Weapon Bay CG	10.0 m	10.54 m
Nose Landing Gear CG	1.53 m	3.4 m
Main Landing Gear CG	11.9 m	14.45 m
Constraints		
Nose Landing Gear load	$8\% \leq NLG_{load} < 20\%$	
Weapon Bay clash	Weapon bay most forward point inside LE; Weapon bay most aft point inside TE	
Main Landing Gear clash	Avoid clash with weapon bays, comply with landing gear loads	
Static Margin	$-30\% \leq K_{n_i} < 10\%$	
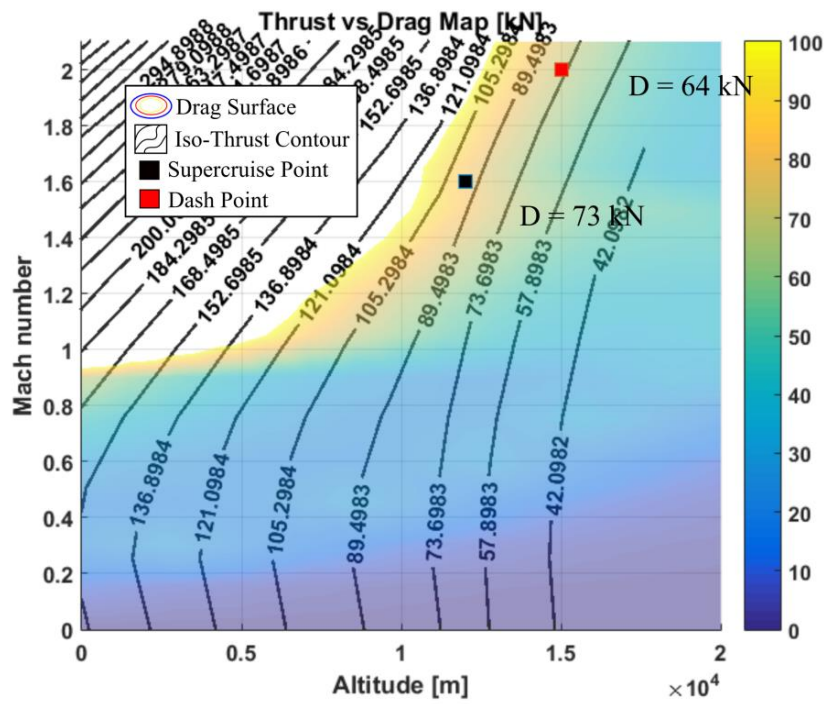
a) Thrust contour and drag surface; supercruise and dash drag
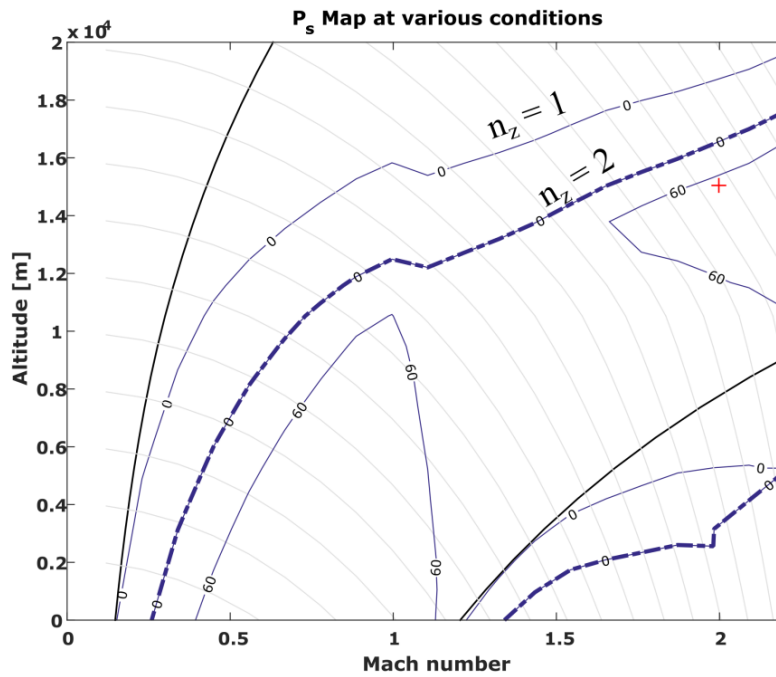
b) Specific excess power map at 1g and 2g conditions

Figure 7-11 - Thrust and specific excess power constraints
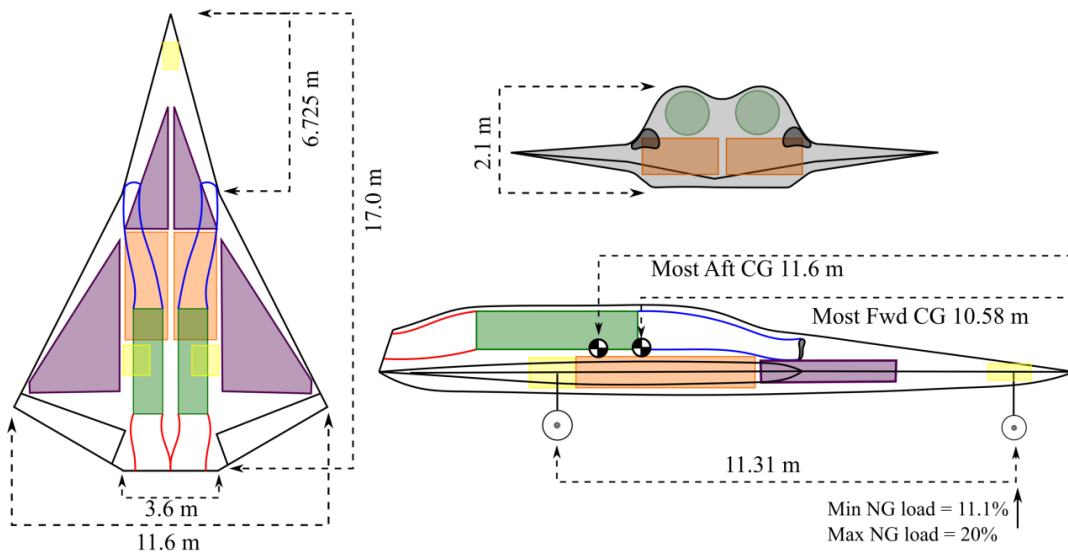
Figure 7-12 - Schematic Three-View of baseline interdiction UCAV
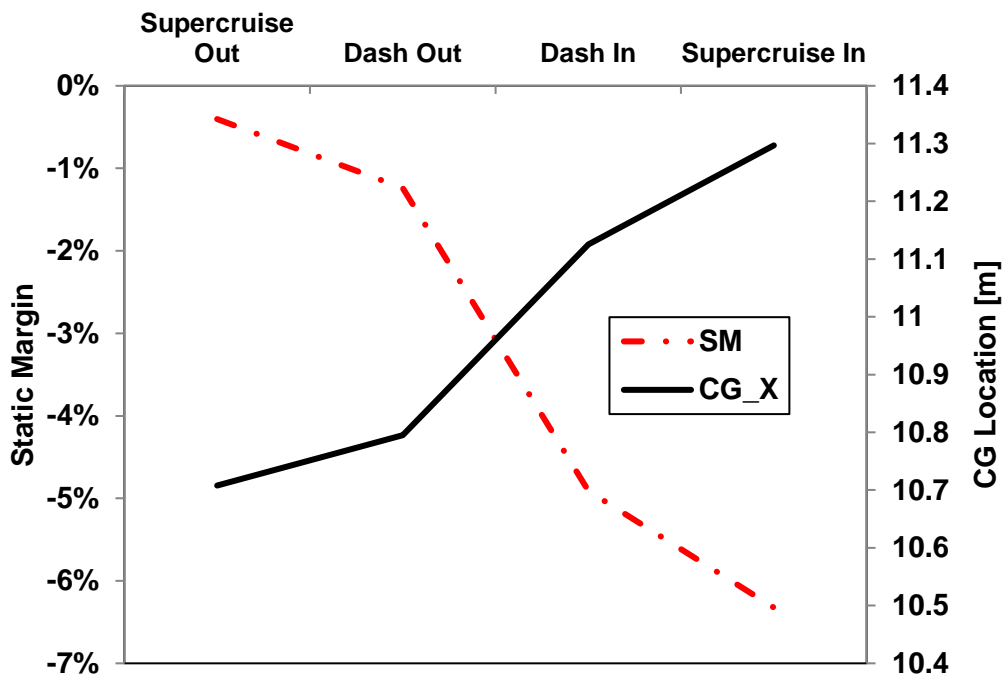
Figure 7-13 - CG and static margin during cruise segments

Prior to the operational trade-studies, it should be mentioned that additional work should be carried out in order to validate the results of the overall vehicle's masses, size, propulsion system characteristics, and general performance. In this particular case, the payload requirements and the large structural cut-outs might impose some mass penalties not yet accounted for through the existing models.

The specific strategies required have been acknowledged as further work, and are mentioned in §9.2.

7.2.3 Operational Trade-Off Studies

Given that the main purpose of this mission is to establish a new aircraft which can effectively deliver tactical payload at long range and with a rapid response, the main factors to investigate will be the supercruise Mach number and the dash Mach number; variations of ±20% from the baseline will be investigated.

From the initial sizing results, it has been observed that a specific excess power requirement of 60 m/s at max power, 1g, 50% fuel and 100% payload largely drives the engine sizing. Therefore, this requirement will be reduced by 10% and 20% accordingly, but it will not be increased by the same amounts. The variations on mission parameters are summarised in Table 7-6.

Table 7-6 - Operational trade study parameters for deep interdiction UCAV

Requirement	B-20%	B-10%	Baseline	B+10%	B+20%
Supercruise Mach	1.3	1.45	1.6	1.75	1.9
Dash Mach	1.6	1.8	2.0	2.2	2.4
SEP$_1$ (1g, mil power, @M$_{Dash}$)	0 m/s	0 m/s	0 m/s	0 m/s	0 m/s
SEP$_2$ (1g, max power, @M$_{Dash}$)	48 m/s	55 m/s	60 m/s	60 m/s	60 m/s
SEP$_3$ (2g, max power, @M$_{Dash}$)	0 m/s	0 m/s	0 m/s	0 m/s	0 m/s

A summary of the masses, propulsion output, and achieved performance is shown in Table 7-7, while the trends for take-off, empty, and fuel masses are shown in Figure 7-14. It can be seen that masses increase at reduced Mach numbers, with a marked increase in fuel consumption, while also showing that specific excess power is still the dominating design constraint for all cases except at a dash Mach number of 2.4; this is related to the increased performance of the afterburner at very high speeds.

Table 7-7 – Mach trade-off mass and performance results

Setting	MTOM [kg]	OEM [kg]	Fuel [kg]	SL Thrust [kN]	SEP$_1$ [m/s]
B-20%	28228	16573.45	7654.6	149.7	48.0
B-10%	27367.3	16474.8	6892.5	160	55.0
Baseline	26690	16224	6465	154	60.0
B+10%	26749.6	16182.6	6567	144.4	60.0
B+20%	27214.1	16680.3	6533.8	156.9	107.8
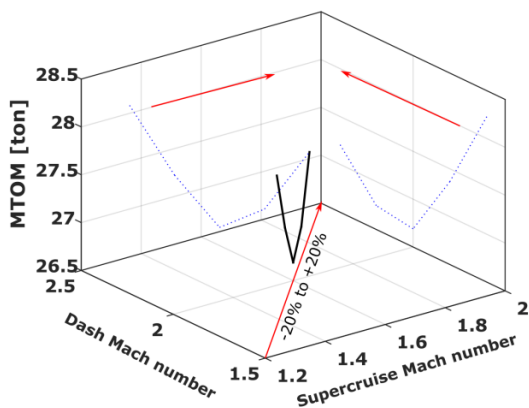
a) Maximum Take-Off Mass
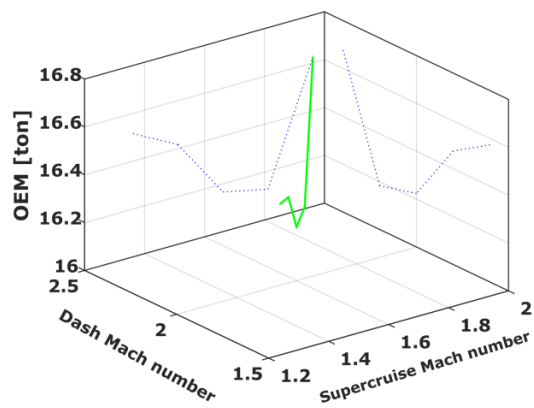
b) Operating Empty Mass
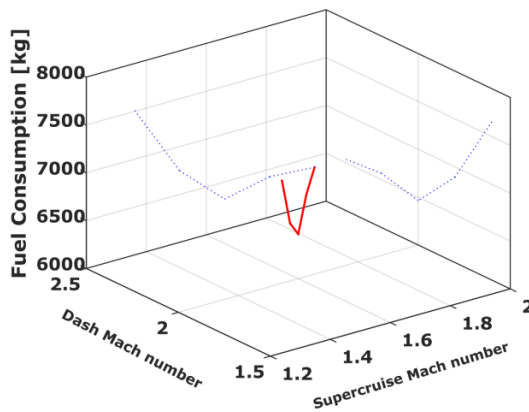
c) Total Fuel Consumption

Figure 7-14 - Take-off, empty, and fuel mass trends

The increase in fuel at reduced Mach numbers is a result of the longer mission durations and the engine sizing mostly being dictated by the specific excess power requirements. The total mission durations are 213, 188, 175 (baseline), 159, and 147 minutes respectively, as shown in the mission profiles of Figure 7-15.

The changes in several mass components and component groups as compared to the baseline configuration are shown in Figure 7-16. It can be seen that the fuel mass shows the largest change across configurations, followed by systems (propulsion system excluded), the wing structure and the overall structural mass. Conversely, despite an increment in take-off mass, the fuselage structure mass is highly dependent on the maximum Mach number, as shown in function form in Eq. (7-3).
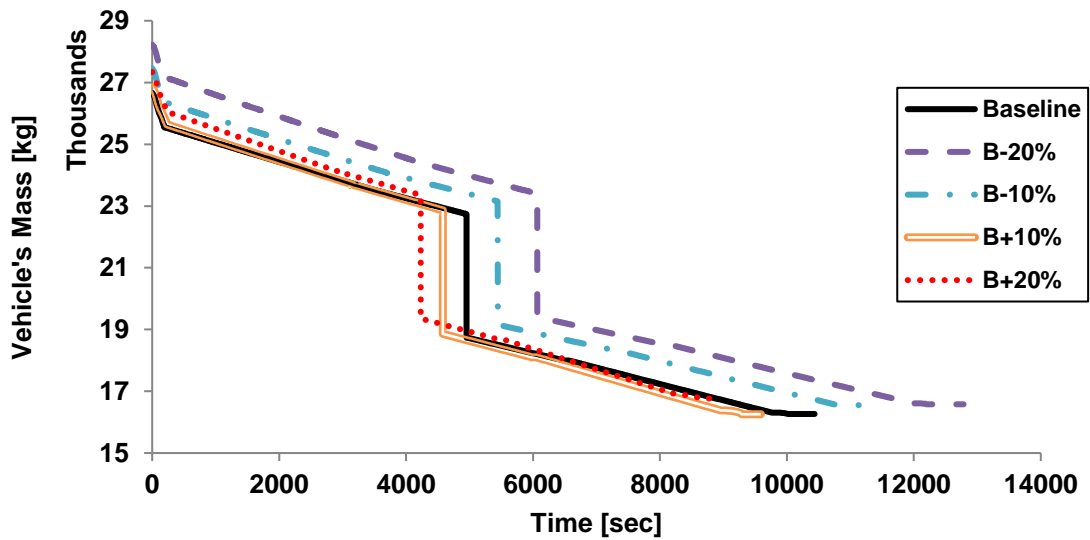
a) Vehicles' masses vs time
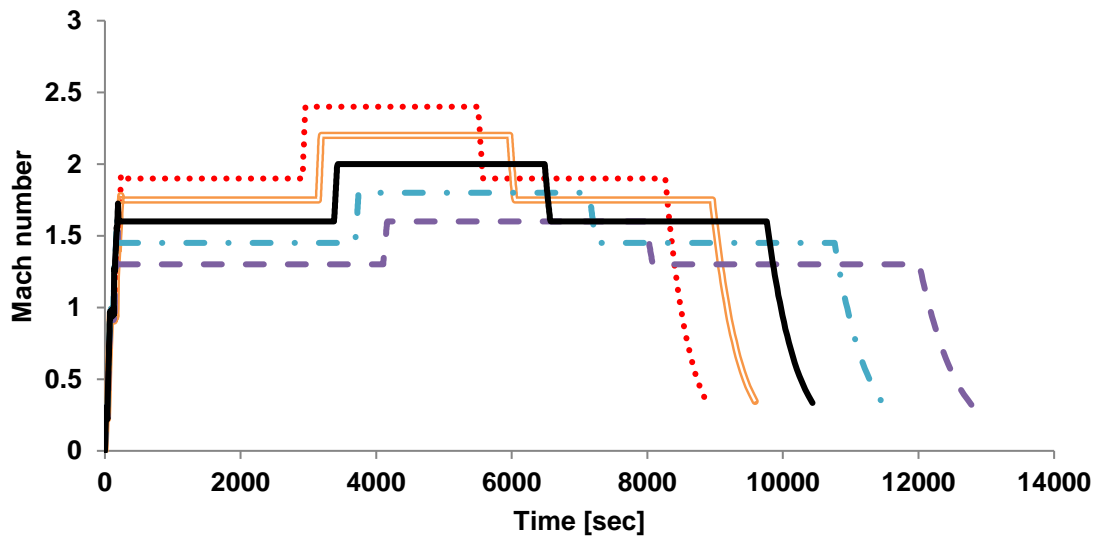
b) Mach number mission profiles

Figure 7-15 - Mass and Mach number mission profiles for all configurations
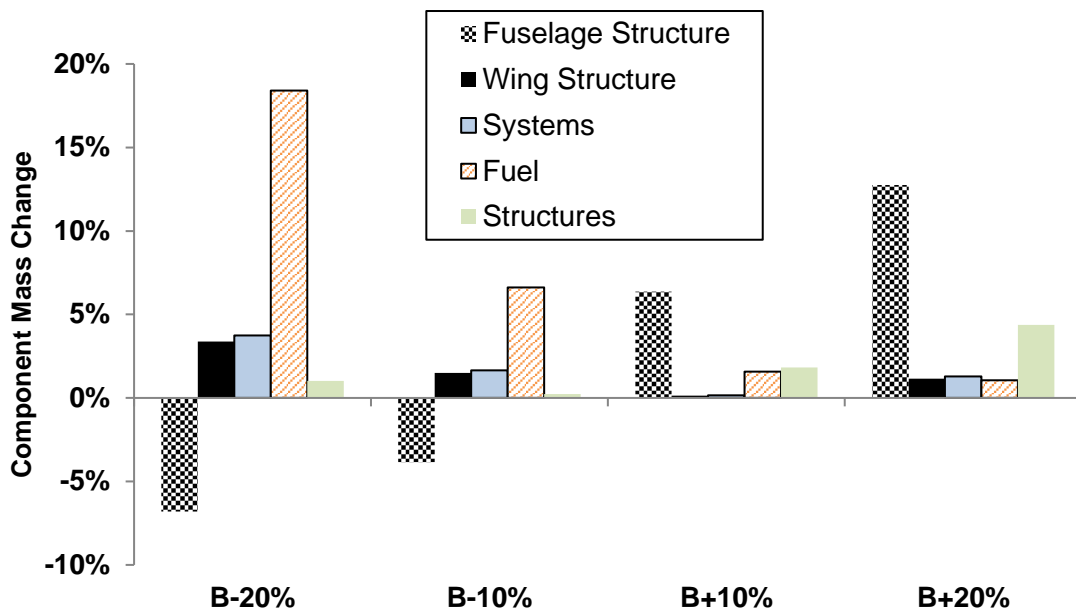
Figure 7-16 - Change in component's masses compared to the baseline

$$M_{Fuselage} = f(MTOM, M_{max}, H_{max}, W_{max}, \dots) \quad \textbf{(7-3)}$$

7.2.3.1 Expanded Design Space Exploration

Due to the observed behaviour with respect to supercruise and dash Mach numbers, an expanded design space exploration has been carried out based on the operational requirements given in Table 7-8. Specific excess power requirements follow the values set in the original variants.

Table 7-8 - Expanded operational design space parameters

Supercruise Mach	Dash Mach numbers		
B-20%: 1.3	1.5	1.6	1.8
B-10%: 1.45	1.6	1.8	2
Baseline: 1.6	1.8	2.0	2.2
B+10%: 1.75	2	2.2	2.4
B+20%: 1.9	2.2	2.4	2.5

The surface responses in Figure 7-17 show the original responses for the expanded design space exploration in the coloured patches, while the grey semi-transparent surface has been obtained through a spline interpolation across rows of constant supercruise Mach numbers. The complete data set is given in Table

205

7-9 with the extrapolated values coloured in red. Sharp increases in empty and take-off masses, fuel, and sea level thrust are shown for low supercruise Mach numbers in combination with very high dash Mach numbers. These mission points do not offer balance between the various performance criteria and are unlikely to have any operational value.

a) Maximum Take-Off Mass

b) Operating Empty Mass

c) Fuel consumption

d) Sea Level Thrust
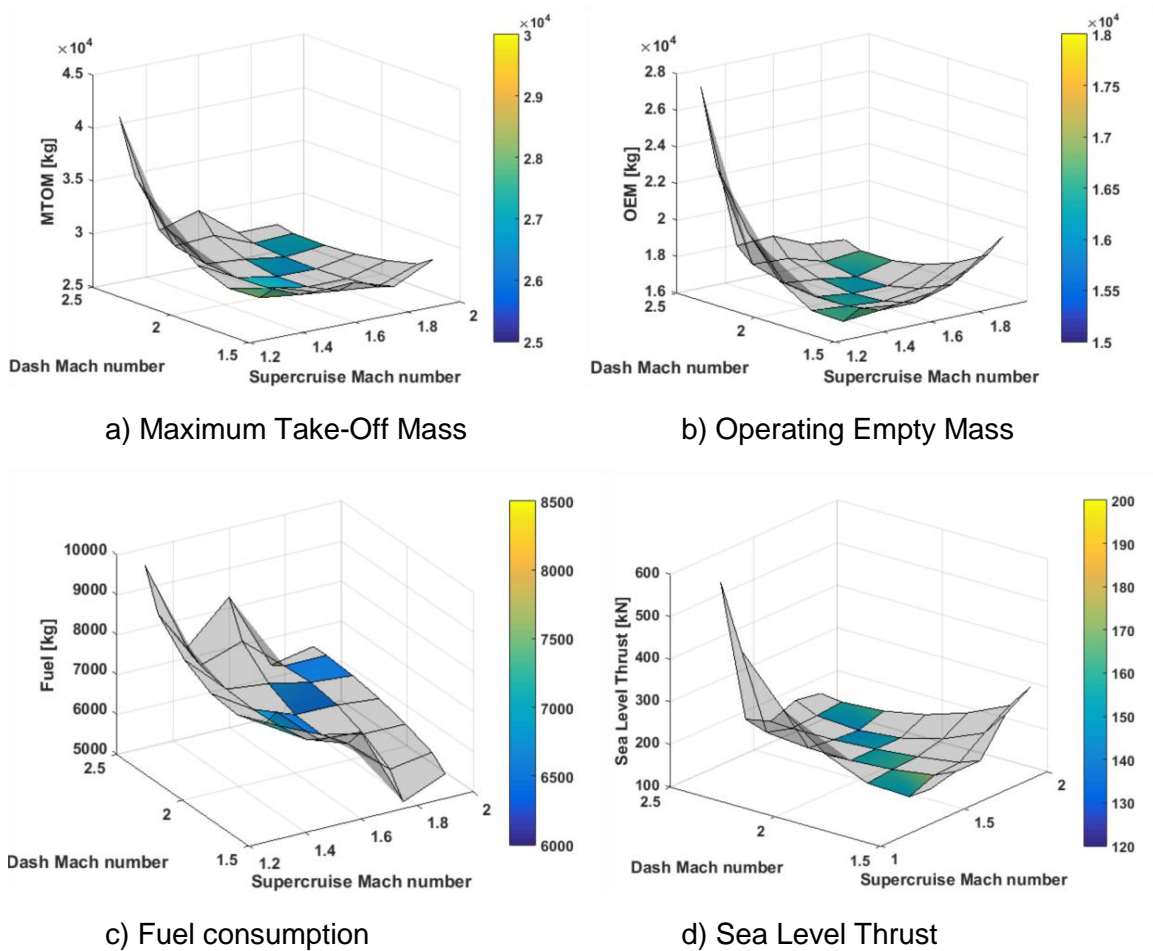
Figure 7-17 - Mach trade-off response surfaces with interpolated data

Contrary to the other trends, the minimum fuel consumption is located at an operational point of supercruise Mach ~1.8 and dash Mach ~1.5; this does not offer an operational advantage compared to the possible optimum mission point established before.

Additionally, 7 operational points have been investigated and compared to the extrapolated surfaces. The new extrapolated surfaces are shown by the red semi-transparent surfaces in Figure 7-18.

Table 7-9 - Expanded design space results (extrapolated values in red)

	Dash Mach Number						
	1.5	**1.6**	**1.8**	**2.0**	**2.2**	**2.4**	**2.5**
Supercruise	MTOM [kg]						
1.3	29717.1	28228.0	28057.6	29205.9	31672.9	35458.6	40563.0
1.45	28558.5	27788.5	27367.3	27294.9	27571.2	28196.3	29170.2
1.6	28738.0	27427.1	26744.4	26690.0	27263.9	28466.0	30296.3
1.75	27620.8	27110.5	26795.1	26674.6	26749.0	27018.3	27482.5
1.9	29461.0	28497.2	27790.7	27341.3	27149.1	27214.1	27536.3
Supercruise	OEM [kg]						
1.3	17528.6	16573.5	16631.7	17703.4	19788.4	22886.9	26998.7
1.45	17323.1	16768.4	16474.8	16442.3	16670.9	17160.6	17911.4
1.6	17569.1	16770.4	16322.1	16224.0	16476.2	17078.8	18031.6
1.75	18435.6	17344.5	16605.3	16218.0	16182.6	16499.1	17167.6
1.9	19837.2	18562.2	17609.0	16977.6	16668.1	16680.3	17014.4
Supercruise	Fuel [kg]						
1.3	8188.5	7654.6	7425.8	7502.1	7883.5	8570.0	9561.6
1.45	7235.4	7020.1	6892.5	6852.5	6900.1	7035.4	7258.3
1.6	7177.0	6659.7	6422.4	6465.0	6787.6	7390.2	8272.8
1.75	5176.2	5761.2	6188.0	6456.6	6567.0	6519.2	6313.2
1.9	5623.4	5934.8	6181.5	6363.6	6481.0	6533.8	6521.9
Supercruise	Sea Level Thrust [kN]						
1.3	181.3	149.7	153.9	193.9	269.8	381.4	528.8
1.45	196.3	174.3	160.0	153.5	154.8	163.9	180.8
1.6	196.1	177.8	163.8	154.0	148.4	147.1	149.9
1.75	278.7	221.1	179.5	154.0	144.4	150.8	173.3
1.9	317.0	259.4	214.6	182.6	163.3	156.9	163.3
Supercruise	SEP$_1$ [m/s] (1g, max power)						
1.3	48.5	48	48	-	-	-	-
1.45	-	55	55	58	-	-	-
1.6	-	-	60	60	64.8	-	-
1.75	-	-	-	60	60	97.5	-
1.9	-	-	-	-	87.5	107	184

These new points do not necessarily represent realistic operational requirements, especially those with a higher supercruise Mach number than the dash segment Mach number.
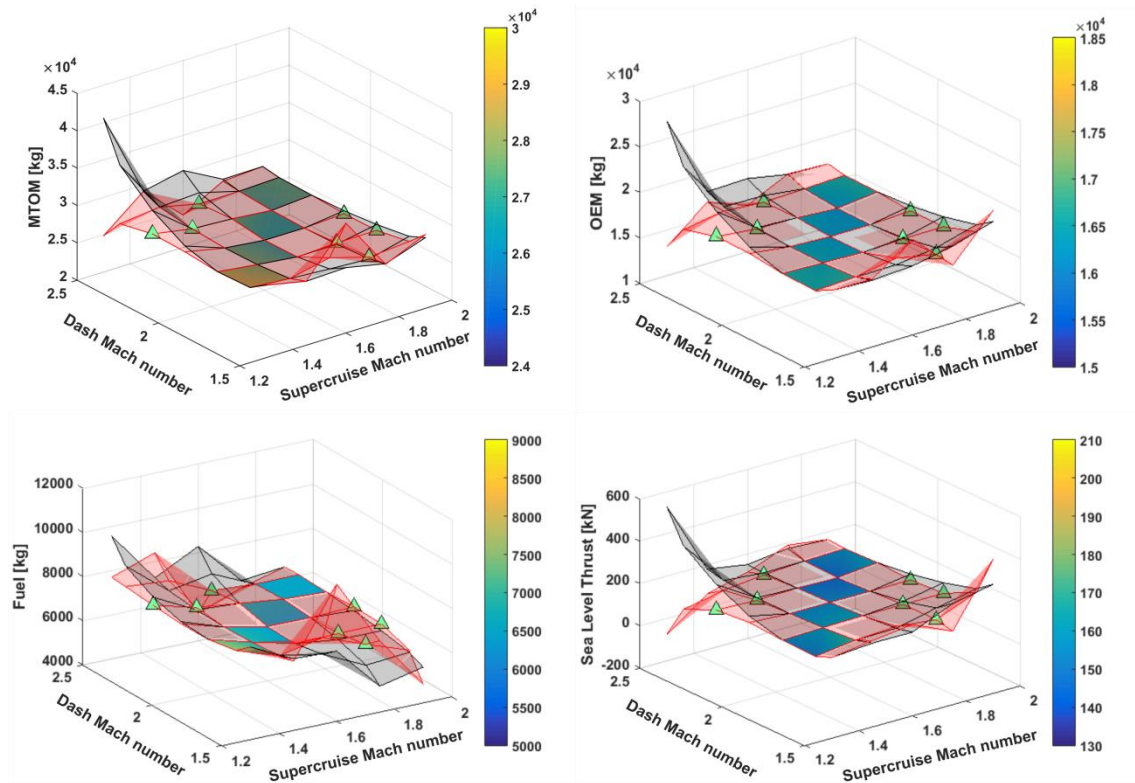
Figure 7-18 - Revised response surfaces

The main difference between the extrapolated response surfaces is seen at the low supercruise Mach and very high dash Mach numbers, with the direction of the response being completely reversed, especially obvious for take-off mass, empty mass, and sea level thrust. This is due to the afterburner performance being able to easily meet the mission requirements at very high Mach numbers, and thus not driving a growth in mass as originally forecasted.

These results emphasize the sensitivity of the responses to operational criteria such as supercruise and dash Mach numbers, and performance requirements like specific excess power.

7.2.4 Study Summary

This study focused around the design of a fully supersonic, long range, deep interdiction UCAV, the payload requirements are also high in mass and volume.

The initial design assumptions and an initial baseline configuration were tested through the GENUS framework methodologies and found to be inadequate in terms of wing loading, and thus, wing area; this mainly due to the volumetric and packaging constraints imposed by the large payload, which dictates the centre wing geometry, has a strong interaction with the landing gear and engine locations, as well as a potential major impact on CG control throughout the mission.

The revised baseline configuration was achieved by balancing packaging constraints, required fuel tank volume, performance, geometric constraints for subsonic leading edges and control surface effectiveness, and low-observability from the nose-on view angle. The engine sizing was determined mainly by the specific excess power requirement during the high-altitude, high-speed dash segment, under 1g loading conditions, full payload, 50% fuel and afterburner.

Regarding the proposed stealth considerations, the nose-on RCS signature requirement can be considered as a target for current and future configurations. The results for clean geometries and perfect electric conductor materials obtained by POFACETS have been found to be consistently optimistic throughout this research. However, the trends observed for RCS against sweep angles are indicative of possible design solutions.

Reducing both supercruise and dash Mach numbers results in increased masses and engine sizes, mainly due to increased mission duration, even for reduced levels of performance. However, specific excess power requirements at Mach numbers higher than 2.2 are not a significant design constraint due to the improved afterburner performance as speed increases.

As a result of the Mach number trade studies, it has become apparent that the original mission point can be improved by modifying the supercruise Mach number requirement, from M1.6 to ~M1.8, while the high-altitude dash Mach number can be increased to ~2.1 with no significant penalties in take-off, empty and fuel masses, engine sizing, or achieved performance.

Finally, the additional operational points investigated showcase the sensitivity of the responses to changes in mission parameters and the importance of well-balanced mission requirements. Furthermore, it can be seen that applying strategies such as design of experiments (DOE) can provide valuable information on optimal mission conditions, sensible requirements, and potential results. This capability has been identified as a potential improvement to the GENUS multidisciplinary design and optimisation procedures which will allow the designers to acquire new knowledge in a quick and interactive way.

7.3 Mach 3+ Supersonic Strike UCAVs

The Thunderbolt UCAV project was initiated in Cranfield University's Aircraft Design group in 2014 with the purpose of exploring the feasibility of a high speed Unmanned Combat Air Vehicle capable of naval operations. It is intended that the vehicle would be integrated with other UK/EU defence assets[203]. Costs are to be the minimum required to achieve a basic operational capability. The estimated service entry date is relatively short, potentially as early as 2030; appropriate TRL levels (7 to 9) as given by Table 7-10, should be considered through the design. The principal objectives of such a vehicle are:

1. To provide a robust and effective weapons delivery system that is not overly dependent on very low-observable technology.
2. To provide a weapons delivery system suitable for time critical missions without the need for persistence capability.
3. Being compatible with other systems operating in the envisaged In Service Period.

Table 7-10 - Technology readiness levels (US DoD)

TRL	Definition
1	Basic principles observed and reported
2	Technology concept and/or application formulated
3	Analytical and experimental critical function and/or characteristic proof of concept
4	Component and/or breadboard validation in laboratory environment

5	Component and/or breadboard validation in relevant environment
6	System/subsystem model or prototype demonstration in a relevant environment
7	System prototype demonstration in an operational environment
8	Actual system completed and qualified through test and demonstration
9	Actual system proven through successful mission operations

7.3.1 Mission Design

The most important mission parameter for this class of vehicles relates to time-critical strike against high value targets (HVT), with launch to weapon on target of 30 minutes (essential), and 20 minutes (desirable) assuming the vehicle is in a high state of readiness. To do so, the vehicles need to be operated from aircraft carriers. For the same reason, combat radii values will be limited within a range of 500 km to 850 km at speeds as high as Mach 4.0. The weapons bay should be at least the size of one F-35 weapons bay and also be able to carry 1 x 2000 lb JDAM. Payloads will be limited to the 1000-2000 kg range.

An indicative flight envelope is given in Figure 7-19, which corresponds to a maximum dynamic pressure of 45.4 kPa, chosen as a compromise between performance, structural penalties, and material choices. Another aspect of the flight envelope will consider the maximum allowable structural temperatures achieved during high supersonic flight, with an estimated temperature limit around 330-400 °C (depending on material selection).

A preliminary mission plan is given by the phases below:

0-1	Warm up and take-off. Carrier based take-off variants will be investigated
1-2	Minimum time to climb to cruise Mach and altitude
2-3	Supersonic cruise out (best speed)
2-3 (b)	Supersonic ingress (best range)
3-4	Descent to M 1.5/15 km altitude
4-5	Payload drop
5-6	Climb to supersonic cruise altitude and speed

6-7	Supersonic cruise in (best speed)
6-7 (b)	Supersonic egress (best range)
7-8	Descent and landing

Another important aspect of this mission is to evaluate the effectiveness of time-critical missions when compared to current defence assets such as *Eurofighter Typhoon*, *Rafale*, and other 4+ and 5th generation aircraft (however, technical data on fighter performance is hard to obtain).
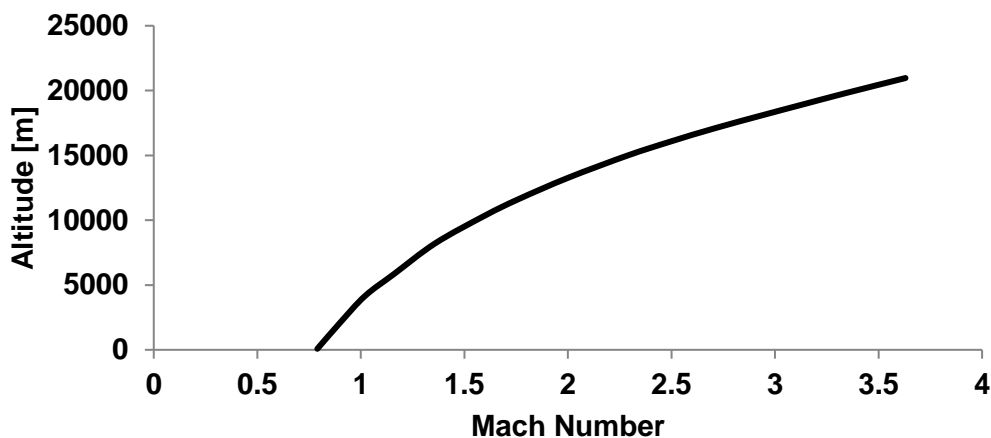
Figure 7-19 - Indicative flight envelope for high supersonic UCAVs

7.3.2 Initial Design Assumptions

The Thunderbolt project has gone through several design iterations, starting as a twin engine configuration with a MTOM of 23514 kg[204,205], followed by a subsequent revision leading to a central engine configuration with a MTOM of 17500 kg[206]. The engine modelled during these conceptual design studies was a scaled version of the Pratt & Whitney J58 turboramjet used in the SR-71. A side by side comparison of both configurations is shown in Figure 7-20. Overall dimensions and other technical data for both variants are given in Table 7-11.

The mass of both configurations has been verified through the GENUS mass estimations methods for a fixed engine size and total fuel mass with good agreement for both cases, especially for Howe's mass methods, as shown in Figure 7-21 (a) for the twin engine case and Figure 7-21 (b) for the single engine configuration.

Due to the fully supersonic mission, biconvex aerofoils with low thickness to chord ratios will be assumed throughout this design study.
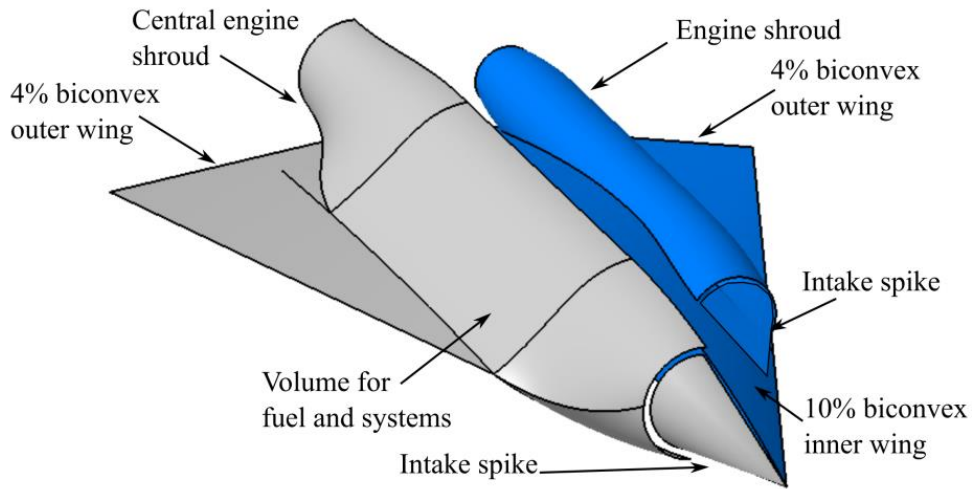
Figure 7-20 - Comparison of single-engine and twin-engine geometries
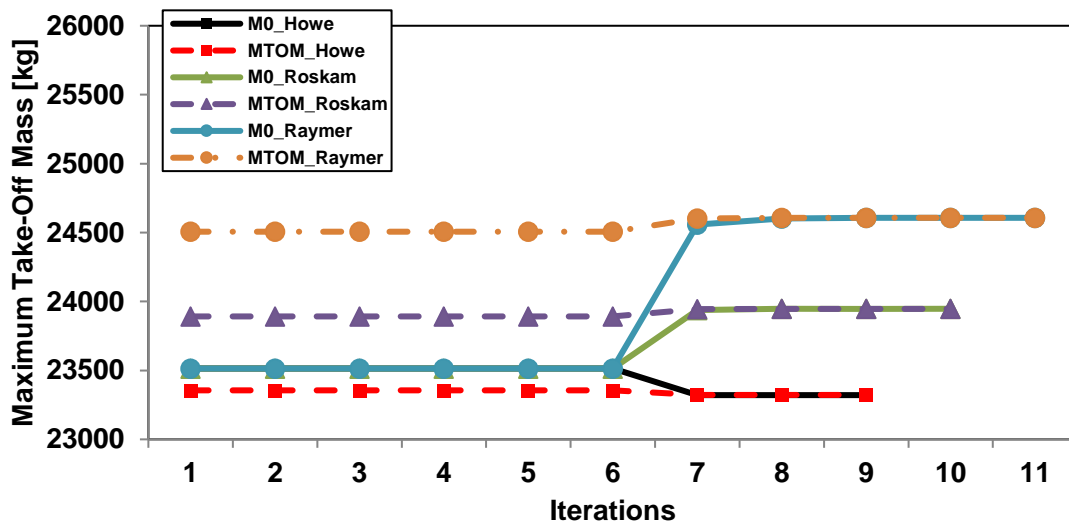
a) Mass verification for twin engine Thunderbolt
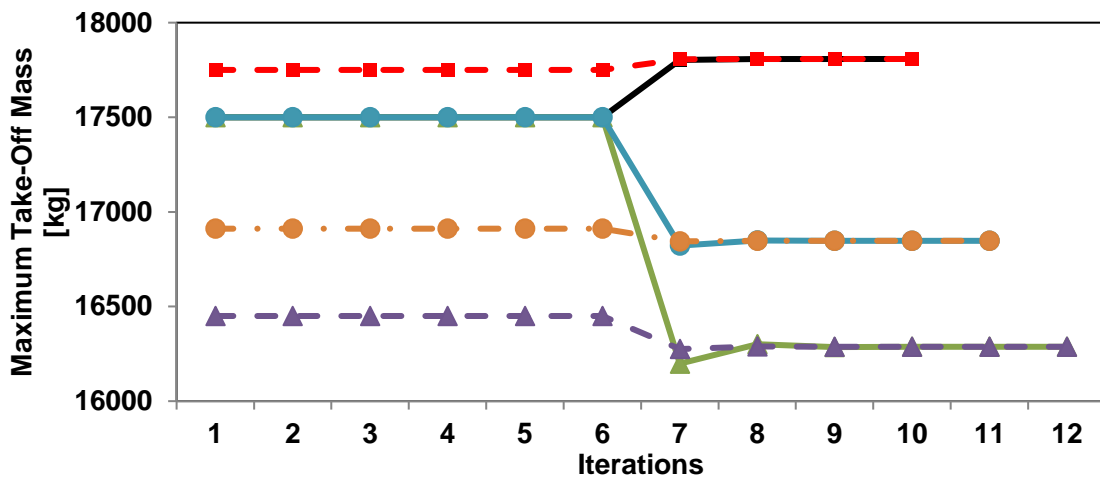
b) Mass verification for single engine Thunderbolt

Figure 7-21 - Comparison of mass methods for Thunderbolt variants

Table 7-11 - Thunderbolt configurations technical data

Design Parameter	Twin Engine	Single Engine
MTOM [kg]	23514	17500
OEM [kg]	13867	7785
Fuel [kg]	8435	8500
Total Length [m]	14	16
Wing Span [m]	10	10
Wing Area [m^2]	70.4	70.4
Wing LE Sweep	68°	68°
Wing t/c	10% inner to 4% outer	4%
Wing Loading [N/m^2]	3276.6	2438.6
Thrust Loading [-]	0.65	Not available

The conceptual design studies for Thunderbolt have been carried out with similar conceptual methods as those present in the GENUS framework. Therefore, similarly to previous results obtained during this research, additional work should be carried out in order to validate the results of the overall vehicle's masses, size, propulsion system characteristics, and general performance, as well as the effects of aerodynamic heating and the system heat loads. The specific strategies required have been acknowledged as further work, and are mentioned in §9.2.

7.3.3 Mission and Performance Trade Studies

A high-supersonic strike mission has been evaluated through the GENUS framework; the initial mission parameters are: a cruise altitude of 25 km at a Mach number of 3.75, a payload of 1224 kg, and a combat radius of 700 km. The geometric characteristics of the twin-engine configuration have been used for an initial convergence and optimisation check.

The initial results match very well with the original Thunderbolt data, with a calculated take-off mass of 23990 kg, a total fuel consumption of 8646 kg, and a total sea level thrust of 154 kN, with a twin turboramjet configuration. The mission profile plotted in Figure 7-22 shows that the initial climb takes over 6 minutes and 250 km, the cruise out duration is 7 minutes, and the rapid descent lasts around 3 minutes, achieving a time-to-target of 16 minutes, well within the 'desirable' requirement. The subsequent climb takes slightly over 3 minutes and 163 km. A large portion (49%) of the fuel is consumed during the initial climb, followed by the secondary climb (26.6%), the cruise in segment (9.6%), and the cruise out segment (8.5%). The final descent consumes around 5% of the total fuel, while the rapid descent consumes only 0.25% of the fuel. This has been identified as an area of potential fuel savings; however, the high loads experienced during the rapid descent might have a detrimental effect on the life of the aircraft.
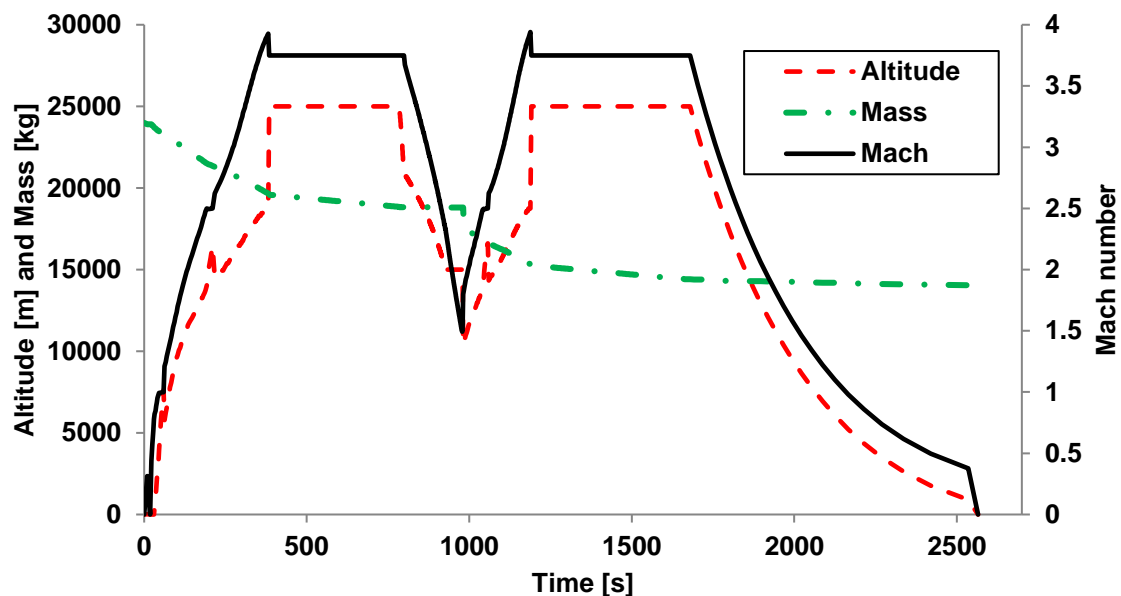
Figure 7-22 - Baseline high-supersonic mission profile, from GENUS

The take-off procedure has been assumed as a ski-jump with the performance shown in Figure 7-23. The deck length has been assumed as 70 meters, the ski ramp radius as 255 meters, the maximum ramp angle is 13.6°, and the carrier speed is 14 m/s. The total take-off distance is 182 meters, at a speed of 78 m/s (Mach 0.23) and 3° angle of attack. A total of 54.6 kg of fuel were consumed during take-off.
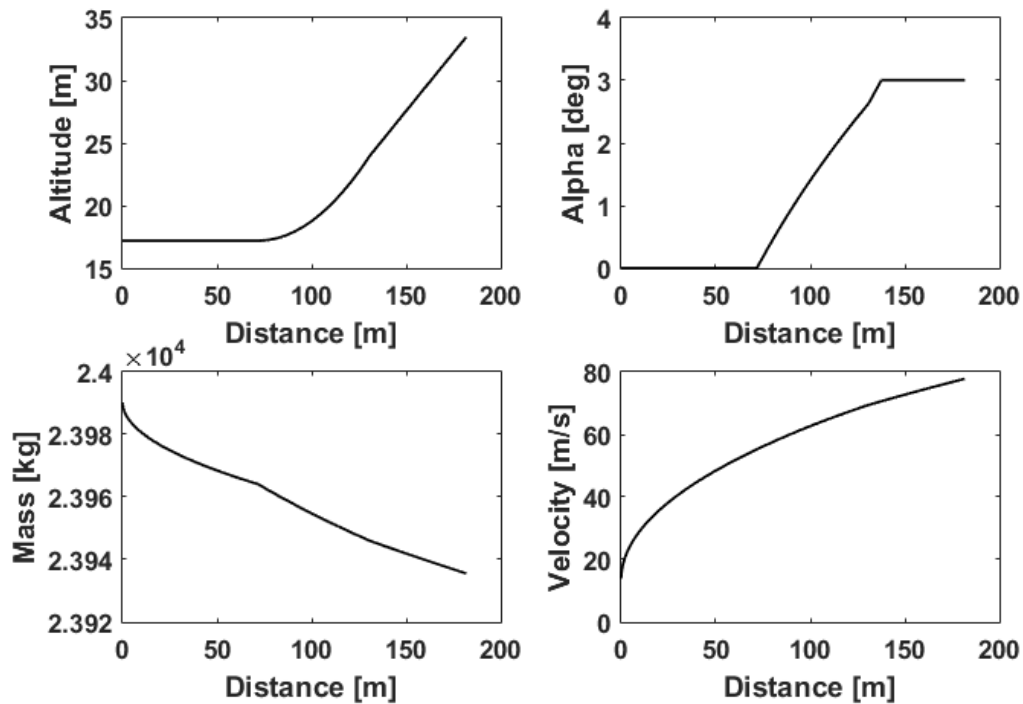
Figure 7-23 - Ski jump take-off performance for baseline high supersonic UCAV

The total mission duration from take-off to landing is 43 minutes; from the FTMS performance plots, Figure 7-24, the thermal endurance of the vehicle at the equilibrium temperature of the cruise segments (without additional heat input, $Q_{Sink} = 0$) is 59 minutes. It can be seen that no recirculation fuel is required for this case. The FTMS performance deteriorates as additional heat load from the systems is added to the fuel, as shown by Figure 7-25.

Under an additional systems heat load of 375 kW, the thermal endurance is equal to the mission duration, but the residual fuel (the amount of fuel remaining at the moment the fuel in the tanks reaches its maximum temperature) is approximately 3800 kg. This would severely limit the endurance of the vehicle and would incur

in additional fuel weight to ensure that no spontaneous fuel ignition occurs during the flight.
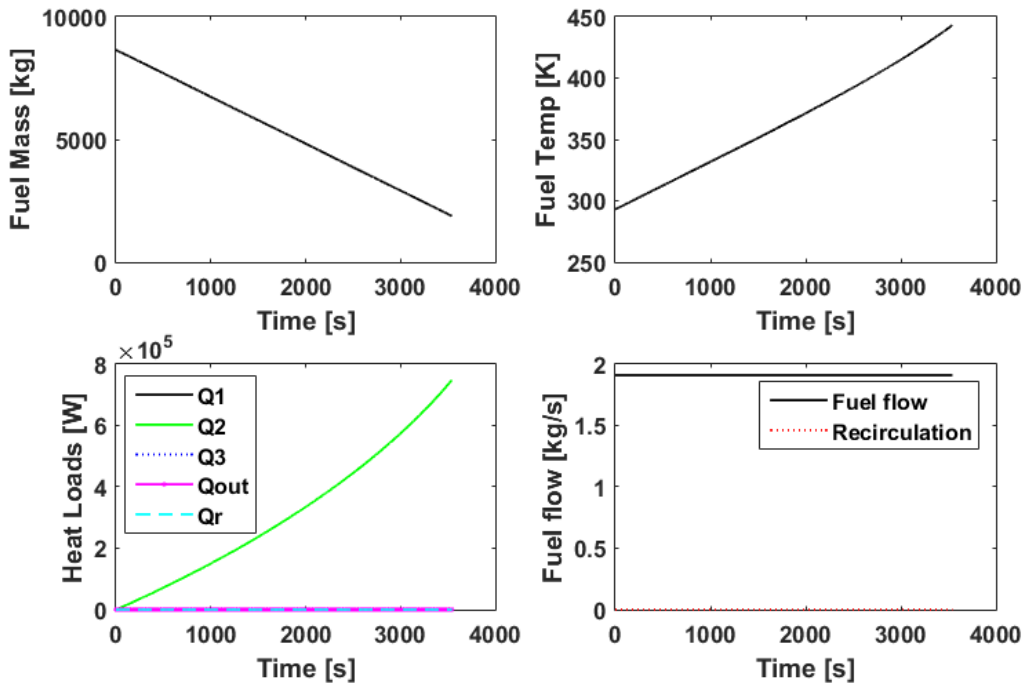
Figure 7-24 - FTMS performance at cruise conditions

$$\tau = -0.0008Qsink^2 - 2.3018Qsink + 3543.8$$
$$R^2 = 1$$
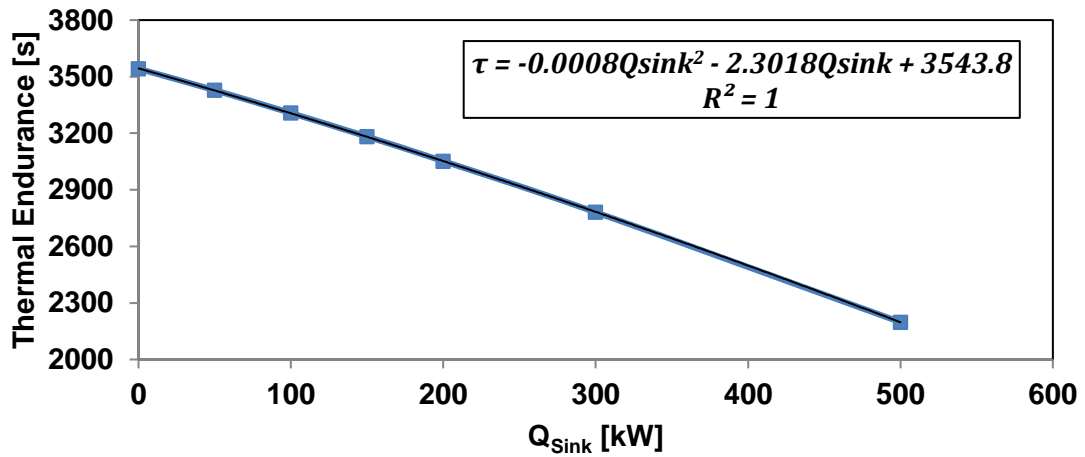
Figure 7-25 - Thermal endurance vs additional system heat loads

The maximum and minimum temperatures for the upper and lower skins are 712K, 545K, 707K, and 510K respectively. This is 40 degrees higher than the limit temperature of titanium alloys, set here as 400 °C or 673K. This temperature is obtained under conservative assumptions including midday sun exposure, no

water vapour dissipation, and it does not take into consideration the cooling from the fuel system.

7.3.3.1 Cruise Mach and Altitude Trade-Offs

The purpose of varying mission parameters will be to determine the most beneficial mission conditions for minimum take-off mass, fuel consumption, and for maximising thermal endurance at a minimum residual fuel penalty.

The cruise Mach number will be varied from 3.5 to 4.0, while the cruise altitude will be varied from 21 km to 28 km. At this stage, the combat radius, payload mass, and payload drop Mach-altitude have been kept constant at 700 km, 1224 kg, and M 1.5/15 km. Furthermore, an environmental heat load of 375 kW has been applied to all mission cases.

The response contours for MTOM and total fuel consumption are shown in Figure 7-26. It can be seen that the minimum take-off and fuel values are found at low Mach-altitude values, while the maximum values are found at the high Mach-altitude combinations.

The initial climb, which has been specified as a minimum time-to-climb trajectory, has a large influence on the overall fuel consumption and the total mass of the vehicle; the climb trajectories for all altitudes and Mach numbers are shown in Figure 7-27. The first discontinuity during the climb relates to the transonic acceleration, where a drop in altitude is used to surpass the transonic barrier and the sharp increase in drag that comes with it. The second discontinuity in the trajectory occurs at a constant Mach number of 2.5 due to the transition Mach number defined for the combined turbine-based propulsion system assumed for all designs. It can also be seen that the last segment of the climb trajectory consists of a constant energy height climb; the maximum speed encountered throughout the mission is likely to occur at the end of the climb segment, and this has been found to be one of the main engine sizing requirements.

The time-to-climb and the climb segment's fuel consumption as a fraction of the total fuel consumption for all cases are shown in Figure 7-28.
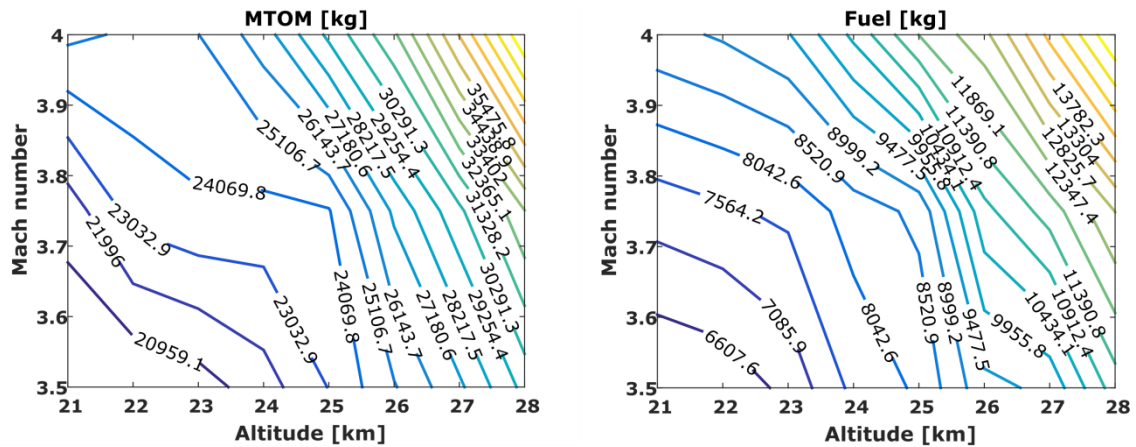
Figure 7-26 - Take-off and fuel mass response for various Mach and altitudes
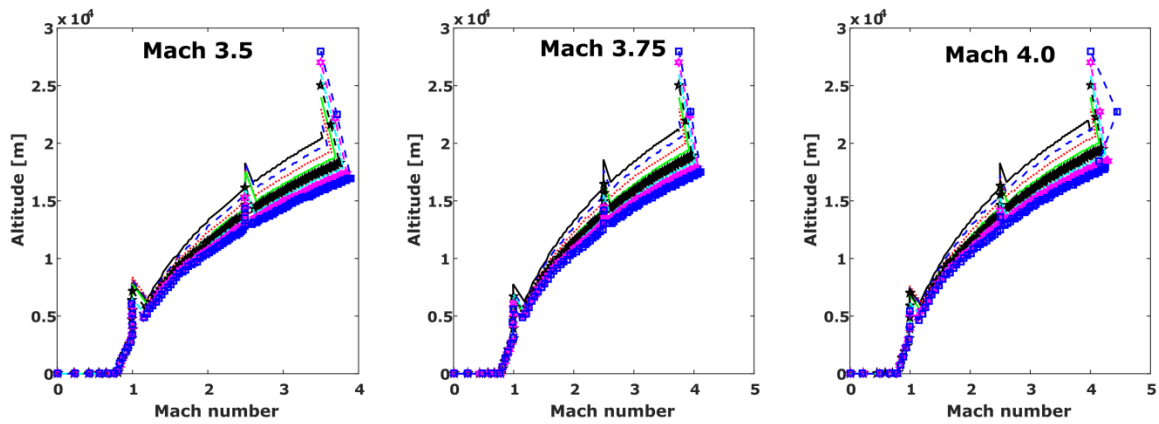
Figure 7-27 - Minimum time to climb trajectories
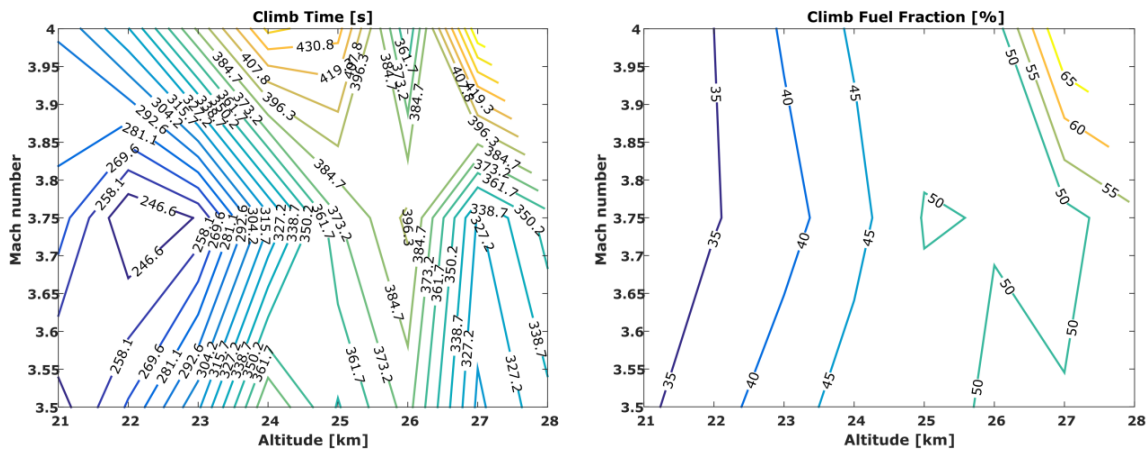
Figure 7-28 - Time and fuel fraction for all climb trajectories

An important mission constraint is related to the time-to-target, here defined as the time to reach the payload drop Mach-altitude point, and being 20 minutes considered as 'desirable' and 30 minutes as 'essential'. From Figure 7-29, it can

be seen that all mission points investigated (for a fixed combat radius of 700 km) comply with the desirable status, which could point towards relaxed mission parameters.
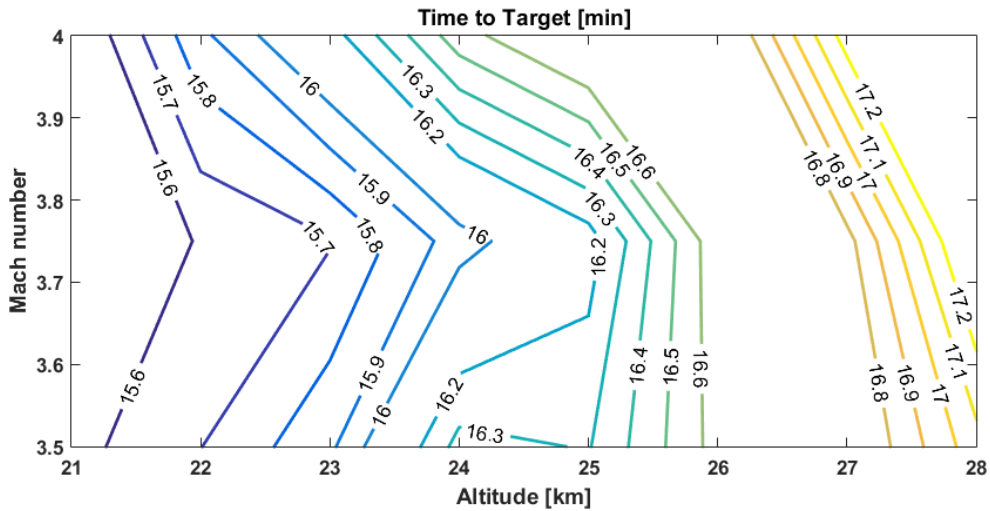
Figure 7-29 - Time-to-target contour for all Mach and altitudes

An interesting result corresponds to the fuel thermal management system performance. Results show that the Mach-altitude pairs that maximise thermal endurance are in the opposite direction for minimising residual fuel, as shown in Figure 7-30.
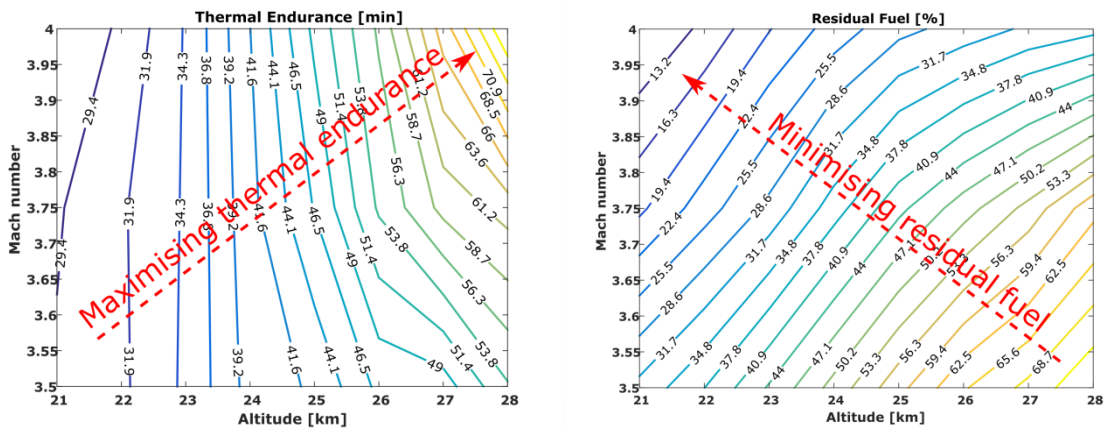
Figure 7-30 - Thermal endurance and residual fuel for various Mach and altitudes

Furthermore, thermal endurance can constraint the entire mission at those Mach numbers and altitudes where its value is less than the duration of the mission, as shown by the red area in Figure 7-31, thus establishing minimum safe operational altitudes and speeds. The residual fuel has not been fully accounted for in the

overall sizing loop, which could reduce the vehicle's endurance or increase the total mass of the aircraft.
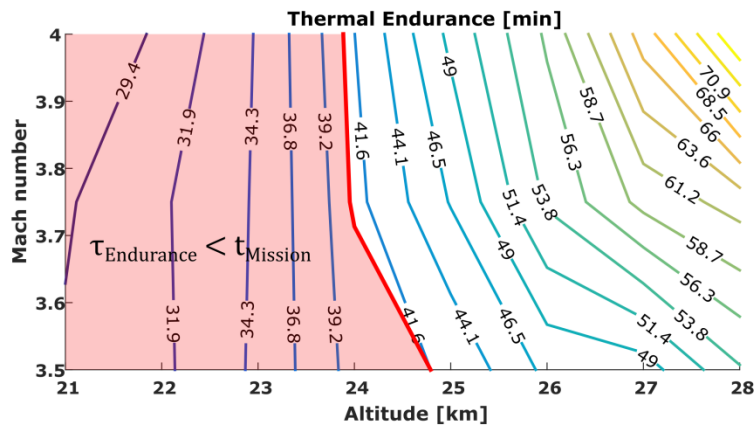
Figure 7-31 - Thermal endurance constraint

7.3.3.2 Combat Radius Trade-Offs

Variations in combat radius, from 500 km up to 850 km, have been investigated at a constant cruise altitude of 25 km for all operational Mach numbers previously defined (3.5, 3.75, and 4.0). Payload mass and payload drop Mach-altitude have also been kept constant.

The MTOM and fuel consumption maps shown in Figure 7-32 show that both parameters have an influence on the mass growth of the vehicle. However, examining the results of the OEM show that increases in the cruise Mach number have a much larger effect on the mass increments of the vehicle when compared to combat radius, as shown in Figure 7-33.
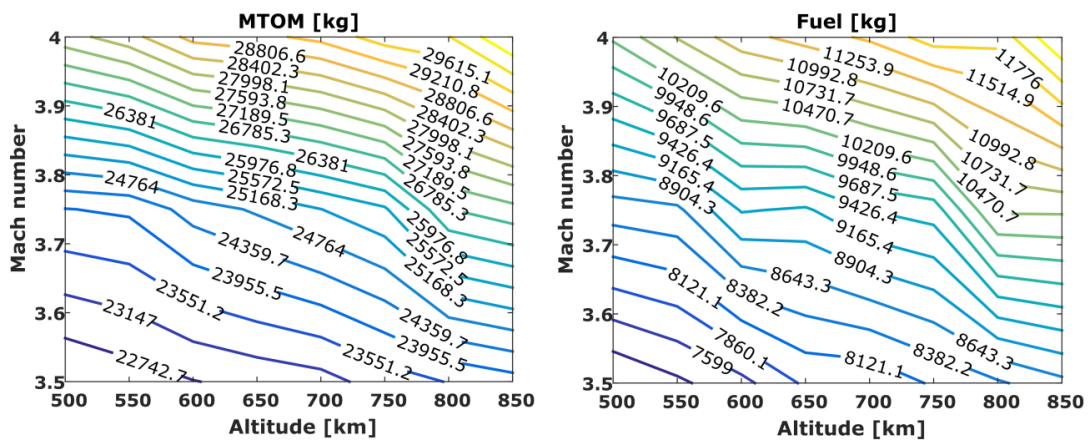
Figure 7-32 - MTOM and Fuel for various Mach numbers and combat radii
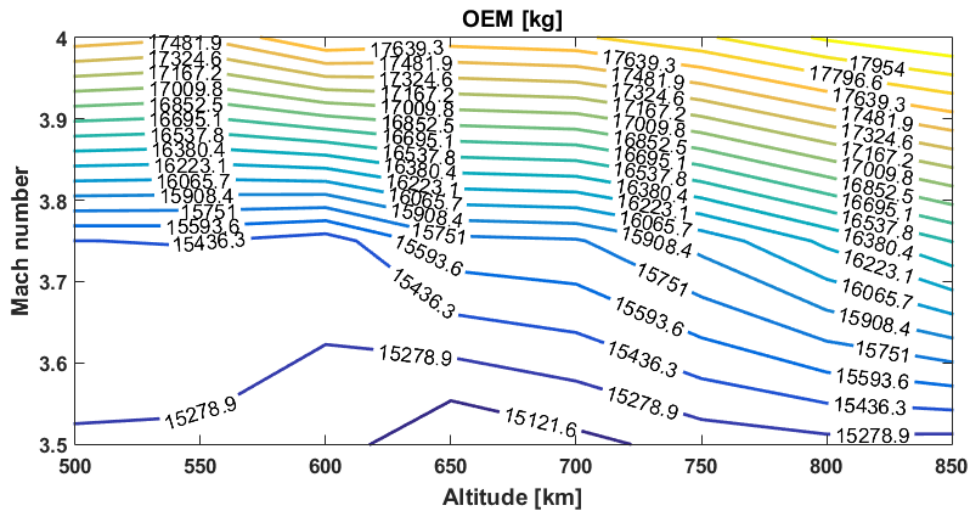
Figure 7-33 - OEM for various Mach numbers and combat radii

Furthermore, as can be seen from Figure 7-34, the time-to-target is mainly dependent on combat radius and not on the cruise Mach number. Initially, the fact that increasing the cruise speed does not contribute significantly to reducing the time-to-target is counterintuitive. Further analysis shows that this behaviour can be explained by the differences in climb time and descent time for the various Mach numbers and combat radii.
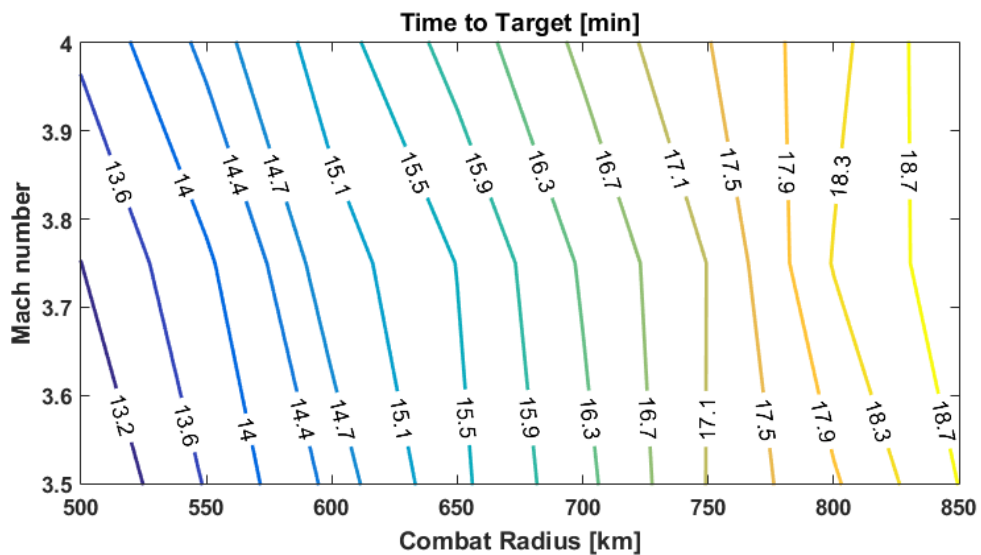
Figure 7-34 - Time-to-target for various Mach numbers and combat radii

The minimum time-to-climb and rapid descent times are shown in Figure 7-35 for all Mach numbers and combat radii. The trend in climb time shows several discontinuities due to the fact that it is highly sensitive to the engine sizing; however, the time to climb generally increases as the desired cruise Mach

222

number increases. For the rapid descent segment, since the engines are operating at idle condition, the descent time is directly proportional to the initial Mach number. Therefore, a relaxed cruise Mach number requirement can result in equivalent time-to-target results, at a reduced empty mass and engine size.
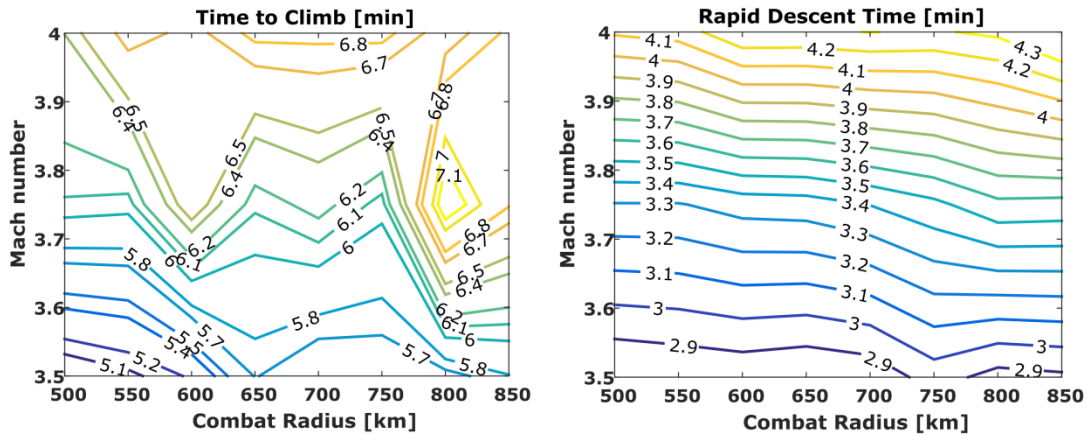
Figure 7-35 - Climb and descent time for various Mach numbers and combat radii

7.3.3.3 Modified Mission

The time-to-target results shown in the section above highlight the potential for equivalent performance at reduced speeds. However, this is a result of the assumption that the maximum Mach and altitude for weapons release is significantly lower than the cruise condition, at Mach 1.5 and 15 km altitude.

Assuming a weapon design exists that, along with its accompanying systems (weapon bay structure and doors, release mechanism and release trajectory), is capable of being released at the cruise conditions, there would be no need for a rapid descent segment and the subsequent climb back to cruise conditions. Therefore, a modified mission was established in order to quantify the effects of speed and combat radius on the time-to-target requirement; this new mission schematic is shown in Figure 7-36.

The results shown below have been obtained at a fixed operating altitude of 25 km. It should also be noted that these results do not account for any potential structural penalties resulting from the severe aero-acoustic environment inside and around the weapon bays due to weapons release at very high speeds.
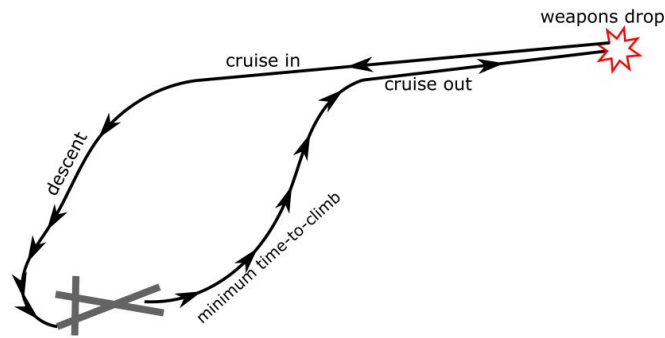
Figure 7-36 - Modified high-supersonic mission, no intermediate descent

The time-to-target contour in Figure 7-37 shows that at low values of combat radius there is little effect of increased speeds due to the distance travelled during the initial climb; for a combat radius of 550 km, operating at Mach 4.0 results in a time-to-target improvement of approximately 45 seconds compared to operating at Mach 3.5. However, for larger values of combat radius, the time saving starts to increase at a higher rate; for instance, the time-to-target at Mach 4.0 and 850 km combat radius is approximately 14 minutes and 40 seconds, while at Mach 3.5 it is 16 minutes with 10 seconds.
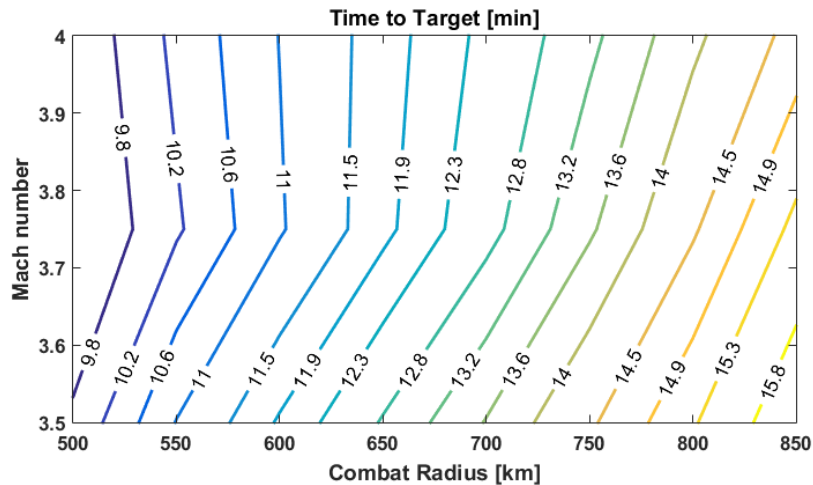
Figure 7-37 - Time to target for modified high-supersonic mission

The discontinuity in the contour lines of Figure 7-37, especially evident at low values of combat radius, is a result of the initial climb segment time and distance, which has been shown to be very sensitive to the engine sizing. As can be seen from Figure 7-38, the minimum percentile distance and time for the initial climb has been found close to the operational Mach number of 3.75, from 500 km to 750 km combat radius. These results could be a function of the objective function

used for the convergence check in the GENUS framework and the optimiser performance, which in this case was the MTOM. This design characteristic prioritises diminishing the engine dimensions to the lowest acceptable value so as to reduce the OEM and fuel consumption during cruise. This reduces the effectiveness of the minimum time-to-climb trajectory. The effect of choosing different objective functions has not been fully explored due to time constraints.
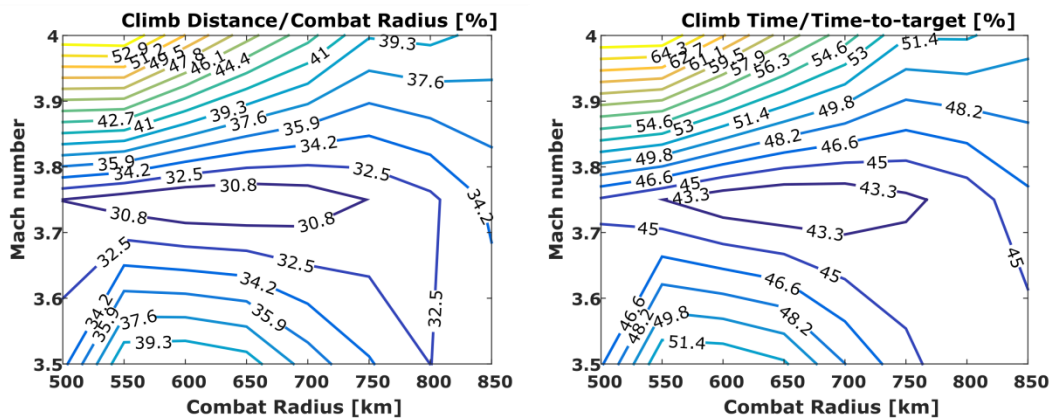
Figure 7-38 - Climb time and distance as a fraction of combat radius and time to target, respectively

7.3.4 Summary of High-Supersonic UCAVs

This section has shown the operational and mission trade-off studies for a high-supersonic strike mission. The basic geometric characteristics of the UCAV have been selected as those of the Thunderbolt UCAV previously investigated at Cranfield University's Aircraft Design Group. Good agreement has been achieved between the available data and the data generated by the GENUS framework.

The baseline mission fuel consumption data shows that the initial climb and the secondary climb are costly in terms of fuel consumption, with approximately 75% of the fuel being consumed between those two segments. Ski-jump take-off procedure has been investigated showing that the baseline engine size does not result in a typical ballistic trajectory while consuming little fuel (<1%).

From the Mach number and cruise altitude studies in §7.3.3.1, it has been shown that the OEM is mainly dependent on the cruise Mach number, which drives the engine size through the minimum time-to-climb segment. The throttle setting at cruise conditions normally ranges from 70% at Mach 3.5 to 85% at Mach 4.0. It

can also be observed that the percentage of total fuel consumed during the initial climb segment is mainly dependent on the target altitude, which ranges from 35% to over 50% of the total fuel. Low altitudes generally result in lower fuel consumption; however, from a survivability aspect, lower altitudes would increase the vehicle's susceptibility due to the partial neglect of low-observability design requirements.

The minimum time-to-climb results in trajectories that closely follow the maximum dynamic pressure, initially estimated as 45 kPa for an acceptable trade-off between potential structural mass penalties and material temperature limits. Preliminary results show that increasing the maximum dynamic pressure results in shorter and faster climb segments; however, the mass penalties resulting from these changes have not been fully quantified.

Further, the conditions that maximise the vehicle's thermal endurance are in direct opposition to those conditions that minimise the residual fuel. These conflicting requirements highlight the importance of including thermal effects in the sizing loop of supersonic vehicles. Low altitudes values have also been restricted by the FTMS performance and the thermal endurance.

The Mach number and combat radius studies in §7.3.3.2 have shown that an equivalent time-to-target can be achieved at reduced speeds due to the reductions in time-to-climb and time for rapid descent, which are generally proportional to the cruise Mach number. These results have been obtained under the assumption that the maximum Mach number and altitude for weapons release is Mach 1.5 at 15000 meters.

Due to the fact that the rapid descent and subsequent climb back to cruise altitude segments are quite costly with regards to mission time, survivability, and fuel consumption, a modified mission was investigated assuming the payload can be released at the cruise conditions. The results in §7.3.3.3 show the advantage of operating at very high speeds, specifically at higher values of combat radius.

The results shown here are limited to the initial design assumptions considering a pre-defined geometry, mission, and the basic set of requirements identified as

226

relevant to this class of vehicles. Through these studies several trade-offs have been recognised that cannot be currently modelled with sufficient levels of fidelity; these include studies concerning the optimised trajectories as a function of thermal requirements, and trade studies for asymmetric speed/altitude mission profiles, and system studies for thermal protection.

8 DISCUSSION

This section will briefly summarise the methodologies developed, the main research findings and the contributions to knowledge.

8.1 The GENUS Aircraft Design Environment

Starting in 2012, Cranfield University's Aircraft Design Group has engaged in the development of a multidisciplinary aircraft conceptual design framework, with the main philosophies of being flexible, robust, license independent, and with potentially unlimited expandability. The GENUS framework consists of nine essential 'abstract' aircraft design modules, and as many 'special' modules as required to analyse non-conventional aircraft design disciplines such as stealth, aerodynamic heating, sonic boom, and cost, to mention a few. Additionally, a custom-made genetic algorithm and a robust gradient-based optimiser can be used to perform large-scale design space explorations and trade studies.

Moreover, it has been shown that the graphic user interface of the GENUS framework allows the designers to quickly and intuitively select the methodologies appropriate for their class of aircraft, as well as selecting the main design inputs and optimisation objective and constraints. The optimisation tab displays a useful summary of the objective function, the constraints and their setting, the design input variables with lower and upper bounds, the optimisation algorithm selected, the history of the objective function, and a summary table with the compliance status of the constraints. Despite its simple and intuitive layout, the GENUS framework is not to be used as a 'black box' tool, but it should complement a 'knowledgeable user' in its aircraft design tasks, furthering these tasks from the experience of the user and the capabilities of the framework.

The GENUS framework has gone through a series of quasi-validations and verifications which have provided ample confidence in the framework and its methodologies. GENUS has been utilised in the conceptual design of hypersonic transports, tube-and-wing and blended wing body airliners, solar powered UAVs, supersonic business jets and finally, low-observable UCAVs. Numerous publications in peer-reviewed journals and major aerospace conferences have

been published as a result of developing and using the GENUS framework, proving its value as an effective aircraft conceptual design environment.

8.2 UCAV Design Methodologies

Due to the wide variety of missions and operational requirements relevant to low-observable UCAVs, the conceptual design methodologies developed throughout this research have emphasised flexibility and robustness. Moreover, low to medium fidelity methods have been integrated in order to maintain the expandability and license-free philosophies of the GENUS framework, as well as prioritising versatile tools without high time or computational costs.

Validation and verification has been achieved for semi-empirical and statistical mass breakdown methods, propulsion system modelling, aerodynamic calculations including friction and wave drag, take-off procedures, and radar cross section estimates.

The aerofoil library has been significantly expanded to include NACA5, NACA6, and biconvex aerofoils, and a general procedure for including aerofoils without an analytical definition has been developed, including supercritical aerofoils.

The propulsion system fidelity has been increased from simple empirical regression methods, to a flexible, physics-based engine design module. This improvement allows the designers to investigate the effects of the various engine design characteristics and off-design performance on the overall configurations.

A complete aerodynamic characterisation has been achieved through a combination of empirical, numerical, and analytical methods, which are not limited to UCAV configurations, but that directly contribute to the GENUS vision of a common robust framework populated with well-proven methods used in the conceptual design of novel and unconventional configurations.

Similarly, the performance module has been expanded from a simple climb-cruise-descent definition to a powerful module with internal methods able to set-up and analyse a multitude of mission types and flight segments.

A packaging procedure has been developed that automatically decides the number of weapon bays based on user inputs such as weapon types, payload mass, number of engines, and geometric constraints. An analytical fuel volume calculation has been developed in order to improve the accuracy when compared to empirical methods. Longitudinal and lateral clashes between various components such as engines, weapon bays, and landing gear locations can be handled inside the packaging module.

Special modules have been developed and integrated directly into the design loop (if chosen by the user) to quantify non-typical aircraft design disciplines; these are radar cross section, aerodynamic heating, fuel thermal management system, and RDT&E cost, some of which are vital for the design of UCAVs and future combat systems.

Sufficient confidence for these methodologies has been generated through the various peer-reviewed publications achieved during the course of this research project. Nevertheless, the following limitations and reservations have been identified (for further work see §9.2):

o The main aerodynamic analysis tool, PANAIR, is capable of capturing the overall aerodynamic behaviour of UCAV configurations at subsonic and supersonic speeds (Mach ≤ 4.0) with relatively good accuracy, as demonstrated by the validation results. PANAIR is not capable of generating accurate aerodynamic data at high angles of attack, which might impact flight segments such as climbs, manoeuvres, and field performance. Moreover, digital DATCOM has been used for the sizing of control surfaces through empirical methods, without considering the complex aerodynamics of UCAVs. However, both PANAIR and DATCOM have been used extensively by external sources during the design of combat aircraft, ensuring its applicability during the conceptual design stages.

o The turbine-based combined engine model, turboramjet, has been idealised as two separate engines with an estimated transition Mach number so as to provide a smooth thrust profile at all speeds. While this might not represent the most realistic or efficient procedure, the thrust and TSFC estimates match

well with previous models generated during the conceptual design of a high-supersonic UCAV. The detailed modelling of the complex intake geometry, actuation, and aerodynamics has not been carried out.

o The radar cross section calculations have been integrated directly into the design loop which represents a distinct advantage over other reported design frameworks, despite the fact that they are currently limited to monostatic RCS of clean geometries. The inclusion of bi-static or multi-static RCS calculations and a database of radar absorbent materials would increase the capabilities of this additional module, and its effect on the design of UCAVs.

o The aerodynamic heating and fuel thermal management system analysis tools have been included through a special module, assuming steady state conditions throughout a given cruise segment. A fully integrated module would require this analysis to be performed in parallel with the mission performance in order to allow for trajectory optimisation, increasing the accuracy due to the smaller time steps used during the steady state analysis. Even so, it has been shown that this module can have an impact on defining mission parameters such as minimum speeds and altitudes for a given thermal endurance requirement or maximum allowable temperatures.

o The cost model should be updated to include the cost of advanced software for potentially fully autonomous vehicles and network-centric operations.

8.3 UCAV Design Space Exploration

Following the piece-wise validation and verification of the individual design methodologies, an initial framework validation for subsonic UCAVs was performed; this exercise has been published under a peer-reviewed journal and repeated in Appendix E. Subsequently, several large-scale design space exploration studies have been carried out for subsonic, moderately supersonic, and high-supersonic UCAV configurations.

From the subsonic strike mission trade studies in Chapter 5, it is clear that the requirements for specific excess power values have the largest influence on the engine sizing, which can account for up to 20% of the empty mass of the vehicle, depending on the payload requirements. Leading edge sweep also has a large

influence on engine sizing through the effects of compressibility drag at high subsonic and transonic speeds. Increasing the specific excess power requirement to levels comparable to air superiority fighters neglects the aerodynamic benefits of high sweep, even for very high sweep angles. Moreover, high sweep angles result in reduced radar signatures at the ±30° view angle. The RDT&E cost results show a high correlation to gross and empty mass, as well as sea level thrust requirements. Increases in the vehicle's autonomy might offset this trend by focusing on the development cost of sophisticated software architectures, and its accompanying hardware. It is recommended that future designers explore different cost models in order to quantify the effects of increased autonomy.

The conceptual design of a 5th generation UCAV design, or *loyal wingman*, shown in Chapter 6 shows the versatile mission definition available in the GENUS performance module. Numerous design aspects such as aerofoil thickness and type, and propulsion system choice can be easily investigated and their effects quantified prior to large-scale multivariate optimisation. This helps reduce the complexity of the optimisation problem and to achieve rapid convergence of the design inputs.

The subsequent preliminary design studies have identified several limitations in the conceptual design process, mainly related to the complex structural arrangement and packaging of such a compact and stealthy vehicle. Several mass penalties resulting from the transportation requirements, specifically a wing-fold mechanism, have not been accounted for during the conceptual design procedure and would need to be addressed during the next design iteration. It has also been shown that in order to align this vehicle with the new technologies like power-by-wire and advanced avionics through the use of high voltage electrical distribution systems, the sizing of the engine must consider large power off-take requirements and not just the mission performance. Lastly, the large structural cut-outs required for engine maintenance, landing gears, and weapon bays severely limits the structural depth and effectiveness, which could result in a heavier structure, and a more expensive aircraft.

The supersonic UCAV studies presented in Chapter 7 have been divided into a deep interdiction (Hi-Hi-Hi) mission, and a high-supersonic (Mach ≥ 3.5) strike mission. The operational trade studies for the deep interdiction mission have shown that the large payload demand dictated a lower value of wing loading when compared to manned aircraft in the same category. The engine sizing was a result of the specific excess power requirements at high-altitude, high-Mach conditions. For this reason, increasing the cruise and dash Mach numbers by 10% to 20% does not result in a significant gross mass increase, despite a small fuel increment. In contrast, reducing the operational Mach numbers while reducing the SEP requirement proportionally results in a large mass increment, resulting from higher fuel consumption due to the longer mission duration, and a reduced efficiency in the afterburner performance at lower Mach numbers.

For the high-supersonic strike mission, the GENUS modules were tested against previously generated data by two conceptual design studies for a Mach 3.5-4.0 UCAV. Initial data matches well with the reported data for both the twin-engine and single-engine configurations. Mission trade studies regarding the cruise Mach number and altitude have been carried out for a Mach range of 3.5 to 4.0 and an altitude range from 21km to 28km. The initial climb segment, considered as a minimum time-to-climb trajectory, results in a large portion of the time-to-target and the total fuel consumption, generally increasing with Mach and altitude. Furthermore, due to the assumed limitations for the weapon release conditions, the time used during the rapid descent segment is proportional to the initial Mach number, resulting in a time-to-target performance which is mainly dependent on the cruise altitude, and not overly dependent on the operational Mach number. Moreover, the Mach and altitude conditions that maximise the thermal endurance have been found to be in direct opposition to those that minimise the residual fuel. These conflicting mission requirements highlight the importance of including thermal effects in the trajectory and mission planning of high-supersonic vehicles. The thermal endurance of the vehicle has also been used to limit the operational altitudes, with a minimum allowable altitude of 24km for Mach numbers from 3.7 to 4.0, and a minimum allowable altitude of 25km for Mach numbers below 3.7.

A revised mission profile that ignores the assumed limitations for the maximum weapon release Mach and altitude conditions was then investigated. In this case, there is a distinct advantage regarding the time-to-target for the higher operational Mach numbers, and more so at higher values of combat radius. Regardless of the mission configuration, the initial climb segment is the most critical design stage, having a large influence on the total fuel consumption, the time-to-target, and the engine size due to the fact that the maximum speed occurs at a lower altitude than the cruise altitude, immediately before the constant energy-height climb.

It has been observed that the initial climb segment is highly dependent on the operational envelope, specifically the maximum dynamic pressure limit, which points towards potentially revised mission parameters. A preliminary study showed, informally, that higher dynamic pressures result in shorter and faster climb segments; however, the effect of increasing the maximum dynamic pressure on the structural mass and the spill over effects on engine size and fuel consumption were not fully quantified.

8.4 Contributions to Knowledge

As a result of this research, an initial literature revision and compilation of technological and operational challenges of stealth UCAVs has been published at a peer-reviewed journal under the title *Technology challenges of stealth unmanned combat aerial vehicles*. This publication lacks the challenges of supersonic configurations but it represents an important starting point for future UCAV designers.

Further, the integration of conceptual design methodologies into the GENUS framework, as well as a proof of the optimisation capabilities has also been published at a peer-reviewed journal under the title *Multidisciplinary analysis of subsonic stealth unmanned combat aerial vehicles.* This publication addresses the already mentioned need of a highly-coupled framework with consistent fidelity levels across several design disciplines, including non-typical aircraft design aspects such as integrated packaging and stealth considerations.

Following the integration and validation of the subsonic design methodologies, a large-scale mission trade-off study has been carried out for subsonic ground strike missions at various speeds, combat radii, and performance requirements. This study has been published at a peer-reviewed journal under the title *Impact of mission requirements on the design of low-observable UCAV configurations.*

Lastly, the conceptual design procedure for a future 5th generation UCAV design has been published at a major aerospace conference under the title *Conceptual design of a fifth generation unmanned strike fighter.* Following, a series of preliminary design studies have been carried out concerning the structural concept, systems design, avionics integration, and stealth. Vast amounts of data have been generated during these preliminary design studies, leading to high-quality information and lessons learned regarding the complex design of future high-performance UCAV configurations, which will feed into the future design iterations. This vehicle has been labelled as a *loyal wingman*, which is an emerging trend concerning UCAVs. Therefore, Cranfield University is at an advantageous position to make an impact and contribution in this area.

9 CONCLUSIONS

Unmanned aircraft have transformed the way military forces all around the world make use of airspace, air power, and aeronautical technology. This transformation is expected to continue and expand to the point of highly cooperative operations between manned and unmanned aircraft, with increases in unmanned aircraft capabilities and autonomy. As observed from the UCAV advanced technology demonstrator programmes, as well as the loyal wingmen designs currently emerging and the future supersonic and hypersonic strike concepts, UCAVs will perform in a wide variety of roles, dominated by very different requirements and technologies. Low-observability design practices are still relevant and are often the driving factor behind numerous design aspects such as the basic planform, the mission design, the systems architecture, and the material and structural choices.

This chapter will briefly summarise how this research project has addressed the identified gaps in the literature, the achievements with respect to the aim and objectives, and finally, the identified areas of further work.

9.1 Achievements and General Conclusions

Through the literature review, it was identified the need for a flexible conceptual design framework that incorporates consistent fidelity levels across all aircraft design disciplines, and that does not ignore important design aspects such as packaging and stealth, especially relevant for UCAV designs.

During the course of this research, the GENUS framework has been the main tool used and developed to aid in the conceptual design of UCAVs. Keeping with the main philosophies of the GENUS environment, flexible and robust analysis tools have been developed and integrated into the framework in order to standardise the design, analysis, and optimisation of multiple aircraft types.

In the field of aerodynamics, the panel method PANAIR has been integrated into the framework. A meshing algorithm has been developed which can convert a geometry from the LAWGS format to structured grids with boundary conditions

237

and wakes in less than a tenth of a second (limitations in Appendix C, §C.1). The aerodynamic analysis in PANAIR takes around 5 seconds to evaluate 25 different Mach-attitude conditions, providing lift, induced drag, moment coefficients, and the total forces and moments. Furthermore, at supersonic speeds, Harris wave drag calculations based on the area ruling procedure have been implemented for arbitrary geometries.

An engine design and sizing procedure has also been developed, which combined with a parametric mission specification and performance evaluations modules significantly improve the analysis capabilities of the GENUS framework, especially when it comes to non-civilian classes of aircraft.

The inclusion of low-observability constraints and objectives into the design loop has been achieved through the physical optics approximation code POFACETS. An automated faceting algorithm has been developed for flying wing configurations, which is expandable to more complex geometries. The fully spherical radar cross section results can be obtained for any configuration in only a couple of seconds.

Finally, a first approach to a significant revision in the sizing procedure of supersonic UCAVs has been included through the aerodynamic heating and fuel thermal management system. It has been shown that this module can serve to constraint the operational conditions, despite the fact that it has not been implemented in parallel to the performance module.

Through the methodologies integrated into the GENUS framework, more than 300 design evaluations and were carried out for 4 different classes of UCAV concepts and missions, including fully subsonic configurations, moderately supersonic vehicles, to fully supersonic and high-supersonic designs.

To conclude, it has been shown that the methodology developed has resulted in a flexible, expandable, and robust framework that offers the knowledgeable users and designers the capability to study large areas of the design space for particular mission requirements and specific technology constraints. This methodology also

offers the capability to investigate the impact of changing and emerging mission requirements behind the current and future operational concepts.

9.2 Identified Areas of Opportunity and Future Work

Regarding the overall functionality and performance of the GENUS aircraft design environment, the following improvements have been identified:

1. Development of a robust geometry engine capable of supporting the design of future combat systems, and other non-typical geometrical features such as distributed propulsion systems and boundary layer ingestion.
2. The framework and designers would benefit from the inclusion of additional design of experiments (DOE) tools, multi-objective optimisers, and multivariate data visualisation tools available freely through Java libraries.
3. Saving and loading of the generated configurations onto the framework is not currently implemented. This functionality would greatly reduce the time and effort to design new configurations and to carry out trade studies.

The availability in the open literature of high-quality technical data concerning UCAV concepts and prototypes is extremely limited. For this reason, the validation of various design disciplines has proven extremely challenging, and in some areas the accuracy of the models has not been rigorously tested. The following improvements are proposed to various aircraft design disciplines:

1. Aerodynamics: Following the current approach of the aerodynamics module within GENUS, additional methods should complement the high angle of attack aerodynamics, and the approximations during transonic conditions. These aspects are especially relevant for field performance, control surface sizing, and manoeuvrability evaluations. The inclusion of high-fidelity CFD methods has been considered impractical at this stage of the development of the GENUS framework, but the high-fidelity results from individual studies could form the basis of a comprehensive aerodynamic surrogate model.
2. Propulsion: The installed propulsion losses originating from the complex intake geometries, the use of high aspect ratio nozzles, and the demanding power off-takes from the electric and power systems require a more detailed

239

modelling in order to improve the accuracy of the performance and fuel consumption results, which will impact the overall sizing of the configurations.

3. Mass Estimation: Improved mass estimation models for structural and system components can be developed through the statistical analysis of highly detailed technical data. This technique could be applied to the limited number of existent UCAV designs and concepts, were the information available. Moreover, the detailed design of several UCAV configurations could be completed and the information generated used retroactively in the development of mass estimation equations. Particularly relevant data includes the mass of structural reinforcements around large cut-outs such as those used for the internal weapon bays and the buried engines, as well as structural masses of low-observable intakes, and radar absorbent paints and structures.

4. Volume Accounting: The volume occupied by the various systems such as avionics, electrical, and hydraulics, are difficult to evaluate during the conceptual design stage. Through the evaluation of detailed configurations, an empirical value of occupied and usable fuel fractions (in percent of usable volume for various sections such as the fuselage and the wing) can be established. Total volume can be a severe design constraint for UCAV configurations, and needs to be fully integrated into the packaging module.

Finally, future GENUS users and developers focusing on advanced combat systems would benefit from defining a more explicit systems architecture philosophy that incorporates 5th and 6th generation trends, a conceptual level structural layout and sizing procedure, and the modelling of their interaction with the packaging, stealth, and thermal management modules.

REFERENCES

1. DIXON JR. UAV Employment in Kosovo: Lessons for the Operational Commander. Newport; February 2000.

2. COMMITTEE FOR THE REVIEW OF ONR'S UNINHABITED COMBAT AIR VEHICLES PROGRAM - NAVAL STUDIES BOARD. Review of ONR ' s Uninhabited Combat Air Vehicles Program. Washington DC: National Academies Press; 2000.

3. ADAMSON A., SNYDER M. The challenge of fifth-generation transformation. *The Rusi Journal.* 2017; 162(4): 60–66. Available at: DOI:10.1080/03071847.2017.1353256

4. MINISTRY OF DEFENCE. [Withdrawn]Joint Concept Note 3/12: Future Air and Space Operating Concept. London; September 2012.

5. DASSAULT AVIATION. Dassault Aviation and Airbus join forces on Future Combat Air System. 2018. Available at: https://www.dassault-aviation.com/en/group/press/press-kits/dassault-aviation-airbus-join-forces-future-combat-air-system/ (Accessed: 25 February 2019)

6. BAE SYSTEMS. The future of combat air: UK military aircraft technology. 2018. Available at: https://www.baesystems.com/en/feature/the-future-of-combat-air (Accessed: 8 November 2018)

7. EVERETT HR. Unmanned Systems of World Wars I and II. Massachusetts Institute of Technology; 2015.

8. NEWCOME L. Unmanned Aviation : A Brief History Of Unmanned Aerial Vehicles. 1st ed. Reston, VA: AIAA; 2004.

9. NATIONAL NAVAL AVIATION MUSEUM. TDR-1 Edna III. 2016. Available at: http://www.navalaviationmuseum.org/attractions/aircraft-exhibits/item/?item=tdr (Accessed: 3 May 2018)

10. WHITMORE BA. Evolution of Unmanned Aerial warfare: A historical look at remote airpower - A case study in innovation. U.S. Army Command and General Staff College; 2016.

11. EHRHARD TP. Air Force UAVs: The Secret History. Arlington; July 2010. Available at: http://oai.dtic.mil/oai/oai?verb=getRecord&metadataPrefix=html&identifier=ADA525674

12. USAF. MQ-1B Predator. 2015. Available at: https://www.af.mil/About-Us/Fact-Sheets/Display/Article/104469/mq-1b-predator/ (Accessed: 7 October 2019)

13. USAF. MQ-9 Reaper. 2015. Available at: https://www.af.mil/About-Us/Fact-Sheets/Display/Article/104470/mq-9-reaper/ (Accessed: 7 October 2019)

14. GENERAL ATOMICS AERONAUTICAL. Predator C Avenger RPA. 2019.

Available at: http://www.ga-asi.com/predator-c-avenger (Accessed: 7 October 2019)

15. THE BUREAU OF INVESTIGATIVE JOURNALISM. Drone Warfare. 2019. Available at: https://www.thebureauinvestigates.com/projects/drone-war (Accessed: 7 October 2019)

16. HARRISON GJ. Unmanned Aircraft Systems (UAS): Manufacturing Trends. January 2013. Available at: http://www.fas.org/sgp/crs/natsec/R42938.pdf

17. US DoD. Joint Publication 1-02: Department of Defense Dictionary of Military and Associated Terms (As Amended Through 31 October 2009). April 2001.

18. WISE KA. First Flight of the X-45A Unmanned Combat Air Vehicle (UCAV), AIAA 2003-5320. AIAA Atmospheric Flight Mechanics Conference and Exhibit. Austin, Texas 11-14 August Reston, VA: AIAA; 2003. Available at: DOI:doi:10.2514/6.2003-5320

19. DE NEVE A., WASINSKI C. Looking Beyond the J-UCAS's Demise. *Defense & Security Analysis*. 2011; 27(3): 237–249. Available at: DOI:10.1080/14751798.2011.604484

20. GERTLER J. History of the Navy UCLASS Program Requirements : In Brief. August 2015.

21. MALENIC M. USN demonstrates autonomous aerial refuelling with X-47B. *IHS Jane's Defence Weekly*. Washington D.C.; April 2015; Available at: http://www.janes.com/article/50923/usn?demonstrates?autonomous?aerial?refuelling?with?x?47b

22. BOEING. Boeing's MQ-25 is ready. 2018. Available at: http://www.boeing.com/defense/mq25/index.page#/overview (Accessed: 10 May 2018)

23. POPULAR MECHANINCS. Lockheed Martin Unveils MQ-25 'Stingray' Tanker Drone Design for the Navy. 2018. Available at: https://www.popularmechanics.com/military/aviation/a19600045/lockheed-martin-unveils-mq-25-stingray-tanker-drone-design-for-the-navy/ (Accessed: 12 April 2018)

24. BAE SYSTEMS. Taranis. 2018. Available at: http://www.baesystems.com/en/product/taranis (Accessed: 10 April 2018)

25. DASSAULT AVIATION. NEURON. 2018. Available at: http://www.dassault-aviation.com/en/defense/neuron/introduction/ (Accessed: 10 April 2018)

26. POPULAR SCIENCE. Meet China's Sharp Sword, a stealth drone that can likely carry 2 tons of bombs. 2017. Available at: https://www.popsci.com/china-sharp-sword-lijian-stealth-drone (Accessed: 10 April 2018)

27. WONG K. Airshow China 2018: CASC reveals stealth UCAV development.

Jane's International Defence Review; 2018.

28.   VRANIC M., NOVICHKOV N. Russia unveils Okhotnik heavy UAV. Jane's 360. 2019. Available at: https://www.janes.com/article/86010/russia-unveils-okhotnik-heavy-uav (Accessed: 16 July 2019)

29.   AERONAUTICAL DEVELOPMENT AGENCY. 31st Annual Report 2015-2016. Bangalore; March 2016.

30.   WRIGHT-PATTERSON AFB. XQ-58A Valkyrie demonstrator completes inaugural flight. 2019. Available at: https://www.wpafb.af.mil/News/Article-Display/Article/1777743/xq-58a-valkyrie-demonstrator-completes-inaugural-flight/ (Accessed: 29 March 2019)

31.   JENNINGS G., CRANNY-EVANS S. UK to use 'swarming drones' to defeat enemy air defences. Jane's 360. 2019. Available at: https://www.janes.com/article/86286/uk-to-use-swarming-drones-to-defeat-enemy-air-defences (Accessed: 8 August 2019)

32.   HOYLE C. RIAT: UK takes wraps off unmanned LANCA concept. FlightGlobal. 2019. Available at: https://www.flightglobal.com/news/articles/riat-uk-takes-wraps-off-unmanned-lanca-concept-459803/ (Accessed: 8 August 2019)

33.   JANE'S 360. Aero India 2019: HAL unveils Unmanned Wingman concept. 2019. Available at: https://www.janes.com/article/86831/aero-india-2019-hal-unveils-unmanned-wingman-concept (Accessed: 29 March 2019)

34.   BOEING. Boeing Airpower Teaming System. 2019. Available at: https://www.boeing.com/defense/airpower-teaming-system/index.page (Accessed: 16 July 2019)

35.   UK DEFENCE JOURNAL. Boeing introduces new unmanned aircraft. 2019. Available at: https://ukdefencejournal.org.uk/boeing-introduces-new-unmanned-aircraft/ (Accessed: 29 March 2019)

36.   POPULAR MECHANINCS. DARPA Picks Aerojet Rocketdyne to Build Hypersonic Jet Engine. 2017. Available at: https://www.popularmechanics.com/military/aviation/news/a28577/darpa-aerojet-rocketdyne-hypersonic-jet-engine/ (Accessed: 24 April 2018)

37.   CHUANREN C. China Reveals a Supersonic UCAV. AINonline. 2018. Available at: https://www.ainonline.com/aviation-news/defense/2018-06-12/china-reveals-supersonic-ucav (Accessed: 14 June 2018)

38.   MACDIARMID I. The survivability balance. *Encyclopedia of Aerospace Engineering.* 2010; Available at: DOI:10.1002/9780470686652.eae440

39.   RAO GA., MAHULIKAR SP. Integrated review of stealth technology and its role in airpower. *The Aeronautical Journal.* 2002; December: 629–641. Available at: DOI:10.1017/S0001924000011702

40.   ZENKNER S., TROST M., BECKER R., VOß C. Preliminary engine design and

inlet optimization of the MULDICON concept. *Aerospace Science and Technology*. Elsevier Masson SAS; 2019; Available at: DOI:10.1016/j.ast.2019.105318

41. Marenghi Y., Rosenblum J-P., Hallard R., Molton P. Low Observable Afterbody Aerodynamic Design and Integration : Methodology and Challenges, AIAA 2007-4570. 25th AIAA Applied Aerodynamics Conference. Miami, Florida 25-28 June Reston, VA: AIAA; 2007. Available at: DOI:10.2514/6.2007-4570

42. Lee C. Taranis and beyond: Inspiring aerodynamic capability. *Aeronautical Journal*. 2014; 118(1206): 845–859. Available at: DOI:10.1017/S0001924000009593

43. Merlin PW. Design and Development of the Blackbird: Challenges and Lessons Learned, AIAA 2009-1522. 47th AIAA Aerospace Sciences Meeting. Orlando, Florida 5-8 January Reston, VA: AIAA; 2009. Available at: DOI:10.2514/6.2009-1522

44. Chin WS., Lee DG. Development of the Composite RAS (Radar Absorbing Structure) for the X-Band Frequency Range. *Composite Structures*. 2007; 77(4): 457–465. Available at: DOI:10.1016/j.compstruct.2005.07.021

45. Ahmad H., Tariq A., Shehzad A., Faheem MS., Shafiq M., Rashid IA., et al. Stealth technology: Methods and composite materials—A review. *Polymer Composites*. 2019; (January): 1–16. Available at: DOI:10.1002/pc.25311

46. Kim J., Hespanha P. Cooperative Radar Jamming for Groups of Unmanned Air Vehicles. *Proceedings of the IEEE Conference on Decision and Control*. 2004; 1: 632–637. Available at: DOI:10.1109/CDC.2004.1428715

47. Mahulikar SP., Sane SK., Gaitonde UN., Marathe AG. Numerical studies of infrared signature levels of complete aircraft. *Aeronautical Journal*. 2001; 105(1046): 185–192. Available at: DOI:10.1017/S0001924000025422

48. Baranwal N., Mahulikar SP. IR signature study of aircraft engine for variation in nozzle exit area. *Infrared Physics and Technology*. Elsevier B.V.; 2016; 74: 21–27. Available at: DOI:10.1016/j.infrared.2015.11.001

49. An CH., Kang DW., Baek ST., Myong RS., Kim WC., Choi SM. Analysis of Plume Infrared Signatures of S-Shaped Nozzle Configurations of Aerial Vehicle. *Journal of Aircraft*. 2016; 53(6): 1768–1778. Available at: DOI:10.2514/1.C033685

50. Epstein A., Miake-Lye RC. US20100122519A1: Ulta-low sulfur fuel and method for reduced contrail formation. United States; 2010.

51. Noppel FG., Singh R., Taylor MD. US20100043443A1: Method and apparatus for suppressing aeroengine contrails. United States; 2010.

52. Noppel FG., Singh R., Taylor MD. US20100132330A1: Method and apparatus for suppressing aeroengine contrails. United States; 2010.

53. NELSON RC., PELLETIER A. The Unsteady Aerodynamics of Slender Wings and Aircraft Undergoing Large Amplitude Maneuvers. *Progress in Aerospace Sciences.* 2003; 39(2–3): 185–248. Available at: DOI:10.1016/S0376-0421(02)00088-X

54. MUNRO CD., KRUS P., JOUANNET C. Implications of scale effect for the prediction of high angle of attack aerodynamics. *Progress in Aerospace Sciences.* 2005; 41(3–4): 301–322. Available at: DOI:10.1016/j.paerosci.2005.05.001

55. GURSUL I. Review of Unsteady Vortex Flows over Slender Delta Wings. *Journal of Aircraft.* 2005; 42(2): 299–319. Available at: DOI:10.2514/1.5269

56. BREITSAMTER C. Unsteady Flow Phenomena Associated with Leading-Edge Vortices. *Progress in Aerospace Sciences.* 2008; 44(1): 48–65. Available at: DOI:10.1016/j.paerosci.2007.10.002

57. DELERY JM. Aspects of Vortex Breakdown. *Progress in Aerospace Sciences.* 1994; 30: 1–59. Available at: DOI:10.1016/0376-0421(94)90002-7

58. LUCCA-NEGRO O., O'DOHERTY T. Vortex Breakdown: A Review. *Progress in Energy and Combustion Science.* 2001; 27(4): 431–481. Available at: DOI:10.1016/S0360-1285(00)00022-8

59. MITCHELL AM., DÉLERY J. Research into Vortex Breakdown Control. *Progress in Aerospace Sciences.* 2001; 37(4): 385–418. Available at: DOI:10.1016/S0376-0421(01)00010-0

60. GURSUL I., GORDNIER R., VISBAL M. Unsteady Aerodynamics of Nonslender Delta Wings. *Progress in Aerospace Sciences.* 2005; 41(7): 515–557. Available at: DOI:10.1016/j.paerosci.2005.09.002

61. GURSUL I. Vortex Flows on UAVs: Issues and Challenges. *Aeronautical Journal.* 2004; 108(1090): 597–610. Available at: DOI:10.1017/S0001924000000439

62. NATO SCIENCE AND TECHNOLOGY ORGANIZATION. RTO-TR-AVT-080 - Vortex Breakdown over Slender Delta Wings. Brussels; October 2009.

63. NATO SCIENCE AND TECHNOLOGY ORGANIZATION. RTO-TR-AVT-113 - Understanding and Modeling Vortical Flows to Improve the Technology Readiness Level for Military Aircraft. Brussels; October 2009.

64. TOMAC M., RIZZI A., NANGIA RK., MENDENHALL MR., PERKINS SC. Engineering Methods on the SACCON Configuration - Some Design Considerations, AIAA 2010-4398. 28th AIAA Applied Aerodynamics Conference. Chicago, Illinois 28 June - 1 July Reston, VA; 2010. Available at: DOI:doi:10.2514/6.2010-4398

65. CUMMINGS RM., SCHÜTTE A. Integrated Computational/Experimental Approach to Unmanned Combat Air Vehicle Stability and Control

Estimation. *Journal of Aircraft*. 2012; 49(6): 1542–1557. Available at: DOI:10.2514/1.C031430

66. VICROY DD., LOESER TD., SCHÜTTE A. SACCON Forced Oscillation Tests at DNW-NWB and NASA Langley 14x22-foot Tunnel, AIAA 2010-4394. 28th AIAA Applied Aerodynamics Conference. Chicago, Illinois 28 June - 1 July Reston, VA: AIAA; 2010. Available at: DOI:10.2514/6.2010-4394

67. SCHÜTTE A., HUMMEL D., HITZEL SM. Flow Physics Analyses of a Generic Unmanned Combat Aerial Vehicle Configuration. *Journal of Aircraft*. 2012; 49(6): 1638–1651. Available at: DOI:10.2514/1.C031386

68. WOOLVIN SJ. A Conceptual Design Study of the 1303 UCAV Configuration, AIAA 2006-2991. 24th Applied Aerodynamics Conference. San Francisco, California 5-8 June Reston, VA: AIAA; 2006.

69. WOOLVIN SJ. UCAV Configuration & Performance Trade-Offs, AIAA 2006-1264. 44th AIAA Aerospace Sciences Meeting and Exhibit. Reno, Nevada 9-12 January Reston, VA: AIAA; 2006.

70. TOMAC M., RIZZI A., NANGIA RK., MENDENHALL MR., PERKINS SC. Engineering Methods Applied to an Unmanned Combat Air Vehicle Configuration. *Journal of Aircraft*. 2012; 49(6): 1610–1618. Available at: DOI:10.2514/1.C031384

71. COPPIN J. Aerodynamics, Stability and Shape Optimisation of Unmanned Combat Air Vehicles. University of Sheffield; 2014.

72. LUCKRING JM., BOELENS OJ., BREITSAMTER C., HÖVELMANN A., KNOTH F., MALLOY DJ., ET AL. Objectives, approach, and scope for the AVT-183 diamond-wing investigations. *Aerospace Science and Technology*. Elsevier Masson SAS; 2016; 57: 2–17. Available at: DOI:10.1016/j.ast.2016.05.025

73. HÖVELMANN A., KNOTH F., BREITSAMTER C. AVT-183 diamond wing flow field characteristics Part 1: Varying leading-edge roughness and the effects on flow separation onset. Aerospace Science and Technology Elsevier Masson SAS; 2016. pp. 18–30. Available at: DOI:10.1016/j.ast.2016.01.002

74. HÖVELMANN A., GRAWUNDER M., BUZICA A., BREITSAMTER C. AVT-183 diamond wing flow field characteristics Part 2: Experimental analysis of leading-edge vortex formation and progression. *Aerospace Science and Technology*. Elsevier Masson SAS; 2016; 57: 31–42. Available at: DOI:10.1016/j.ast.2015.12.023

75. CUMMINGS RM., SCHÜTTE A. The NATO STO task group AVT-201 on 'extended assessment of stability and control prediction methods for NATO air vehicles'. 32nd AIAA Applied Aerodynamics Conference. 16-20 June. Atlanta, Georgia 2014. Available at: DOI:10.2514/6.2014-2000

76. NELSON DM., IRVING JP., GHOREYSHI M., JIRASEK A., LOFTHOUSE AJ.

Experimental and numerical investigation of flight dynamics of a generic lambda wing configuration. *Aerospace Science and Technology.* 2017; 71: 706–724. Available at: DOI:10.1016/j.ast.2017.10.011

77. CUMMINGS RM., LIERSCH CM., SCHÜTTE A., HUBER KC. Aerodynamics and conceptual design studies on an unmanned combat aerial vehicle configuration. *Journal of Aircraft.* 2018; 55(2): 454–474. Available at: DOI:10.2514/1.C033808

78. CUMMINGS RM., LIERSCH CM., SCHÜTTE A. Multi-disciplinary design and performance assessment of effective, agile NATO air vehicles. 2018 Applied Aerodynamics Conference 2018. pp. 1–35. Available at: DOI:10.2514/6.2018-2838

79. SCHÜTTE A., VORMWEG J., MAYE RG., JEANS TL. Aerodynamic shaping design and vortical flow design aspects of a 53deg swept flying wing configuration. 2018 Applied Aerodynamics Conference. 25-29 June. Atlanta, Georgia Reston, VA: AIAA; 2018. Available at: DOI:10.2514/6.2018-2841

80. KARAKOÇ A., KAYA H. A multi-objective multi-disciplinary optimization approach for NATO AVT 251 UCAV – MULDICON. 2018 Applied Aerodynamics Conference 2018. pp. 1–9. Available at: DOI:10.2514/6.2018-3001

81. LÖCHERT P., HUBER KC., GHOREYSHI M., ALLEN J. Control device effectiveness studies of a 53∘ swept flying wing configuration. Experimental, computational, and modeling considerations. *Aerospace Science and Technology.* Elsevier Masson SAS; 2019; 93: 105319. Available at: DOI:10.1016/j.ast.2019.105319

82. RÜTTEN M. Numerical investigation of thrust vectoring for a high-aspect ratio nozzle of an unmanned combat air vehicle. *2018 Applied Aerodynamics Conference. 25-29 June. Atlanta, Georgia.* 2018; Available at: DOI:10.2514/6.2018-3340

83. EDEFUR H., TORMALM M., TYSELL L., QUAS MJ. Design and integration of a low observable intake for the MULDICON platform. 2018 Applied Aerodynamics Conference. 25-29 June. Atlanta, Georgia 2018. Available at: DOI:10.2514/6.2018-3162

84. LIERSCH CM., BISHOP G. Conceptual design of a 53deg swept flying wing UCAV configuration. 2018 Applied Aerodynamics Conference 2018. pp. 1–19. Available at: DOI:10.2514/6.2018-2839

85. SCHWEIGER JM., CUNNINGHAM AM., DALENBRING M., VOß A., SAKARYA E. Structural Design Efforts for the MULDICON Configuration. 2018 Applied Aerodynamics Conference. 25-29 June. Atlanta, Georgia Reston, VA: AIAA; 2018. Available at: DOI:10.2514/6.2018-3325

86. SAKARYA E., KOÇAN Ç., OKUMUŞ B. A study on evaluation of aeroelastic characteristics of a UCAV configuration. 2018 Applied Aerodynamics

Conference. 25-29 June. Atlanta, Georgia Reston, VA: AIAA; 2018. Available at: DOI:10.2514/6.2018-3328

87. LOCKHEED MARTIN. X-56A. 2019. Available at: https://www.lockheedmartin.com/en-us/products/X-56A.html (Accessed: 6 June 2019)

88. SMITH H. U-99 Uninhabited Tactical Aircraft Preliminary Structural Design. *Aircraff Engineering and Aerospace Tecnology*. 2001; 73(1): 31–56. Available at: DOI:10.1108/00022660110367051

89. SMITH H. U-99 uninhabited tactical aircraft preliminary systems design. *Aircraft Engineering and Aerospace Technology*. 2001; 73(3): 244–265.

90. BARONE M., ARUNAJATESAN S. Pressure loadings in a rectangular cavity with and without a captive store. *Journal of Aircraft*. 2016; 53(4): 982–991. Available at: DOI:10.2514/1.C033600

91. LIU H., YAN C., ZHAO Y., QIN Y. Analysis of pressure fluctuation in transonic cavity flows using modal decomposition. *Aerospace Science and Technology*. Elsevier Masson SAS; 2018; 77: 819–835. Available at: DOI:10.1016/j.ast.2018.03.033

92. BACCI D., SADDINGTON AJ., BRAY D. The effect of angle of attack on the aeroacoustic environment within the weapons bay of a generic UCAV. *Aerospace Science and Technology*. Elsevier Masson SAS; 2019; 93: 105315. Available at: DOI:10.1016/j.ast.2019.105315

93. LOUPY GJM., BARAKOS GN., TAYLOR NJ. Cavity flow over a transonic weapons bay during door operation. *Journal of Aircraft*. 2018; 55(1): 339–354. Available at: DOI:10.2514/1.C034344

94. JOHNSON RA., STANEK MJ., GROVE JE. Store Separation Trajectory Deviations Due to Unsteady Weapons Bay Aerodynamics. AIAA 2008-188. 46th AIAA Aerospace Sciences Meeting and Exhibit. Reno, Nevada 7-10 January Reston, VA: AIAA; 2008. Available at: DOI:10.2514/6.2008-188

95. SONG W., LU W., JIANG Z., BAI P. The crucial technique investigation of wind-tunnel drop- model testing for the supersonic internal weapons (in Chinese). *Lixue Xuebao/Chinese Journal of Theoretical and Applied Mechanics*. 2018; 50(6): 1346–1355. Available at: DOI:10.6052/0459-1879-18-180

96. MARSH G. Automating aerospace composites production with fibre placement. *Reinforced Plastics*. Elsevier Ltd; 2011; 55(3): 32–37. Available at: DOI:10.1016/S0034-3617(11)70075-3

97. GKN AEROSPACE. GKN produces components for X-47B Navy. *Reinforced Plastics*. February 2006;

98. DI SANTE R. Fibre Optic Sensors for Structural Health Monitoring of Aircraft Composite Structures: Recent Advances and Applications. *Sensors*. 2015;

15(8): 18666–18713. Available at: DOI:10.3390/s150818666

99. GAGNÉ M., THERRIAULT D. Lightning strike protection of composites. *Progress in Aerospace Sciences*. Elsevier; 2014; 64: 1–16. Available at: DOI:10.1016/j.paerosci.2013.07.002

100. KUTLU Z., CHANG F-K. Modeling Compression Failure of laminated Composites Containing Multiple Through-the-Width Delaminations. *Journal of Composite Materials*. 1992; 26(3): 350–387. Available at: DOI:10.1177/002199839202600303

101. BORRELLI R., RICCIO A., SELLITTO A., CAPUTO F., LUDWIG T. On the use of global-local kinematic coupling approaches for delamination growth simulation in stiffened composite panels. *Composites Science and Technology*. Elsevier Ltd; 2015; 115: 43–51. Available at: DOI:10.1016/j.compscitech.2015.04.010

102. TZETZIS D., HOGG PJ. Infield composites repair techniques for combat aircraft: research and development perspective. *Materials Technology*. 2007; 22(1): 2–9. Available at: DOI:10.1179/175355507X196475

103. HUDA Z., EDI P. Materials Selection in Design of Structures and Engines of Supersonic Aircrafts: A Review. *Materials & Design*. Elsevier Ltd; 2013; 46: 552–560. Available at: DOI:10.1016/j.matdes.2012.10.001

104. JOHANSSON M. Propulsion Integration in an UAV, AIAA 2006-2834. 24th Applied Aerodynamics Conference. San Francisco, California 5-8 June Reston, VA: AIAA; 2006. Available at: DOI:doi:10.2514/6.2006-2834

105. GEORGES MJ., JONES SR. An integrated approach to propulsion and power for unmanned vehicles, AIAA 2003-6527. 2nd AIAA 'Unmanned Unlimited' Conference and Workshop and Exhibit San Diego, California: AIAA; 2003. pp. 1–7. Available at: DOI:doi:10.2514/6.2003-6527

106. SIMON PC., BROWN DW., HUFF RG. Performance of External-Compression Bump Inlet at Mach Numbers of 1.5 to 2.0. NACA RM-E56L19. Washington; April 1957.

107. CHENG S., ZHAN H., SHU Z., FAN H., WANG B. Effective optimization on Bump inlet using meta-model multi-objective particle swarm assisted by expected hyper-volume improvement. *Aerospace Science and Technology*. Elsevier Masson SAS; 2019; 87: 431–447. Available at: DOI:10.1016/j.ast.2019.02.039

108. HEITMEIR FJ., LEDERER R. Turboramjets And Installation. In: Murthy SNB, Curran ET (Eds) *Developments In High-Speed Vehicle Propulsion Systems*. Reston, VA: AIAA; 1996. pp. 159–204. Available at: DOI:10.2514/5.9781600866401.0159.0204

109. NIYOMTHAI N. Packaging and Configuration Design Aspects of UCAV Concept Synthesis and Optimization. Cranfield University; 2002.

110. NGUYEN N-V., CHOI S-M., KIM W-S., LEE J-W., KIM S., NEUFELD D., ET AL. Multidisciplinary Unmanned Combat Air Vehicle system design using Multi-Fidelity Model. *Aerospace Science and Technology*. Elsevier Masson SAS; 2013; 26(1): 200–210. Available at: DOI:10.1016/j.ast.2012.04.004

111. JEON K., LEE J., BYUN Y., YU YH. Multidisciplinary UCAV System Design and Optimization Using Repetitive Response Surface Enhancement Technique, AIAA 2007-1972. 48th AIAA/ASME/ASCE/AHS/ASC Structures, Structural Dynamics, and Materials Conference Honolulu, Hawaii: AIAA; 2007. Available at: DOI:10.2514/6.2007-1902

112. AMADORI K., JOUANNET C., KRUS P. Aircraft Conceptual Design Optimization. 26th International Congress of the Aeronautical Sciences. Ancorage, Alaska 14-19 September ICAS; 2008.

113. LEE DS., GONZALEZ LF., SRINIVAS K., PERIAUX J. Robust Evolutionary Algorithms for UAV/UCAV Aerodynamic and RCS Design Optimisation. *Computers and Fluids*. 2008; 37(5): 547–564. Available at: DOI:10.1016/j.compfluid.2007.07.008

114. ÇAVUS N. Multidisciplinary and Multiobjective Design Optimization of an Unmanned Combat Aerial Vehicle (UCAV). Middle East Technical University; 2009.

115. SATHE A., PANT RS. Conceptual Design Studies of an Unmanned Combat Aerial Vehicle, AIAA 2010-9306. 10th AIAA Aviation Technology, Integration, and Operations (ATIO) Conference. Fort Worth, Texas 13-15 September Reston, VA: AIAA; 2010. Available at: DOI:10.2514/6.2010-9306

116. ALLISON D., MORRIS C., SCHETZ J., KAPANIA R., SULTAN C., DEATON J., ET AL. A Multidisciplinary Design Optimization Framework for Design Studies of an Efficient Supersonic Air Vehicle, AIAA 2012-5492. 12th AIAA Aviation Technology, Integration, and Operations (ATIO) Conference and 14th AIAA/ISSMO Multidisciplinary Analysis and Optimization Conference. 17-19 September, Indianapolis, Indiana Reston, VA: AIAA; 2012. Available at: DOI:10.2514/6.2012-5492

117. MORRIS C., ALLISON D., SCHETZ J., KAPANIA R. Parametric Geometry Model for Multidisciplinary Design Optimization of Tailless Supersonic Aircraft. *Journal of Aircraft*. 2014; 51(5): 1455–1466. Available at: DOI:doi:10.2514/6.2012-4850

118. KULFAN BM. Universal Parametric Geometry Representation Method. *Journal of Aircraft*. 2008; 45(1): 142–158. Available at: DOI:10.2514/1.29958

119. MORRIS C., ALLISON D., SULTAN C., SCHETZ J., KAPANIA R. Towards Flying Qualities Constraints in the Multidisciplinary Design Optimization of a Supersonic Tailless Aircraft, AIAA 2012-5517. 12th AIAA Aviation Technology, Integration, and Operations (ATIO) Conference and 14th

AIAA/ISSMO Multidisciplinary Analysis and Optimization Conference. Indianapolis, Indiana 17-19 September Reston, VA: AIAA; 2012. Available at: DOI:10.2514/6.2012-5517

120. AHN J., LEE S., KIM J. A Robust Approach to Pre-Concept Design of UCAV Considering Survivability, AIAA 2002-5605. 9th AIAA/ISSMO Symposium on Multidisciplinary Analysis and Optimization Atlanta: AIAA; 2002.

121. SEPULVEDA E., SMITH H. Technology challenges of stealth unmanned combat aerial vehicles. *The Aeronautical Journal.* 2017; 121(1243): 1261–1295. Available at: DOI:10.1017/aer.2017.53

122. SMITH H., SZIROCZÁK D., ABBE G., OKONKWO P. The GENUS aircraft conceptual design environment. *Proc. IMechE Part G: Journal of Aerospace Engineering.* 2018; 233(8): 2932–2947. Available at: DOI:10.1177/0954410018788922

123. SZIROCZÁK D. Conceptual Design Methodologies Appropriate to Hypersonic Space and Global Transportation Systems. Cranfield University; 2015.

124. SMITH S., LASDON L. Solving large sparse nonlinear programs using GRG. *ORSA J. Comput.* 1992; 4: 1–15.

125. OKONKWO PPC. Conceptual Design Methodology for Blended Wing Body Aircraft. Cranfield University; 2016.

126. ABBE G. Conceptual Design Methodologies for Small Solar Powered Unmanned Aerial Vehicles. Cranfield University; 2015.

127. CRAIDON CB. A description of the Langley Wireframe Geometry Standard (LaWGS) format. Langley, Virginia; February 1985.

128. GUNDLACH J. Designing Unmanned Aircraft Systems - A Comprehensive Approach. 1st edn. Reston, VA: American Institute of Aeronautics and Astronautics; 2012.

129. RAYMER DP. Aircraft Design: A conceptual approach. 2nd edn. Przemieniecki J (Ed) Washington D.C.: AIAA; 1992.

130. HOWE D. Aircraft Conceptual Design Synthesis. London: Professional Engineering Publishing Limited; 2000.

131. ROSKAM J. Airplane Design Part V: Component Weight Estimation. *Airplane Design.* Roskam Aviation and Engineering Corporation; 1985.

132. CRANFIELD COLLEGE OF AERONAUTICS. Aircraft Mass Prediction: Structural Components - DAeT 9317. Cranfield;

133. MILITARY FACTORY. BAe Systems Taranis. Military Factory. 2018. Available at: https://www.militaryfactory.com/aircraft/detail.asp?aircraft_id=986 (Accessed: 6 June 2017)

134. Lewis SJ. The use of carbon fibre composites on military aircraft. *Composites Manufacturing*. 1994; 5(2): 95–103. Available at: DOI:10.1016/0956-7143(94)90060-4

135. Resetar SA., Rogers JC., Hess RW. Advanced Airframe Structural Materials: A Primer and Cost Estimating Methodology. AD-A253 371. 1992.

136. Kuz'michev VS., Ostapyuk YA., Tkachenko AY., Krupenich IN., Filinov EP. Comparative analysis of the computer-aided systems of gas turbine engine designing. *International Journal of Mechanical Engineering and Robotics Research*. 2017; 6(1): 28–35. Available at: DOI:10.18178/ijmerr.6.1.28-35

137. NASA Glenn Research Center. EngineSim Version 1.8a. EngineSim. 2015. Available at: https://www.grc.nasa.gov/WWW/k-12/airplane/ngnsim.html (Accessed: 23 June 2017)

138. Benson TJ. An Interactive Educational Tool for Turbojet Engines. Cleveland, Ohio: NASA Lewis Research Center; 1995. Available at: https://www.grc.nasa.gov/www/k-12/airplane/EngineTheory.pdf

139. Hendricks ES., Falck RD., Gray JS. Simultaneous Propulsion System and Trajectory Optimization. *18th AIAA/ISSMO Multidisciplinary Analysis and Optimization Conference*. American Institute of Aeronautics and Astronautics; 2017. Available at: DOI:doi:10.2514/6.2017-4435

140. Meier N. Military Turbojet/Turbofan Specifications. Jet Engine Specification Database. 2005. Available at: http://www.jet-engine.net/miltfspec.html (Accessed: 15 May 2017)

141. Chen M., Jia Z., Hailong T., Xiao Y., Yang Y., Yin F. Research on Simulation and Performance Optimization of Mach 4 Civil Aircraft Propulsion Concept. *International Journal of Aerospace Engineering*. 2019; 2019. Available at: DOI:10.1155/2019/2918646

142. Chen M., Zhu Z., Tang H., Zhu D., Zhang J. Mode Transition Study of Turbine Based Combined Cycle Engine Concepts. AIAA 2007-5374. 43rd AIAA/ASME/SAE/ASEE Joint Propulsion COnference & Exhibit. 8-11 July Reston, VA: AIAA; 2007. Available at: DOI:10.2514/6.2007-5374

143. Goldsmith EL., Seddon J. (Eds) Practical Intake Aerodynamic Design. Oxford: Blackwell Scientific Publications; 1993.

144. US Department of Defense. Model Specification for Engines Aircraft Turbojet, MIL-SPEC MIL-E-5008B. January 1959.

145. Nicolai LM., Carichner GE. Fundamental of Aircraft and Airship Design: Volume I - Aircraft Design. Schetz J (Ed) Reston, VA: AIAA; 2010.

146. Virginia Tech. Program FRICTION. Available at: http://www.dept.aoe.vt.edu/~mason/Mason_f/FRICTman.pdf

147. Torenbeek E. Synthesis of Subsonic Airplane Design. Springer

Science+Business Media; 1982. Available at: DOI:10.1017/CBO9781107415324.004

148. GUR O., MASON WH., SCHETZ J. Full-Configuration Drag Estimation. *Journal of Aircraft.* 2010; 47(4): 1356–1367. Available at: DOI:10.2514/1.47557

149. HARRIS RV. J. An Analysis and Correlation of Aircraft Wave Drag, NASA TM X-947. Langley, Virginia; March 1964.

150. TSENG W., FEINBERG E., CENKO A. Tranair applications to fighter configurations. 7th Applied Aerodynamics Conference. 2 August. Seattle, Washington Reston, VA: AIAA; 1989. Available at: DOI:10.2514/6.1989-2220

151. AMADORI K., JOUANNET C., KRUS P. Use of panel code modeling in a framework for aircraft concept optimization. 11th AIAA/ISSMO Multidisciplinary Analysis and Optimization Conference. 6-8 September. Portsmouth, Virginia. Reston, VA: AIAA; 2006. Available at: DOI:10.2514/6.2006-7084

152. MAQSOOD A., MASUD J., MEHDI A. Aerodynamic evaluation of wing-strake modification by higher order panel method. 45th AIAA Aerospace Sciences Meeting. 8-11 January. Reno, Nevada Reston, VA: AIAA; 2007. Available at: DOI:10.2514/6.2007-677

153. HOLT J., GARRY K., SMITH T. A preliminary investigation of the aerodynamic characteristics of a lifting body in ground proximity. 34th AIAA Applied Aerodynamics Conference. Washington D.C. 13-17 June Reston, VA: AIAA; 2016. Available at: DOI:10.2514/6.2016-3881

154. GIBLETTE TN., HUNSAKER DF. Prediction of sonic boom loudness using high-order panel methods for the near-field solution. AIAA Scitech 2019 Forum. 7-11 January. San Diego, California Reston, VA: AIAA; 2019. Available at: DOI:10.2514/6.2019-0605

155. SUN Y., SMITH H. Sonic Boom and Drag Evaluation of Supersonic Jet Concepts. *2018 AIAA/CEAS Aeroacoustics Conference.* 2018; Available at: DOI:10.2514/6.2018-3278

156. FORNASIER L. HISSS - A Higher-Order Subson/Supersonic Singularity Method for Calculating Linearized Potential Flow. AIAA-84-1646. AIAA 17th Fluid Dynamics, Plasma Dynamics, and Lasers Conference. June 25-27. Snowmass, Colorado Reston, VA: AIAA; 1984.

157. SIDWELL KW., BARUAH PK., BUSSOLETTI JE., MEDAN RT., CONNER RS., PURDON DJ. PAN AIR: A computer program for predicting subsonic or supersonic linear potential flows about arbitrary configurations using a higher order panel method. NASA CR-3252. Volume II - User's Manual (Version 3.0). Seattle, Washington; March 1990.

158. CARMICHAEL R. PANAIR. Public Domain Aeronautical Software (PDAS). 2015. Available at: http://www.pdas.com/panair.html (Accessed: 24 April

2017)

159. McPARLIN SC., BRUCE RJ., HEPWORTH AG., RAE AJ. Low Speed Wind Tunnel Tests on the 1303 UCAV Concept, AIAA 2006-2985. 24th Applied Aerodynamics Conference. San Francisco, California 5-8 June Reston, VA: AIAA; 2006.

160. CAPONE FJ. Wind tunnel/flight data correlation for the Boeing 737-100 Transport Airplane. NASA TM X-72715. Hampton, Virginia; August 1975.

161. LYNN S., PETE M. takeoff2.c. Blacksburg, VA: Virginia Tech; 1994. Available at: http://www.dept.aoe.vt.edu/~mason/Mason_f/MRsoft.html#TakeOff

162. KRENKEL AR., SALZMAN A. Takeoff Performance of Jet-Propelled Conventional and Vectored-Thrust STOL Aircraft. *Journal of Aircraft.* 1968; 5(5): 429–436. Available at: DOI:10.2514/3.43962

163. AUSTYN MAIR W., BIRDSTALL DL. Aircraft Performance. Cambridge. Birdstall D., Barker P (Eds) Cambridge: Cambridge University Press; 1992.

164. VINH NX. Flight Mechanics of High-Performance Aircraft. 1st edn. Birdsall D., Barker P (Eds) Cambridge: Cambridge University Press; 1995.

165. BIRCKELBAW LG. Ski Jump Takeoff Performance Predictions for a Mixed-Flow, Remote-Lift STOVL Aircraft. NASA-TM-103866. Moffett Field, California; February 1992.

166. BRANDT S., STILES RJ., BERIN JJ., WHITFORD R. Introduction to Aeronautics: A Design Perspective. 2nd edn. Shetz JA (Ed) Reston, VA: American Institute of Aeronautics and Astronautics; 2004.

167. ESDU. Aerodynamics of parachutes. - ESDU 09012. Engineering Sciences Data Unit, Data Items. August 2009. Available at: DOI:10.1016/S1290-0958(00)80071-4

168. ESDU. Energy Height method for flight path optimisation - ESDU 91016. September 1991.

169. ESDU. Energy height method for flight path optimisation - ESDU 90012. 1990.

170. GUDMUNDSSON S. General Aviation Aircraft Design: Applied Methods and Procedures. 1st edn. Oxford: Butterworth-Heinemann; 2014.

171. JENN DC. Radar and laser cross section engineering. 2nd edn. Reston, VA: American Institute of Aeronautics and Astronautics; 2005.

172. MATHWORKS. POFACETS4.1. 2012. Available at: http://www.mathworks.com/matlabcentral/fileexchange/35861-pofacets4-1 (Accessed: 17 March 2016)

173. GARRIDO EJ. Graphical User Interface For A Physical Optics Radar Cross Section Prediction Code. Naval Postgraduate School; 2000.

174. ANSYS. ANSYS HFSS 19 – New Capability, New Look, More Power. 2019. Available at: https://www.ansys.com/blog/ansys-hfss-19 (Accessed: 28 October 2019)

175. JEONG YR., PARK CS., KO YK., YOOK JG. Analysis of RCS of Low Observable Aircraft in VHF Band. *International Journal of Antennas and Propagation*. 2018; 2018. Available at: DOI:10.1155/2018/5435837

176. ZIKIDIS K., SKONDRAS A., TOKAS C. Low Observable Principles, Stealth Aircraft and Anti-Stealth Technologies. *Journal of Computations & Modeling*. 2014; 4(1): 129–165. Available at: http://www.scienpress.com/Upload/JCM/Vol 4_1_9.pdf

177. KOPP C. Assessing Joint Strike Fighter Defence Penetration Capabilities: Annex A, B, C. Air Power Australia. 2009. Available at: http://www.ausairpower.net/APA-2009-01-Annex.html (Accessed: 13 September 2018)

178. TOUZOPOULOS P., BOVIATSIS D., ZIKIDIS KC. 3D modelling of potential targets for the purpose of Radar Cross Section (RCS) prediction: Based on 2D images and open source data. ICMT 2017 - 6th International Conference on Military Technologies. May 31 - June 2. Brno, Czech Repulbic IEEE; 2017. pp. 636–642. Available at: DOI:10.1109/MILTECHS.2017.7988835

179. LLOYD JE. QuickHull3D. 2004. Available at: https://www.cs.ubc.ca/~lloyd/java/quickhull3d.html

180. ESDU. Heat Balance for Flight Vehicles - ESDU 69009. Engineering Sciences Data Unit, Data Items. 1969.

181. ESDU. Heat transfer by forced convection between a two-dimensional laminar boundary layer and a smooth flat plate, with application to wedges, cylinders and cones - ESDU 69010. July 1973.

182. ESDU. Effects of Kinetic Heating on Equilibrium Temperature of Flight Vehicles - ESDU 69012. Data Item 69012. 1973.

183. ESDU. Reynolds number, speed of sound, dynamic viscosity, kinetic pressure and total pressure coefficient in air - ESDU 73017. 1973.

184. QUINN R., GONG L. A Method for Calculating Transient Surface Temperatures and Surface Heating Rates for High-Speed Aircraft. NASA/TP-2000-209034. Edwards, CA; December 2000.

185. ESDU. Solar Heating. Total Direct Irradiance Within the Earth's Atmosphere - ESDU 69015. Data Item 69015. 1969.

186. FISCHER A. Design of a Fuel Thermal Management System for Long Range Air Vehicles. 3rd International Energy Conversion Engineering Conference. 15-18 August, San Francisco, CA Reston, VA: AIAA; 2005. Available at: DOI:10.2514/6.2005-5647

187. JASA JP., MADER CA., MARTINS J. Trajectory Optimization of a Supersonic

Aircraft with a Thermal Fuel Management System. 2018 Multidisciplinary Analysis and Optimization Conference. 25-29 June. Atlanta, GA. Reston, VA: AIAA; 2018. pp. 1–16. Available at: DOI:10.2514/6.2018-3884

188. ALYANAK EJ., ALLISON DL. Fuel Thermal Management System Considerations in the Aircraft Conceptual Design Process. 57th AIAA/ASCE/AHS/ASC Structures, Structural Dynamics, and Materials Conference. 4-8 January. San Diego, CA. Reston, VA: AIAA; 2016. Available at: DOI:10.2514/6.2016-0670

189. BOREN JR HE. DAPCA: A computer program for determining aircraft development and production costs. Santa Monica, California: The RAND Corporation; 1967.

190. SEPULVEDA E., SMITH H., SZIROCZÁK D. Multidisciplinary analysis of subsonic stealth unmanned combat aerial vehicles. *CEAS Aeronautical Journal*. 2019; 10(2): 431–442. Available at: DOI:10.1007/s13272-018-0325-0

191. SEPULVEDA E., SMITH H. Impact of mission requirements on the design of low observable UCAV configurations. *Aircraft Engineering and Aerospace Technology*. 2019; 91(10): 1295–1307. Available at: DOI:10.1108/AEAT-09-2018-0249

192. SEPULVEDA E., SMITH H. Conceptual design of a fifth generation unmanned strike fighter, AIAA 2019-0811. AIAA SciTech Forum. San Diego, CA. 7-11 January Reston, Virginia: AIAA; 2019. Available at: DOI:10.2514/6.2019-0811

193. STILLION J. Trends in air-to-air combat: Implications for future air superiority. Center for Strategic and Budgetary Assessments; 2015.

194. WHITTENBURY J. Configuration Design Development of the Navy UCAS-D X-47B, AIAA 2011-7041. AIAA Centennial of Naval Aviation Forum '100 Years of Achievement and Progress'. Virginia Beach, Virginia 21-22 September Reston, VA: AIAA; 2011. Available at: DOI:10.2514/6.2011-7041

195. MATTINGLY JD., HEISER WH., PRATT DT. Aircraft Engine Design. 2nd edn. Reston, VA: American Institute of Aeronautics and Astronautics; 2002. Available at: DOI:10.2514/4.861444

196. GOON P., KOPP C. Joint Strike Fighter. Air Power Australia. 2016. Available at: http://www.ausairpower.net/jsf.html (Accessed: 15 January 2019)

197. SLEIGHTHOLME A. Development of a structural concept for a fifth generation unmanned combat aerial vehicle. Cranfield University; 2019.

198. CATALA R. Preliminary design of a 5th generation Unmanned Combat Aerial Vehicle. Cranfield University; 2019.

199. MANGION P-A. Preliminary design of a 5th generation UCAV. Cranfield

University; 2019.

200. CHAILLOUS G. Study of stealth of a 6th generation combat aircraft and a 5th generation Unmanned Combat Aerial Vehicle. Cranfield University; 2019.

201. MORAILLON P-L. Preliminary Design of a 5th Generation Unmanned Combat Aerial Vehicle & A Conceptual Design Study of a 6th Generation Combat Aircraft. Cranfield University; 2019.

202. JENKINSON L., MARCHMAN J. Aircraft Design Projects for Engineering Students. Oxford: Elsevier Science; 2003.

203. SMITH H. U-14 Thunderbolt: High Speed Unmanned Combat Air Vehicle - Pre-feasibility Requirements and Analysis. Cranfield: Cranfield University; 2014.

204. BEQUET T. Thunderbolt - Conceptual Design of a High Speed UCAV - Packaging Analysis. Cranfield University; 2015.

205. VITALE B. Thunderbolt - Conceptual Design of a New Class of High Speed UCAV - Performance Analysis. Cranfield University; 2015.

206. PAPPOT M. Conceptual design of a single engine Thunderbolt UCAV. Cranfield University; 2017.

207. AEROSPACEWEB. NACA Airfoil Series. Aerospaceweb.org. Available at: http://www.aerospaceweb.org/question/airfoils/q0041.shtml (Accessed: 1 December 2017)

208. LADSON CL., BROOKS CWJ. Development of a computer program to obtain coordinates for NACA 6- and 6A- airfoils. NASA TM X-3069. Hampton, Virginia; 1974.

209. CARMICHAEL R. Algorithm for calculating coordinates of cambered NACA airfoils at specified chord locations. AIAA 2001-5235. 1st AIAA Aircraft Technology Integration and Operations Forum. Oct 16-18. Los Angeles, CA Reston, VA: AIAA; 2001. Available at: DOI:10.2514/6.2001-5235

210. CARMICHAEL R. NACA Airfoils. Public Domain Aeronautical Software (PDAS). 2017. Available at: http://www.pdas.com/naca456.html (Accessed: 1 March 2017)

211. CHATZIGEORGIADIS F. Development of Code for a Physical Optics Radar Cross Section Prediction and Analysis Application. Naval Postgraduate School; 2004.

212. AIAA. Draft from the AIAA Unmanned Strike Fighter RFP for AIAA Team Student Design Competition. Available at: http://www.dept.aoe.vt.edu/~mason/Mason_f/SD1RFP.pdf

APPENDICES

The following Appendices are provided for additional details where needed:

1. Appendix A: Aerofoil Library Additions
2. Appendix B: Mass Breakdown
3. Appendix C: Aerodynamics
4. Appendix D: Radar Cross Section
5. Appendix E: Subsonic UCAV Framework Validation
6. Appendix F: Publications

Appendix A Aerofoil Library Additions

This appendix includes the methods included in GENUS to generate various aerofoil families.

A.1 NACA5 Aerofoils

The NACA5 family of aerofoils is defined in a very similar manner as the well-known NACA4 aerofoils. However, the mean camber line is defined in a more complex way. Figure A-1 illustrates the NACA5 nomenclature[207].
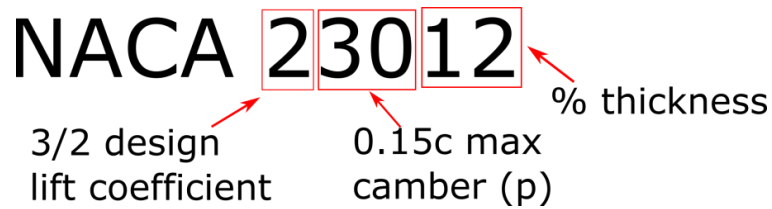
Figure A-1 - NACA5 nomenclature

The mean camber line equations are given by:

$$y_c = \begin{cases} \dfrac{k_1}{6}[x^3 - 3mx^2 + m^2(3 - m)x], & 0 < x \le p \\ \dfrac{k_1 m^3}{6}(1 - x), & p < x \le c \end{cases} \quad \textbf{(A-1)}$$

Where c is the non-dimensional chord value, with range $c = [0, 1]$. The values of m and k_1 are given in Table A-1.

Table A-1 - NACA5 series camber line definition

Mean-line designation	Position of maximum camber	m	k_1
210	0.05	0.0580	361.400
220	0.1	0.1260	51.640
230	0.15	0.2025	15.957
240	0.2	0.2900	6.643
250	0.3	0.3910	3.230

Thickness distribution and final coordinates follow the same procedure as NACA4 series.

A.2 NACA6 Aerofoils

The NACA6 series symmetrical aerofoils were designed by specifying the desired pressure or velocity distribution and using conformal mapping to achieve the right geometry in order to maximise the region of laminar flow over the aerofoil, therefore reducing drag at particular lift coefficients. Non-symmetrical aerofoils were experimentally developed by varying two family functions, the so-called ψ and ε functions. For these reasons, NACA6 aerofoils have no analytical formulation. Their nomenclature is also quite complex and is explained in Figure A-2[207].
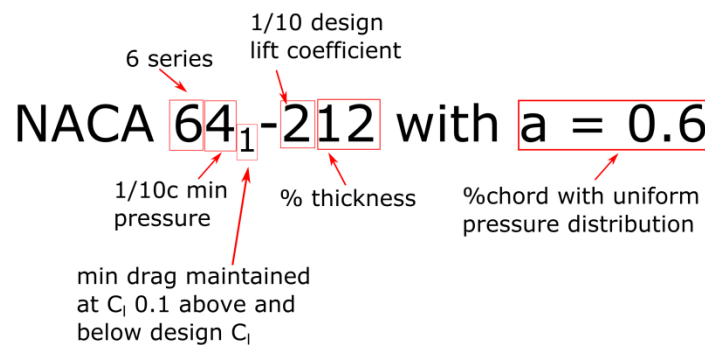
Figure A-2 - NACA6 nomenclature

The camber line for NACA6 aerofoils can be generated by specifying the design lift coefficient and the value of the 'a' parameter.

$$y_c = \frac{Cl_i}{2\pi(a+1)}\left\{\frac{1}{1-a}\left[\begin{array}{c}0.5\left(a-\frac{x}{c}\right)^2 \ln\left|a-\frac{x}{c}\right| - 0.5\left(1-\frac{x}{c}\right)^2 \ln\left(1-\frac{x}{c}\right) \\ +0.25\left(1-\frac{x}{c}\right)^2 - 0.25\left(a-\frac{x}{c}\right)^2\end{array}\right] - \frac{x}{c}\ln\frac{x}{c} + g - h\frac{x}{c}\right\} \tag{A-2}$$

$$g = \frac{-1}{1-a}[a^2(0.5\ln(a) - 0.25) + 0.25] \tag{A-3}$$

$$h = \frac{1}{1-a}[0.5(1-a)^2 \ln(1-a) - 0.25(1-a)^2] + g \tag{A-4}$$

Only eight families of NACA6 aerofoils have been included in GENUS due to the availability of family function data, which was taken from a NASA aerofoil generating code[208], and various other sources[209,210].

The tabular ψ and ε data for the *63, 64, 65, 66, 67, 63A, 64A*, and *65A* families have been translated into 8$^{\text{th}}$ degree polynomials, given by Eqns. (A-5) to (A-18).

$$\varepsilon_{63} = -0.001500009\varphi^8 + 0.019917103\varphi^7 - 0.110621216\varphi^6 + 0.3389922\varphi^5 - 0.63186028\varphi^4 \quad \textbf{(A-5)}$$
$$+ 0.70772016\varphi^3 - 0.417624161\varphi^2 + 0.132330248\varphi - 7.43223E - 6$$

$$\psi_{63} = -0.000614574\varphi^8 + 0.008095377\varphi^7 - 0.045442291\varphi^6 + 0.138587113\varphi^5 \quad \textbf{(A-6)}$$
$$- 0.228002951\varphi^4 + 0.1540454\varphi^3 + 0.0120365\varphi^2 - 0.0572753\varphi$$
$$+ 0.1524051$$

$$\varepsilon_{64} = -0.001500009\varphi^8 + 0.019917103\varphi^7 - 0.110621216\varphi^6 + 0.3389922\varphi^5 - 0.63186028\varphi^4 \quad \textbf{(A-7)}$$
$$+ 0.70772016\varphi^3 - 0.417624161\varphi^2 + 0.132330248\varphi - 7.43223E - 6$$

$$\psi_{64} = -0.000614574\varphi^8 + 0.008095377\varphi^7 - 0.045442291\varphi^6 + 0.138587113\varphi^5 \quad \textbf{(A-8)}$$
$$- 0.228002951\varphi^4 + 0.1540454\varphi^3 + 0.0120365\varphi^2 - 0.0572753\varphi$$
$$+ 0.1524051$$

$$\varepsilon_{65} = -0.001500009\varphi^8 + 0.019917103\varphi^7 - 0.110621216\varphi^6 + 0.3389922\varphi^5 - 0.63186028\varphi^4 \quad \textbf{(A-9)}$$
$$+ 0.70772016\varphi^3 - 0.417624161\varphi^2 + 0.132330248\varphi - 7.43223E - 6$$

$$\psi_{65} = -0.000614574\varphi^8 + 0.008095377\varphi^7 - 0.045442291\varphi^6 + 0.138587113\varphi^5 \quad \textbf{(A-10)}$$
$$- 0.228002951\varphi^4 + 0.1540454\varphi^3 + 0.0120365\varphi^2 - 0.0572753\varphi$$
$$+ 0.1524051$$

$$\varepsilon_{66} = -0.001500009\varphi^8 + 0.019917103\varphi^7 - 0.110621216\varphi^6 + 0.3389922\varphi^5 - 0.63186028\varphi^4 \quad \textbf{(A-11)}$$
$$+ 0.70772016\varphi^3 - 0.417624161\varphi^2 + 0.132330248\varphi - 7.43223E - 6$$

$$\psi_{67} = -0.000614574\varphi^8 + 0.008095377\varphi^7 - 0.045442291\varphi^6 + 0.138587113\varphi^5 \quad \textbf{(A-12)}$$
$$- 0.228002951\varphi^4 + 0.1540454\varphi^3 + 0.0120365\varphi^2 - 0.0572753\varphi$$
$$+ 0.1524051$$

$$\varepsilon_{63A} = -0.001500009\varphi^8 + 0.019917103\varphi^7 - 0.110621216\varphi^6 + 0.3389922\varphi^5 \quad \textbf{(A-13)}$$
$$- 0.63186028\varphi^4 + 0.70772016\varphi^3 - 0.417624161\varphi^2 + 0.132330248\varphi$$
$$- 7.43223E - 6$$

$$\psi_{63A} = -0.000614574\varphi^8 + 0.008095377\varphi^7 - 0.045442291\varphi^6 + 0.138587113\varphi^5 \quad \textbf{(A-14)}$$
$$- 0.228002951\varphi^4 + 0.1540454\varphi^3 + 0.0120365\varphi^2 - 0.0572753\varphi$$
$$+ 0.1524051$$

$$\varepsilon_{64A} = -0.001500009\varphi^8 + 0.019917103\varphi^7 - 0.110621216\varphi^6 + 0.3389922\varphi^5 \qquad \textbf{(A-15)}$$
$$- 0.63186028\varphi^4 + 0.70772016\varphi^3 - 0.417624161\varphi^2 + 0.132330248\varphi$$
$$- 7.43223E - 6$$

$$\psi_{64A} = -0.000614574\varphi^8 + 0.008095377\varphi^7 - 0.045442291\varphi^6 + 0.138587113\varphi^5 \qquad \textbf{(A-16)}$$
$$- 0.228002951\varphi^4 + 0.1540454\varphi^3 + 0.0120365\varphi^2 - 0.0572753\varphi$$
$$+ 0.1524051$$

$$\varepsilon_{65A} = -0.001500009\varphi^8 + 0.019917103\varphi^7 - 0.110621216\varphi^6 + 0.3389922\varphi^5 \qquad \textbf{(A-17)}$$
$$- 0.63186028\varphi^4 + 0.70772016\varphi^3 - 0.417624161\varphi^2 + 0.132330248\varphi$$
$$- 7.43223E - 6$$

$$\psi_{65A} = -0.000614574\varphi^8 + 0.008095377\varphi^7 - 0.045442291\varphi^6 + 0.138587113\varphi^5 \qquad \textbf{(A-18)}$$
$$- 0.228002951\varphi^4 + 0.1540454\varphi^3 + 0.0120365\varphi^2 - 0.0572753\varphi$$
$$+ 0.1524051$$

Where $\varphi = [0, \pi]$. The family functions are multiplied by a scaling factor depending on the aerofoil thickness (t/c), as given by Eq. (A-19) and Table A-2.

$$sf = k_1(t/c) + k_2(t/c)^2 + k_3(t/c)^3 + k_4(t/c)^4 \qquad \textbf{(A-19)}$$

Table A-2 - NACA6 scaling factors

Family	k_1	k_2	k_3	k_4
63	8.18277	1.3776209	-0.0928517	7.5942563
64	4.6535511	1.038063	-1.5041794	4.7882784
65	6.5718716	0.4937629	0.7319794	1.9491474
66	6.7581414	0.1925377	0.8128826	0.852090
67	6.627289	0.0989966	0.9675977	0.9053758
63A	8.1845925	1.0492569	1.3115094	4.4515579
64A	8.2125018	0.7685596	1.4922345	3.6130133
65A	8.2514822	0.4656936	1.5013018	2.0908904

Finally, the camber line, family functions, and aerofoil thickness are combined through the transformation between the $z \to z' \to \zeta$ planes as shown below.

$$z = e^{\psi_0 - i\varphi} \qquad \textbf{(A-20)}$$

$$z' = z \cdot e^{\psi - \psi_0 - i\varepsilon} \qquad \textbf{(A-21)}$$

$$\zeta = z' + 1/z \tag{A-22}$$

$$\zeta_{final} = (\zeta_0 - \zeta)/|\zeta_{last} - \zeta_0| \tag{A-23}$$

$$xt = real(\zeta_{final}) \tag{A-24}$$

$$yt = -imag(\zeta_{final}) \tag{A-25}$$

$$xu = xt + yt \cdot sin\theta \tag{A-26}$$

$$yu = y_{camber} + yt \cdot cos\theta \tag{A-27}$$

$$xl = xt + yt \cdot sin\theta \tag{A-28}$$

$$yl = y_{camber} - yt \cdot cos\theta \tag{A-29}$$

Where

$$\theta = \tan^{-1}(y'_{camber}) \tag{A-30}$$

A.3 Modified Supercritical Aerofoils

Several supercritical aerofoils have been added to the GENUS library. However, all aerofoil coordinates have been modified for compliance with the LAWGS geometry format, which requires independent rotation of the upper and lower surfaces, so that: $z_{TE_{up\&low}} = 0$. For aerofoils with low values of design lift coefficient the effect is almost negligible; however, large design lift coefficients result in trailing edges well below the $z = 0$ axis. The transformation follows the procedure given below, with results shown in Figure A-3:

$$\theta_{up} = \tan^{-1} z_{TE_{up}} \tag{A-31}$$

$$\theta_{low} = \tan^{-1} z_{TE_{low}} \tag{A-32}$$

$$z_{up_{rot}} = Xsin\theta_{up} + Z_{up}cos\theta_{up} \tag{A-33}$$

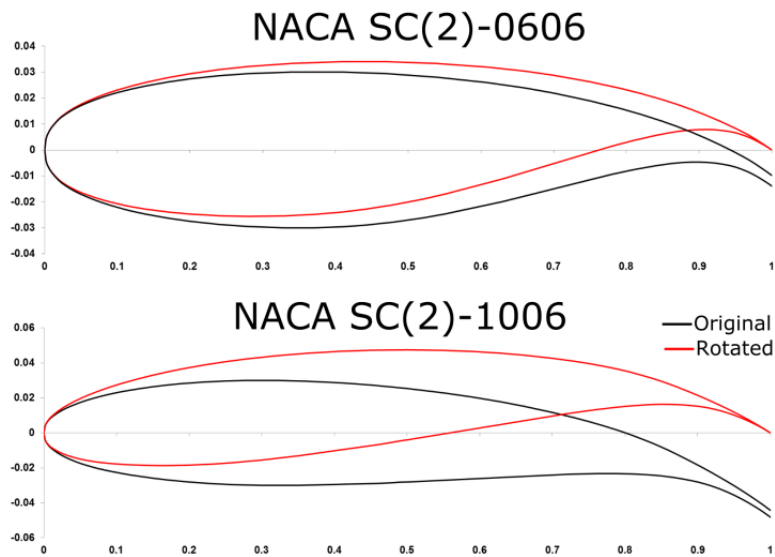$$z_{low_{rot}} = Xsin\theta_{low} + Z_{low}cos\theta_{low} \tag{A-34}$$

Figure A-3 – Modified supercritical aerofoils

A.4 Supersonic Aerofoils

Biconvex airfoils are included via the following equations:

$$y = a(x - x^b) \tag{A-35}$$

$$x_{tmax} = \left(\frac{1}{b}\right)^{\frac{1}{b-1}} \tag{A-36}$$

$$t_{max} = 2a(x_{tmax} - x_{tmax}^b) \tag{A-37}$$

Where x is the non-dimensional chord with range $x = [0, 1]$, and t_{max} is the maximum thickness to chord ratio. Iteration is required to find the value of parameter b.
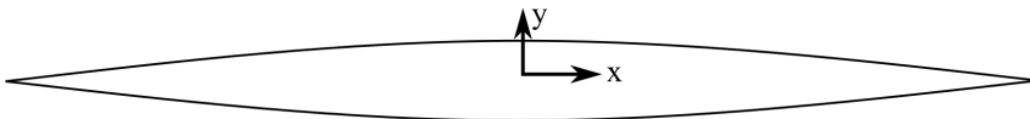

Figure A-4 - 7% thickness biconvex aerofoil, x_{tmax} at 50%

Appendix B Mass Breakdown

This appendix contains the set of Class II mass estimation methods used for subsonic and supersonic UCAV designs. Several methods have been employed during the course of this research.

B.1 Systems Mass Estimation

System mass equations, in kg, are given by Eqns. (B-1) to (B-8)[130–132].

$$M_{Elec} = 0.17M^{0.84} \tag{B-1}$$

$$M_{De-ice} = 0.13M^{0.7} \tag{B-2}$$

$$M_{Hyd} = 0.012M \tag{B-3}$$

$$M_{FCS} = 1.08M_{lb}^{0.7} \tag{B-4}$$

$$M_{Avi} = 0.4536\left[15 + \frac{0.32M_{lb}}{1000} + 5 + \frac{0.06M_{lb}}{1000} + \frac{0.15M_{lb}}{1000} + 0.12M_{lb}\right] \tag{B-5}$$

$$M_{ECS} = 0.4536\left[212\frac{M_{Avi_{lb}}}{1000}^{0.538}\right] + 0.0075M \tag{B-6}$$

$$M_{FuelSys} = 0.4536\left[80\left(N_{Eng} + N_{Tanks} - 1\right) + 0.15\sqrt{N_{Tanks}} \right.$$
$$\left. + \left(\frac{M_{fuel_{lb}}}{6.55}\right)^{0.33}\right] \tag{B-7}$$

$$M_{PropSys} = M_{EngCool} + M_{OilCool} + M_{Starter} + M_{EngCtrl} + M_{EngMounts} \tag{B-8}$$

Where M is the maximum take-off mass in kg; M_{lb} is the maximum take-off mass in lbs; $M_{fuel_{lb}}$ is the fuel mass in lbs; N_{Eng} is the total number of engines, and N_{Tanks} is the total number of fuel tanks.

Engine mass estimations are available through EngineSim as mentioned in *Section 4.5.2.2*, and through empirical estimations provided by Raymer[129, sect.10.3]. For a non-afterburning engine, the mass is given by:

$$M_{Eng} = 14.7T_{0_{kN}}^{1.1}e^{-0.045BPR} \tag{B-9}$$

While for an afterburning engine, the mass is given by:

$$M_{Eng} = 11.1 T_{0_{kN}}^{1.1} M_{N_{lim}}^{0.25} e^{-0.81BPR}$$ **(B-10)**

Where $T_{0_{kN}}$ is the sea-level thrust in kN, and $M_{N_{lim}}$ is the engine's maximum Mach number.

B.2 Miscellaneous Items Mass Estimation

Miscellaneous items include paint, and items such as parachutes and arresting hooks. The generic formula in Eq. (B-12) is applied to all elements that result from a sizing procedure where the initial dimensions are unknown and depend on a convergent design solution.

$$M_{Paint_{kg}} = 0.5 S_{wing_{m^2}}$$ **(B-11)**

$$M_{item} = V_{item} \rho_{item}$$ **(B-12)**

Other mass penalties and allowances, such as the mass dedicated to stealth measures are normally specified by the user.

Raymer recommends that the mass of furnishings be added with a crew number of 0.5 for unmanned vehicles, so that the furnishings mass in kg is:

$$M_{furnish} = 98.7 N_{crew}$$ **(B-13)**

B.3 Structures Mass Estimation

Structural mass component equations are given by Eqns. (B-14) to (B-21)[131].

$$M_{Wing} = 0.4536 \left\{ C_1 \left[10^{-6} \cdot \frac{N_Z M_{0_{lb}}}{t/c} \left\{ tan\Lambda - \frac{2(1-\lambda)}{AR(1+\lambda)} \right\}^2 + 1 \right]^{C_2} \right.$$
$$\left. \cdot AR(1+\lambda)^{C_3} S_{Wing_{ftsq}}^{C_4} \right\}$$ **(B-14)**

Where N_Z is the maximum normal acceleration factor, Λ is the sweep angle, λ is the taper ratio, t/c is the average thickness to chord ratio, AR the aspect ratio, and $S_{Wing_{ftsq}}$ is the reference wing area in squared feet.

$$M_{Fuselage} = 0.4536 \left[C_1 K_{inl}^{C_2} \left(\frac{q_{Dive_{psf}}}{100} \right)^{C_3} \left(\frac{M_{lb}}{1000} \right)^{C_4} \left(\frac{l_f}{h_f} \right)^{C_5} \right] \qquad \textbf{(B-15)}$$

Where K_{inl} is equal to 1.25 for fuselage mounted or buried engines, and 1.0 for inlets located elsewhere; $q_{Dive_{psf}}$ is the design dive dynamic pressure in lb/ft², l_f and h_f are length and maximum fuselage height in feet, respectively.

$$M_{NoseLG} = 0.4536 \left[C_1 + C_2 M_{lb}^{C_3} \right] \qquad \textbf{(B-16)}$$

$$M_{MainLG} = 0.4536 \left[C_1 + C_2 M_{lb}^{C_3} + C_4 M_{lb} \right] \qquad \textbf{(B-17)}$$

$$M_{Armament} = 0.02M \qquad \textbf{(B-18)}$$

$$M_{PowerPlantStruc} = 0.003M \qquad \textbf{(B-19)}$$

$$M_{Intake} = 0.4536 \left[13.29 K_{vg} L_{intake_{ft}}^{0.643} K_d^{0.182} N_{Eng}^{1.498} \left(L_s / L_d \right)^{-0.373} D_{Eng_{ft}} \right] \qquad \textbf{(B-20)}$$

$$M_{Tailpipe} = 0.4536 \left[3.5 D_{Eng_{ft}} N_{Eng} L_{ft} \right] \qquad \textbf{(B-21)}$$

Where $D_{Eng_{ft}}$ is the engine diameter in feet, L_{ft} is the length of the tailpipe in feet, and the intake factor K_{vg} is equal to 1.62 for a variable geometry inlet or 1.0 otherwise.

The non-dimensional intake factors K_d, L_s/L_d of Eq. (B-20) and the intake geometry definition are shown in Figure B-1.
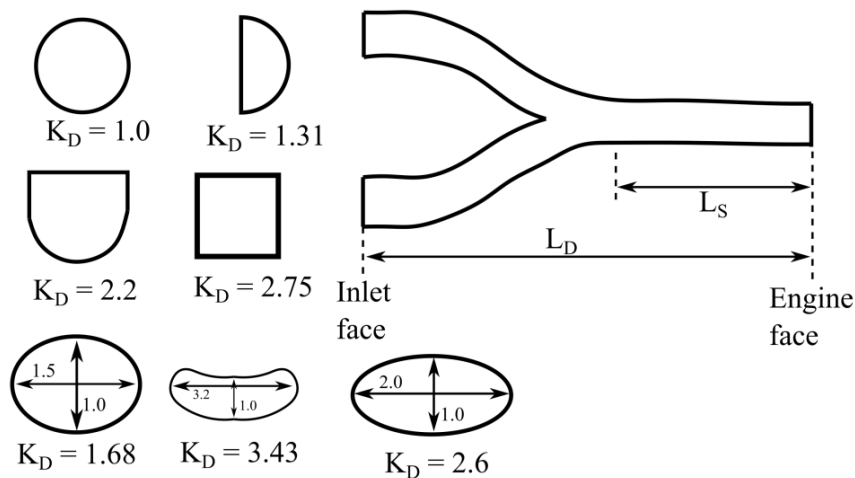

Figure B-1 - Intake geometry factors

For supersonic mixed compression inlets, Nicolai[145, chap.20] provides empirical mass estimations. For variable geometry ramps (all units in English system):

$$M_{intake} = 4.079[N_{Eng}L_{Intake}A_{intake}^{0.5}K_{TE}]^{1.201} \tag{B-22}$$

$$K_{TE} = \begin{cases} 1.0, & M_D < 3.0 \\ (M_D + 2)/5, & 3.0 \leq M_D \geq 6.0 \end{cases} \tag{B-23}$$

Where L_{Intake} and A_{Intake} are the length and frontal area of the intake in feet and squared feet, respectively, and M_D is the engine design Mach number.

For a half-round fixed spike (all units in English system):

$$M_{Intake} = 12.53[N_{Eng}A_{Intake}] \tag{B-24}$$

For a full-round translating spike (all units in English system):

$$M_{Intake} = 15.65[N_{Eng}A_{Intake}] \tag{B-25}$$

For a full-round translating and expanding spike (all units in English system):

$$M_{Intake} = 51.8[N_{Eng}A_{Intake}] \tag{B-26}$$

The structural masses coefficients vary for carrier-based and normal operations, with values summarised in Table B-1.

Table B-1 - Naval and regular mass coefficients[131]

Component	Normal	Naval
Wing	$C_1 = 3.08$	$C_1 = 19.29$
	$C_2 = 0.593$	$C_2 = 0.464$
	$C_3 = 0.89$	$C_3 = 0.70$
	$C_4 = 0.741$	$C_4 = 0.58$
Fuselage	$C_1 = 20.86$	$C_1 = 11.03$
	$C_2 = 1.42$	$C_2 = 1.23$
	$C_3 = 0.283$	$C_3 = 0.245$
	$C_4 = 0.95$	$C_4 = 0.98$
	$C_5 = 0.71$	$C_5 = 0.61$
Nose landing gear	$C_1 = 12.48$	$C_1 = 0.0$

	$C_2 = 0.0624$	$C_2 = 0.203$
	$C_3 = 0.75$	$C_3 = 0.66$
Main landing gear	$C_1 = 34.32$	$C_1 = 0.0$
	$C_2 = 0.0416$	$C_2 = 1.1491$
	$C_3 = 0.75$	$C_3 = 0.66$
	$C_4 = 0.02184$	$C_4 = 0.0$

Additionally, a *technology reduction factor* can be applied to structural mass components, especially to the wing and fuselage, to account for composite materials. A conservative estimate for subsonic and moderately supersonic aircraft is a structural mass reduction between 10% and 15% due to advanced materials and manufacturing practices.

Appendix C PANAIR Geometry Format

This section provides additional details on the structured grids geometric processing algorithm developed for the aerodynamic analysis of arbitrary three-dimensional geometries in PANAIR.

C.1 Meshing Algorithm

Due to the specific geometrical input required for the aerodynamic analysis in PANAIR, a special algorithm had to be developed. This algorithm has been applied to configurations with a central fuselage and an array of lifting surfaces, as well as flying wings.

In its present form this algorithm cannot account for the following geometries and configurations:

1. Bi-planes
2. Box wings
3. Wing or fuselage mounted nacelles
4. Blended engine nacelles and serpentine inlets
5. Distributed propulsion systems
6. Twin tail boom body components
7. Rotorcraft

The meshing algorithm follows a three-step process by which all the geometrical components are first identified and classified; subsequently, the various components are independently meshed according to the correct point order and mesh divisions; the last step includes making sure the network edges match and that the *{XYZ}* coordinate lists, boundary conditions, and wakes are in the correct order. This process is schematically shown in Figure C-1.

The central component for the meshing algorithm is the main wing, the order and location of additional lifting surfaces (canard, tail plane) has a large influence over the fuselage network number and arrangement. Furthermore, the root airfoils

coordinates of all lifting surfaces have to be mapped to the fuselage side or top surface in order to avoid geometric discontinuities.
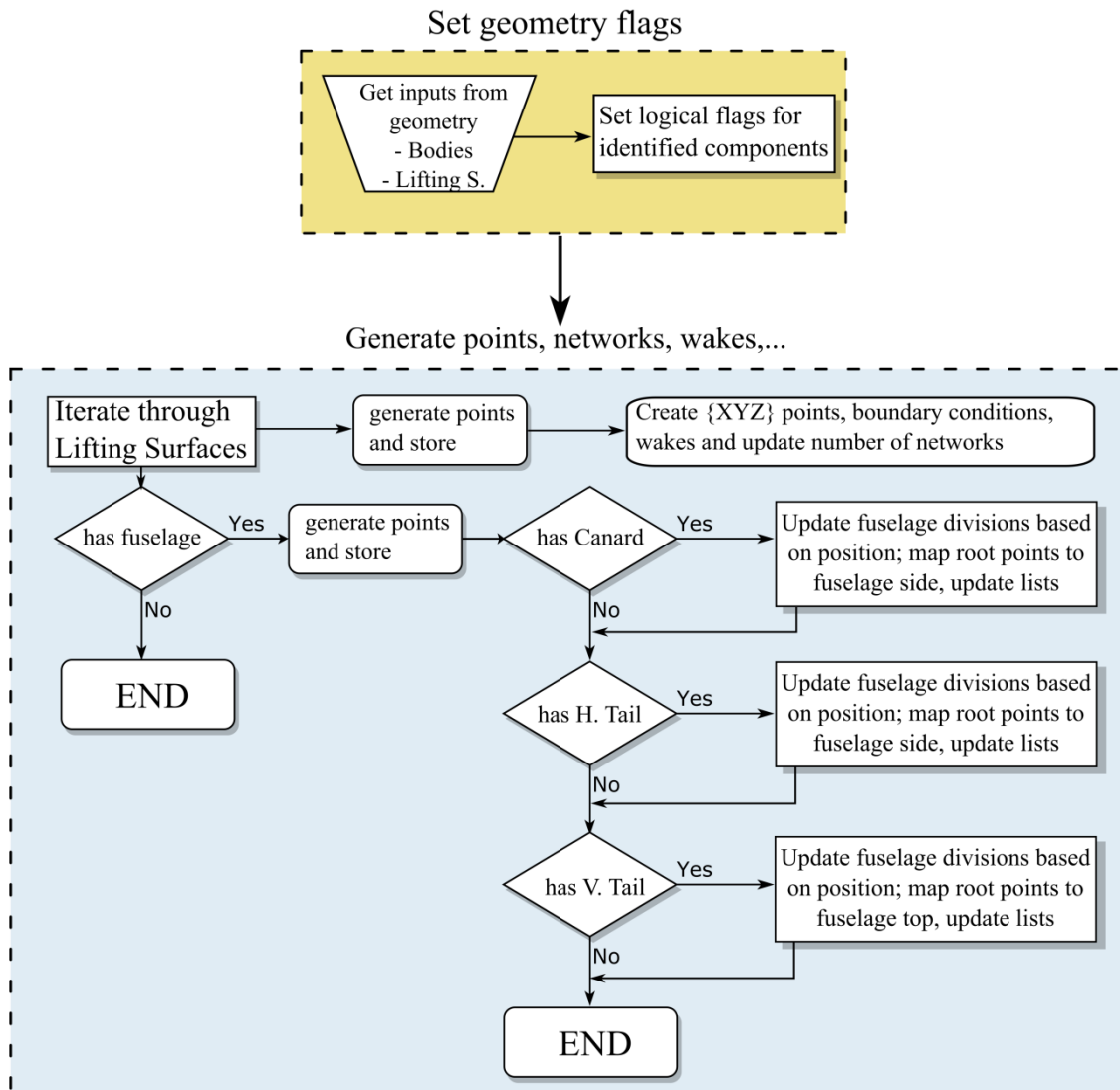

Figure C-1 - PANAIR meshing algorithm flow chart

The lifting surface designated as the main wing is meshed as a thick impermeable surface, with the mesh density controlled by chord-wise and span-wise divisions (per kink) in the order depicted by the arrows and axes shown in Figure C-2. All other lifting surfaces are idealised as thin surfaces meshed at the camber line and declared as 'thick' surfaces during the analysis through a special boundary condition available in the PANAIR code.
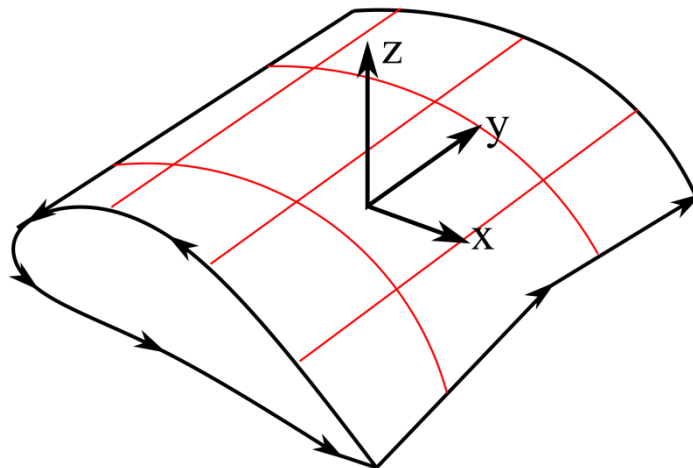
Figure C-2 - Panel order for lifting surfaces

For body components, the mesh density is controlled by divisions in the Z axis and the longitudinal axis, with the correct point order shown by the arrows and axes shown in Figure C-3 (longitudinal symmetry plane).
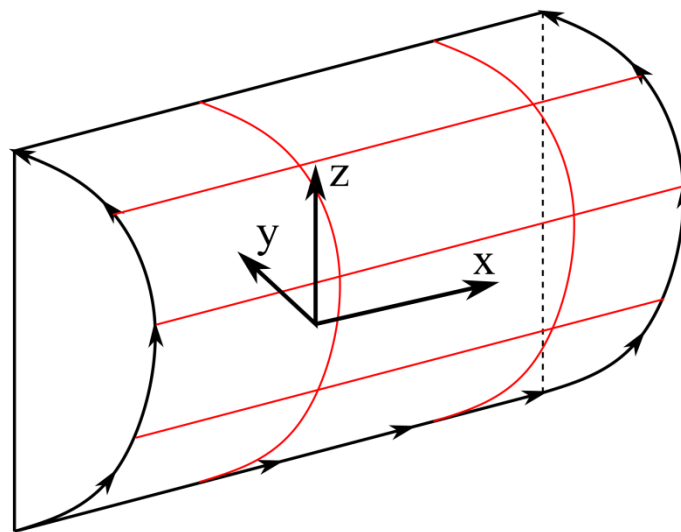
Figure C-3 - Panel order for body components

During the next step of the meshing process, the fuselage networks (if there are any) are corrected according to the number and position of the lifting surfaces. Specifically, the location and overlapping (on the longitudinal axis) of the surfaces needs to be considered. Figure C-4 shows only some of the variations in fuselage network divisions due to multiple lifting surfaces.
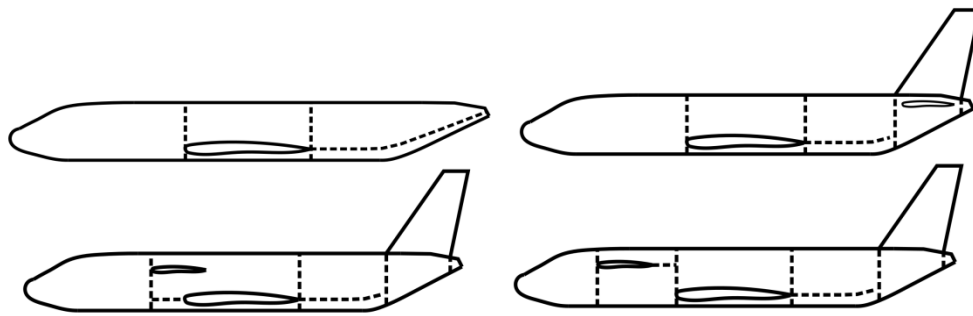
Figure C-4 - Fuselage network divisions

C.1.1 Network Abutments

The final step in the meshing algorithm is to ensure that the edges of contiguous networks match point by point. This can happen between the networks of a lifting surface and a body component, or several networks in a single body component. Since the variables that control mesh density for lifting surfaces and body components are independent of each other, this is done once the entirety of the three-dimensional grid points have been generated.

For the case of the root aerofoil coordinates mapped onto the surface of a body component, longitudinal and vertical locations of the root aerofoil points are located, the generated points on the body component skin that are closest to the root aerofoil are then substituted with the exact copies in {XYZ} of the root aerofoil, as schematically shown in Figure C-5.
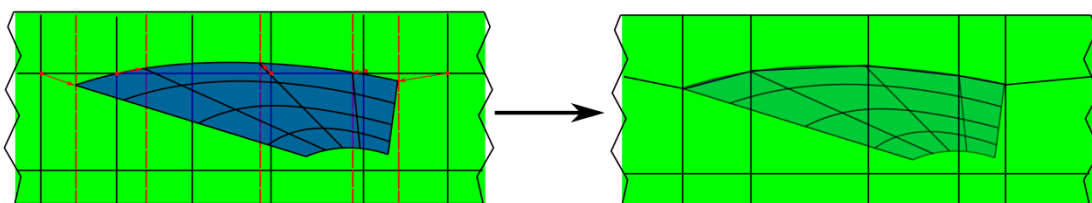

Figure C-5 - Fuselage point correction and root chord mapping

For contiguous body component networks in the presence or vicinity of a lifting surface, several non-dimensional ratios need to be obtained with reference to the main lifting surfaces in the configuration. These ratios are then used to substitute and correct the vertical positions of the abutting edges of the body component networks, as schematically shown in Figure C-6. The longitudinal panel locations

need to be mapped to any existing root aerofoils, including canard, vertical and horizontal tail planes.

The complexity and number of correction performed during this part of the process increases with the number of lifting surfaces, with the most complex scenario being that of a three-surface configuration.

$$\xi_{TE} = \frac{Z_{TE}}{Z_{Fus}}$$
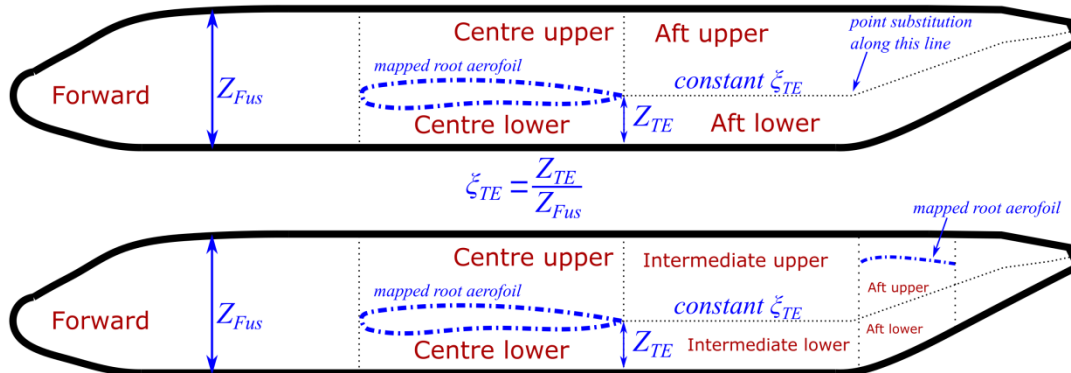
**Figure C-6 - Body component network abutment schematic**

Finally, visualisation of the structured grids and aerodynamic results (pressure coefficients) is available through the open source post-processing tool pyNastran GUI (external to GENUS). Figure C-7 shows various configurations meshed through the algorithm here explained; the point correction and additional lines due to overlapping lifting surfaces is clearly visible in the supersonic business jet configuration for the wing-canard combination, and for the tail segment of the airliner geometry. Also, the pressure distribution on the upper and lower sides of a three-surface supersonic business jet can be observed.
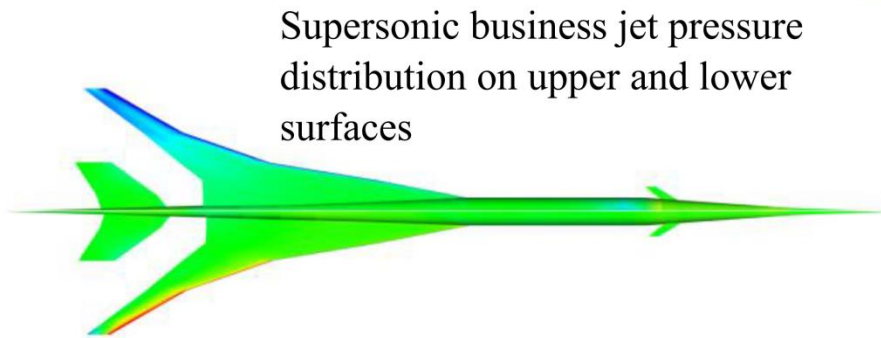
275
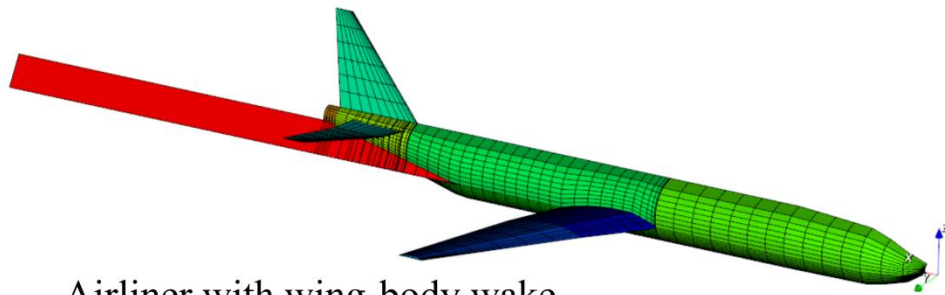
Airliner with wing-body wake
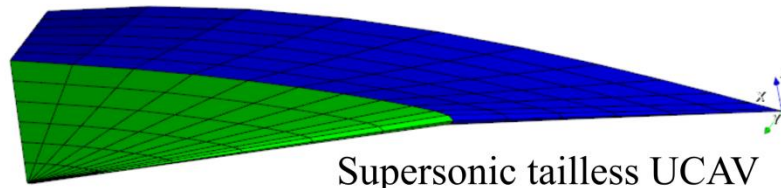
Supersonic tailless UCAV
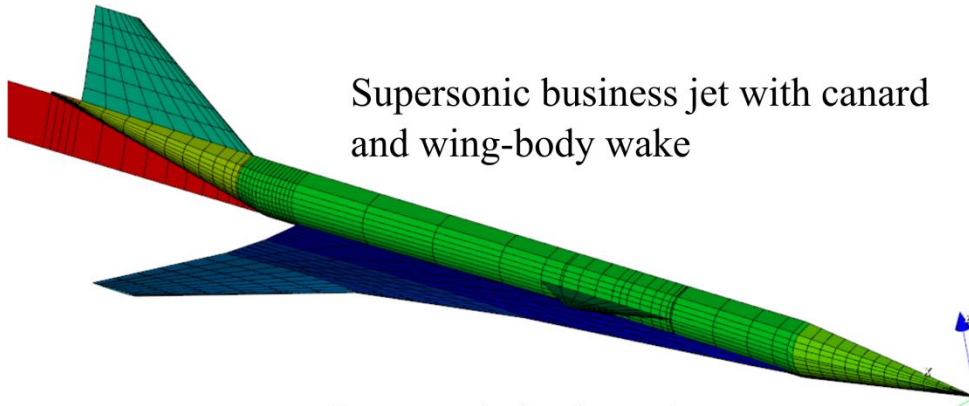
Supersonic business jet with canard and wing-body wake

Supersonic business jet pressure distribution on upper and lower surfaces

Figure C-7 - Panel visualisation over several configurations

C.2 Java Native Interface - C++ - FORTRAN Integration

As explained previously, PANAIR's FORTRAN source code has been linked to the GENUS framework through the JNI functionality, a C++ wrapper file, and finally, a static DLL file. For a schematic diagram of this process, see Figure 4-20.

A brief example of the code structure will be included in this appendix for future references. The native method that calls PANAIR at a given Mach number in the Java file `callPANAIR.java` is:

```
/**
 * This calls the program from the .dll
 */
```

```
native void runPANAIRatM(double[] Mach, double[] alpha, double[] beta, int
Nrmachs, int Nralphas, double span, double cbar, double dref, double sref, double
xref, double yref, double zref, int[] kt, int[] nm, int[] nn, double[] stuffx,
double[] stuffy, double[] stuffz, int[] netsid, int[] netwithwake, int[]
wakeedge, double xwake,int networks, int wakes, int wakenetworks, int geomsize,
double WingApex, double WingEnd, int[] wingnetsid, int wingnetsnum, int
sectional);
```

This method is then called inside the Java method that returns the aerodynamic coefficients matrix `getCoefficients`. A header file (.h) is created by the JNI compiler, which identifies the native method as:

```
JNIEXPORT void JNICALL Java_genus_aerodynamics_PANAIR_callPANAIR1_runPANAIRatM
(JNIEnv *, jobject, jdoubleArray, jdoubleArray, jdoubleArray, jint, jint,
jdouble, jdouble, jdouble, jdouble, jdouble, jdouble, jdouble, jintArray,
jintArray, jintArray, jdoubleArray, jdoubleArray, jdoubleArray, jintArray,
jintArray, jintArray, jdouble, jint, jint, jint, jint);
```

This file is referenced in the C++ wrapper (.cpp) file by including the following line:

```
#include "genus_aerodynamics_PANAIR_callPANAIR1.h"
```

Inside the C++ file, the FORTRAN subroutines inputs are specified by:

```
extern "C" void panairaerodynamics_( /All the necessary inputs/)
```

And these FORTRAN subroutines are linked to Java native methods through:

```
JNIEXPORT void JNICALL Java_genus_aerodynamics_PANAIR_callPANAIR1_runPANAIRatM
(/All inputs from Java/) {

* Perform the necessary data conversion from Java data types to C++ types *

        panairaerodynamics_( /All the necessary inputs/)

}
```

To compile the DLL, the following files are necessary:

1. Java class file with the native methods (*.java)

2. JNI header file (*.h)

3. The C++ wrapper file (*.cpp)

4. The FORTRAN source code (*.f90, or *.f)

The compiling procedure is as follows: The FORTRAN source code is compiled into an object file '*.o' through the compiler command:

```
gfortran -c fortranfile.f -m64 -O3
```

The header file is generated through the following command:

```
javah -jni genus.aerodynamics.PANAIR.callPANAIR
```

The C++ file (which includes the JNI header file) is compiled into an object file through the following command

```
g++ -c cppfile.cpp -m64
```

Finally, to combine all files into a DLL, the following command is used

```
g++ fortranfile.o cppfile.o -o DLLname.dll -m64 -shared -static -lgfortran
```

The *static* flag guarantees the ability to copy, or cut, and paste the DLL file into a different folder. Finally, to call the DLL file from the GENUS framework, the DLL file must be located in the main GENUS folder, and the following statement must be included in `callPANAIR.java`:

```
static {

    System.loadLibrary("DLLname");

}
```

Appendix D Radar Cross Section

This section provides details on the implementation of the physical optics approximation method for RCS estimation. The core calculations have been adapted from the original POFACETS code in its Matlab form, and transcribed into a Java method integrated in a special module inside GENUS.

D.1 Geometry Discretization

Due to the discrete geometric definition within GENUS, which divides a vehicle into body components and lifting surfaces, a RCS-specific geometry format had to be developed. According to POFACETS' documentation[173,211], the target geometry must be discretized in triangular facets, with each facet having an area and a normal vector, which contribute to the overall scattered field. Normal vectors should point outwards in order to properly evaluate if they are being 'illuminated' by the incident wave.

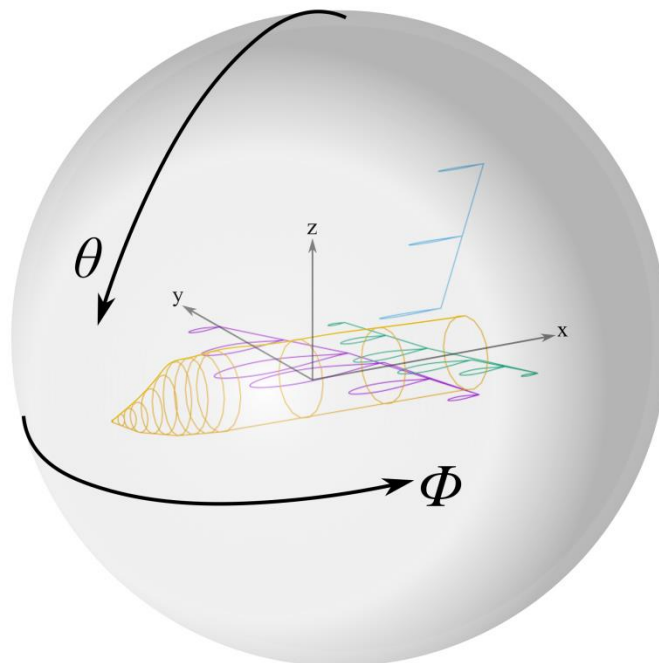The main body axes as well as the rotation axes are illustrated in Figure D-1.

Figure D-1 - Rotation axes for radar cross section calculations

Research into geometry discretization algorithms resulted in the use of convex hulls for three dimensional objects. An easy visualization of the convex hull for a set of points on a plane is the shape enclosed by a rubber band stretched over the points, imagining the points as sticking out of the plane, as shown in Figure D-2. A formal mathematical definition of convex hulls in N-dimensional space is out of the scope of this research.
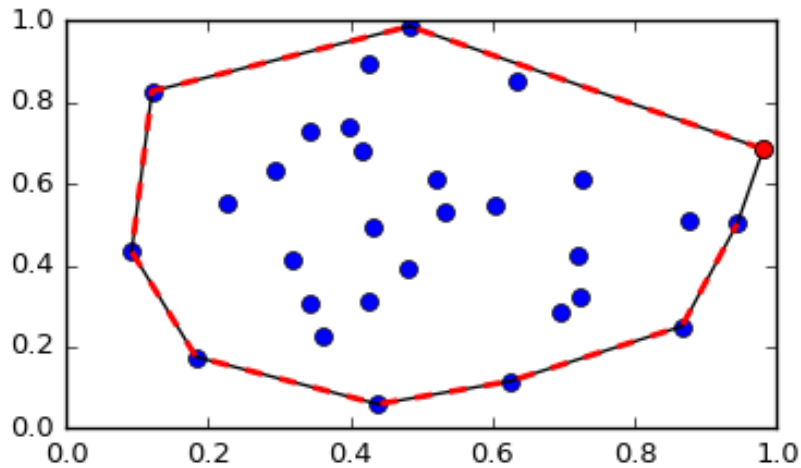

Figure D-2 - Convex hull of a set of 2D points

To alleviate computational complexity the Java library "QuickHull3D"[179] has been used. This library allows the user to build a convex hull from an array of three dimensional points, as well as triangulate the hull's surfaces through a Delaunay triangulation algorithm. To correctly capture the geometry, multiple convex hulls are created at each geometrical section; otherwise the geometry is inaccurately represented by its overall convex hull, as schematically shown in Figure D-3 for a simple lambda wing configuration. This process involves generating a set of three dimensional points over the specified range, generating individual hulls, and assigning them to a list in a particular order. After this operation, the QuickHull3D library performs a Delaunay triangulation in order to generate only triangular facets. The facet properties are stored in a list over which the physical optics approximation equations will iterate. The facets are then stored in the right order along with their nomenclature and geometric properties, which are shown in Figure D-4.
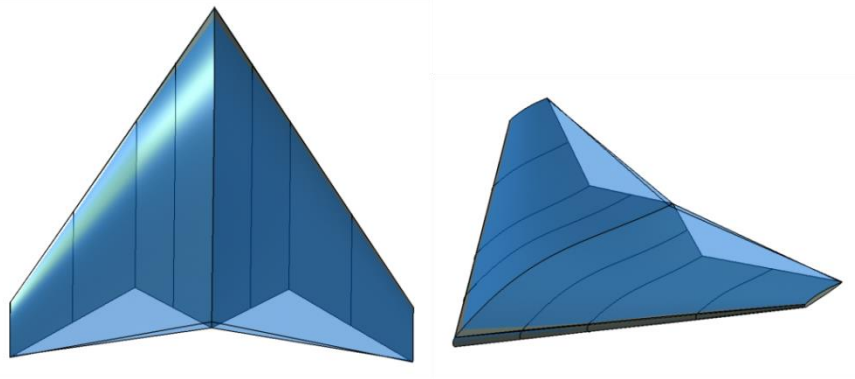
Figure D-3 - Convex hull (blue transparency) over a lambda wing geometry
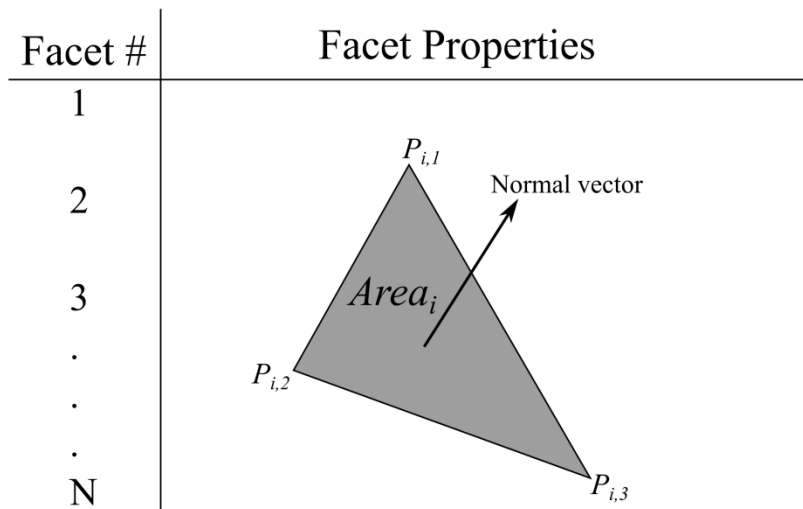

Figure D-4 – Schematic of facet list and properties

Two parameters control the fineness of the convex hulls over a wing section; divisions per kink and chord-wise divisions. A mesh sensitivity analysis has been performed and results are shown in the following section.

D.2 Mesh sensitivity study

Due to the complex shapes of aerofoils, and their translation and rotation along the span direction, it is necessary to determine mesh densities that provide accurate results without greatly compromising computational costs.

Divisions in the span-wise and chord-wise directions were varied while maintaining one fixed in order to evaluate the influence of each parameter. The total number of facets and the execution time were also compared.
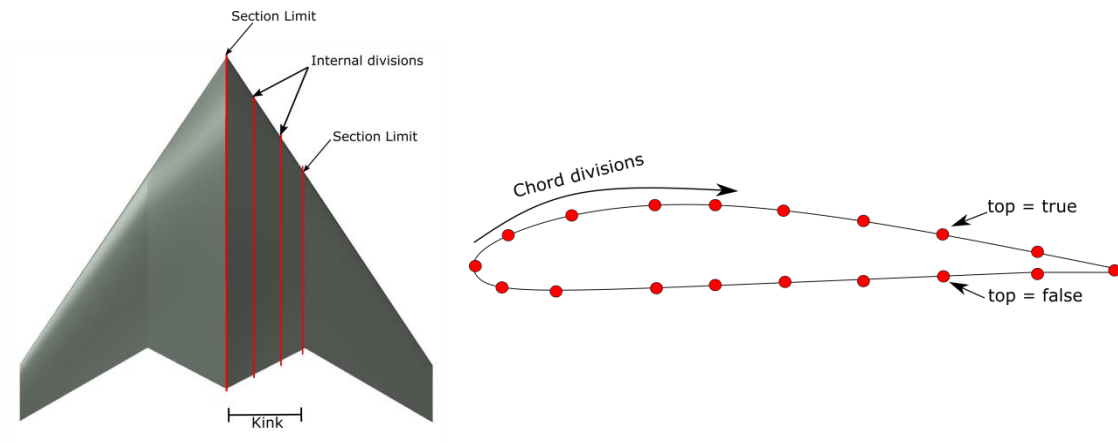
Figure D-5 - Divisions along the span and chord directions

The results shown below are for varying divisions along the span while maintaining chord-wise division constant (10 on extrados and 10 on intrados).
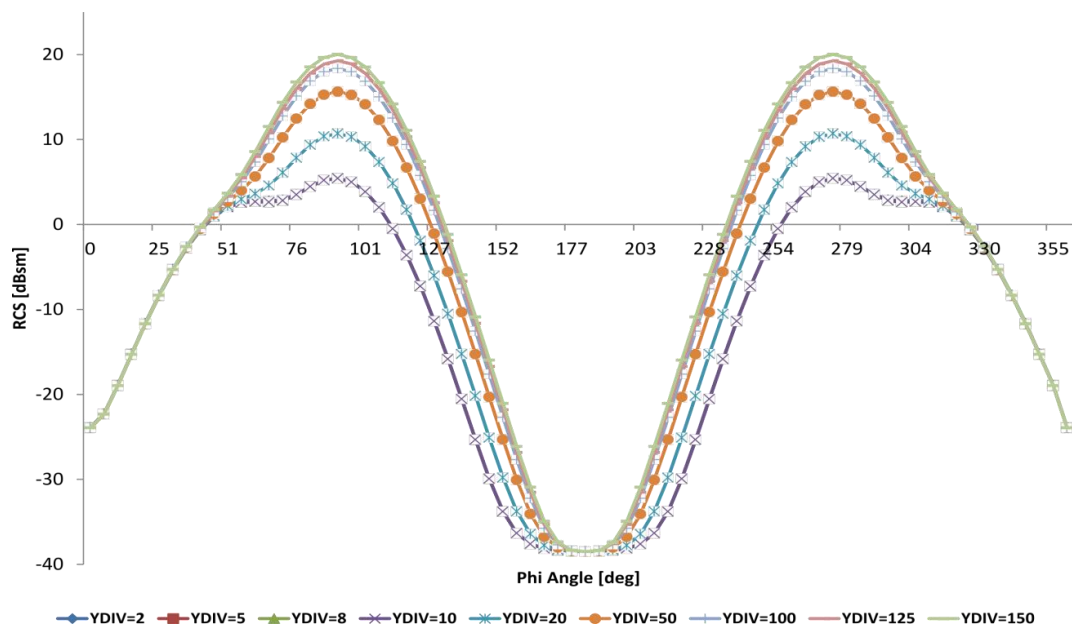
Figure D-6 - Results over a lambda wing UCAV for variations in span-wise divisions

It can be seen that at very low values, below 10 divisions per kink, results do not vary; a similar trend can be seen for very high values, greater than 100 divisions per kink. At intermediate values, such as 20 and 50, results vary significantly, however the same trend in results is followed by all span-wise divisions. The result for number of facets versus execution time is shown in Figure D-7.
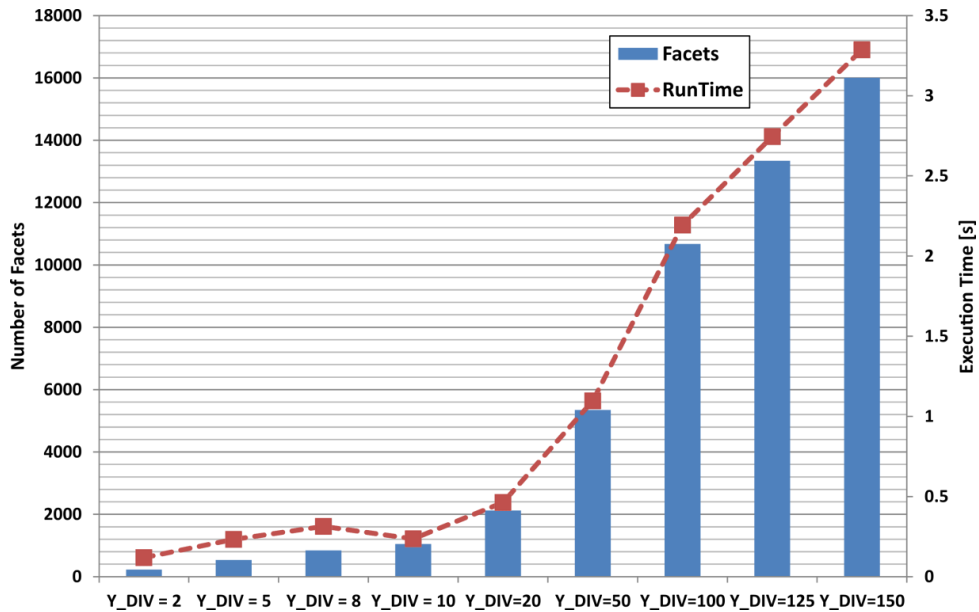
Figure D-7 - Facets versus execution time for increases divisions in the span-wise direction

Variations in the chord-wise direction were done for a fixed value of 100 divisions per kink; results are shown in Figure D-8. It can be seen that at values higher than 10, and converging for values as high as 80 chord divisions, a higher RCS value is captured at orientations between 20 and 75 degrees. Similarly, the trade-off between number of facets and execution time is shown in Figure D-9.

The conclusion from this analysis shows that to obtain accurate results span-wise divisions per kink should be at least 100 while chord-wise divisions should exceed 15. If a maximum 10% error across all angles is tolerable, span divisions could be reduced to 50 and chord divisions fixed at 15, which results in run times 80-100% shorter compared to a 100 x 15 grid.
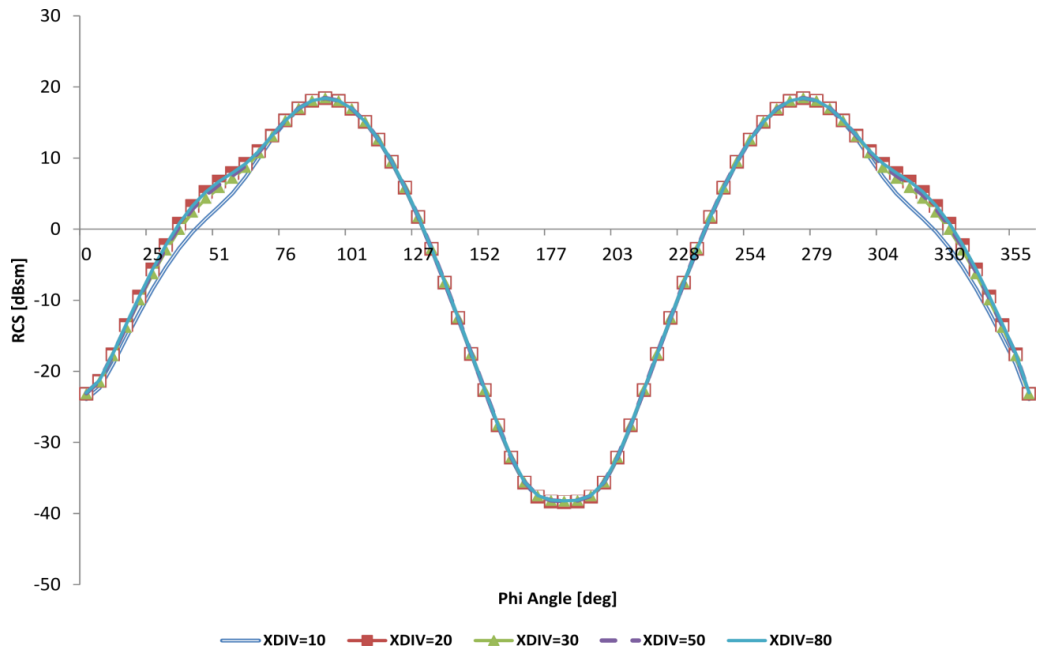
Figure D-8 - Results over a lambda wing UCAV for variations in chord-wise divisions
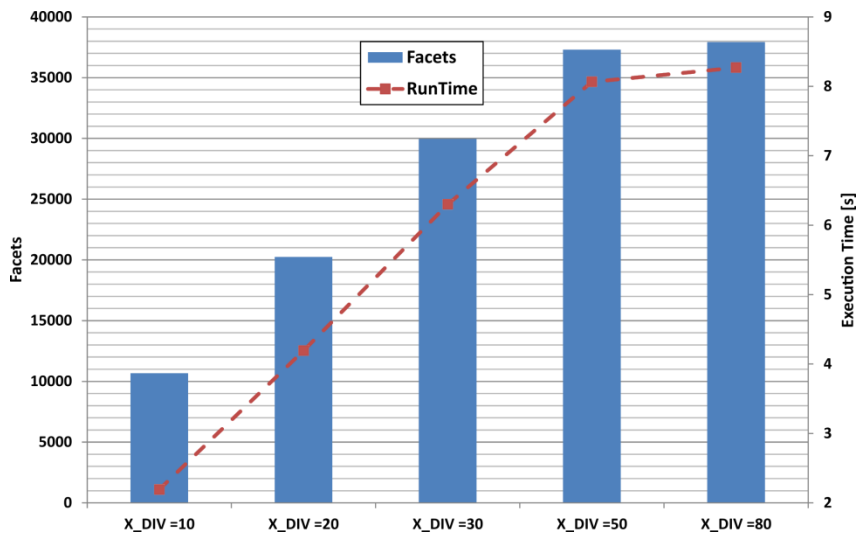

Figure D-9 - Facets versus execution time for increases divisions in the chord-wise direction

Appendix E Subsonic UCAV Framework Validation

This section will repeat the GENUS framework validation exercise published in the journal article "*Multidisciplinary analysis of subsonic stealth unmanned combat aerial vehicles*" by the CEAS Aeronautical Journal (2019).

E.1.1 Validation Exercise

The presented methodologies (subsonic UCAV design methodologies) are evaluated through AIAA's Unmanned Strike Fighter Request for Proposal (RFP)[212]. The relevant requirements are summarised in Table E-1.

Table E-1 - Unmanned Strike Fighter RFP

Payload	2000 lb JDAM
Range/performance	800 nm radius, cruise Mach ≥ 0.7 at 40,000+ ft with 1.5 turns mid-mission at cruise speed/alt., instant. turn rate ≥ 20 deg/s. Ingress/egress of 100 nm each at Mach 0.9 and 250 ft.
Acceleration	M = 0.4 to 0.8 at 5000 ft. in 40 sec
Specific excess power	> 200 ft/s at 5000 ft. and M = 0.4
Ferry Range:	3,000 nm (external tanks allowed)
Take-off/landing:	< 5000 ft
Propulsion	Off-the-shelf commercial jet engine
Signature	Low-observables (RCS & IR) ~ set as <-20 dBsm nose-on view S-band (~3 GHz)
Avionics	500 lb allowance for classified treatments avionics

The design starting point consists of a lambda-wing UCAV geometry, which can be parametrised with the 7 inputs shown in Figure E-1, with the addition of the aerofoil incidence angle at each wing station. NACA6 aerofoils are used through design process, with thicknesses varying across the span, from 15% at the centre to 10% at the tip. This initial design does not comply with several mission constraints.

The propulsion system is assumed to be a buried, central low-bypass turbofan. The payload has been divided into 2 internal weapon bays, each carrying one GBU-32 JDAM. Longitudinal control is achieved through elevons located in the first wing kink, with the chord ratio chosen as that to satisfy trim constraints for all flight conditions. Table E-2 shows the lower and upper bounds on the input variables, as well as the initial and final design points' characteristics.
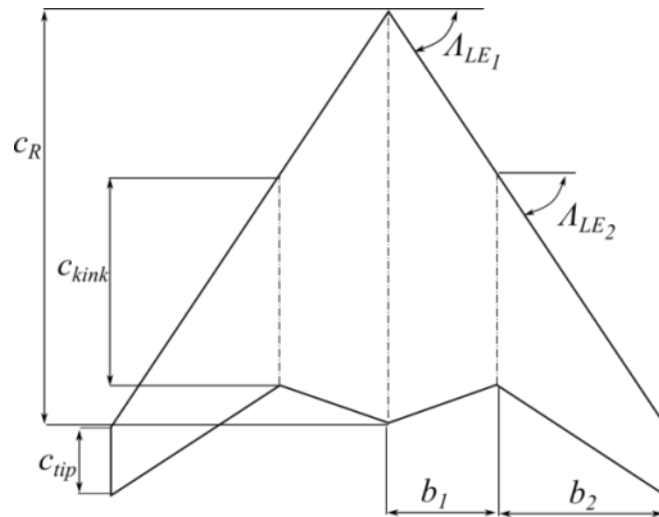
Figure E-1 - Geometry input parameters, lambda wing UCAV

Figure E-2 shows the top view comparison between the initial design point and the optimised configurations, overall length and wing span, as well as the location of the internal weapon bays.

It can be seen that the resulting configurations shows a significant improvement in the aerodynamic performance of the vehicle, which results in a smaller engine and consequently 25.2% less fuel required. The gross mass reduction is approximately 8%. Furthermore, an improvement in longitudinal stability is also observed, however the upper static margin limit was violated. Figure E-3 shows mass and static margin profiles throughout the mission segments, the drag polar for both configurations at the cruise condition, as well as the mass breakdown.

**Table E-2 - Unmanned Strike Fighter optimisation results**

Design Parameters	Lower Bound	Upper Bound	USF_0	USF_{Opt}
C_{Root} [m]	5	6.5	6	5.85
C_{Kink} [m]	2.5	3.8	3.6	3.8

C_{Tip} [m]	0.1	1	0.5	1
b_1 [m]	1	3	1.25	1.69
b_2 [m]	2.5	4	2.98	3.45
Λ_{LE1}	40°	65°	56.7°	55.7°
Λ_{LE2}	40°	65°	56.7°	53.6°
Incidence$_{Root}$	-2°	2°	0°	2°
Incidence$_{Kink}$	-2°	2°	0°	-2
Incidence$_{Tip}$	-3°	1°	0°	-1.5°
MTOM [kg]	5500	7500	6758	6221
OEM [kg]	-	-	3601	3588
Fuel [kg]	1200	2800	2250	1682
(L/D)$_{Cruise}$	-	-	16.6	18.4
(L/D)$_{Ingress/Egress}$	-	-	10.4	19.4
S_{Wing} [m^2]	-	-	24.2	32.9
Span [m]	-	-	8.46	10.28
AR	-	-	2.96	3.21
Sea Level Thrust [kN]	-	-	46.6	44.32
Mission and Design Constraints				
$L_{Take-off}$ [m]	-	1500	1102	460
$L_{Landing}$ [m]	-	1500	1513	1448
Specific E. Power [m/s]	60	-	69	67.9
Acceleration time [s]	-	40	35	37
Nose-on RCS[dBsm]	-	-20	-27.8	-25.3
Static Margin [%]	-15	15	-16.6(min)	-13.6(min)
			-1.5(min)	21.2(max)

Figure 15 shows the comparison of RCS signatures for both configurations, assuming perfect electric conductor as material. The integration of the RCS

analysis into the optimisation loop, added with a library of radar absorbent materials is still in progress and will be the topic of a dedicated paper.
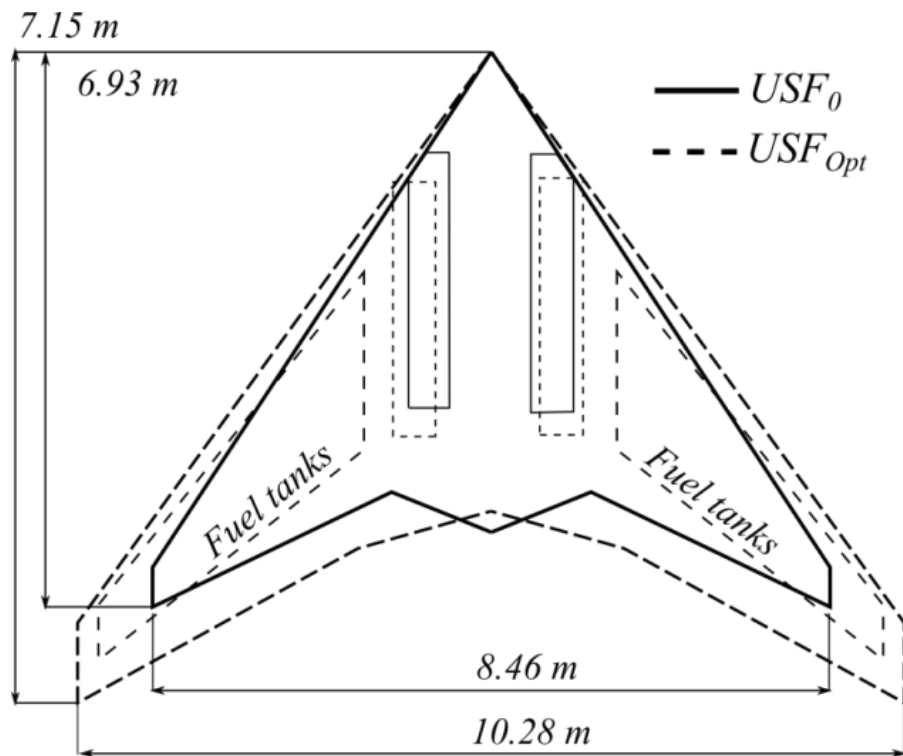
Figure E-2 - Top view comparison between design starting point and optimised design

Figure E-4 shows the comparison of RCS signatures for both configurations, assuming perfect electric conductor as material. The integration of the RCS analysis into the optimisation loop, added with a library of radar absorbent materials is still in progress and will be the topic of a dedicated paper.
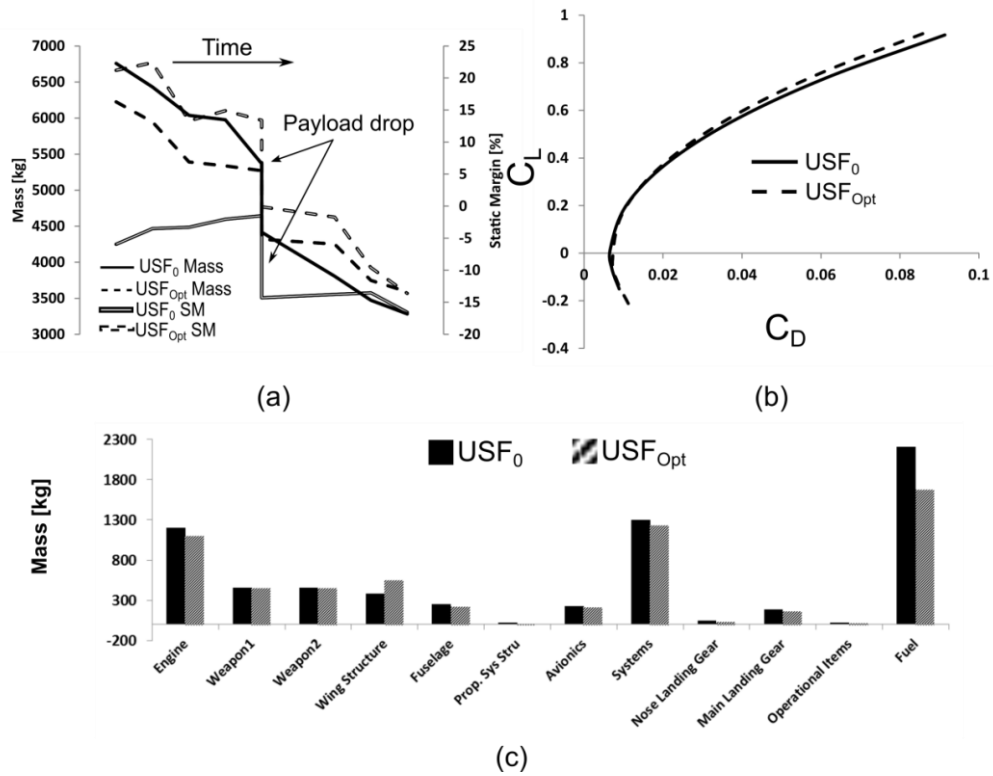
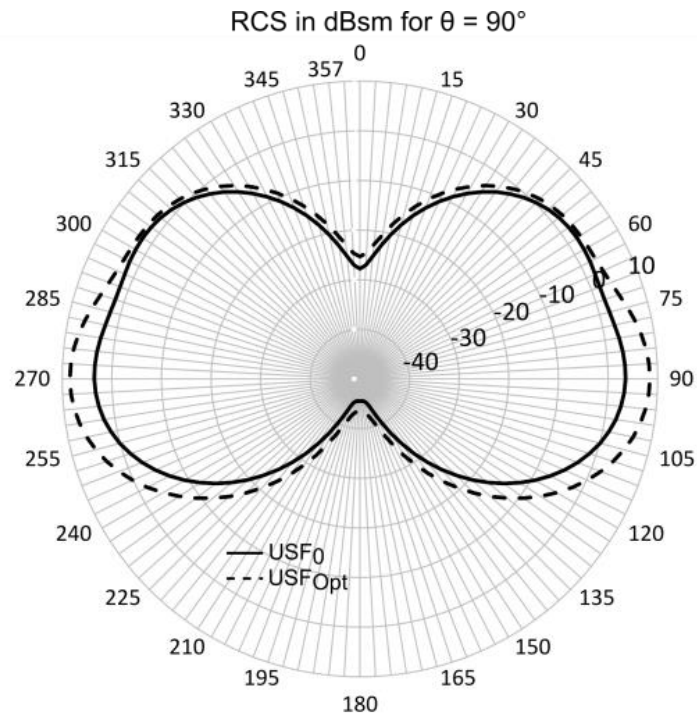Figure E-3 - Mass and static margin profiles (a), drag polar M = 0. 7 (b), and mass breakdown (c)

Figure E-4 - RCS signature comparison

289

E.1.2 Conclusions from the publication

An aircraft design, analysis, and optimisation environment has been shown in its application to low-observable Unmanned Combat Aerial Vehicles. The methodologies vary from empirical regressions to physics-based numerical solutions, with multiple fidelity levels included for various disciplines. The methodologies so far cover subsonic and low supersonic designs and missions, which are the most likely roles for UCAVs to perform in the near future.

Mass breakdown methods resulted in good agreement between UCAV quoted data and calculated maximum take-off mass and operating empty mass, while maintaining design sensitivity, and not purely statistical approximations.

The higher order panel method Panair has been efficiently integrated into the design environment to perform automatic aerodynamic analysis of arbitrary configurations for speed regimes up to Mach 4.0. Similarly, USAF digital Datcom performs automatic stability and control analysis for full configurations including longitudinal control surfaces such as elevons.

Low-observability analysis is currently limited to monostatic radar cross section signatures of clean configurations. This analysis has been adapted from the well-known POFACETS code, with excellent agreement of results between platforms.

Finally, a lambda-wing unmanned strike fighter UCAV configuration has been designed following AIAA's Unmanned Strike Fighter RFP. The GENUS framework UCAV modules are applied to improving the initial design point in order to comply with the mission requirements. A significant improvement in aerodynamic performance is shown, as well as a take-off mass reduction of 8% and a fuel mass reduction of 25%.

Appendix F Publications

This research project has resulted in the following publications:

F.1 Journal Articles

1. Sepulveda E., Smith H. *Technology challenges of stealth unmanned combat aerial vehicles.* The Aeronautical Journal. 2017; 121(1243): 1261–1295; Available at: DOI: 10.1017/aer.2017.53.

2. Sepulveda E., Smith H., Sziroczák D. *Multidisciplinary analysis of subsonic stealth unmanned combat aerial vehicles.* CEAS Aeronautical Journal. *2019; 10(2): 431–442.* Available at: DOI: 10.1007/s13272-018-0325-0

3. Sepulveda E., Smith H. *Impact of mission requirements on the design of low-observable UCAV configurations.* Aircraft Engineering and Aerospace Technology. 2019; 91(10): 1295–1307. Available at: DOI: 10.1108/AEAT-09-2018-0249

F.2 Conference Papers

1. Sepulveda E., Smith H. *Conceptual design of a fifth generation unmanned strike fighter.* AIAA SciTech (2019). 7-11 January. San Diego, California; Available at: DOI: 10.2514/6.2019-0811.